Resolved gamma ray emission of the supernova remnant W51C and HESS J1857+026 obtained with the MAGIC telescopes

Julian D. G. Krause

München 2012

Resolved gamma ray emission of the supernova remnant W51C and HESS J1857+026 obtained with the MAGIC telescopes

Julian D. G. Krause
geboren in Bad Honnef

Dissertation in Physik

angefertigt am

Max Planck Institut für Physik

vorgelegt

der Fakultät für Physik

der

Ludwig-Maximilians-Universität München

München, den 14. Dezember 2012

Zusammenfassung

Diese Dissertation untersucht den Urspung der kosmichen Strahlung mit Beobachtungen der MAGIC Teleskope im Bereich der hoch energeticher Gammastrahlenastronomie. Gammastrahlung wird bei der Wechselwirkung relativistischer Teilchen erzeugt. Im Gegensatz zur geladenen kosmichen Strahlung, werden Gammastrahlen nicht von interstellaren Magnetfeldern beeinflusst. Daher erlaubt die Ankunftsrichtung von Gammastrahlen die Bestimmung ihres Ursprungs. Ein Teil dieser Arbeit widmet sich der Verbesserung der Analyse von MAGIC-daten. Im besonderen wurde ein neuer Algorithmus zur Hintergrundbestimmung entwickelt, wodurch die systematischen Unsicherheiten deutlich verbessert werden konnten. Zudem wurde die Reflekivität und Fokusierung beider MAGIC Teleskope anhand des Vergleichs zwischen echten und simulierten Muonereignissen bestimmt.

Die heutige Meinung ist, dass die Überreste von Supernovae, die expandierende Schockwellen der Sternimplosionen, der Ursprung der galaktischen kosmischen Strahlung sind. Obwohl hoch energetische Gammastrahlung von vielen dieser Objekte beobachtet wurde, erlaubt die schwierige Unterscheidung von leptonisch und hadronsich produzierter Gammastrahlung in den meisten Faellen keine klaren Schlussfolgerungen über die Anwesenheit relativistischer Hadronen und damit kosmischer Strahlung. Da Gammastrahlung aus hadronischen Wechselwirkungen, nahezu ausschließlich in inelastischen Proton-Proton Kollisionen erzeugt wird, ist ihre Produktion umso effektiver, desto höher die Dichte des mediums ist. Die Region W51 beherbergt den 30000 Jahre alten Supernovaüberrest W51C, welcher teilweise mit der grossen Molekülwolke W51B kollidiert. MAGIC hat ausgedehnte Gammastrahlung von dieser Region mit hoher statistischer Signifikanz ($> 11\sigma$) gemessen. Es konnte gezeigt werden, dass das Zentrum der Emission in dem Bereich hoher Dichte liegt, wo der Supernovaüberrest mit der Molekülwolke kollidiert. Das Energiespektrum wurde im Bereich von 75 GeV bis 5.5 TeV gemessen und folgt einem Potenzgesetz. Die mögliche Kontamination dieser Emission durch einen nahegelegenen potentiellen Pulsarwindnebel zeigt keine Energieabhängigkeit und wurde als $\sim 20\%$ der Gesamtemission bestimmt. Die Modellierung der nicht thermischen Multiwellenlängenemission deutet stark auf einen hadronischen Ursprung der Gammastrahlung hin. Diese Beschreibung impliziert, dass in etwa 16% der kinetsiche Energie der Schockwelle von W51C zur Produktion kosmischer Strahlung genutzt wurden. Damit is W51C eine der wenigen bekannten Supernovaüberreste wo eine Beschleunigung von Protonen der komsischer Strahlung, zumindestens bis 50 TeV, direkt beobachtet wird.

HESS J1857+026 ist eine nicht identifizierte TeV-Quelle, die möglicherweise den Pulsarwindnebel des, von der Gammastrahlung umschlossenen, hochenergetischen Pulsares PSR J1856+0245 darstellt. Eine augedehnte Emission wurde von MAGIC mit einer statistischen Signifikanz von mehr als 12σ gemessen. Das berechnete Spektrum verbindet die vorherigen Daten von *Fermi*/LAT und HESS, wobei es mit beiden Messungen überlappt. Anhand der MAGIC und *Fermi*/LAT Daten wurde ein Abweichung von einem einfachen Potenzgesetz bei ca. 100 GeV festgestellt. Bei höheren Energien werden zwei Emissionsregionen aufgelöst. Überhalb von einem TeV können zwei voneinander getrennte, einzeln signifikante Regionen festgestellt werden.

Diese Dissertation zeigt die ersten morphologischen Untersuchungen, die mit den MAGIC Teleskopen durchgeführt wurden. Es wurde gezeigt, dass die Fähigkeit Strukturen in galaktischen Quellen auflösen zu können, wichtige Informationen über die Physik der Teilchenbeschleunigung in astrophysikalischen Objekten liefert.

Abstract

This work addresses the long standing question of the origin of galactic cosmic rays by the use of very high energy gamma ray emission observed with the MAGIC telescopes. Gamma rays are produced in the interaction of relativistic particles. In contrast to the charged cosmic rays, gamma rays are not deflected by interstellar magnetic fields and therefore point back to their origin. A part of this work was dedicated to the improvement of the the MAGIC data analysis. In particular a new method to determine the background has been developed resulting in a reduction of the systematic uncertainties. Moreover, the optical point spread function and the light collection efficiency of both MAGIC telescopes have been determined by the comparison of real and simulated muon events.

The common believe is that supernova remnants are the sources of galactic cosmic rays. While several supernova remnants are known to emit very high energy gamma rays, the difficulty to distinguish between leptonic and hadronic production mechanisms prevents in most cases clear evidence for the presence of relativistic hadrons and therefore cosmic rays. Gamma rays originating from relativistic hadrons are almost exclusively produced in inelastic proton-proton interactions and therefore more efficiently produced in regions of high matter density. The region W51 host the middle-age supernova remnant W51C which partially collides with the large molecular cloud W51B. MAGIC detected extended gamma ray emission in the W51 region with $> 11\sigma$. It could be shown that the centroid of the emission is spatially consistent with the high density region of the interaction zone between the remnant and the molecular cloud. The differential energy spectrum extends from 75 GeV up to 5.5 TeV and follows simple power-law. A possible contribution of a nearby pulsar wind nebula candidate is constrained to be $\sim 20\%$ of the overall emission and shows no dependence on energy. A modeling of the non-thermal multiwavelength emission strongly suggests a hadronic origin of the observed emission. This models implies that about 16% of kinetic energy of the supernova remnant W51C has been converted into cosmic rays. W51C is therefore one of the few known supernova remnants where most likely the acceleration of cosmic rays, at least up to energies of 50 TeV per proton, is directly observed. HESS J1857+026 is an unidentified TeV source which could be explained as a pulsar wind nebula of the energetic pulsar PSR J1856+0245 enclosed in the gamma ray emission. MAGIC detected extended gamma ray emission with $> 12\sigma$ from the object. The derived spectrum connects previous measurements of *Fermi*/LAT and HESS and overlaps with both of them. The MAGIC and *Fermi*/LAT data reveal a spectral break at around 100 GeV. At high energies, the emission resolves in two regions. Two spatially distinct and statistically significant emission regions are established above 1 TeV. This thesis shows the first morphological studies in very high energy gamma rays performed with the MAGIC telescopes. The ability to resolve structures in galactic gamma ray sources has been proven to give important insights into the underlying physics of particle acceleration in astrophysical environments.

Contents

Contents

Contents

List of Figures

List of Figures

VIII

List of Tables

List of Tables

Chapter 1

Introduction and motivation

One hundred years ago, in 1912, the Austrian physicist Victor Hess discovered Cosmic Rays (CRs) (Hess 1912). CRs are charged relativistic particles reaching the earth from outer space. CRs consist to $\sim 98\%$ of nuclei and $\sim 2\%$ of electrons. The composition of the nuclei is dominated by protons ($\sim 87\%$) and helium nuclei ($\sim 12\%$) while only a small fraction ($\sim 1\%$) is due to heavier elements. The CR spectrum spans an energy range from $\sim 10^8$ eV up to $\sim 10^{20}$ eV per particle. Thus, CRs are the most energetic particles found in the universe. In 1936 V. Hess was awarded the Nobel prize for the discovery of CRs. Since then they have not only been object of countless research projects themselves, but they have also been used as a reservoir of highly relativistic particles to carry out early elementary particle physics experiments.

Examples for the variety of physical problems investigated with the help of CRs are the discovery of the positron (Anderson 1933) and the time dilatation predicted by the theory of special relativity (Rossi & Hall 1941). Furthermore, CRs also influence the radiation environment of the Earth (Ferrari & Szuszkiewicz 2009). Low energy cosmic rays ($\lesssim$GeV) produced in solar flares are responsible for the beautiful aurora borealis. Thus, CRs offer plenty of possibilities for interdisciplinary research. However, many details concerning CRs themselves are only poorly understood. As of today, no unambiguous, clear evidence is found that allows one to pinpoint the sources of cosmic rays. The mechanisms which are able to produce such ultra relativistic particles and then release them into outer space are still a matter of debate. Also the propagation of CRs from their sources through space is only roughly understood. The current believe is that CRs are accelerated in the expanding shock waves of supernovae, so called supernova remnants (SNRs), via diffusive shock acceleration.

This work investigates the origin of CRs within the milky way by means of very high energy gamma-ray astronomy. Photons are produced in the interactions of relativistic particles with ambient magnetic fields, photon fields, and matter. These photons can reach energies comparable to the energies of the interacting particles. Sources of CRs are therefore expected to be sources of highly energetic gamma rays. These gamma rays can be observed at Earth with satellites or ground based telescopes. Gamma ray astronomy opens the high energy end of the spectral window to the universe. This thesis is based on observations of gamma rays in the energy range of ~ 50 GeV up to multi TeV with the MAGIC telescopes. The MAGIC telescopes are a system of two 17 meter diameter imaging air Cherenkov telescopes, located at the canary island La Palma. The discovery of gamma ray emission from potential cosmic ray sources, such as SNRs, is mandatory to reveal the origin of CRs. Moreover, the energy spectrum of gamma rays carries the footprint of the underlying distributions of CRs. Gamma

ray emission alone is not sufficient to identify the gamma ray source as a source of CRs. While most CRs are nuclei, gamma ray emission, however, can be produced in the interactions of both relativistic protons and electrons. Therefore, only gamma ray emission produced in hadronic interactions allows to access the main component of CRs.

The flux of gamma ray emission is proportional to the product of relativistic particles and target density. While protons produce gamma rays mainly in the interaction with ambient matter (through inelastic proton proton collisions), electrons produce gamma rays both, in interactions with matter (Bremsstrahlung) and with ambient photon fields (Inverse Compton scattering). Moreover, electrons suffer strongly from synchrotron losses. Therefore, the optimal conditions to assure hadronically dominated gamma ray emission are environments of high matter density and strong magnetic fields. Obviously, a higher CR flux will linearly increase the gamma ray flux. Currently it is believed that the majority of CRs is accelerated and accumulated during the Sedov phase of the SNR. The Sedov phase lasts for several 10000 years, and describes the adiabatic expansion of the shock wave. However, the maximum particle energy achieved in SNRs ($\sim$PeV for protons) is believed to be reached at the beginning of the Sedov phase, $\lesssim 1000$ years after the supernova. As the shock wave decelerates during the Sedov phase the maximum achievable energy drops and particles with higher energies escape the accelerator. Even though the exact time dependence of the maximum achievable energy and the escape of CRs is not yet fully understood, a qualitative statement can be made: the highest CR energies are expected in *young* SNRs and the highest flux of CRs (below the escape energy) is expected in *middle-age* remnants. A potential high energy cut-off in *middle-age* SNRs can shed light on the maximum energy still achievable in these objects. Moreover, synchrotron losses of the electron component become more important on longer timescales and thus any leptonic VHE gamma ray emission is likely to be stronger suppressed in older remnants. Even though VHE gamma ray emission has been discovered for almost 20 SNRs (see e.g. http://tevcat.uchicago.edu/), only a handful clearly favor a hadronic origin of the observed emission and thus allow direct conclusions on the acceleration of CRs.

The observations carried out in this work mainly focus on the region W51. The system hosts a middle-age supernova remnant (W51C), which partially collides with the giant molecular cloud W51B. Gamma ray emission from the region has been already discovered below ~ 50 GeV by the *Fermi*/LAT (Abdo et al. 2009c) and an integral flux above 1 TeV has been reported by the HESS collaboration (Fiasson et al. 2009). The emission is significantly extended with respect to the angular resolution of both instruments. Moreover, MILAGRO reported a 3.4σ excess with median energy of 10 TeV coinciding with the *Fermi*/LAT source (Abdo et al. 2009d). The modeling of Abdo et al. (2009c) favors a hadronic origin of the non-thermal emission. The aims of the observation with MAGIC are to extend the spectral measurement to VHEs and to verify the hadronic emission model. The advantage of the low energy threshold of MAGIC offers the possibility to continue the spectrum obtained by *Fermi*/LAT without gap. The spectral behavior at TeV energies will allow to constrain the maximum energy still achievable in the system and potentially to test the hint reported by MILAGRO. Important information can be obtained from the morphology of the emission. The previous measurements did not allow to precisely determine the spatial origin of the gamma ray emission. A nearby possible pulsar wind nebula could also contribute to the observed emission. In a hadronic scenario the centroid of the emission is expected at the interaction region between the remnant and the

molecular cloud. Moreover, a higher angular resolution of the gamma ray emission could help to distinguish between a scenario in which the molecular cloud is illuminated by escaping CRs or the case in which the emission is concentrated on the acceleration region. The peculiar high density environment, the age of the remnant, and its known flux-level in VHE energies, make this object a very promising candidate to test and study cosmic ray acceleration in SNRs.

The second object investigated in this thesis is the unidentified VHE gamma ray source HESS J1857+026 (Aharonian et al. 2008a). The object shows extended emission and has no counterpart in any other wavelength. The spectrum of the VHE emission follows a single power law in the energy range between 800 GeV and 45 TeV with a spectral index of 2.39 ± 0.08. It has been suggested that gamma ray emission represents the pulsar wind nebula (PWN) of the highly energetic pulsar PSR J1856+0245 (Hessels et al. 2008). If the object is indeed a PWN the characteristic peak of Inverse Compton scattering is expected at energies below those reported by HESS. The low energy threshold of MAGIC allows to extend the spectral measurement to lower energies and thus possibly to reveal the expected spectral turnover in the PWN scenario. Moreover, the morphology reported by HESS indicates a feature towards the North of the source, potentially indicating an additional source. Detailed morphological studies in the energy range comparable to that used by HESS ($\gtrsim 1$ TeV) and at lower energies can shed light on a possibly energy dependent morphology and might reveal more insights in the nature of the emission. In addition, the overall flux of the source is with $\sim 15\%$ of flux of the Crab Nebula rather strong and therefore the source can be used to study the technical performance of the MAGIC telescopes for the observation of extended sources.

The following section describes the outline and structure of this work. An introduction into the field of cosmic rays and the search for their origin is given in chapter 2. Moreover, chapter2 illustrates how gamma ray observations can be used to tackle the question of the origin of cosmic rays. The chapter 3 introduces the imaging air Cherenkov Technique to observe very high energy gamma rays. The production of extensive air showers caused by relativistic particles impinging on the atmosphere and the subsequent production of Cherenkov light are discussed. A brief introduction is then given on how the measurement of the Cherenkov light by imaging air Cherenkov telescopes (IACTs) can be used to constrain the properties of the primary particle. This chapter ends with a short overview of the major IACTs of the current generation.

In chapter 4 the MAGIC telescopes are introduced. The general performance of the instrument as well as the systematic uncertainties are discussed. Chapter 5 is devoted to the calibration of the MAGIC telescopes by using cosmic muons. The aim of this analysis is to adjust the Monte-Carlo (MC) simulations to achieve a best possible match with the data. Based on the selected events, ratios between data and MC are built to determine the optical point spread function (PSF) and the light collection efficiency (related to the so called mirror fraction, MF). The effects of different PSF and MF values are investigated in MC simulations to validate the applied method and the analysis is applied for both MAGIC telescopes.

A detailed description of the analysis of the data obtained with the MAGIC telescopes is given in chapter 6. It gives a comprehensive overview of the data treatment covering the topics of data quality and the subsequent steps of event classification aiming the detection of

a gamma ray signal. This work addresses the treatment of bright stars in the field of view, the development of a data quality selection tool, and provides a well-tested general purpose analysis pipeline to the whole collaboration.

The main contribution to the analysis software was the development and implementation of a generalized background determination for MAGIC (section 6.6.3). The new method significantly reduces the systematic uncertainty of the background determination for off-axis sources. Based on this development the standard observation modus of MAGIC was changed, allowing to reduce the statistical error of the background estimation. The new background determination developed in this work is particularly important for the study of extended sources like pulsar wind nebulae (PWNe) or supernova remnants (SNRs).

Chapter 7 presents the major scientific results of this thesis, the VHE gamma ray emission of the W51 complex and its implications on the search of galactic cosmic ray sources. A possible contribution of gamma ray emission from the nearby PWN candidate is investigated. Based on the spectral and morphological properties in gamma rays and other wavelength data the emission is modeled to distinguish between a hadronic or leptonic nature of the observed emission. Based on the models the possibility of W51C being a galactic cosmic ray source is discussed. The Chapter concludes with a discussion on the impact of W51C and other middle-age SNR-MC systems on the research area of the origin of galactic cosmic rays.

Chapter 8 presents the results of the scientific observations of the object HESS J1857+026 (Aharonian et al. 2008a). The astrophysical origin of this unidentified VHE source is investigated. The low energy threshold of MAGIC allows us to extend the spectrum towards lower energies. The morphology of the source is investigated in differential energy bins and the possibility of a multiple source-scenario is discussed. Moreover, the source was used to investigate the abilities of the MAGIC system to observe extended sources.

In Chapter9 the results and work of this thesis are summarized. Based on the obtained scientific results of this thesis and recent developments in the field of cosmic ray research a short outlook is presented.

Chapter 2

Cosmic rays and gamma rays

This chapter introduces the field of cosmic ray (CR) physics. Special attention is payed to the perspective of very high gamma ray astronomy. The main theoretical concepts of acceleration of CRs is introduced and discussed on the example of supernova remnants (SNRs). The current view that supernova remnants are the sources of the galactic component of CRs is reviewed. Furthermore, the interactions of cosmic rays and the production mechanisms of gamma rays are provided. The possibilities to distinguish gamma rays produced by hadronic interactions and leptonic interactions are discussed. A brief introduction into the field of gamma ray astronomy and the types of known sources is given. Finally, the expected gamma ray emission from supernova remnants is discussed and an overview of the current status of our understanding of CR acceleration in SNRs is given.

2.1 Cosmic rays

Figure 2.1 shows the overall CR flux. The flux level of CRs over the entire energy range changes by more than 30 orders of magnitude. Due to the extreme low flux at the highest energies direct measurements of the cosmic ray flux, with satellites or balloon born experiments, are only possible up to energies $\lesssim 10^{15}$ eV due to the small detector areas of such experiments. For higher energy measurements extensive air shower arrays are used which measure the secondary particles produced in the interaction of CRs with the atmosphere. Over many orders of magnitude in energy the differential CR flux can be described as a power law E^{-s}, where s is called the spectral index.

The most prominent features of the CR spectrum are the so called *knee* located at $\sim 3 \times 10^{15}$ eV and the *ankle* at $\sim 3 \times 10^{18}$ eV. At energies smaller than the location of the knee the spectral slope is $s \sim 2.7$, between knee and ankle $s \sim 3$, and above the ankle $s \sim 2.7$ (see e.g., Longair 2010 and references therein). The almost featureless spectrum below the knee suggest a common underlying physical process for these particles. The part of the spectrum below the knee is attributed to a galactic origin of the particles, the so called galactic cosmic rays (GCRs). A proton in a magnetic field of $\sim 5\mu$G (a typical value for the interstellar medium) has a gyroradius exceeding the size of the milky way for energies of $\gtrsim 10^{19}$ eV. Therefore, a galactic origin of such energetic particles seems very unlikely. On the other hand, the possibility that extragalactic particles of energies below the knee contribute significantly into the GCR contribution appears unlikely because of their very low density after traveling intergalactic distances. At some energy above the knee the dominant GCR contribution to the overall CR spectrum will thus be replaced by extragalactic cosmic rays (EGCRs), possibly indicated by the ankle. To obtain detailed information about the origin of CRs is very challenging. As CRs are charged particles, they suffer from deflections on interstellar (and potentially intergalactic)
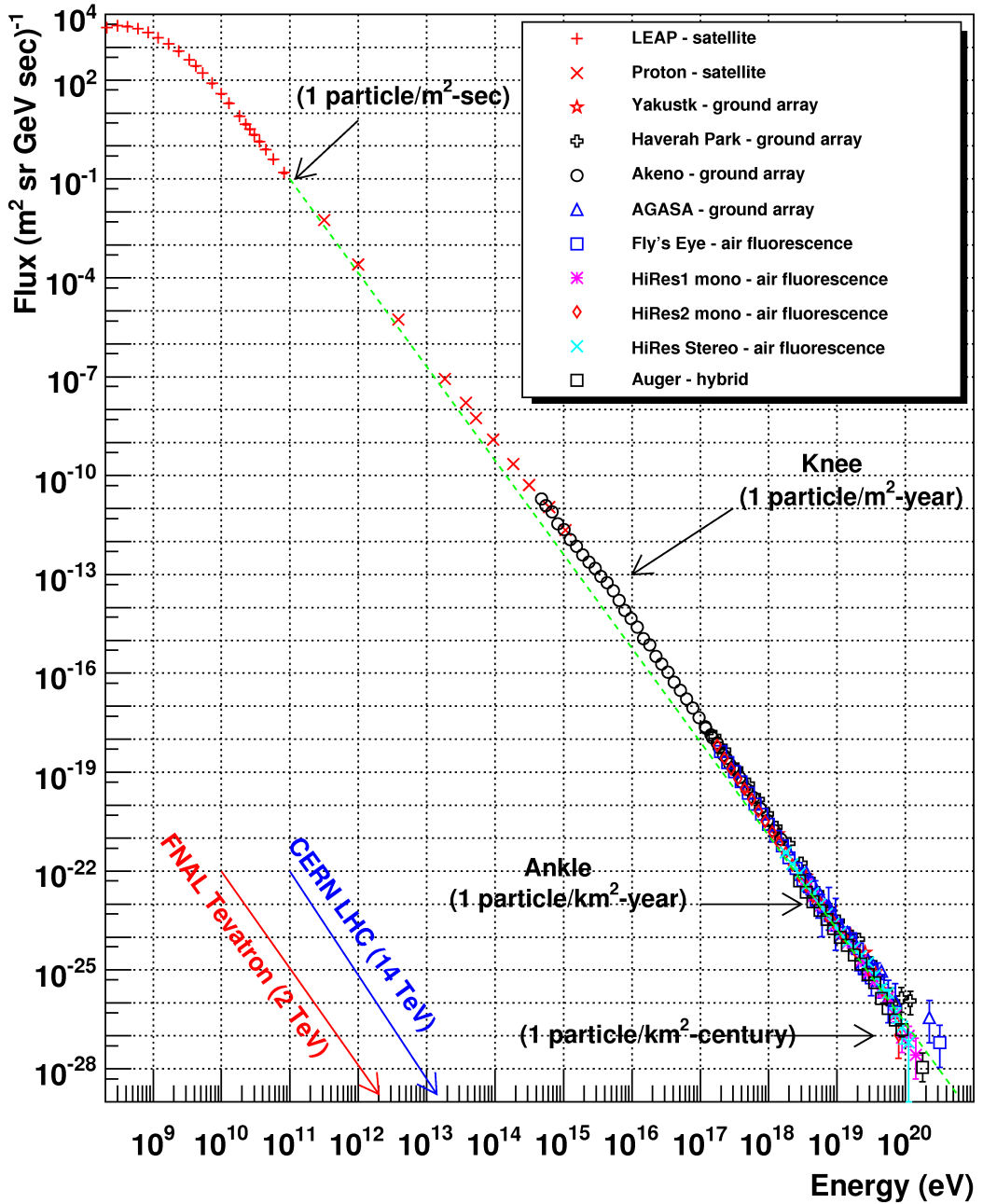
Figure 2.1: The overall energy spectrum of cosmic rays. Marked are the *knee* and the *ankle*. For selected energies the flux is indicated. The center of mass energy for different accelerator experiments is also indicated. Note that the maximum energy reached by the LHC translated into a frame where one particle is at rest is 10^{17} eV, still much below the maximum energy observed in CRs. Data points have been obtained by various experiments (Courtesy of Dr. William Hanlon, from www.physics.utah.edu/~whanlon/spectrum.html).

magnetic fields, resulting in a highly isotropic flux observed at earth. Thus, CRs carry no (very little) information on their spatial origin, preventing the identification of possible sources of cosmic rays.

This work focuses on GCR with energies below the knee. Concerning research on ultra high energy cosmic rays (UHECR) with energies $\gtrsim 10^{18}$ eV the reader is referred to Letessier-Selvon & Stanev (2011) for a recent review on the current status of the field. A historical review on UHECR and the experimental techniques used to study them can be found in Kampert & Watson (2012). Further in the text CRs refers to the galactic component (if not otherwise stated).

2.1.1 Galactic cosmic rays

Figure 2.2 shows the spectra and composition of GCRs in the energy range up to $\sim 10^{14}$ eV (for a recent review on direct observations of CRs see Müller 2012). It can be seen that the contribution of protons and helium strongly dominate the overall spectrum. The elemental abundance found in CRs is partly similar but with some significant differences to that found in the interplanetary matter of the solar system. While it has been long disputed if CRs have their origin within the solar system (see for example Alfvén 1949 and Compton & Getting 1935 arguing in favor or against a solar origin), the different compositions provide clear evidence for extrasolar origin. While the overall flux is only marginally affected by most of the contributing elements and isotopes they carry very helpful information on the possible sites of cosmic ray acceleration and their propagation through space. Simpson (1983a) reviewed the status of the elemental and isotopic abundances when the first detailed information was available. Among his conclusion was that the overabundance of carbon and oxygen in the CR spectrum (compared to solar abundances) can be interpreted as an indication that CRs originate in the vicinity of supernovae. In recent decades the precision measurements of the CR composition both concerning elements and isotopes has significantly improved our knowledge about CRs. A measurement of different radionucleides (Yanasak et al. 2001) revealed the age and thus the confinement time of CRs in the galaxy to be independent on species and $15 \pm 1.6 \times 10^6$ years (for energies $\sim$ GeV). Note that the larger gyro-radius of particles with higher energies will allow them to escape the galaxy even faster. Bhandari (1986) reported, based on isotope data found in meteorites that the GCR-flux (energies $\sim$ GeV) shows no significant deviation over the past two million years compared to that over the past 10^7 years.

This suggests the need of a constant replenishment of CRs. All elements show a very similar spectral behavior, indicating that the same process is responsible for all of them. Note, that the electron component is unique in the sense that the electron to proton ratio in CRs is only about 1/50 (Simpson 1983a) and shows a significantly steeper spectral slope around E^{-3} (Ackermann et al. 2010). The lower and steeper flux of cosmic ray electrons compared to protons is explained by a potentially less efficient acceleration and by much higher energy losses due to inverse compton scattering and synchrotron radiation. The estimated distance over which a 1 TeV electron loses half of its energy is estimated to be 300–400 pc (Aharonian et al. 1995). Due to the low contribution of electrons to the overall cosmic ray spectrum the expression CRs often refers to the hadronic/ion component only.
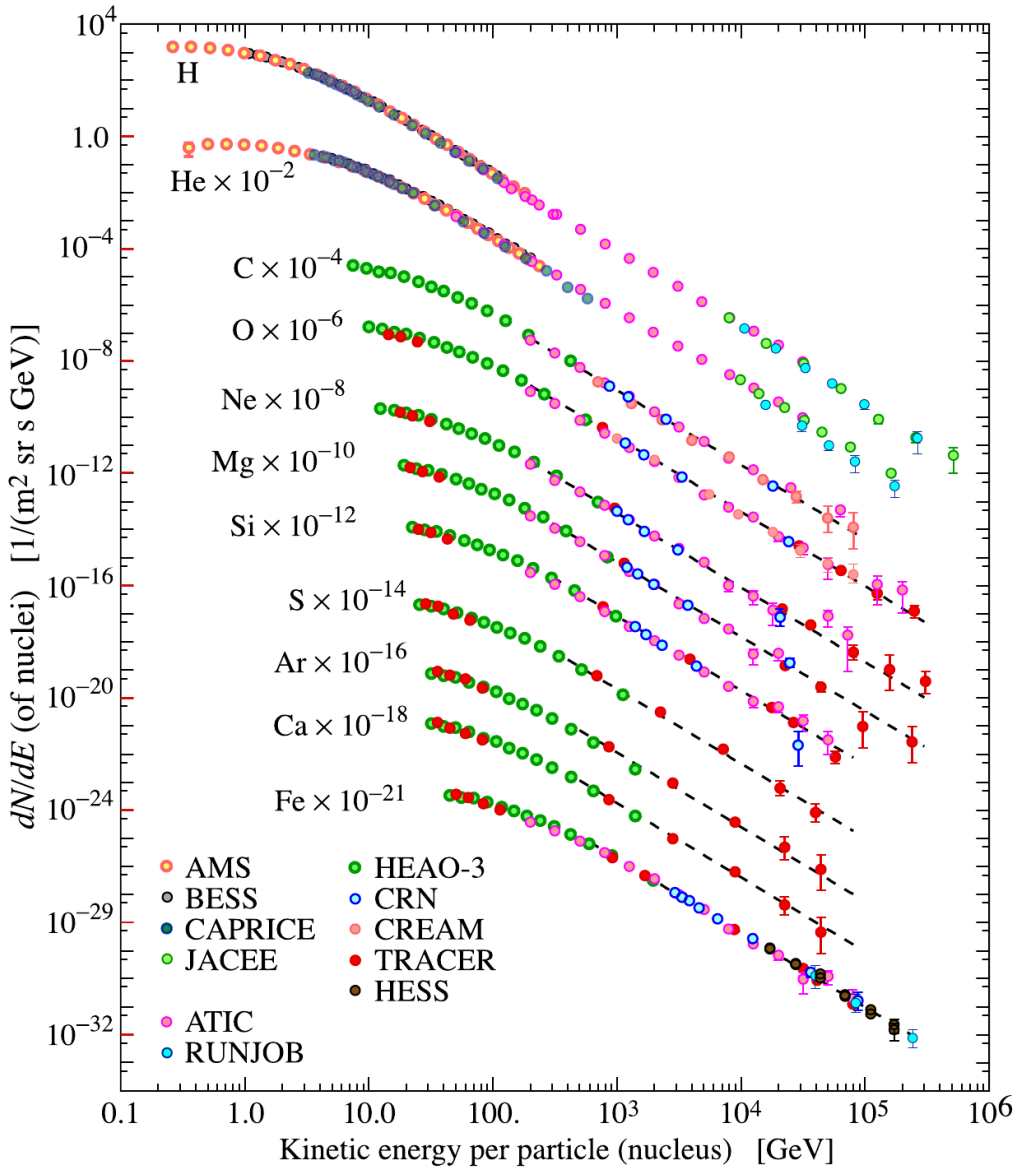
Figure 2.2: Galactic cosmic ray spectra of different elements. To display all contributions in one plot different scaling factors have been used as indicated in the figure. Picture adopted from Beringer et al. (2012).

The knee of the CR spectrum is widely interpreted as a rigidity[1] dependent effect, either of the propagation or of the maximum achievable energy in the sources of galactic cosmic rays. The most common theory as of today is that the knee arises indeed from the maximum achievable energy in galactic cosmic rays sources. Antoni et al. (2005) could show that the

---

[1]Rigidity is defined as $R = B\rho = p/q$, measured in Gigavolts (GV), where B is the magnetic field strength, ρ the gyro-radius, p the particle momentum, and q its charge. The rigidity is a measure of the bending of a particles trajectory in a magnetic field.

knee is consistent with a steepening of the spectra of the light elements and thus confirmed a rigidity dependent effect. For recent reviews see Gaisser (2007) or Blümer et al. (2009).

Until recently it was a common believe that the spectral shape of each element follows the same power law. However, there are small, but important differences in the spectra of individual elements as recently reported by Adriani et al. (2011). Besides the difference between the slope of the proton and helium spectra, the authors also find a significant deviation from a single power law resulting in a change of the spectral slope around a rigidity of 200 GV. The observed hardening shows an index change of $\sim +0.2/ + 0.3$ for protons and helium, respectively. An indication of such a hardening was already previously reported by Ahn et al. (2010). At this moment it is an open discussion if the difference of the spectra for different elements and the observed hardening is a source intrinsic effect or if it occurs during the propagation of CRs. Erlykin & Wolfendale (2012) presented an explanation including a new component of CR produced in the winds of giant stars. On the other hand Blasi & Amato (2012a,b) suggest that a propagation effect may be responsible. More data of CRs measured at earth and of the spectrum at their sources are needed to understand these behaviors.

2.2 The origin of galactic cosmic rays

Sources of galactic cosmic rays have to fulfill three main requirements:

- provide sufficient energy to explain the observed intensity

- reproduce the power law spectrum

- accelerate charged particles at least up to the knee

Zwicky suggested already in 1939 the possibility of supernovae being responsible for the origin of CRs. A simple energetic argument (see e.g. Ginzburg & Syrovatskii 1964 or Longair 2010) is still one of the main arguments in favour of this theory. By using the confinement time of CRs within the galaxy one can estimate the energy needed to maintain the CR flux to be $\sim 10^{34}$ J/s. For comparison the energy release from the luminosity of the Sun[2] is only $\sim 10^{26}$ J/s. The average release of kinetic energy in the implosion of supernova is, however, $\sim 10^{44}$ J. The supernova rate within our galaxy is estimated to be ~ 3/century (see Diehl et al. 2006 for a recent measurement and van den Bergh & Tammann 1991 for a review on the rate determination of supernovae). Thus a conversion of $\sim 10\%$ of the kinetic energy of supernova implosions into cosmic ray particles would be sufficient to maintain the observed flux.

It was then Enrico Fermi who prepared the foundation of todays theory of cosmic ray acceleration (Fermi 1949). Fermi could show that particles can gain energy by scattering between interstellar clouds of different velocities. He showed that if the particle velocity ,v, is much higher than the velocities of the clouds, head on collision occur more frequent than *following* collisions. Therefore a net energy gain is achieved, resulting in a power law spectrum in momentum. Colorfully speaking, particles scatter elastically like balls between moving targets, where the targets move with random relative velocities. The original theory had, however, a few caveats. The energy gain per encounter (averaging over all scattering angles) is

---

[2]Estimation taken from http://nssdc.gsfc.nasa.gov/planetary/factsheet/sunfact.html

$$\frac{\Delta E}{E} = \frac{8}{3}\left(\frac{v}{c}\right)^2 \tag{2.1}$$

where v is the velocity of the cloud and c is the speed of light. Thus, the average energy gain is second order in v/c. For typical random velocities of clouds in the galaxy ($v/c \leq 10^{-4}$, see e.g. Longair 2010) the number of encounters for reaching high energies is thus very large. Moreover, the mean free path of particles in the galaxy is ~ 0.1 pc which would result in a very slow acceleration. The second major caveat is that even though the theory predicts a power law distribution in energy, there is no prediction for the exact slope.

2.2.1 Diffusive shock acceleration

In the late 1970's several authors proposed diffusive shock acceleration (DSA) in astrophysical shock waves as the underlying mechanism of cosmic ray acceleration (Krymskii 1977; Axford et al. 1977; Blandford & Ostriker 1978; Bell 1978a,b). A shock wave is a sudden change in the velocities, U_1 and U_2, of the medium between two regions. In the limit of a contact discontinuity in velocity between the two regions one speaks about a blast wave or a jump shock. Figure 2.3 illustrates such a case in the rest frame of the shock wave.
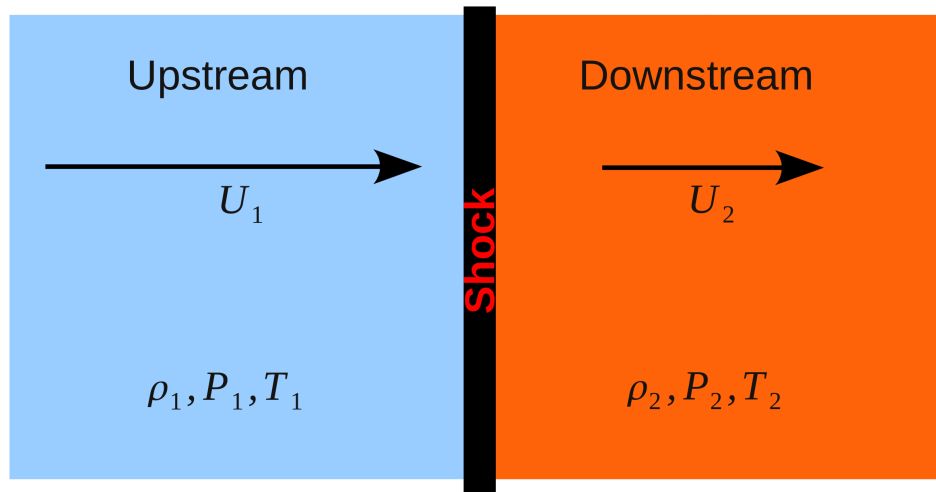
Figure 2.3: Illustration of a shock wave in the rest frame of the shock. The unshocked, upstream, plasma ahead of the shock approaches the shock wave from the left. The shocked, downstream plasma leaves the shock with a lower velocity (U_2) but higher pressure (P_2), temperature (T_2) and density (ρ_2).

Considering the conservation of number of particles, momentum and energy across the discontinuity one can derive the so called Rankine-Hugoniot conditions:

$$\frac{\rho_2}{\rho_1} = \frac{U_1}{U_2} = \frac{(\gamma+1)M_1^2}{(\gamma-1)M_1^2+2} \,, \tag{2.2}$$

$$\frac{P_2}{P_1} = \frac{2\gamma M_1^2}{\gamma+1} - \frac{\gamma-1}{\gamma+1} \,, \tag{2.3}$$

$$\frac{T_2}{T_1} = \frac{\{2\gamma M_1^2 - (\gamma-1)\}\{(\gamma-1)M_1^2+2\}}{(\gamma+1)^2 M_1^2} \,, \tag{2.4}$$

where ρ is the density, v the flow velocity, M the Mach number , P the pressure, T the temperature and γ the ratio of specific heats. The index 1 indicates the upstream (unshocked) region and the index 2 the downstream (shocked) region. For large Mach numbers the compression ratio (s) reaches a maximum. In this case one speaks about a strong shock.

$$s = \frac{\rho_2}{\rho_1} = \frac{U_1}{U_2} = \frac{(\gamma+1)M_1^2}{(\gamma-1)M_1^2+2} \tag{2.5}$$

and

$$lim_{Ma\to\infty}(s) = 4 \,. \tag{2.6}$$

Here $\gamma = 5/3$ was used, which is valid for a mono-atomic gas or a fully ionized gas (plasma). For a detailed review on astrophysical shock waves see Ostriker & McKee (1988).

Consider a particle of velocity v approaching the shock from upstream. For simplicity it is assumed that the particle velocity v is much larger than the upstream flow velocity U_1 and $v \sim c$. In that case the particle can cross the shock front freely. It is assumed that the particle scatters elastically on magnetic field irregularities on the downstream side. After several scatters the particle might have changed its direction by more than 90 degrees heading again upstream. Now the particle will see the upstream side approaching with the speed

$$U_{H2\to1} = \frac{v + U_1 \cos\phi_1}{1 + (vU_1 \cos\phi_1/c^2)} \,. \tag{2.7}$$

where ϕ_i is the angle between the particle velocity and the upstream velocity vector and c is the speed of light. Assuming a head-on collision $\phi_i = 0$ with a scattering center on the upstream side, the particle will gain a momentum of

$$\Delta p = (U_1 - U_2)m \,. \tag{2.8}$$

Assuming an efficient scattering on both, the upstream and the downstream site, one can assume that the velocity distributions of the high energetic particles is isotropic in the rest frames of each side. Figure 2.4 illustrates the high energy particles see the other side of the shock wave approaching with 3/4 of the shock velocity U in all cases. All collisions which lead to a crossing of the shock wave are collisions under an angle $\phi_i < 90°$ thus lead a velocity gain given in equation 2.7.
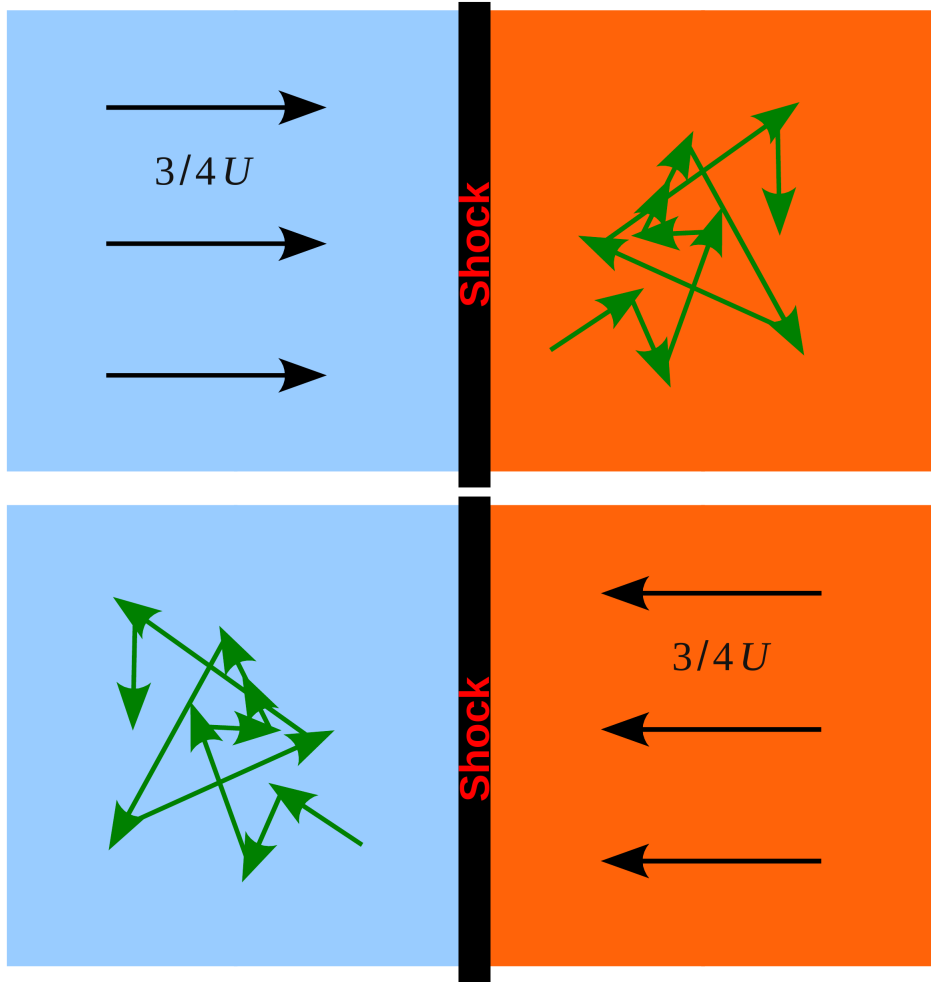
Figure 2.4: Illustration of the shock and the high energy particles as seen in different reference frames in the case of a strong shock ($s = 4$). Top: The flow of gas observed in the frame of reference in which the downstream gas is stationary and the velocity of high energy particles is isotropic. Bottom: The flow of gas as seen from the reference frame in which the upstream gas is stationary and the velocity distribution of high energetic particles is isotropic. In both cases the particles *see* the other side of shock approaching with $3/4$ of the shock velocity U. Illustration idea adopted from Longair (2010)

By averaging over all crossing angles, and assuming an isotropic velocity distribution of the high energy particles in the rest frames of the upstream/downstream side, the relative energy gain per cycle (i.e., upstream to downstream and back or vice versa) is given by:

$$\overline{\frac{\Delta E}{E}} = \frac{4}{3}(U_1 - U_2)/c\,. \tag{2.9}$$

Compared to the original version proposed by Fermi, the energy gain by crossing a shock wave is linear in $(U_1 - U_2)/c$ and thus allows a much more efficient acceleration. The reason for this

is that no matter if the particle crosses the shock front from downstream to upstream or vice versa, the velocity of the scattering centers is always directed against the velocity vector of the particle itself. In second order Fermi acceleration also following collisions (angle between the involved velocity vectors of more than 90°) occur, which result in energy losses and reduces the overall energy gain. The structure of the shock wave does not allow such collisions. Thus, diffusive shock acceleration is similar to a ball bouncing between two approaching walls.

2.2.2 The spectrum of diffusive shock acceleration (DSA)

The spectrum of particles can be obtained either by solving the transport equation (Krymskii 1977; Axford et al. 1977; Blandford & Ostriker 1978) or by the use of a microscopic kinetic approach (Bell 1978a,b). A detailed introduction in the topic of DSA including both derivations was given by Drury (1983). In the test particle approach the obtained distribution function in phase space can be rewritten as:

$$f(x, p, t) = C(t) \left(\frac{p}{p_0} \right)^{-q(t)} , \tag{2.10}$$

$$q = \frac{3s(t)}{s(t) - 1} . \tag{2.11}$$

Where $s(t)$ is the compression ratio of the shock wave, $C(t)$ the normalization constant, t is the time, and p_0 the minimum momentum for which the solution is valid. For strong shocks ($s(t) = \text{constant} = 4$) one obtains a canonical power law in momentum of p^{-4}, i.e., for highly relativistic isotropic particles the well-known power law in energy of E^{-2}. The slope of the power law depends only on the compression ratio and is thus determined by the kinematics of the shock wave. Furthermore, the power-law form and its spectral slope do not depend on the particle species (neglecting any kind of energy losses). Thus, DSA in the shock waves of supernova remnants (SNRs) appears to be a very attractive process to explain the origin of CRs.

It should be mentioned that the existence of appropriate scattering centers on the upstream and downstream sites is an assumption. While the highly turbulent plasma downstream of the shock surely provides enough magnetic field irregularities, it is not obvious why the upstream plasma should provide sufficient scattering centers. The absence of such scattering centers leads to a breakdown of the complete mechanism as the particles could escape ahead of the shock. This problem was realized already in the original work of Bell (1978a) who suggested self-generated Alfven ways to act as these scattering centers:

'Fast particles are prevented from streaming away upstream of a shock front by scattering off Alfven waves which they themselves generate. This scattering confines the particles to the region around the shock and results in first-order Fermi acceleration due to the particles crossing the shock many times' (Bell 1978a).

This picture has two major consequences: First, the accelerated particles are confined to a region close to the shock front of approximately one diffusion length in each direction (Drury et al. 1999). Second, the acceleration of particles is a highly non linear process resulting from the feedback of the accelerated particles on the upstream plasma. Moreover, the energy

converted from the shock wave into relativistic particles will affect the shock wave itself. Another important aspect is the pressure in cosmic rays which can substantially affect the shock structure. Malkov & O'C Drury (2001a) provide a review discussing the main effects of non linear diffusive shock acceleration (NLDSA). A general trend in most NLDSA models considered is that one obtains very hard $\sim E^{1.7}$ spectra of a concave shape (see for example Caprioli et al. 2010).

2.2.3 Propagation of cosmic rays

If the source spectrum of cosmic rays is $\sim E^{-2.0}$ (or harder) one needs to explain the reason for the steeper (softer) spectrum ($\sim E^{-2.7}$) observed on earth. The general explanation is that the CR spectrum steepens during its propagation through the galaxy. Due to the interstellar magnetic fields cosmic rays do not propagate on straight lines but diffuse. The diffusion is usually parametrized by a diffusion coefficient of the form $D = D_0 \times E^{-\delta}$. The spectral slope observed at earth is then $\propto E^{-(q+\delta)}$, where q is the source intrinsic slope and δ the steepening caused by the energy dependent diffusion (for a review on CR diffusion see Strong & Moskalenko 1998 or Strong et al. 2007). Typical values for δ range between 0.3 and 0.6. From theoretical considerations one would expect that the magnetic field irregularities in interstellar space can be described by Kolmogorov-type turbulences, resulting in $\delta = 0.3$. However, this would imply a source spectrum as steep as $E^{-2.4}$ which seems hard to achieve in DSA. On the other hand Blasi & Amato (2012b) showed that a $\delta \geq 0.6$ would lead to an anisotropy in the cosmic ray flux much larger than observed. The current status of the field restricts the energy dependence of the diffusion to a range around $0.3 \geq \delta < 0.6$ and thus implies a spectral slope of the source spectrum in the range $2.1 < q \leq 2.4$. Note, that Blasi & Amato (2012a) showed that the stochastic nature of source events (supernovae) invalidates that the observed index is strictly given as $(q+\delta)$, therefore small deviations can be expected. Furthermore, the contribution of a close-by CR source may produce additional deviations from a pure power law spectrum. In any case these studies severely challenge the process of DSA by requiring such steep source spectra.

Only recently, Caprioli (2012) proposed a framework in which, by taking into account the finite velocities of the scattering centers, such steep spectra are indeed possible. In his work Caprioli showed that the spectral slope of the accelerated particles depends on the injection efficiency of particles into the DSA process. As the scattering centers are self induced by the particles, such a dependency is not unexpected. In the proposed framework a higher injection leads to a steeper spectrum.

2.2.4 Injection

The process of the injection of particles into the DSA mechanism is still a poorly understood problem. For particles to be efficiently accelerated they have to be able to cross the shock surface freely. Thus, the gyro-radius has to be larger than the shock thickness. In addition, the particles have to have velocities high enough to return to the upstream side and not being dragged away with the downstream plasma. In the work of Malkov & Voelk (1995) and Malkov (1998), referred to as the *ion-leakage*-model it could be shown that the injection process can be described as a self-regulated process. Particles, fast enough to reach back upstream will excite hydrodynamic waves via the Ion-Zyklotron-instability. These waves will be dragged

downstream and suppress the injection mechanism. The interplay between injected particles and waves excited subsequently leads to a self regulated system. It turns out that the effective injection momentum for protons is linked to the shock dynamics and is given as:

$$p_{inj} \approx (2.2 - 2.3) \cdot p_{th} \,, \quad \text{where} \quad \mathrm{p_{th}} = 2\sqrt{\mathrm{m} \cdot \mathrm{k_B} \cdot \mathrm{T_2}} \tag{2.12}$$

Here m is the mass of the proton, k_B the Boltzmann-constant and T_2 the downstream temperature. The factor of 2.2–2.3 has been obtained in numerical simulations by Gieseler et al. (2000). It is noted, that a small deviation in this factor can lead to a significant change of the injection efficiency. That is, assuming a Maxwellian momentum distribution downstream, the amount of particles with momentum higher than p_{th} is sharply decreasing with increasing momentum. Gieseler et al. (2000) show that the injection efficiency is rather constant over time and the fraction of injected particles to those passing the shock wave is in the order of 10^{-3}–10^{-4}. Later, Kang et al. (2002) investigated the interplay between the injection of particles and the modification of the shock by the accelerated particles. They concluded that for strong shocks ($M \gtrsim 30$) the injection becomes largely independent of the initial Mach number of the shock wave and the injection efficiency approaches $\sim 10^{-3}$. Blasi et al. (2005) could reveal a similar behavior and could furthermore show that the amount of multiple solutions, appearing usually in such highly non-linear problems, can be significantly reduced considering a self regulated injection model. An important aspect was discussed by Völk et al. (2003), who showed that the injection efficiency depends strongly on the magnetic field orientation with respect to the shock normal. Similar results have been found in numerical simulations by Gargaté & Spitkovsky (2012). The suppressed diffusion of particles perpendicular to magnetic field lines leads to a very inefficient injection. Thus, depending on the magnetic field orientation the injection of particles and subsequently their acceleration can strongly vary across the shock surface. Support for this theory has been found in the supernova remnant SN 1006 (Cassam-Chenaï et al. 2008), where non-thermal emission of the supernova remnant is observed only at two regions around the magnetic poles of the spherical shock wave.

Summarizing our understanding the proton injection is not yet complete but even more challenging is the understanding of the electron injection. The lower mass and subsequently lower gyro radius of sub-relativistic electrons requires a much higher momentum of electrons to freely cross the shock surface. Therefore, a lower injection efficiency for electrons can be expected. In addition, electrons will suffer much higher energy losses which could make the acceleration mechanism less efficient (see e.g. Erlykin & Wolfendale 2002 for a detailed discussion). Several attempts have been made considering Whistler Waves (Riquelme & Spitkovsky 2011), Ionization process of nuclei (Morlino 2011), or shock surfing acceleration (Amano & Hoshino 2007) to describe electron injection. However in most cases the electron injection is introduced as a free parameter described by the electron to proton ratio in CRs. The low electron to proton ratio observed at earth and the challenging description of an efficient electron injection suggest that indeed the amount of accelerated ions exceeds the amount of accelerated electrons.

2.2.5 Maximum energy

As supernovae provide sufficient energy, and DSA in their shock waves offer a very promising mechanism the next step to address is the maximum achievable energy of CRs in such a system. The maximum achievable energy E_{max} is determined by three main processes: E_{max} is reached if acceleration and energy losses are equal, the particle escapes the accelerator, or

the accelerator stops working. For the acceleration of protons (nuclei) the energy losses are usually negligible. To derive the maximum energy one needs the acceleration time scale, the lifetime of the shock wave, and the capability of the region surrounding the shock wave to confine high energy particles. The acceleration time scale is given by the time to complete one cycle as

$$T_{\text{cycle}} = \frac{4}{v} \left(\frac{D_1}{U_1} + \frac{D_2}{U_2} \right), \tag{2.13}$$

where v is the velocity of the particle, D_i the diffusion coefficient, and U_i the flow velocity on the upstream and downstream side. Particles will mostly scatter on magnetic field irregularities of compatible spatial size to the Larmour radius of the particle. It can be approximated that $D \propto r_g = \frac{p}{ZB}$ where p and Z are the momentum and charge of the particle and B is the magnetic field strength. If the Larmour radius becomes larger than the accelerator itself, the particles can escape. Thus, both the acceleration time scale and the confinement are strongly coupled to the magnetic field strength. A detailed discussion of maximum achievable energy has been given by Lagage & Cesarsky (1983). They derive an upper limit for the maximum energy per particle over the lifetime of a supernova shock wave of

$$E_{max} \lesssim 10^{14}\, B[\mu\text{G}]\, Z \quad \text{eV}. \tag{2.14}$$

In their derivation it was assumed that the diffusion coefficient is the lowest possible (Bohm limit). This result has two major consequences: First the maximum achievable energy increases linearly with the charge Z. This could explain the steepening of light elements observed at the knee as an effect of reaching the maximum energy of the accelerator. The charge dependence appears as a general feature of the proportionality between the Lamour radius and the diffusion coefficient. However the second consequence is that the maximum achievable energy in an average galactic field ($B \approx \mu\text{G}$) is one order of magnitude too low to reach the knee.

The inability to reach energies around the knee was a long-standing problem for the considerations of SNRs as the sources of CRs. Bell & Lucek (2001) and Bell (2004) presented the mechanism of self amplified magnetic fields. In this scenario the magneto-hydrodynamic waves are excited by relativistic particles accelerated by the shock can lead to an amplification of the average magnetic field in the vicinity of the shock wave. From equation 2.14 it is clear that a magnetic field amplification would allow to reach energies of the knee and beyond. Evidence for such a magnetic field amplification has been found in several young supernova remnants (e.g. SN 1006, Tycho, Cas A) in the form of thin non thermal X-ray filaments (see Bamba et al. 2005; Uchiyama et al. 2007; Berezhko et al. 2003; Völk et al. 2005; Reynolds et al. 2012 and references therein). Thus with magnetic field amplification SNRs are able to reach sufficiently high energies. Moreover, Caprioli (2012) pointed out the importance of magnetic field amplification to achieve spectra with spectral slopes steeper than -2. Schure et al. (2012) provides a comprehensive review on the field.

2.2.6 Supernova remnants as sources of galactic cosmic rays

Today SNRs are the most promising candidates for cosmic accelerators and there is wide consensus that SNRs are indeed the major sources of galactic cosmic rays.

There are many observational hints supporting this view. A complete listing of all of them would go far beyond the scope of this work. Among the most crucial are the possibility to explain the observed elemental composition of CRs at earth by acceleration of interstellar matter around SNRs (e.g. Ellison et al. 1997; Blasi & Amato 2012a), the detection of strong (probably self-amplified) magnetic fields in supernova shock waves, the indications of CR modified shocks, and the discovery of high (HE, $\sim$ GeV) and very high (VHE, $\sim$ TeV) gamma rays emitted by SNRs (see Helder et al. 2012 and references therein).

Gamma rays are produced in interactions of relativistic particles and are therefore a tracer of CRs (including electrons). Photons are not affected by magnetic fields and point back to the interaction point. Gamma-ray observations are therefore one of the major tools to study the origin of cosmic rays.

However, there is no definite proof that SNRs are indeed the major sources of galactic CRs (see also O'C. Drury 2012 and Hillas 2005). To resolve all doubts the following aspects have to be proven: SNRs are able to accelerate protons (ions) up to the knee. The total amount of produced CRs by SNRs in our galaxy is sufficient to maintain the CR flux. The spectral shape and composition produced in SNRs is compatible with the CR spectrum after propagation observed at earth.

To do so a detailed understanding of the acceleration process, the injection, and the escape of particles in SNRs is mandatory. Moreover, a detailed understanding of the propagation of CRs in interstellar space is crucial.

The most successful observational tool in the last 10–20 years used to investigate CRs in SNRs was and still is gamma-ray astronomy.

2.3 Gamma rays

Ginzburg (1988) reviewed the status of CR research 75 years after their discovery. Even though at this time the gamma-ray sky was largely unexplored with $\sim$ 20 high energy (HE) and 0 very high energy (VHE) sources known, Ginzburg comments in his review:

'it is hoped, however, that even the rather fragmentary comments which we have offered here clearly show just how powerful and promising the gamma-astronomy method is for studying cosmic rays in the universe' (Ginzburg 1988).

One year later, the Whipple collaboration (Weekes et al. 1989) announced the discovery of TeV emission from the Crab Nebula and thus the discovery of the first TeV source in the sky. Since then the field of both, ground based and space based gamma ray astronomy, has been rapidly expanding and is now an established window to the universe. As of today about 1900 sources in the energy range 100 MeV – 100 GeV have been discovered by the Large Area Telescope (LAT) on board the *Fermi* satellite (Nolan et al. 2012). In VHE a total of about 140 sources are known (see e.g. http://tevcat.uchicago.edu) which have been discovered by ground based telescopes. This work is based on VHE gamma ray astronomy using the imaging air Cherenkov telescopes MAGIC (see Chapter3 for an introduction in the technique and Chapter 4 for a description of the instrument). For a comprehensive introduction to very high energy gamma ray astronomy see Weekes (2003). For a historical review on the development in ground based gamma ray astronomy see Lorenz & Wagner (2012). The processes which produce high and

very high energy gamma rays are ,however, similar and will be described in the following section.

2.3.1 Production of gamma rays

Note that gamma rays with energies from $\gtrsim 100$ MeV up to multi-TeV discussed here have much higher energies than gamma rays produced in radioactive decays ($\sim$MeV). For a discussion on extraterrestrial radioactive gamma ray emission see, e.g., Diehl & Timmes (1998). The discussed here HE and VHE gamma rays can only be produced by the interactions of relativistic particles. From now on gamma ray is used for HE and VHE gammas, if not mentioned explicitly else.
This section describes the most important production mechanisms for gamma rays (see also Longair (2010)). The production mechanisms of gamma rays are usually divided into two groups: leptonic processes and hadronic processes. The naming refers to the nature of the interacting relativistic particle, i.e. leptonic processes for electrons (and positrons) and hadronic processes for protons. Two competing processes exist for leptonic gamma ray production:

- **Inverse Compton scattering (IC)** is the interaction between a (relativistic) electron and ambient photons. Hereby most of the electron's energy is transferred to the photon, thus reaching VHE. The IC process can be divided in the Thompson regime ($\alpha \ll 1$) and the Klein-Nishina regime ($\alpha \gg 1$) depending on the ratio between the photon energy in the rest frame of the electron and the rest mass of the electron $\alpha = E'_\gamma / m_e c^2$.

  - In the Thompson regime the cross section is independent of the energy and given by the Thompson cross σ_T section. The maximum energy of the photon after the scattering in the laboratory frame is: $E_{\gamma,\,\mathrm{max},\,\mathrm{T}} \approx 4\gamma^2 E_{\gamma,\,0}$ where γ is the Lorentz factor of the electron and $E_{\gamma,\,0}$ the initial energy of the photon in the laboratory frame. Assuming a electron population in the form of a power law $E^{-\Gamma_e}$ the resulting photon spectrum will be also a power law but with a harder slope $\Gamma_\gamma = (\Gamma_e + 1)/2$.

  - In the Klein-Nishima regime the energy transfer to the photon is $\propto \gamma m_e$ i.e., the photon obtains all the energy from the electron in one interaction. The cross section can be approximated as $\sigma_{kn} \approx \pi r_e^2 \frac{1}{\alpha} \left(\ln 2\alpha + \frac{1}{2} \right)$. Here r_e is the classical electron radius. The cross section decreases roughly with $1/\gamma$ resulting in a photon spectrum with a softer slope of $\Gamma_\gamma = (\Gamma_e + 1)$.

  The overall photon spectrum produced by IC scattering of relativistic electrons on ambient photon fields has a typical structure of an asymmetric peak: at high energies the suppression of the cross section in the Klein-Nishina regime leads to a significant steepening of the spectrum. The efficiency of the gamma ray production by the IC depends linearly on the density of the photon field and thus a higher density of background photons leads to a higher gamma ray luminosity. In addition to locally varying photon fields (e.g. star light, or reprocessed starlight) the cosmic microwave background (CMB) acts as a persistent target for IC scattering of relativistic electrons throughout the universe.

- **Bremsstrahlung** is the interaction of electrons with ambient matter. Here, electrons are decelerated in the electric field of nuclei emitting energy in form of a photon. On average one or two photons are emitted per radiation length. The average energy of an

emitted photon is $\sim 1/3$ of the energy of the electron. An electron population in the form of a power law will produce a gamma-ray spectrum of the same power law form. The magnitude of the cross section depends on the chemical composition ($\sigma_{Brems} \propto Z^2$) and the degree of ionization of the medium.

In the hadronic channel gamma rays are almost exclusively produced in inelastic proton-proton collisions. Therefore, the intensity of the expected hadronic gamma ray emission depends strongly on the product of CR density and ambient matter density. Such collisions produce mesons and in particular pions. Example interactions are:

$$\text{p} + \text{p} \rightarrow \pi^0 + \text{p} + \text{p} \tag{2.15}$$

$$\text{p} + \text{p} \rightarrow \pi^0 + \pi^+ + \pi^- + \text{p} + \text{p} \tag{2.16}$$

$$\text{p} + \text{p} \rightarrow \pi^\pm + \text{n} + X \ . \tag{2.17}$$
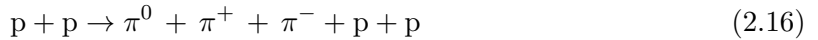
Charged pions will decay into muons (finally to electrons and positrons) and neutrinos. For typical slopes around -2 and e/p-ratios of $\sim 1/50$ the secondary electrons (positrons) produced in pp-collisions play no role as an additional source for gamma ray production for SNRs. The main decay channel ($> 99\%$) of the neutral pion is:

$$\pi^0 \rightarrow 2\gamma \tag{2.18}$$

In average about one tenth of the energy of the primary CR proton is transfered into each gamma. The cross section for π^0 production is almost independent of energy. Thus, the slope of the produced gamma-ray spectrum is identical to the spectral slope of the protons. A unique footprint of the hadronic channel is the production of highly relativistic neutrinos which come from the decay of charged pions.

Comparing the efficiency of the gamma ray production in leptonic and hadronic channels one finds that, almost independent of the environment, leptonic gamma ray emission is produced more efficiently. The typical *cooling time* $\tau = \frac{E}{dE/dt}$ for relativistic particles affected by the different processes are:

- IC scattering (assuming for simplicity scattering on CMB only):

$$\tau_{IC} \approx \frac{2.3 \times 10^{12}}{\gamma} \text{ years} \tag{2.19}$$

- Bremsstrahlung[3]:

$$\tau_{Brems} \approx 10^6/n \text{ years,} \tag{2.20}$$

  where n is the ambient particle number per cm^3.

- Pion production (inelastic pp-collisions)

$$\tau_{pp} \approx 10^7/n \text{ years} \tag{2.21}$$

---

[3]A primordial hydrogen and helium contribution as a fully ionized target material was assumed. Furthermore the weak energy dependence on the cross section was neglected. The lifetime for ultra relativistic electrons ($\gamma \gtrsim 10^8$) might thus be slightly over estimated. It is important that Bremsstrahlung of electrons is usually somewhat more efficient for production of photons compared to pp collisions.

An important competing process of energy loss for electrons is synchrotron radiation in ambient magnetic fields. This mechanism does not result in the production of VHE gamma rays (at least for the typical environments of the sources discussed here) but rather in radio and x-ray emission and can even reach to HE (i.e., Crab Nebula). The cooling time of a relativistic electron affected by synchrotron radiation depends quadratically on the magnetic field strength and linearly on the energy of the electron:

$$\tau_{Sync} = \frac{2.4 \times 10^{13}}{\gamma \left(\frac{B}{\mu G} \right)^2} \text{ years} \tag{2.22}$$

Assuming 1 TeV particles in a typical average interstellar medium ($n = 1/\text{cm}^3$, $B = 3\mu G$) one can estimate the relative importance of the individual processes. The cooling times in years for electrons are: $\tau_{IC} \approx 1.2 \times 10^5$, $\tau_{Brems} \approx 1 \times 10^6$, and $\tau_{Sync} \approx 1 \times 10^6$. For protons the cooling time due to inelastic pp interactions is $\tau_{pp} \approx 10^7$ years, one order of magnitude higher. Here, the most dominant emission in the gamma-regime arises from IC scattering. However, synchrotron losses are important when considering the total flux.
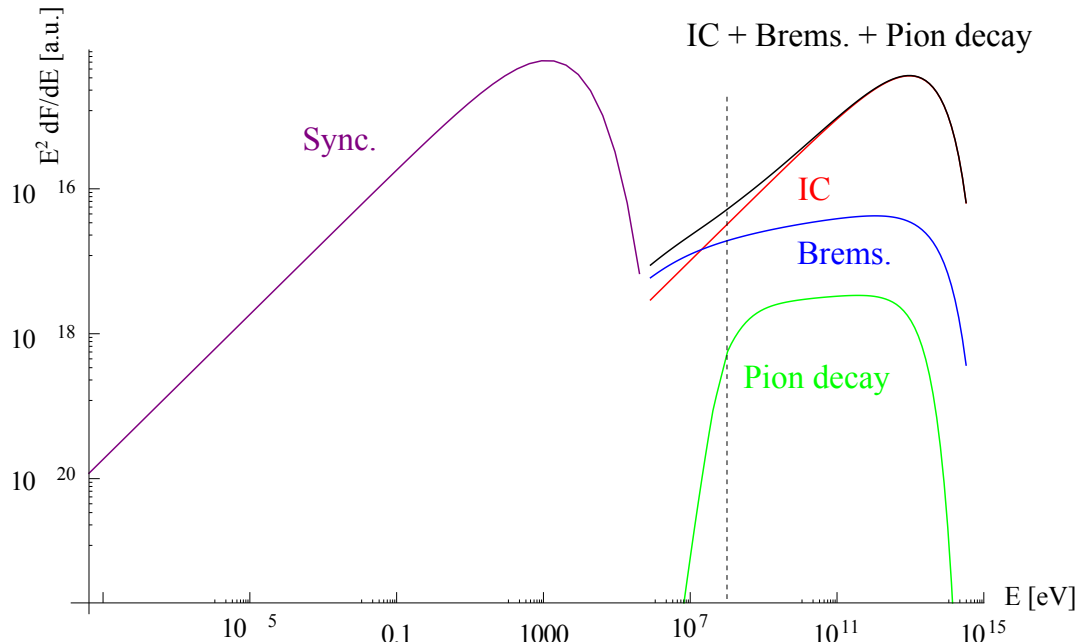
Figure 2.5: Example of the broad band spectral energy distribution in arbitrary units caused by a power law distribution of relativistic electrons and protons (electron proton ratio = 1). The slope of both distributions is -2, and an exponential cut-off has been assumed at 10^{14} eV. The parameters of the interstellar material chosen are: $n = 1$, $B = 3\mu G$, and only CMB photons have been considered as target photons for IC scattering. The kinematic cut-off in the emission produced via pion decay is indicated by the dashed line. It can be seen that electrons radiate more efficiently than protons and that IC dominates in low density media. Courtesy of Sara Rebecca Gozzini, private communication.

Figure 2.5 shows the multi wavelength spectra of non-thermal radiation produced by a power law distribution of relativistic electrons and protons (e/p=1, slope=-2).

The high gamma-ray emissivity of electrons is one of the main challenges for the identification of hadronic sources. Depending on the environment (i.e., density, photon field, and magnetic field) the gamma ray emission can be dominated by different processes or be a combination thereof. Only in regions with high density and strong magnetic fields the hadronic process may become the dominant gamma-ray production mechanism.

At this point the following aspects should be stressed: only a hadronically dominated gamma-ray emission allows straightforward conclusions on the proton- and thus on the CR spectrum. However, leptonically dominated gamma-ray emission does not exclude the presence of a significant component of relativistic protons. Moreover, as the spectrum of the underlying particle distribution is not a priori known, VHE gamma-ray without further multiwavelength data are not able to distinguish between a hadronic or a leptonic scenario.

2.3.2 How to distinguish between leptonic and hadronic scenarios

The most powerful way to reveal a hadronic origin of the observed VHE gamma radiation would be the detection of the neutrino flux produced in inelastic pp collisions. Kelner et al. (2006) showed that the luminosities of all end products produced in pp-collisions (gammas, neutrinos, electrons, and positrons) are compatible within factor of 2. The detection of the neutrino flux expected from the observed gamma ray flux would thus ultimately confirm the underlying hadronic nature of the emission. Despite large efforts in building neutrino telescopes, the extremely low cross sections of neutrino interactions and the low expected flux prevented the discovery of distinct neutrino sources to date. A review of the current status in neutrino astronomy and their connection to cosmic rays is given in Gaisser & Stanev (2012). For a historical review on neutrino astronomy the reader is referred to Spiering (2012).

A second very powerful tool to distinguish leptonic and hadronic scenarios is the gamma ray flux of the source at energies around 100 MeV (see also Fig. 2.5). The threshold energy for the production of neutral pions is given by: $E_T = m_p + 2m_\pi + m_\pi^2/m_p = 1.22$ GeV (Kelner et al. 2006). Therefore the produced gamma ray spectrum in hadronic interactions shows a sharp cut-off towards lower energies at ~ 100 MeV, independent of the underlying proton distribution. For gamma rays produced in IC scattering (on CMB photons) or via Bremsstrahlung the gamma ray slope is, as discussed above, $\Gamma_\gamma = (\Gamma_e + 1)/2$ and $\Gamma_\gamma = (\Gamma_e)$, respectively. The detection of a low energy cut-off at 100 MeV is hence a clear signature of a hadronic dominated gamma ray emission. The greatest challenge for observations at such low energies is the high flux of the diffuse galactic gamma-ray emission (Ackermann et al. 2012). This emission is produced during the propagation of cosmic rays in the galaxy. The SNR W44, the brightest known SNR in HE gamma rays (Abdo et al. 2010c), is the only case in which a suppressed gamma ray flux at 100 MeV has been directly discovered. This is interpreted (Giuliani et al. 2011a) as the kinematic cut-off described above and provides strong evidence for CR acceleration in W44.

The most common approach to discriminate between different scenarios is the modeling of the *multi wavelength emission* over all accessible energies. Here, distributions of relativistic particles (either assumed ad hoc or determined implicitly from acceleration models) are used to predict an overall multi wavelength emission produced in the environment of the source. The result is then compared to real data. The complexity of the underlying physical processes and

the incomplete set of all observations often prevent a definite conclusion from this approach. In fact, in many cases the emission of a gamma ray source can be equally well described in a leptonic and a hadronic scenario. Only in cases where the source and its surrounding are well known and well understood is one able to distinguish between different scenarios.

2.3.3 Gamma ray astronomy

It would be narrow-minded to restrict gamma ray astronomy only to the search for CR sources and/or the study of supernova remnants. Gamma ray astronomy is one of the newest windows to space and allows us to investigate the most energetic events in the universe. The development in the field, in particular over the past 10 years, was enormous. Figure 2.6 shows the number of known sources in X-rays, HE, and VHE gamma ray astronomy from the detection of the first source in each regime till now.

More detailed information about the status of the field can be found in Hinton & Hofmann (2009); Funk (2012); Holder (2012). Moreover, the mechanism of diffusive shock acceleration can occur in any astrophysical shock and is by no means restricted to those of SNRs. In addition other processes can produce highly relativistic particles such as the magnetosphere of pulsars, or magnetic reconnection processes (see e.g. Lazarian et al. 2012).
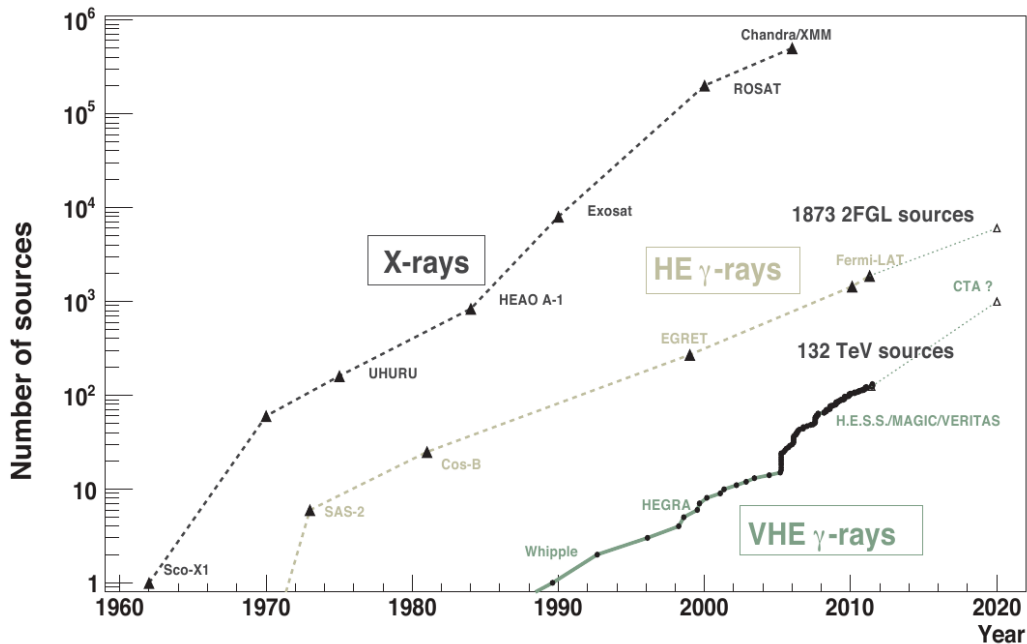
Figure 2.6: *Kifune* plot showing the numbers of sources detected as a function of time for three different wavebands (a similar plot was first presented by T. Kifune at the International Cosmic Ray Conference 1995 in Rome). Picture adopted from Funk (2012)

Gamma ray sources

Nowadays a variety of different types of gamma ray sources are known. They are usually grouped in galactic and extragalactic sources. The most important types of sources are introduced below:

- **Galactic gamma ray sources**

  – Supernova remnants
    SNRs have already been introduced as the candidate sources of galactic cosmic rays. HE and VHE gamma ray emission has been detected from several objects. A short overview of SNRs seen in the light of gamma ray astronomy will be given in section 2.3.4. The supernova event itself (the implosion of the massive star) is not thought to accelerate very high energy particles and thus produces no VHE gamma ray emission. The main reason is that the timescale of the event is in the order of seconds and thus not sufficient to accelerate particles to very high energies.

  – Pulsars
    Pulsars form in supernova explosions. They are highly magnetized, fast rotating neutron stars with a typical mass of $\sim 1.4\,M_{\odot}$. The misalignment of the rotational and magnetic axis leads to periodical electromagnetic emission (*Lighthouse-effect*) in almost all wavelengths. While in HE gamma rays many pulsars have been detected, only one was detected in VHE: the Crab Pulsar (Aliu et al. 2008; VERITAS Collaboration et al. 2011; Aleksić et al. 2011, 2012c). The discovery of pulsed emission above ~ 100 GeV, was completely unexpected and ruled out all pulsar models existing at that time. Time will show if the Crab Pulsar is unique or more pulsars will be discovered in the VHE regime.

  – Pulsar wind nebulae (PWN)
    PWN are a wind of relativistic electrons emerging from the pulsar. When the wind decelerates a standing shock wave is formed at around 0.1 pc distance to the neutron star. Here electrons (and potentially protons) can be accelerated to ultra relativistic energies. Note that a PWN is substantially different from a SNR[4] as the shock is produced and sustained by the relativistic wind of electrons powered by the pulsar. PWN are, together with SNRs, the largest population of galactic VHE sources. The bubble of highly relativistic particles around a PWN can reach a size of ~ 10 pc around the pulsar.

    The most famous example of a PWN is the Crab Nebula. Until recently it was common wisdom that PWNs show no flux variations and the Crab Nebula was used as the standard candle of constant flux in HE and VHE energies. Nature surprised the whole community as strong flares with timescales in order of days have been discovered (Tavani et al. 2011; Abdo et al. 2011b), where the synchrotron flux > 100 MeV increased up to a factor of 6, implying electron acceleration up to PeV energies. In contrast, no flux changes have been found by VHE instruments in the energy range of ~ 100 GeV to 10 TeV (Mariotti 2010; Ong 2010; Zanin 2011) during observations in the flare periods. Moreover, Aielli et al. (2010); Di Sciascio

---

[4]Both the expanding shock wave (SNR) and the neutron star are remnants of a supernova event. For historical reasons only the shock wave is called supernova remnant

& for the ARGO-YBJ Collaboration (2012) reported hints of an increased ∼TeV flux simultaneous with the GeV flare(s), but not strictly simultaneous to the observations from MAGIC and VERITAS. 23 years after the discovery of TeV emission from the Crab Nebula it is still one of the most studied and most interesting TeV sources in the sky.

– Binary systems
Binary systems emitting gamma radiation consist usually of a compact object (neutron star or stellar mass black hole) and a massive star. Two main scenarios are used to explain the gamma radiation. One is based on the interaction between the wind of the massive star and the wind of the pulsar. The other scenario is powered by accretion onto the compact object and emission in a form of a relativistic jet. In the microquasar scenario (black hole as the compact object) the accretion scenario is the only solution. For binaries with a neutron star, both accretion and interaction between the winds are possible (see e.g., Romero et al. 2007, and references therein).

- **Extragalactic gamma ray sources**

  – Active galactic nuclei (AGNs)
  By far the largest population of known extragalactic gamma ray sources are active galactic nuclei (AGNs). AGNs are super massive black holes in the center of galaxies which effectively accrete material. Perpendicular to the accretion disk relativistic outflows (jets) are formed. Within the jets particles are accelerate to ultra relativistic energies through the DSA mechanism. Different AGNs are classified depending on the orientation between the jet and the observer.

    * Blazars are AGNs where the observer is looking into the jet. This is the most common class of know VHE emitters, likely related to their high luminosity.

    * If the viewing angle is large one speaks about radio galaxies or Seyfert I and Seyfert II galaxies.

  All AGNs are highly variable sources at nearly all wavelengths and times scales.

  – Starburst galaxies
  A second source class of HE and VHE gamma ray emission discovered recently are starburst galaxies (Acero et al. 2009; VERITAS Collaboration et al. 2009). Those are galaxies with an extremely high star formation rate. The high star formation rate leads to a high rate of supernovae explosions. The gamma ray emission is thought to reflect the high cosmic ray density accumulated in these systems over many generations of supernovae.

  – Gamma Ray Bursts (GRBs)
  are the most violent events in the universe. The duration of the prompt emission is $\lesssim 200$ s. All observed GRBs are found at cosmological distances. It is believed that a GRB is either a supernova of very massive star, or a merger of a neutron star with a black hole or a second neutron star. Due to their short duration GRBs have been detected only in HE (large field of view satellites) but not yet in VHE. However, the highest photon energy ever observed from a GRB was ∼ 30 GeV (Abdo et al. 2009a) possibly indicating the existence of VHE emission.

Figure 2.7 shows the distribution of all VHE gamma ray sources currently known. A large amount of all HE gamma ray sources (575) could not be associated to any other source of different wavelength (Nolan et al. 2012). Also in the VHE regime a large fraction of sources ($\sim 20\%$, according to http://tevcat.uchicago.edu/) remains unidentified. One might interpret these numbers as an indication that more types of sources exist able to emit gamma rays.

Despite the more classical gamma ray sources discussed above there are also some unusual sources of gamma ray emission. The *Fermi*/LAT detected gamma ray emission from the sun both in quiescent state and also during flaring periods (Abdo et al. 2011c; Giglietto et al. 2012). As the earth is constantly illuminated by cosmic rays our planet acts as a target to produce gamma-ray emission via inelastic proton-proton interactions in the atmosphere. The produced emission has been reported by Abdo et al. (2009b), and is the brightest HE source in the sky. Furthermore, the earth itself can produce HE gamma particles in the lightnings of thunderstorms (Marisaldi et al. 2011; Briggs et al. 2010). The field of HE and VHE gamma ray astronomy is still young, and even though tremendous progress has been made, there are many more fascinating observations to come.
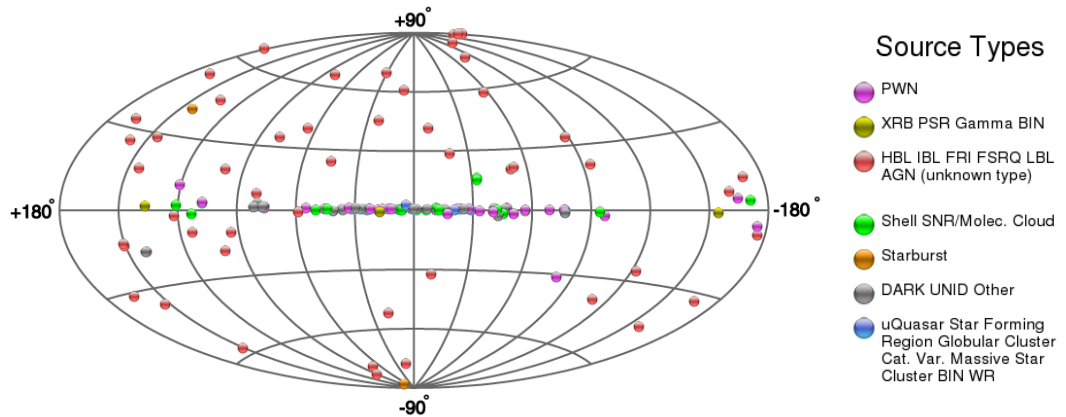
Figure 2.7: All sky distribution of VHE gamma ray sources in galactic coordinates. Picture obtained from TeVCat (http://tevcat.uchicago.edu/).

2.3.4 Supernova remnants in the light of gamma ray astronomy

This section discusses the current understanding of CR acceleration in supernova remnants and the expectations for gamma ray emission in these objects.

First, the question is addressed which material is accelerated in SNRs, either the newly synthesized material of the supernova itself or the matter surrounding the progenitor star. This question was solved by composition measurements of the CR flux observed on earth. It is known that ^{59}Ni is produced in the nucleo-synthesis of a supernova. This Nickel isotope is radioactive and decays into ^{59}Co with a half life time of $0,76 \times 10^5$ years. The decay happens exclusively via electron capture. Any nucleus can only capture an electron if moving with thermal velocity. Wiedenbeck et al. (1999) reported that no contribution of ^{59}Ni has been found in the CR spectrum. Instead a clear contribution of ^{59}Co has been measured. Therefore, Wiedenbeck et al. (1999) conclude that all produced ^{59}Ni decayed before the acceleration. Thus, it is evident that a SNR accelerates the ambient medium and not the matter produced

in the supernova itself. Furthermore, the time between the synthesis of elements and their acceleration has to be much larger than the half life time of the considered Nickel isotope. Therefore, the synthesis of heavy elements and their acceleration to CRs has to happen in different generations of supernovae and their remnants passing the same area in space.

To understand the acceleration of CRs in SNRs, one has to first understand the dynamics of the supernova remnant. The evolution of a SNR can be divided into three sequences: Immediately after the supernova explosion the shock wave undergoes a free expansion phase. In this phase the deceleration of the shock wave can usually be neglected. Therefore the shock speed is approximately constant and the radius $R(t)$ of the shock front grows linearly with time:

$$R(t) \approx U_0 \, t \, . \tag{2.23}$$

U_0 is the expansion velocity in the moment of the supernova, and t the time after the supernova event. The initial expansion velocity can be obtained as $U_0 = \sqrt{2E_{SN}/M_{ej}}$ where E_{SN} is the amount of kinetic energy released and M_{ej} the mass ejected by the supernova. The SNR enters the so called Sedov-Phase when the shock wave has swept up surrounding material of a mass compatible to the ejected mass:

$$R_s = \left(\frac{3M_{ej}}{4\pi\rho_1} \right)^{1/3} \, . \tag{2.24}$$

Here, R_s is the radius of the SNR at the beginning of the Sedov-phase and ρ_1 the matter density of the ambient interstellar medium. The expansion velocity of the shock can now be described as an adiabatic expansion. Assuming a spherically symmetric expansion into a homogeneous medium of density ρ, and neglecting the pressure outside the remnant, one obtains the well known Sedov-solution (Sedov 1959):

$$R(t) = \alpha_s \left(\frac{E_{SN}}{\rho} \right)^{1/5} t^{2/5} \, , \tag{2.25}$$

$$\frac{d}{dt}R(t) = U(t) = \frac{2\alpha_s}{5} \left(\frac{E_{SN}}{\rho} \right)^{1/5} t^{-3/5} \, . \tag{2.26}$$

Here, α_s is a dimensionless constant of order unity (see for example White & Long 1991). When radiative losses become important the shock wave enters the radiative phase. According to Draine & McKee (1993) this happens when the shock velocity drops below a critical value:

$$U_{\text{crit}} = 180(\rho^2 E_{SN})^{1/14} \frac{\text{km}}{\text{s}} \, . \tag{2.27}$$

During this phase the velocity of the shock wave drops even more rapidly until the shock disappears and the SNR dissolves in the intergalactic medium. The typical velocity in the individual phases are ~ 10000 km/s (free expansion phase), ~ 1000 km/s (Sedov phase), and ~ 100 km/s (radiative phase). During its evolution the radius of the shock wave grows from a few parsec at the end of the free expansion phase up to few tens of parsec at the end of the Sedov phase. About $\lesssim 1000$ years after the supernova has occurred, the shock wave enters the Sedov-phase which will last up to several ten thousand years. Note, that the evolution of

an individual remnant might differ depending on its environment, the initial kinetic energy, and ejected mass of the supernova. Furthermore, the assumption of an adiabatic expansion implies energy conservation of the shock wave. If, however, CRs are efficiently accelerated in the SNR this means that a significant fraction of energy ($\gtrsim 10$ %) is transferred to cosmic rays. A fully self consistent description of CR acceleration and its feedback on the shock evolution is very challenging and goes far beyond the scope of this introduction. For further reading see e.g. Blasi et al. (2005); Ellison et al. (2010) and references therein.

In the framework of DSA the shock velocity is strongly connected to the acceleration time needed to reach a given energy. Therefore, the maximum achievable energy strongly depends on the shock velocity and is decreasing with time (Ptuskin & Zirakashvili 2005, 2003). In contrast, the amount of injected particles depends on the spatial size of the shock wave and is thus increasing with time. However, as the shock decelerates the acceleration time increases and thus the energy converted into CRs decreases. In the standard model of DSA it is believed that particles with energies around the knee are produced during the transition of the free expansion phase and the Sedov phase. The main acceleration of CRs below the knee happens during the Sedov phase, due to the much longer duration of this phase. Due to the low shock velocity during the radiative phase it plays only a marginal role in the CR acceleration. SNRs are therefore usually divided in two main sub classes:

- **Young SNRs**
  (age 1000 years and younger) are believed to achieve the highest energies. A young SNR is still in the free expansion phase or in transition between the free expansion and Sedov phase. While the intensity of CRs produced is comparatively low, it is this phase where the highest energetic particles are believed to be produced.

- **Middle age SNRs**
  (age up to several 10000 years) are more frequent in the galaxy and the higher age of this remnants leads to an accumulation of accelerated GCRs which enhances the gamma ray signal. However, the most energetic CRs (around the knee and slightly below) are thought to have escaped the remnant already.

For the gamma-ray emission one can thus expect that the young SNRs are less luminous but with spectra extending to higher energies than middle age remnants. Moreover, the CRs in young SNRs represent a *young* population of CRs. That is, cooling processes may not yet play a major role. The long cooling time for protons, being similar or larger to the age of SNRs at the end of the Sedov-phase, implies that cooling of protons during the complete evolution of the remnant can be neglected.

For electrons the situation is different. The cooling times for synchrotron and IC losses can be comparable or lower than the age of the remnant at the end of the Sedov phase. Moreover, the cooling times of both processes scale linearly with the Lorentz factor of the particles. An electron spectrum of the form $N(E) \propto E^{-\Gamma}$ constantly injected over a time t will, affected by IC and/or synchrotron losses, develop a break at the critical energy $E_c(\tau = t)$, where τ is the cooling time and t is the time after injection. The spectrum above E_c is steeper by one power of E, containing only particles injected at a time $t_i \lesssim \tau$. That means that in particular the high energy end of the electron spectra after a time t_i is steeper than that of protons, even in the case of a constant injected electron to proton ratio. The exact break energy depends on the ambient magnetic field and the photon field. Note that in dense media ($n \gtrsim 10$, $B \lesssim 3\mu$ G,

and CMB as the main photon field) the dominant cooling process for electrons can become Bremsstrahlung which will affect all energies equally. Thus the spectral shape of the electron spectrum is not affected but its absolute intensity is reduced. In general, the total cooling of the electron spectrum is the sum of all three components (IC, Bremsstrahlung, Synchrotron) and is in general more efficient than the cooling for the proton spectrum.

Finke & Dermer (2012) provide a detailed discussion on the evolution of the electron spectrum in the young supernova remnant RX J1713.7-3946. This remnant has been thought to be one of the most promising cases of hadronic gamma ray emission and thus to be a galactic cosmic ray source (Aharonian et al. 2004b, 2007). The discovery of very hard (slope -1.5) GeV emission from this SNR (Abdo et al. 2011a) strongly suggests a leptonic origin of the gamma ray emission. Ellison et al. (2010) show that even with an assumed electron to proton ratio in the source of 2/100 the IC emission of relativistic electrons is by far the most dominant contribution to the observed gamma ray flux.

Hadronic models are severely challenged by thermal x-ray emission which would be much higher than observed. It should be made clear that the leptonically dominated gamma ray emission does by no means exclude the presence of relativistic protons. Instead Ellison et al. (2010) point out that they are a necessary ingredient in their model. Nonetheless, the broad band observations do not imply the need for such a proton population (Finke & Dermer 2012). In other young remnants (e.g. Cas A, SN 1006) it is not clear if the origin of the observed emission is leptonic, hadronic, or a mixture of both (Berezhko et al. 2012a; Araya & Frutos 2012; Abdo et al. 2010a). Also the amount of kinetic energy of the SNR converted into CRs appears rather low (2–5% in the cases of Cas A and SN 1006). However, it may be that the majority of CRs, assumed to be accelerated during the Sedov-phase, might not have been produced yet. The ambiguity between leptonic and hadronic models, and the rather low gamma ray luminosity of young remnants make them very challenging targets both from an observational and theoretical point of view. In addition the amount of young SNRs is very low due to their rather short lifetime of < 1000 years and the low rate of supernova events in our galaxy.

There is, however, one case where the emission from a young SNR is most likely dominated by hadronic emission: Tycho's supernova remnant. Gamma ray emission from Tycho has been detected by *Fermi*/Lat and VERITAS (Giordano et al. 2012; Acciari et al. 2011) which follows a single power law between sub-GeV and multi TeV energies. Morlino & Caprioli (2012) argue based on the shape of the observed gamma ray emission, and the detailed multi-wavelength data, that the emission is of hadronic origin. This implies proton acceleration up to ~ 500 TeV and that $\sim 12\%$ of the kinetic energy of the forward shock has been transferred into CRs. As of today, Tycho is the most promising candidate of a cosmic ray source among all detected young SNRs. While a direct observation of a hadronic gamma ray signal at energies up to the knee is still pending, the indications of 0.5 PeV protons in Tycho is promising that SNRs can indeed achieve energies up to the knee. However, the low flux expected at gamma ray energies > 300 TeV from young SNRs like Tycho is not accessible with the sensitivity of the recent generation of VHE instruments.

The class of middle age SNRs is much more abundant. In addition, more CRs have been accumulated over time and thus the luminosity of middle age remnants is expected to be higher. Furthermore, the electron component might have been reduced due to the cooling processes. Moreover, in many cases the SNR is interacting with or in the vicinity of molecular clouds. This provides a high amount of target material which enhances gamma ray emission

produced by interactions with matter and therefore enhances the hadronic component of the gamma ray emission. A recent overview on the connection between molecular clouds, SNRs and CRs, as well as the status of the field can be found in Gabici (2012).

When a supernova shock wave runs into a molecular cloud, the interaction region acts as an amplifier of the hadronically induced gamma ray flux produced by CRs confined to the acceleration zone around the shock front. Already in the pioneering work of Montmerle (1979) the unique properties of SNRs interacting with molecular clouds have been pointed out, as well as their immense use in understanding the origin of cosmic rays. The main claims of this work concerning SNRs interacting with molecular (SNR-MCs) clouds are:

1. The gamma ray luminosity of SNR-MC systems should be enhanced compared to isolated SNRs due to the higher ambient matter density

2. The gamma ray spectra of these objects can be used to determine if the emission is dominated by hadronic or leptonic processes

3. Due to the high amount of freshly accelerated low energy CRs the CR ionization in molecular clouds close by (or interacting with) SNRs should be enhanced compared to ordinary interstellar clouds.

Indeed, the most luminous SNRs in gamma rays are those interacting with molecular clouds and in most cases the spectral modeling suggests a hadronic origin of this emission. The hadronic nature of the observed emission allows to draw direct conclusions on the CRs produced in the source. It is worth to mention that the list of potential objects provided by Montmerle (1979) contains all four (W51C[5], W28, W44, and IC443) of today's most prominent examples of this type of source.

Moreover, molecular clouds in the vicinity of SNRs can act as *detectors* of the escaping flux of CRs. Gabici et al. (2007) and Gabici et al. (2009a) performed a detailed theoretical discussion on the expected broad band non thermal emission from MC illuminated both by the average CR flux in the galaxy (sea of CRs) and from CRs escaping a close-by SNR. The main conclusions of this works are:

1. The gamma ray emission above 100 MeV is dominated by hadronic emission (for a primary electron proton ratio of ~ 0.02 as it is observed in the CR flux at earth).

2. The shape of the observed Gamma ray spectrum depends strongly on the density profile and diffusion coefficient close to the SNR.

3. For a cloud close to a SNR, the high energy CRs will illuminate the cloud at earlier times as the low energy CRs (as high energy particles both escape the remnant earlier and diffuse faster). Thus, one can expect an energy dependent morphology of the observed gamma ray flux.

The prime example of a scenario where MCs are illuminated by escaping CRs is W28 as revealed by the H.E.S.S. collaboration (Aharonian et al. 2008b). Here three individual molecular clouds show a comparable emission which can be explained by the diffusion of escaping

---

[5]The supernova remnant W51C is the main scientific target of this thesis. The obtained results are presented in Chapter 7

CRs from the remnant to the clouds (Gabici et al. 2010). Recently the observations around GeV energies by Abdo et al. (2010b) and Giuliani et al. (2010) show a morphological change between the TeV and GeV emission which is compatible with the energy depended escape and diffusion of CRs from the SNR to the individual clouds. Similar indications are also seen in IC443 (Tavani et al. 2010).

Chapter 3

The imaging air Cherenkov Technique

This chapter provides a brief introduction into the basics of ground based gamma-ray astronomy using the imaging air Cherenkov (IAC) technique. Telescopes using the IAC technique (so called IACTs) operate in the range of very high energies (VHE, ~ 50 GeV up to ~ 100 TeV) and therefore expand the accessible energy range in astronomical observations towards the highest energies. For a recent historical overview see Lorenz & Wagner (2012). An overview of the status, of gamma ray astronomy in the TeV range is given in Hinton & Hofmann (2009). This chapter which focuses on the experimental technique itself (see also Weekes (2003) for details), which is unique with respect to the need of having an atmosphere in contrast to all other ground bases astronomical observations. For all other wavelengths the atmosphere only disturbs ground based observations, a lot of wavelengths (e.g. x-rays) are even forced to rely on space based observations.

Also for VHE gamma rays the atmosphere is opaque, which prevents such photons to arrive at ground level. A VHE photon hitting the atmosphere of the earth produces a cascade of relativistic particles similar to a jet in a particle detector. Such a cascade is called extensive air shower, where the earths atmosphere acts as a calorimeter. The particles produced in such an air shower are highly relativistic and thus can exceed the speed of light in air. Note that the speed of light in a medium is reduced by the refractive index ($v_{medium} = c/n$) compared to the univerals physical constant, speed of light in vaccum (c). The speed of massive particles is only limited to be $< c$ and thus can overcome the speed of light in a given medium c_{medium}. Hereby they produce the so called Cherenkov radiation mainly in the visible and UV regime. IACTs take images of the Cherenkov radiation produced by air showers, which are used to determine the energy, arrival direction, and nature of the primary particle inducing the shower. Thus the IAC technique provides only an indirect measurement. There are also space born gamma ray experiments which use direct measurements in pair conversion calorimeters. The newest generation instruments of this kind are on board the *Fermi* and the *Agile* satellites. Space and ground based astronomy have to be seen as complimentary fields: Gamma rays of low energies (below few tens of GeV) are not energetic enough to produce enough Cherenkov light to be detectable with IACTs and their observation is therefore limited to space born experiments. For higher energies IACTs take over as the situation is dominated by the low value of the absolute flux of gamma ray sources as illustrated in the following example: The strongest persistent gamma ray source in the sky, the Crab Nebula, has a gamma ray flux of $\sim 85 \times 10^{-13}$ gammas cm^{-2} s^{-1} above 100 GeV (Aleksić et al. 2012). The largest satellite detector, the *Fermi*/LAT, has an effective detector area of $\sim 1\text{m}^2$ which translates into a maximum of 180 detectable events above 100 GeV for one year of observation. In contrast, IACTs use the area of the atmosphere within the field of the telescopes as the detector. In the example above 180 events are detected with MAGIC in only 15 minutes (see also Figure 6.12),

resulting from the $\sim 4 \times 10^4$ larger effective detector area. In addition, the flux of gamma ray sources usually decreases with energy as E^{-2} or steeper and thus the large detector area of IACTs is mandatory to extend the observation to TeV energies and thus to access the highest energy phenomena in the universe.

This chapter is organized as follows: First, the basic principles of air showers are introduced, followed by the description of the Cherenkov effect. A brief explanation on the resulting images is given before the chapter finishes by introducing the latest generation of operating IACTs including a short outlook to the future.

3.1 Air showers

The dominant process for energy losses of VHE gamma rays in the atmosphere is pair production. Note that pair production can not take place in vacuum as momentum and energy can not be conserved without a third body. In the atmosphere the nucleus of air molecules acts as the needed third body which absorbs part of the energy or momentum. At the first interaction point (~ 20 km in height) a VHE gamma ray will therefore produce one electron-positron (both of similar energy) pair in the electric field of a nucleus. For highly relativistic > 85 MeV electrons/positrons the dominant process of energy loss is the Bremsstrahlung, where the electron/positron loses about half of its energy by the radiation of a photon. By subsequent interactions of pair production and Bremsstrahlung a cascade of particles is formed, the air shower. Hereby the number of particles continuously increases till the energy of the electrons falls below the critical energy $\epsilon_{\text{critical}} = 86$ MeV. Then, ionization losses become more important than Bremsstrahlung. The so called shower maximum is reached ~ 10 km above sea level for a 100 GeV gamma ray shower. At lower heights the number of particles in the shower starts to decrease till all particles have lost their energy and the shower died out. For a detailed description of the involved interactions see, e.g., Longair (2010) and references therein. The main features of an air shower produced by a gamma ray are:

- The cascade is purely electromagnetic and consists almost exclusively of $\sim 1/3$ electrons, $\sim 1/3$ positrons, and $\sim 1/3$ gammas.

- The total amount of particles produced is proportional to the energy of the primary gamma-ray.

- The shower is highly collimated along the incident direction of the primary gamma ray. As in all interactions above the critical energy every interacting particle possesses an energy $E_i \gg 2m_e c^2$, the law of momentum conservation forces a highly beamed cascade.

Besides from gamma rays, air showers can also be introduced by any kind of highly relativistic particle. The most common ones are those induced by cosmic rays, in particular protons. A proton induced air shower differs significantly from a gamma ray induced one, as here a fast variety of hadronic interactions has to be considered. These produce a large amount of, e.g., pions and subsequently muons. The high rest mass of the pions and their production accompanied by many particles in each interaction allows much higher transverse momentum in hadronic showers compared to electromagnetic ones. Therefore, hadronic showers can develop sub-showers along with the main shower. From a general point of view a hadronic shower follows the same evolution as a electromagnetic shower:
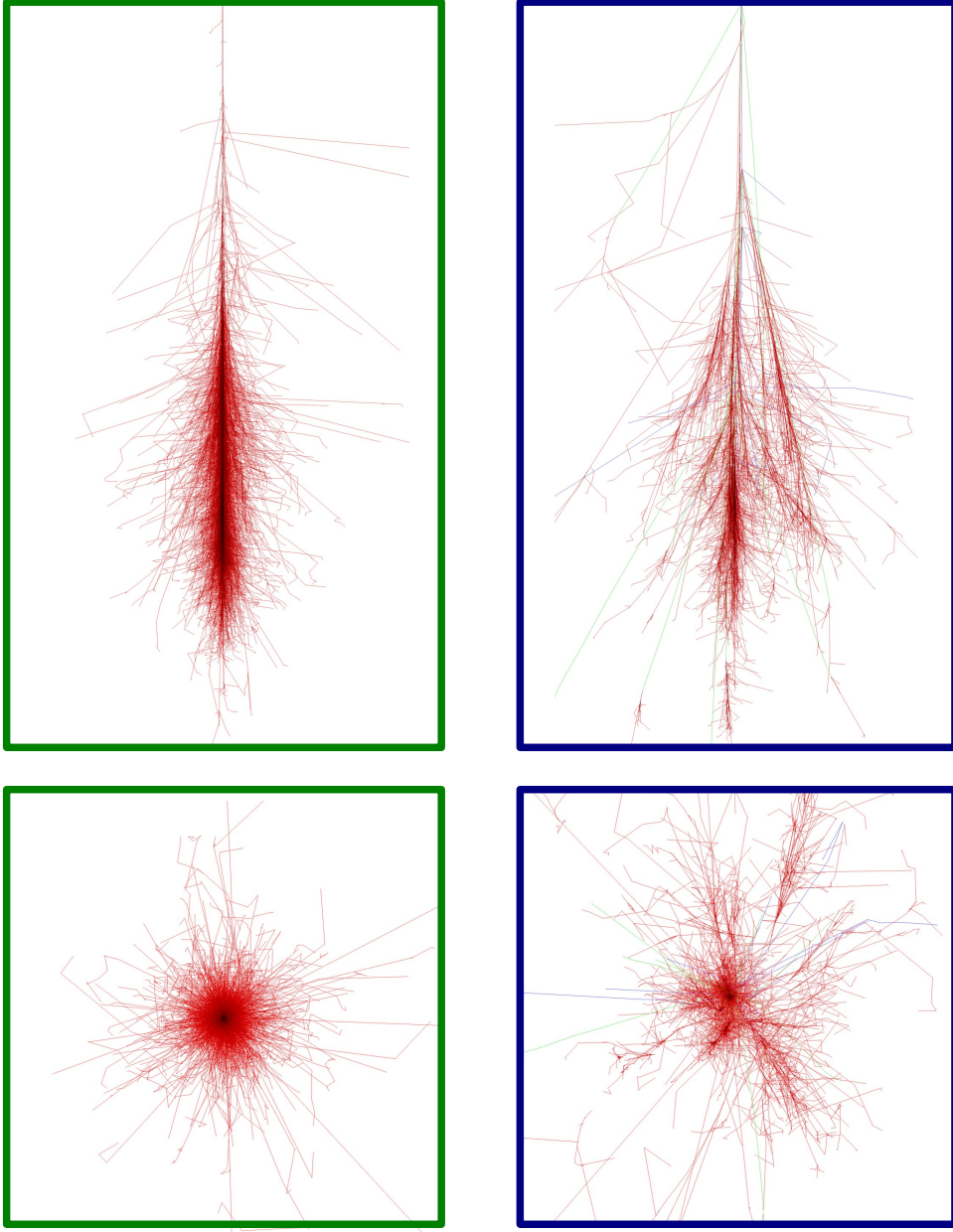
Figure 3.1: Simulation of air showers induced by a photon (green boxes) and a proton (blue boxes) performed with CORSIKA (Heck et al. 1998). The energy of the primary was 100 GeV in both cases. The upper panels show the showers in the plane parallel to the shower axis and the lower panels show the shower in the perpendicular plane. Each red line traces an electron/positron, blue lines trace hadronic particles (mostly pions) and green lines represent muon tracks. It can be seen that the hadronic shower shows a larger lateral spread and appears more irregular, what is a general feature of hadronic showers.

Above a critical energy (depending on the particle type) all secondaries will interact in such a way that the total amount of particles in the shower increases. When most particles fall below their critical energy the total amount of particles in the shower decreases and the shower dies out. Figure 3.1 shows a comparison of the simulations of an air shower induced by a 100 GeV photon and proton, respectively.

3.2 Cherenkov radiation

When charged particles move through a dielectric medium with a speed faster than the speed of light in this medium ($c_m = c/n$, where c is the speed of light in vacuum and n the refractive index of the medium), Cherenkov radiation is produced (Čerenkov 1937). Hereby the charged particle polarizes its surrounding medium. As long as the velocity of the particle is below c_m no net electric field is induced and therefore no radiation is emitted. For velocities larger than c_m a dipole field along the trajectory of the particle is created, causing detectable electromagnetic radiation. Figure 3.2 shows an illustration of the effect on the medium.
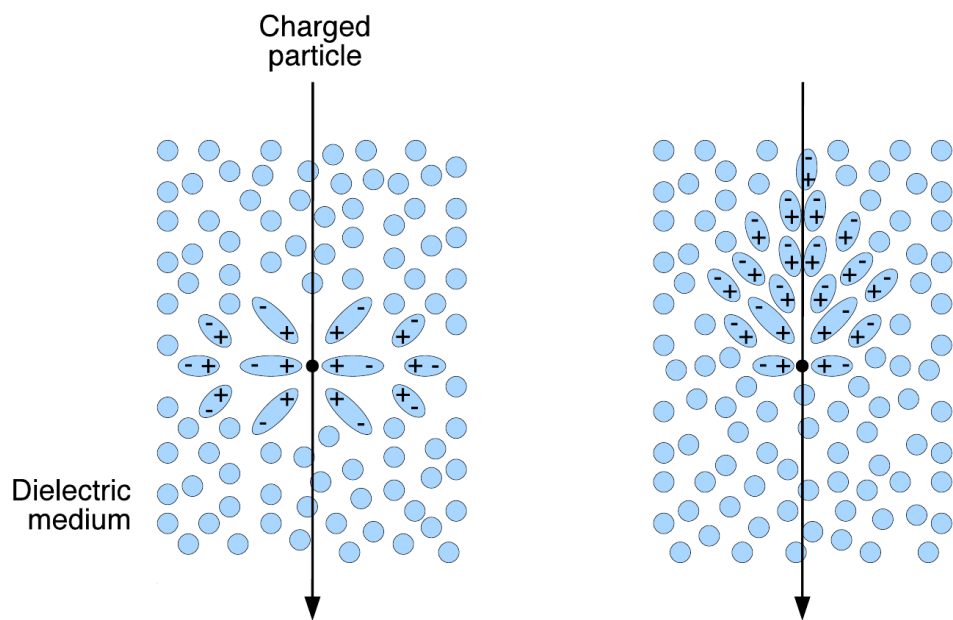
Figure 3.2: Illustration of the induced polarization by a particle traveling through a dielectric medium. The left picture shows the case of a particle with a velocity $v < c_m$ and on the right hand side the case $v > c_m$ is shown. Picture adopted from Weekes (2003)

Each finite element along the path of the particle will radiate an electromagnetic impulse. As the individually created waves propagate slower than the particle itself there exists one particular forward direction where all wavefronts constructively interfere. For all other directions the interference is destructive. Thus, Cherenkov light is emitted under one specific angle, the so called Cherenkov angle:

$$\cos\theta_c = \frac{1}{n\beta}. \tag{3.1}$$

As usual $\beta = v/c$. The Cherenkov angle depends therefore on the medium and on the velocity of the particle. The threshold condition for the production of Cherenkov light is $v > c_m$, above which the Cherenkov angle grows linear with the velocity of the particle. As for $\lim_{v \to c} \beta = 1$ the Cherenkov angle is constant for all energies and particles far above the threshold and only determined by the properties of the medium. The case of $\beta = 1$ is often referred to as the typical Cherenkov angle and is $\sim 1.2°$ in air (2200 meter above sea level). The energy loss rate per unit bandwidth $\frac{du(\omega)}{dt}$ of a particle is given by:

$$I(\omega) = \frac{du(\omega)}{dt} = \frac{\omega e^2 v}{4\pi\epsilon_0 c^3} \left(1 - \frac{c^2}{n^2 v^2}\right) \tag{3.2}$$

Where $I(\omega)$ is the intensity of the Cherenkov radiation, ω the frequency of the Cherenkov light, e the charge of the particle, and ϵ_0 the vacuum permittivity. For highly relativistic particles ($\lim_{v \to c}$) the total amount of produced Cherenkov radiation depends only on the properties of the medium, and the charge of the particle. Note that the intensity depends quadratically on the refractive index and that the refractive index itself is a function of the frequency ω. The spectral shape of the Cherenkov radiation is solely determined by the ambient medium. The total energy loss of a relativistic particle due to Cherenkov radiation is small compared to all other interactions (e.g. Bremsstrahlung, ionization, etc.).

3.2.1 Cherenkov radiation of air showers

When talking about the Cherenkov light produced by an air shower one has to consider two major aspects: many particles (e.g., ~ 800 electrons and positrons for a 100 GeV gamma ray shower) produce Cherenkov radiation at different heights in the atmosphere. First the Cherenkov light produced by a single particle passing through the atmosphere is considered. The density profile of the earths atmosphere follows an exponential law:

$$\rho = \rho_0 \times \exp(-z/h), \tag{3.3}$$

where z is the height above sea level, $h \approx 8.5$ km is the scale height of the atmosphere and $\rho_0 \approx 1.205 \times 10^{-3}\,\mathrm{g\,cm^2}$ the typical atmospheric density at sea level. The values here have been adopted from Aharonian et al. (2008c). By introducing $\eta = n - 1$ and adopting the simplification that η is proportional to the density (Aharonian et al. 2008c), the refractive index can be expressed as a function of the height in the atmosphere:

$$n = \eta_0 \times \exp(-z/h_o) + 1, \tag{3.4}$$

where $\eta_0 = 2.9 \times 10^{-4}$ and $h_0 = 7250$ m. A toy model simulation showing the refractive index, the Cherenkov angle, and the light intensity produced by a highly relativistic particle, as a function of the height is shown in Figure 3.3 .
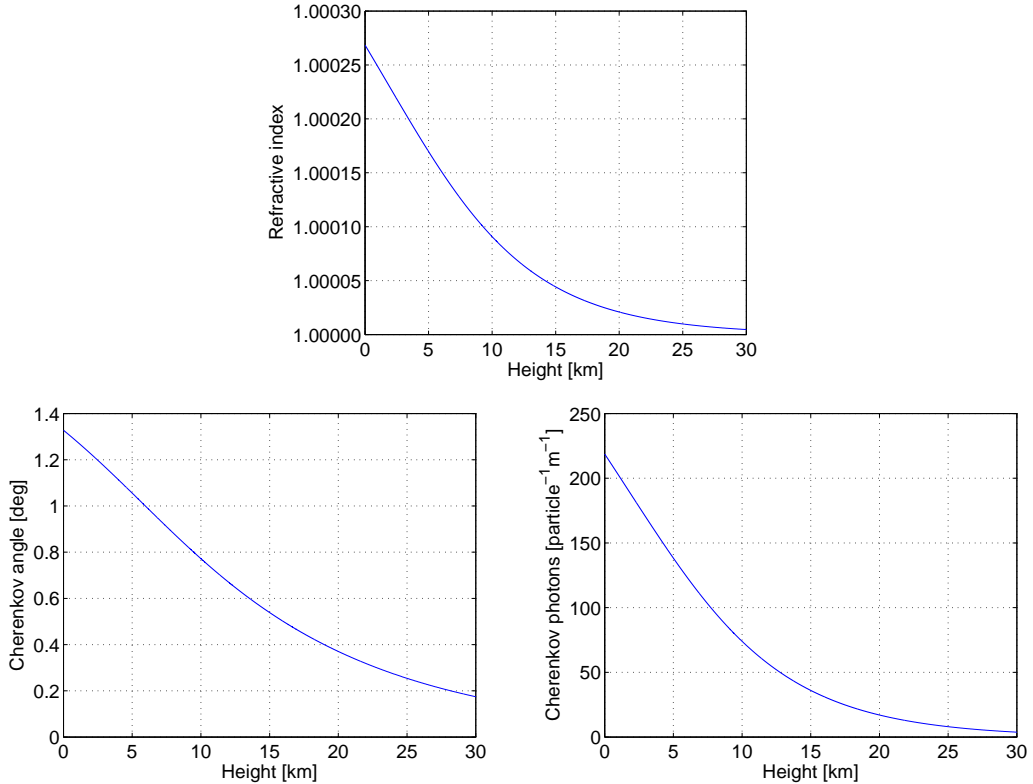
Figure 3.3: Shown are the refactive index, the Cherenkov angle, and the light intensity per meter (integrated between $100-900$ nm) as a function of the height above sea level for a highly relativistic particle ($\beta = 1$). The strong dependence on the exponential inrease of the density is reflected in all parameters. Courtesy of Marcel Strzys, private communication

The light produced by an air shower is the superposition of all Cherenkov light produced by all charged secondary particles during their path through the atmosphere. Aiming to observe the Cherenkov light at ground level (typical height ~ 2000 m) one has to consider the absorption and scattering of the produced Cherenkov light in the atmosphere. The leading process of light attenuation is Rayleigh scattering at air molecules ($d < \lambda$). The cross section of this process scales with λ^{-4} and thus mostly effects the shorter wavelengths (blue/UV). In addition, the Mie scattering of aerosols ($d > \lambda$) reduces the Cherenkov light reaching the ground level. The cross section of Mie scattering shows a much weaker dependence on the wavelength ($\lambda^{-(1-1.5)}$) and thus affects basically all wavelengths. Absorption of photons is especially important for UV ($\lambda < 280$ nm) and infrared ($\lambda > 800$ nm) photons. The main contribution here arises from ozone and water molecules for short and long wavelengths, respectively. Figure 3.4 shows the Cherenkov light produced by gamma ray showers of different energies (solid lines) at 10 km height and the amount of light arriving at ground level (2200 m above sea level) in comparison. The resulting Cherenkov spectrum at ground level peaks around $300-350$ nm and therefore in the UV/blue regime.
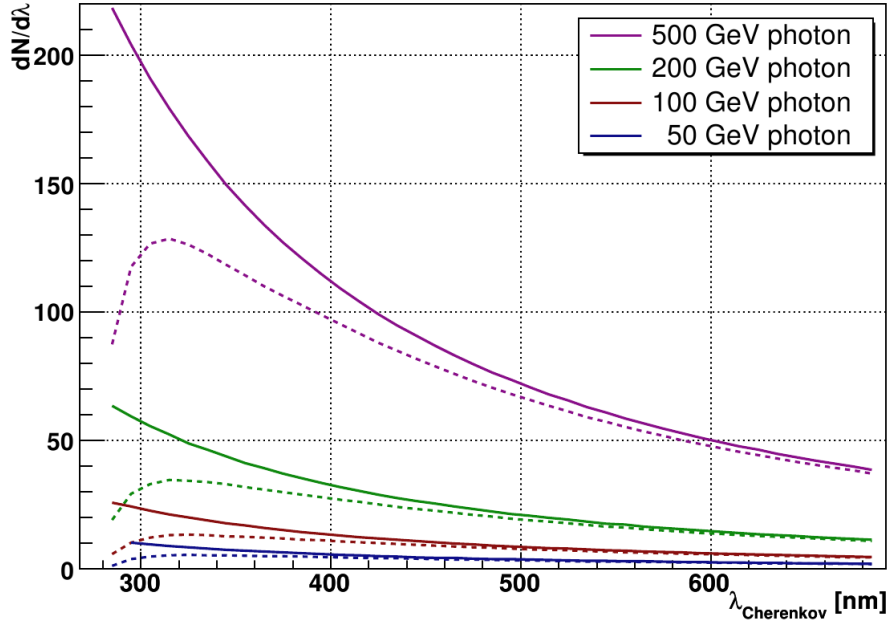
Figure 3.4: Cherenkov light produced in air showers induced by gamma rays of different energies. Shown is the Cherenkov light spectrum at 10 km height (solid lines) and at 2200 above sea level (dotted lines). The effect of the attenuation of the Cherenkov light in the atmosphere is clearly visible. Picture adopted from Wagner (2006).
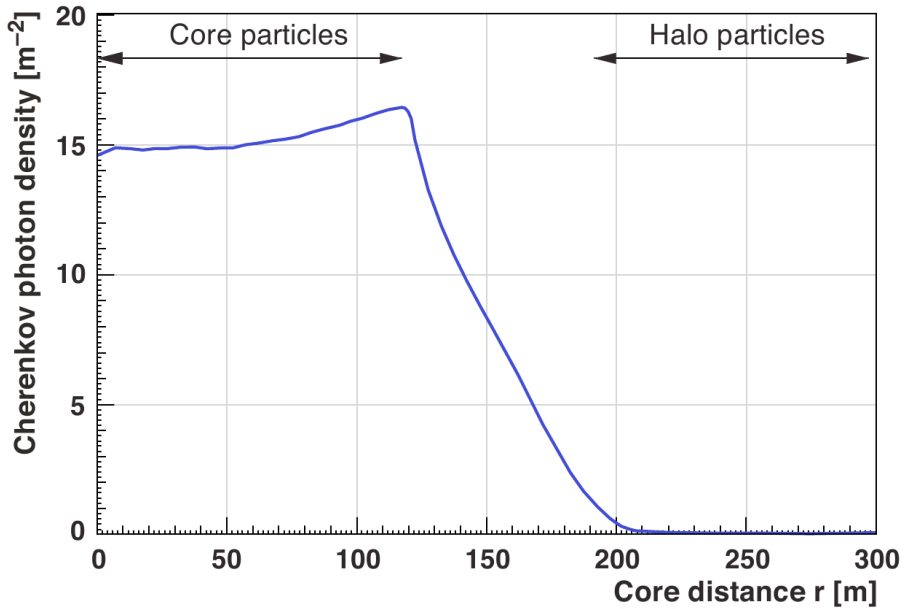
Figure 3.5: Lateral distribution of the Cherenkov light produced by an 100 GeV gamma ray shower (0° inclination) at 2200 above sea level. Picture adopted from Wagner (2006).

The spatial distribution of the Cherenkov light, integrated over all wavelengths, on ground level is the so called Cherenkov pool (see Fig. 3.5). The change of the Cherenkov angle as a function of height leads to the nearly flat distribution of photons up to ~ 70 m distance to the shower core, and also to the characteristic bump at ~ 120 m. In addition the higher production of Cherenkov photons, the increasing amount of particles, and the shorter distance to ground along the shower evolution contribute to the final light distribution at ground level. Above the distances of 120 m from the shower core the Cherenkov light distribution on ground is dominated by the halo-particles of the shower, while below the main contribution arises from the much higher amount of core-particles.

3.3 Imaging Cherenkov flashes of air showers

Note that the total amount of Cherenkov photons arriving at the ground is very low. The typical density lies between $10 - 20$ photons/m^2 for a 100 GeV gamma ray (see Fig. 3.5) shower and increases approximately linear with the energy. To detect this faint light, large optical collectors are needed. The typical reflector diameter of currently operating[1] IACTs ranges from 12 to 17 m. In addition, the typical duration of a Cherenkov light flash from an air shower is < 10 ns, and thus a fast electronic response and read out system is needed to catch the shower and avoid contamination by background light. Figure 3.6 illustrates the spatial distribution of the light emitted by a gamma ray air shower and how the shower image recorded by an IACT is composed.
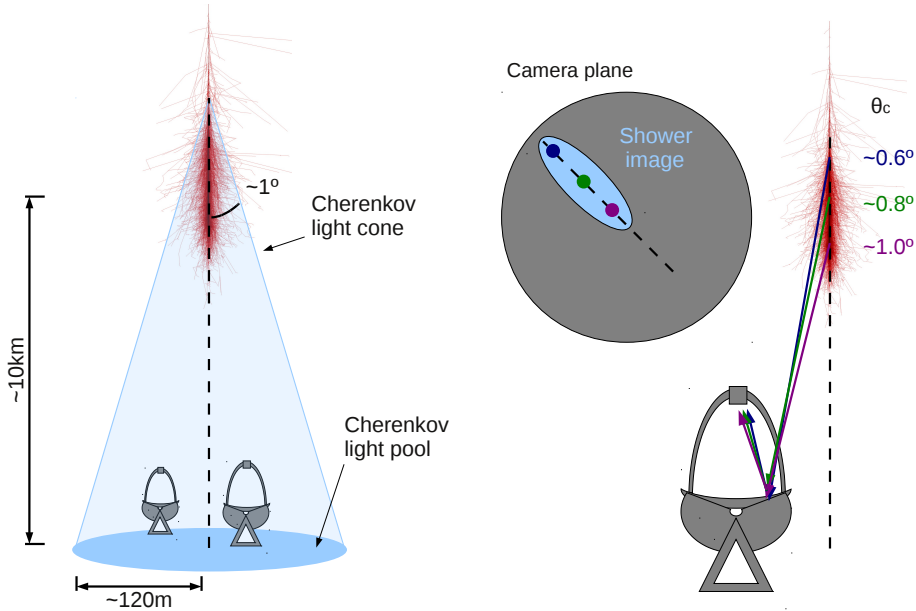
Figure 3.6: Illustration of the Cherenkov light emitted by an air shower (left) and the composition of a shower image recorder by an IACT (right). As the Cherenkov angle changes as a function of the height the longitudinal evolution of the shower is reflected in the shower image.

---

[1]The largest upcoming IACT, H.E.S.S. II, will have a diameter of 28 meters.

Every recorded shower image represents one air shower induced by one primary particle, seen from one specific viewing angle. From the shape and intensity of the obtained image the energy, arrival direction, and type of the primary particle can be obtained (see chapter 6 for a detailed discussion). Note that the different shower properties of hadronic and electromagnetic showers (Fig. 3.1) will reappear as different shower images. By using IACTs in coincidence, so called stereoscopic observations, the event reconstruction can be improved significantly as each shower is observed from multiple viewing angles. The detector area (effective area after the applied analysis) is mainly given by the field of view of the telescopes, and the size of the light pool on ground. Typical values for gamma ray induced showers range from $\sim 10^3 \, \mathrm{m}^2$ at the lowest energies (~ 50 GeV) up to $\sim 10^5 \, \mathrm{m}^2$ at the highest energies ($>$ TeV).

3.4 Recent instruments

The three leading instruments in ground based gamma ray astronomy along with some of the major properties are as follows:

- **MAGIC** (http://magic.mppmu.mpg.de/)

  - Number of telescopes: 2
  - Telescope diameter: 17 m
  - Energy threshold[2]: 50 GeV
  - Location: Roque de las Muchachos, La Palma (Canaries)

- **H.E.S.S.**[3] (http://www.mpi-hd.mpg.de/hfm/HESS/pages/about/telescopes/)

  - Number of telescopes: 4
  - Telescope diameter: 12 m
  - Energy threshold: 160 GeV
  - Location: Gamsberg mountain (Namibia)

- **VERITAS** (http://veritas.sao.arizona.edu/)

  - Number of telescopes: 4
  - Telescope diameter: 12 m
  - Energy threshold[4]: 100 GeV
  - Location: Mount Hopkins (USA)

A joint effort in cooperation with all the above mentioned collaborations and many other scientists around the world is currently designing the next generation Cherenkov experiment, the

---

[2]With a special trigger system MAGIC I reached a trigger threshold of ~ 25 GeV.

[3]One additional telescope, H.E.S.S II, with 28 m diameter is currently in the commissioning phase.

[4]The spectral reconstruction in VERITAS starts at 150 GeV.

Cherenkov Telescope Array (CTA, Actis et al. 2011 see also http://www.cta-observatory.org/) . Current designs foresee a system of ~ 100 IACTs in three different sizes of 7, 12, and 23 meter telescopes which aims to improve the performance of current instruments by one order of magnitude. Two arrays are planned, one in the northern- and one in the southern hemisphere.

Chapter 4

MAGIC

4.1 The MAGIC Telescopes
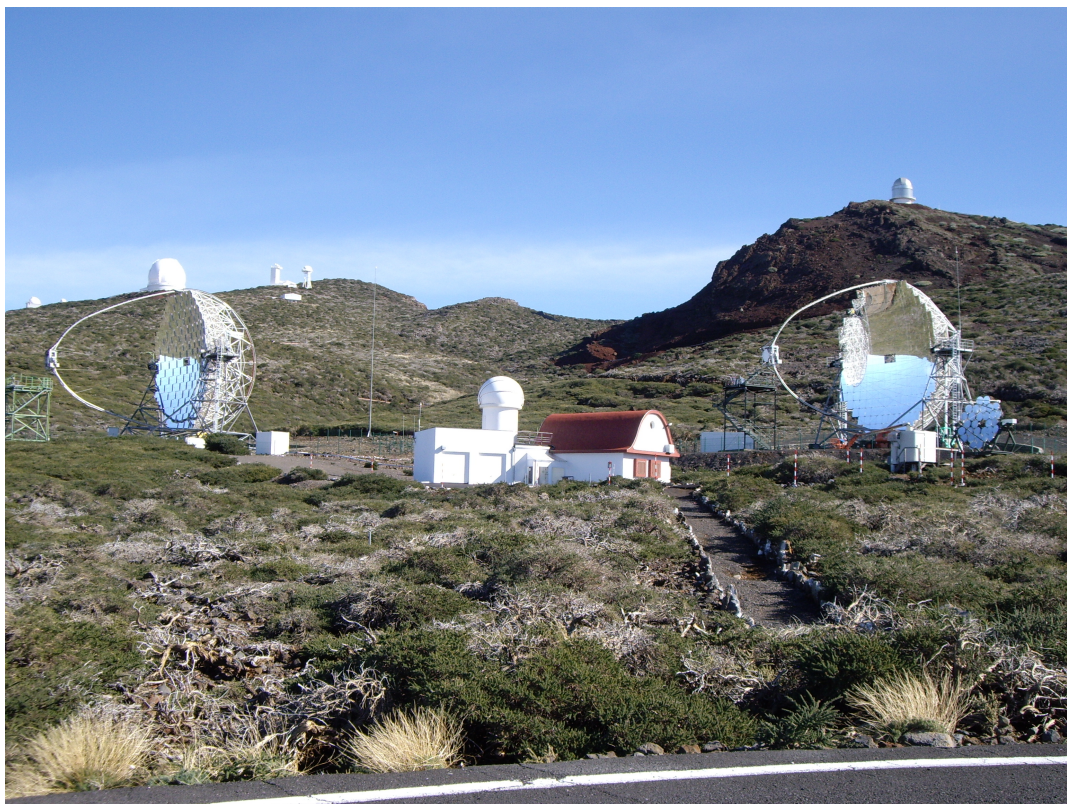
Figure 4.1: Left MAGIC I, right MAGIC II and the Counting house in between.
(Picture taken in 2010)

The **M**ajor **A**tmospheric **G**amma **I**maging **C**herenkov (MAGIC) telescopes are located at the Canary Island La Palma, hosted at the Observatory de Roque de las Muchachos (28.75° N, 17.86° W) at 2225 meter above sea level. MAGIC consists of two 17 meter diameter IACTs placed 85 meter apart from each other. The large diameter of the MAGIC telescope reflectors, makes them the largest IACTs currently in operation and allows the lowest trigger threshold ($\sim$ 50 GeV) among all ground based gamma ray observatories. In 2004, MAGIC I (MI) started operation as a stand alone telescope. Five years later, in 2009, MAGIC II (MII) came

into operation. From late 2009 on, the standard observation mode in MAGIC become the stereoscopic mode. Compared to MAGIC I single telescope observations the sensitivity of the stereoscopic system is increased up to a factor of 3^1. All scientific data in this work are taken in stereoscopic mode.

This chapter is organized as follows: First, each individual MAGIC telescope is described and their differences are pointed out focusing on the most relevant subsystems for the analysis presented in this thesis. In the next section, the stereoscopic MAGIC system is introduced, followed by a section describing the performance of the system during 2010 and 2011. The last section briefly addresses the current upgrades of the MAGIC system and their expected improvements.

4.2 The individual telescopes: MAGIC I vs. MAGIC II
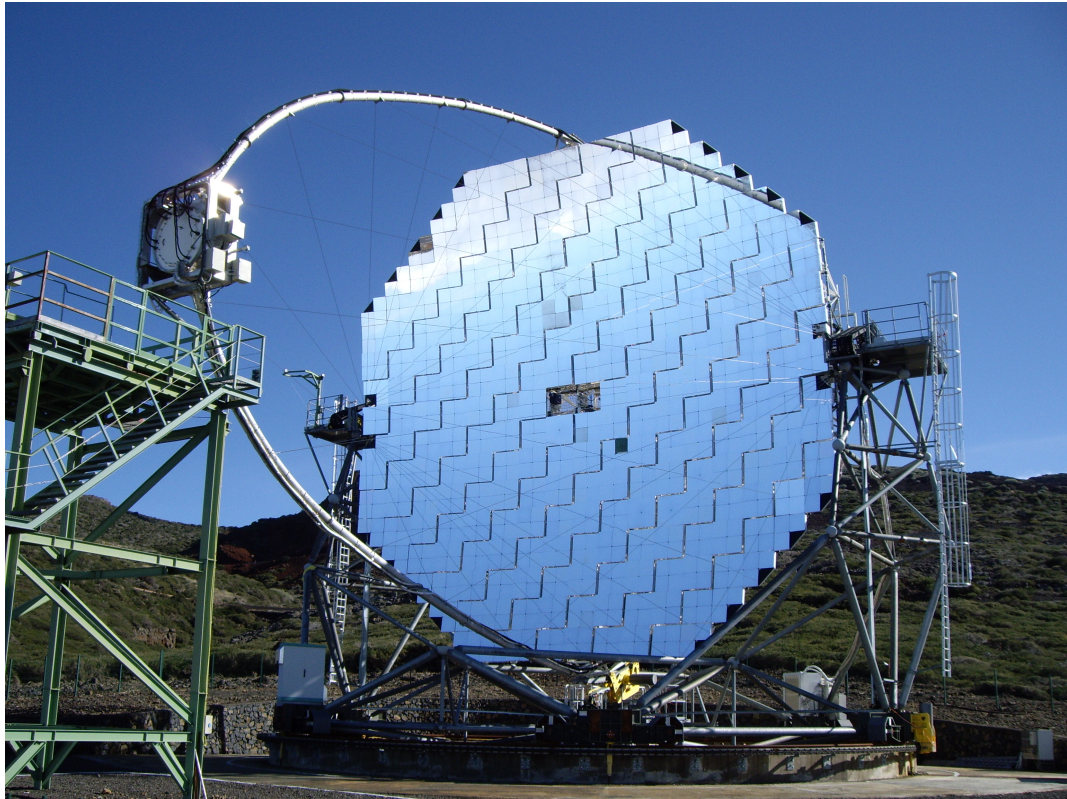
Figure 4.2: MAGIC I close up (Picture taken in 2010)

Each MAGIC telescope is constructed of a light weight carbon-fiber frame supporting the tessellated reflector and an aluminum arc supporting the prime focus photomultiplier tube (PMT) camera. The Cherenkov signals are transmitted via optical fibers to the counting house hosting the complete read-out electronics (incl. trigger and data acquisition). The light structure and the outsourcing of the read-out electronics reduces the total weight of each

---

[1]Details of the performance are presented in 4.4

telescope to 60 tons. The low weight and small moment of intertia enables the telescopes to rotate 180 deg in azimuth in less than 30 s. This places MAGIC as the fastest IACTS concerning the response to transient objects (i.e. GRBs).

Reflector and mirrors Each Telescope has a 17 meter diameter parabolic mirror consisting of individual one square meter movable panels. One of the differences between the MAGIC telescopes is the design of their reflectors. While MI (see Fig 4.2) mirrors have a dimension of 0.495×0.495 meter and are grouped in up to four per panel, the mirrors in MII (see Fig 4.3) have the dimension of 1×1 meter and are therefore mounted one per panel. The change to larger mirrors reduced the cost significantly with no significant reduction of the performance. All mirrors used in M1 are aluminum milled mirrors. For MII the outer mirrors are made of glass and the inner mirrors are aluminum milled like the ones in MI. The total reflective area is $239m^2$ in MI and $240m^2$ in MII. For mounting reasons the panels in M1 are arranged in a chessboard pattern. For a detailed characterization of the mirrors see Kellermann (2011).
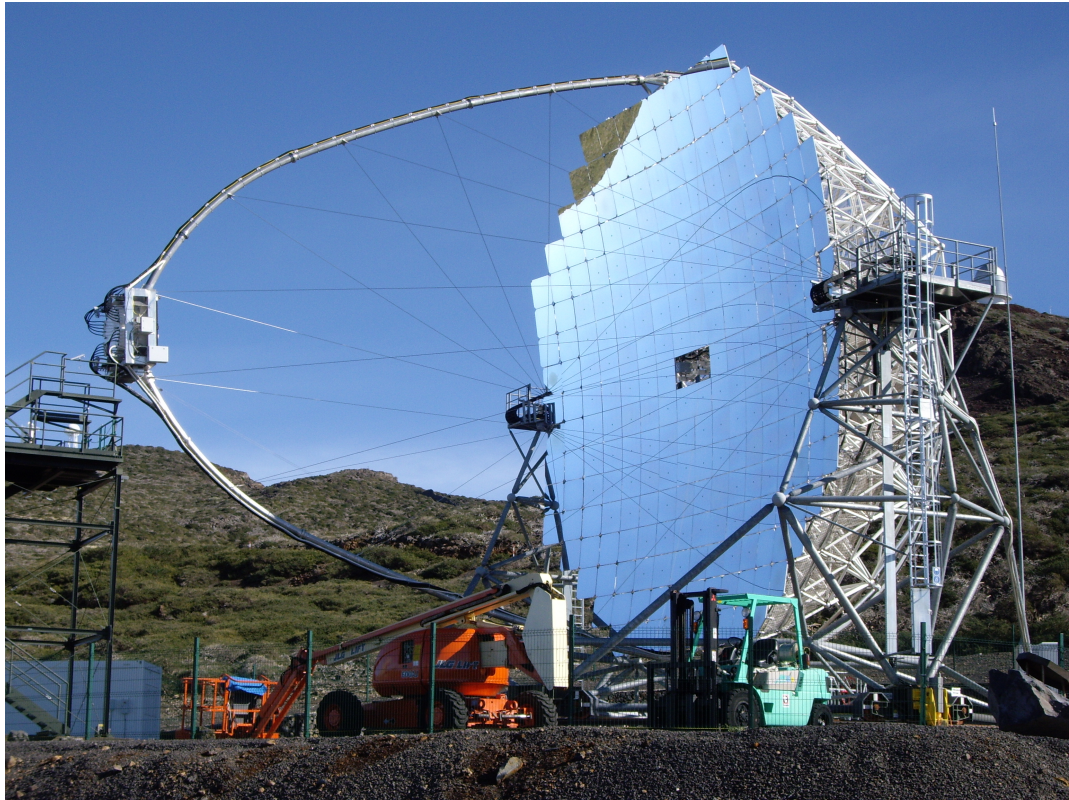
Figure 4.3: MAGIC II close up (Picture taken in 2010)

All the individual panels are adjusted by the active mirror control (AMC, see Biland et al. (2008) for details) to keep the parabolic shape of the overall mirror surface. A parabolic mirror has the advantage of conserving the time structure of the arriving photons, an information, which will be used in the later analysis.

Cameras The focal length of the parabolic mirror is 17 meter for both telescopes. The field of view of the cameras, mounted at the focal plane of the reflector, is about $3.5°$. The cameras of MI and MII differ in shape and type of PMTs. The camera of MI has a hexagonal shape and consists of 576 PMTs, each PMT being one pixel. The inner region of the MI camera is equipped with 396 $0.1°$ diameter PMTs. This region is surrounded with four rings of $0.2°$ diameter PMTs. In contrast the MII camera has a spherical shape and is equipped with 1039 PMTs of $0.1°$ diameter; leading to a much more homogeneous response compared to MI. The PMTs used in MII are Hamamatsu R1408 and have a higher peak Quantum efficiency (QE) then the PMTs of Electrontubes (ET9116 for inner pixels and ET9117 for outer pixels) equipped in MI. Furthermore, the PMTs of MI and MII have different QE curves as a function of the wavelength. The MII QE curve is higher in the blue wavelength regime (Fig 4.4).
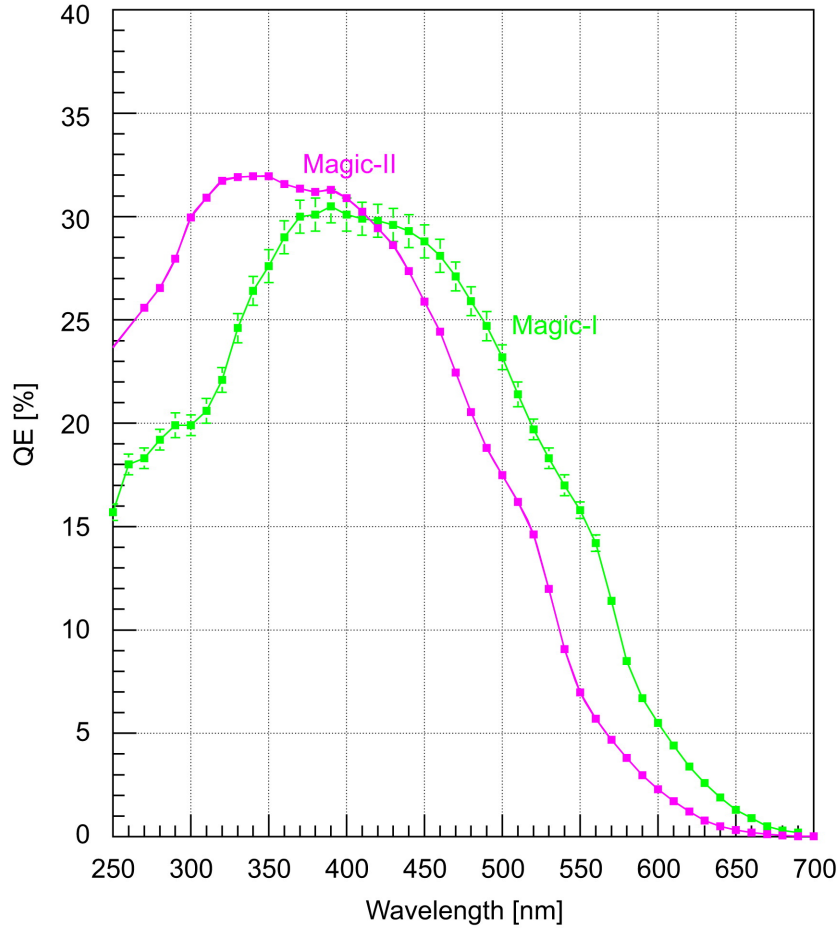
Figure 4.4: Quantum efficiency curves of two PMTs used in MAGIC I (green) and MAGIC II (pink). Plot adpoted from Garczarczyk & MAGIC Collaboration (2011)

All PMTs in both telescopes have an hexagonal shaped Winston cone (Winston 1970) mounted on top to minimize the dead area between the individual pixels.

Trigger Fig 4.5 shows the camera setup for both telescopes. The pixels connected to the trigger, forming the so called trigger region, are marked in yellow.
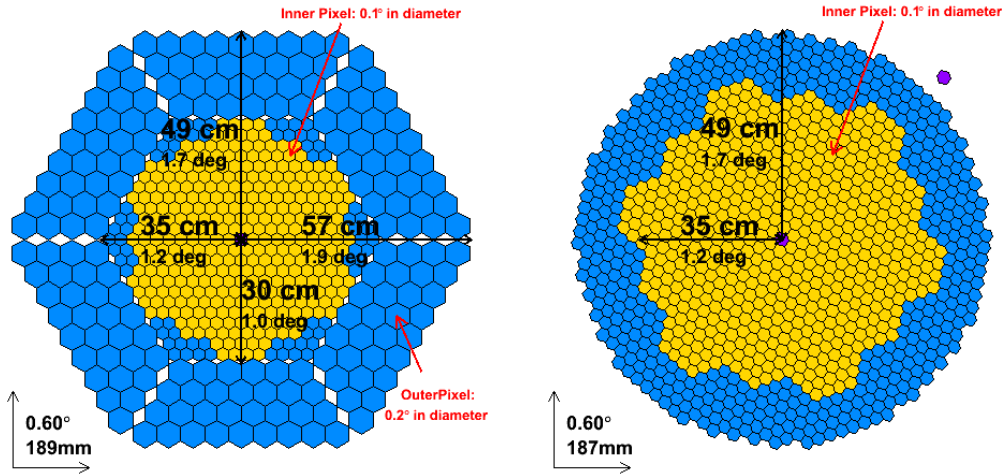
Figure 4.5: Camera of MAGIC I (left) and MAGIC II (right) with the pixels included in the trigger region marked in yellow

Both telescopes use a two level trigger system. The level 0 trigger is a simple discriminator threshold (DT) testing each pixel to be above a certain threshold. The setting of the DTs depends on the observing conditions (dark night or moon light) and is automatically adjusted during the observations (for example to account for bright stars in the field of view). This is done by the individual pixel rate control (IPRC) which adjusts the DT for each pixel to achieve an individual pixel rate (IPR) within a given target range. During stereoscopic observations the individual pixel rate is kept at an value of $0.7 / 0.5$ MHz. The level 0 trigger is used to control the minimum allowed signals per pixel and prevents those pixels to enter the further trigger logic which do not contain any physical signal. The second trigger level, called level 1, is a logical trigger requiring n next neighboring (NN) pixels to fire in coincidence. This trigger accounts for the fact that real showers will be imaged as an extended object in the camera, and due to their short spread in time of less than 5 nanoseconds (for more information on the timing properties see Aliu et al. (2009)) appear for the trigger logic as coincident firing of neighboring pixels. During stereoscopic observations the level 1 trigger in both telescopes requires 3 NN to fire. For the used IPR settings this results in individual level 1 (3NN) trigger rates of about $10 / 18$ kHz for MI and MII, respectively. One major difference in MI and MII is the size of the trigger region. In MI the trigger region has a radius of approximately $0.9°$ and in MII the trigger area is almost twice as big with an approximate radius of $1.25°$. The larger trigger area for MII results in a higher collection area especially for extended sources and off-axis observations. It also explains the difference in the level 1 rate between MI and MII.

Data acquisition systems The data of each telescope are stored with an individual data acquisition (DAQ) system. The DAQ of MI is based on multiplexed flash analogue to digital

converter (FADC). The system uses a 2 GHz sampling which allows to resolve the time evolution of air shower events. The obtained timing information will be used later in the reconstruction and classification of individual events (see Chapter 6). The system is also called MUX, for more details see Goebel et al. (2007). In M2 the read-out system is based on the multi-capacitor ring buffer Domino 2 (DRS2). The sampling speed of DRS2 is equivalent to the MUX system. DRS2 provides a lower cost per channel as well as lower power consumption, both of importance since MII has almost twice the amount of channels than MI. A drawback of the DRS2 chip is the dead-time of approximately 10% during nominal data taking. For details on the DRS2 readout see Tescaro et al. (2009).

4.3 MAGIC as a stereoscopic system

To summarize, the MAGIC II telescope was build as an improved clone of the MAGIC I telescope. Since the end of 2009 MAGIC is operated as a stereoscopic system. This means that regardless of the individual telescope triggers only those events are recorded which trigger both telescopes *simultaneously* (within 500 nanoseconds). A stereoscopic system was first used by the HEGRA experiment (Aharonian et al. 2004a) and nowadays all three major IACT systems (H.E.S.S., VERITAS and MAGIC) are operated in stereoscopic mode. There are two major advantages of stereoscopy:

- **More information about each individual shower**
  By definition any recorded image is seen from two different viewing angles with respect to the shower axis (one per telescope). Therefore, information about the three dimensional shape and location of each shower is accessible in a straight forward way. A not trivial task in mono (single telescope) observations is the determination of the distance of the shower-core to the telescope. This however discriminates two events of similar size in the camera between a close by low-energy event and a distant event of higher energy. Therefore, a clear improvement in the energy resolution is expected. Furthermore, the angular resolution and the event classification (electromagnetic or hadronic shower) will benefit. A detailed description of how this is achieved will be given in the analysis chapter 6.

- **Strong background suppression**
  Background events can be dramatically reduced by requiring a coincidence trigger between two (or more) telescopes. The highest reduction is achieved in reduction of accidental triggers caused by noise and muon events. A major background for single telescope observations arises from muon events. Muons usually do not a develop a shower in the atmosphere and thus due to the small Cherenkov angle of ~ 1 deg, trigger only one telescope most of the time. Therefore, many muon events can be discarded by requiring a stereoscopic trigger. The second, even more important, advantage is that the probability of an accidental trigger occurring in both telescopes at the same time is very low (during nominal data taking the rate of accidentals is around a few Hz). This enables very low DT settings for the individual telescopes, and therefore offers the possibility of a low energy threshold without being overwhelmed by accidental triggers.

The downside of stereoscopic observations is a reduction of the effective field of view and therefore the collection area. Due to the finite size of the Cherenkov light pool created by an

air shower some events are only visible for one telescope. The rate of recorded air showers of a given energy is therefore smaller for stereoscopic observations compared to single telescope observations. However, the stereoscopic events are better classified as gamma-rays or background events yielding a gain by a factor of ≥ 2 in sensitivity compared to monoscopic MAGIC observations. The delays due to the individual telescope positions, the pointing direction, as well as the signal transmission times from the cameras are taken into account before a tight time coincidence between a level 1 trigger in MI and MII is required to issue the stereo trigger. The stereo trigger, also called level 3 trigger for historical reasons, provides a rate of approximately 200 Hz. Among those 200 Hz only a few Hz are accidentals. These numbers show that the stereo trigger allows to operate the individual telescopes deep in the noise allowing a high performance at the trigger threshold of the individual telescopes.

The fact that MAGIC consists only of two telescopes introduces a strong azimuthal asymmetry directly originating from the requirement of coincident triggers. In addition, the relatively small size of the trigger region in MI enhances this effect. Therefore, the challenge of the MAGIC stereo system is to properly deal with an asymmetric acceptance throughout the camera plane. The investigation of this effect and the development of an appropriate background estimation was a major part of this thesis and will be described in detail in chapter 6.6.

4.4 Performance of MAGIC during 2010 and 2011

In this section the performance of the MAGIC system is shown. This part concentrates on the resulting parameters only and shall give an impression of the capabilities of this instrument. See also Aleksić et al. (2012) for a detailed description on the derivation of the parameters presented here.

The performance of any astronomical instrument is characterized by the accessible energy range (or Wavelength regime) and three main properties:

- **Sensitivity**: Defined as the minimum flux level detectable in a given observation time.

- **Energy resolution**: Defines the resolution of any spectral analysis.

- **Angular resolution**: Determines the minimum size of any resolvable structure.

All of these three parameters are functions of the energy. Therefore, each parameter is described by a function and not as a single value. For a fast comparison to other experiments the sensitivity is calculated as the flux S of a source yielding $S = N_{ex}/\sqrt{N_{bgd}} = 5$ after 50 hours effective time. Here N_{ex} is the number of excess events and N_{bgd} is the number of background events. There are two ways to express the sensitivity, the integral sensitivity refers to the integrated flux above a certain threshold while the differential sensitivity addresses the flux in differential bins of energy. Both, the differential and the integral sensitivity curves, are shown in Fig. 4.6.
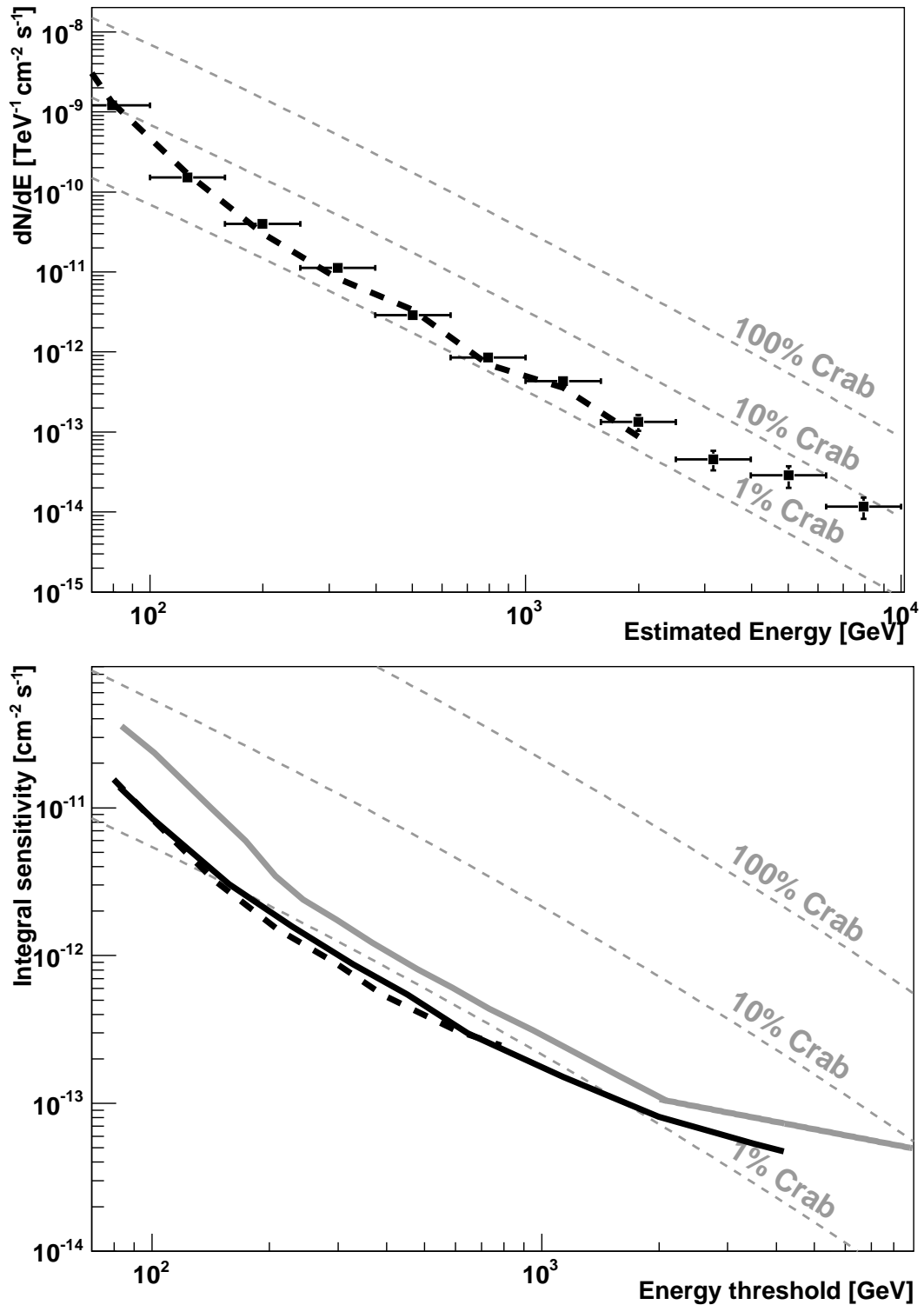
Figure 4.6: Differential (top) and integral sensitivity sensitivity (bottom) obtained from data (black points/solid curve) and Monte-Carlo simulations (black dashed lines). For comparison the flux in units of 1, 0.1, and 0.01 times the flux of the Crab Nebula is shown by the grey dotted lines. To illustrate the improvement of the MAGIC stereo system the MAGIC I single telescope sensitivity is shown as the grey solid line. Plots adopted from Aleksić et al. (2012).

In case of the differential sensitivity we additionally require at least 10 excess events and a signal to noise ratio of more than 5% to exclude fake signals produced by small systematic uncertainties. At low energies ($\lesssim 200$ GeV) the sensitivity is limited by the background suppression, while at the higher energies (> 1 TeV) the sensitivity is limited by the signal itself. At the high energies the very low flux of the signal and the background results in low event statistics and therefore high statistical uncertainties.

The energy resolution and bias of the MAGIC stereo system is shown in Fig.4.7. The curve has been derived from Monte-Carlo simulations of gamma-rays. At the lowest energies the energy reconstruction is limited by the low photon statistics of the individual shower images. Additional challenges are provided by the comparably large shower to shower fluctuations which lead to wide spreads in the reconstructed shower parameters.

At high energies (> 1 TeV) the energy resolution is again getting worse due to many truncated images and lower statistics in the Monte-Carlo simulations. The energy resolution and the bias are taken into account in the calculation of any spectrum by an unfolding algorithm (Albert et al. 2007a).
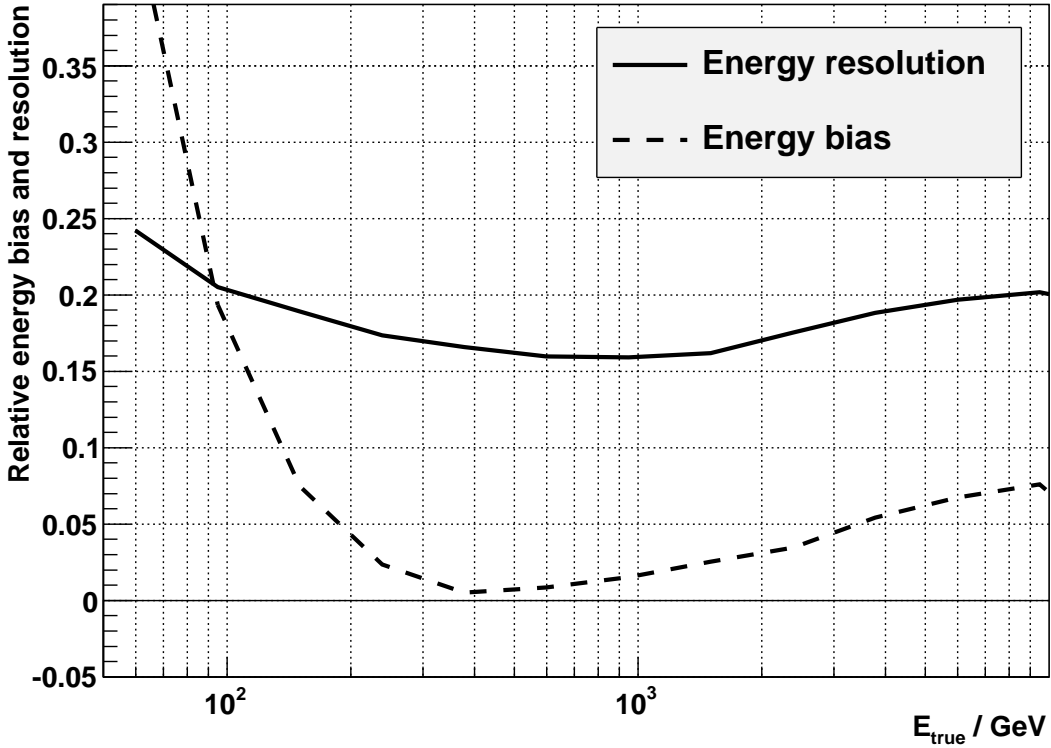
Figure 4.7: Energy resolution and bias of the MAGIC stereo system obtained with MC simulations of gamma-rays. Plot adopted from Aleksić et al. (2012).

The angular resolution is defined as the standard deviation of a 2D Gaussian fit to the angular distribution of the reconstructed excess, corresponding to a radius containing 39% of the gamma-rays for a point-like source. In addition the 68% containment radius is also derived. The angular resolution improves as a function of energy and flattens out around 1 TeV. The

resulting curves are shown in Fig.4.8.

Above an energy of 300 GeV MAGIC is able to detect a source with a flux equivalent of 0.8% of that of the Crab Nebula in 50 hours. The energy resolution at 300 GeV is as low as 17% and the angular resolution already reaches a value of 0.07°. For energies above 1 TeV the angular resolution reaches its maximum of $\sim 0.05°$ while sensitivity and energy resolution are already slightly reduced. With the lowest energy threshold (~ 50 GeV) among all operating IACTs and the very competitive performance at medium energies, MAGIC is one of the leading experiments in very high energy gamma-ray astronomy. Compared to H.E.S.S. and VERITAS the advantage of MAGIC is based on the big individual mirror surfaces and manifests in the low energy regime. On the other hand the disadvantage of only two telescopes compared to four lies in a smaller collection area and manifests in a reduced sensitivity at the highest energies.
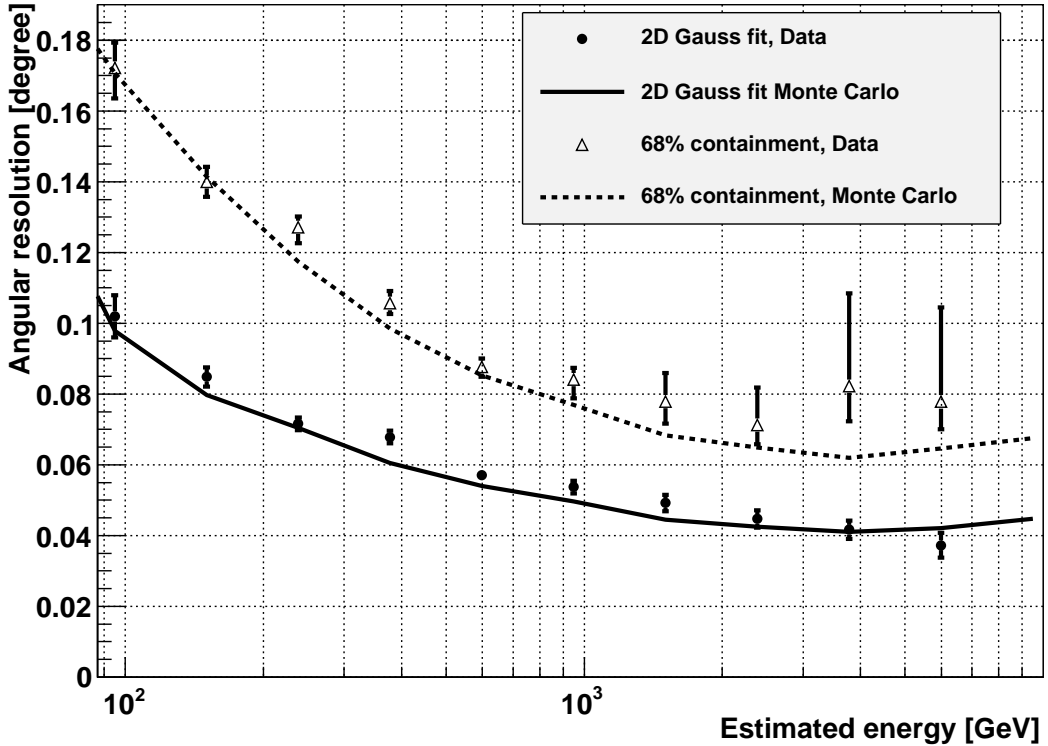
Figure 4.8: Angular resolution of the MAGIC stereo system obtained from data (points) and MC simulations (lines) of gamma-rays. Both the value defined as the standard deviation of a 2D Gauss fit and the values defined as the radius containing 69% of the excess are shown. Plot adopted from Aleksić et al. (2012).

Systematic uncertainties

This section gives a brief overview on the estimated total systematic uncertainties of the results obtained with MAGIC. A full discussion of all systematic uncertainties and their underlying reasons would go far beyond the scope of this work. The systematic uncertainties

which have been investigated in this work will be individually addressed in chapter 5.3.3 and chapter 6.6.4. For an overview on all sources of systematic uncertainties and an estimation of their impact see Aleksić et al. (2012).

Systematic uncertainties in ground based gamma ray astronomy arise mainly from imperfections and simplifications in the Monte-Carlo simulations used in the analysis. Here, the main impact has the simulation of the Earth's atmosphere being a crucial part of an Cherenkov telescope. The density profile and transmission properties are the most important characteristics for the description of the atmosphere. As the real atmosphere shows changing conditions on basically all timescales both parameters can never be perfectly reproduced in the simulations. This results in a systematic uncertainty for a given gamma-ray signal of $\lesssim 10$ % in the energy scale and $10 - 15$ % in the flux normalization (Aleksić et al. 2012).

The uncertainties in the determination of the detector characteristics (e.g., QE of PMTs, calibration, broken pixels, temperature dependence of the read-out chain) and the telescope characteristics (mirror reflectivity, optical point spread function of the reflector) lead to additional systematic uncertainties. Their impact ranges from $2 - 8\%$ in the energy scale and from $1 - 4$ % in the flux normalization.

The systematic uncertainty in the background determination is a major source of systematic uncertainties for weak sources and low energies (see chapter 6.6.4). Being estimated as $\lesssim 1.5$ % of the background level the absolute systematic uncertainty depends linear on the signal to noise ratio and can reach values in the flux normalization in the order of 20% for very weak sources ($\sim 2\%$ flux of the Crab Nebula) at the lowest energies (~ 100 GeV). As the signal to noise ratio improves significantly for higher energies this effect is usually very small for energies ≥ 300 GeV.

It was found that the spectrum of the Crab Nebula is consistent with other IACT experiments within $20 - 30$ % (Aleksić et al. 2012). The systematic errors depend on the flux and spectral shape of the observed source. Oriented on the results obtained in Aleksić et al. (2012) the overall systematic uncertainties are estimated to be $15 - 17$ % in the energy scale and $11 - 19$ % in the flux normalization for high and low energies, respectively. The systematic error on the spectral index is estimated to be 0.15, coming mainly from residual non linearities of the electronic chain and the unfolding procedure. For low values of the signal to noise ratio ($\lesssim 12\%$) the systematic uncertainty in the flux normalization and the spectral slope can be a up to factor two higher.

4.5 Future improvements of the MAGIC system

In June 2011, the MAGIC collaboration started a two stage upgrade program. The aim of the upgrade is the improvement of the performance, achieving a more homogeneous system and reducing the overall maintenance. The first part of the upgrade took place in 2011 to early 2012 and involved the exchange of the DAQ systems from MUX and DRS2 to DRS4 in MI and MII, respectively. In addition, many smaller hardware changes and rearrangements as well as several upgrades in the software of the subsystems have been performed. The second stage of the upgrade mainly covers the exchange of the old MI camera and trigger with new systems based on the ones used in MII.

The expected improvements of the fully upgraded system are:

- A minimization of the DAQ dead-time to a value well below 1%
  (reducing the old value by more than a factor of 10).

- The reduction of the asymmetric acceptance in the camera plane
  (increasing the trigger region in MI by a factor ≈ 2).

- A higher performance for extended and OFF-axis sources due to a bigger effective field
  of view for the stereo trigger (new MI trigger).

- Minimization of intrinsic inhomogeneities between MI and MII
  (same camera, same trigger, same DAQ, same PMT size, very similar QE curves).

- Easy maintenance due to very similar subsystems.

As a part of this thesis a muon analysis for both telescopes was set up during the commissioning of the upgraded system. The aim of this work is to precisely determine and monitor basic properties of the telescopes like the point spread function of the reflectors and the light detection efficiency. Furthermore, this study will be used to improve the Monte-Carlo simulations of the system resulting in better sensitivity and reduced systematics. The muon-analysis and its results based on data taken between January and April 2012 will be described in chapter 5.

Chapter 5

Calibration of the MAGIC Telescopes

As described in chapter 3 the imaging air Cherenkov technique is an indirect measurement of individual high energy events (gamma-ray and cosmic-ray showers). Therefore, events recorded with an IACT have to undergo two steps of calibration:

The first one is the calibration and characterization of the general properties of the instrument itself. This includes the determination of the light collection efficiency, the optical point spread function of the reflector, as well as the conversion factors from ADC counts to number of photoelectrons for the read out system. The last step is usually called calibration or signal calibration. This only refers to the calibration of the absolute amount of detected light given a specific light source (i.e., a laser). Note that the signal calibration only connects the extracted signal with the number of detected photoelectrons and therefore the amount of light arriving at the camera (given the quantum efficiency of the PMTs). It can not access the amount of light produced by the air shower and neither the amount of light reflected by the mirror dish. The connection between the detected light and the responsible air shower can only be achieved by means of Monte-Carlo simulations.

The second stage starts with the correlation of the shape and intensity of the detected light with Cherenkov images from air showers. Here, comparisons to Monte-Carlo simulations are used to identify the particle type, energy, and arrival direction of the primary particle which induced the recorded air shower. The last step is the determination of the collection area which together with the number of excess events and the observation time yields the differential gamma-ray flux. This part is usually called the analysis of the data (see chapter 6 for a detailed description).

It should be stressed that these two stages are at this moment independent. The connection between the absolute amount of detected light (determined in step one) and the shape and intensity of a shower image in the camera (determined in step two) is given by the light of an air shower arriving at the camera. This includes the light production of the shower, the propagation of the light through the atmosphere, the optical point spread function of the reflector, and the reflectivity of the mirrors.

For a highly accurate calibration of the gamma-ray flux one would like to have an artificial gamma-ray source in the orbit of the earth. Such a *calibration-source* would have to reach energies of more than several tens of TeV and therefore would have to be a more powerful accelerator than the Large Hadron Collider (LHC, see http://public.web.cern.ch/public/en/lhc/lhc-en.html for details). Thus, the flux calibration of ground based gamma-ray observatories relies on Monte-Carlo simulations. In addition, one can use observations of the same objects by different instruments to cross-calibrate and verify the independent results. Most out of the ~ 140 sources known to emit VHE gamma rays are either weak sources or their flux is intrinsically variable, making them not suitable as calibration sources. The brightest persistent

VHE gamma-ray source in the sky is the Crab Nebula. Therefore, it is the best calibration source for IACTs. The lack of a high number of calibration sources and the fact that the Crab Nebula is only visible for about 8 month of the year strengthens the importance of well understood and precise Monte-Carlo simulations. It also highlights as well that the major source of systematic errors in IACT experiments are imperfections in the Monte-Carlo simulations.

To achieve a precise calibration between the light produced by an air shower and the recorded image, a refined muon-analysis was developed during on site commissioning of the upgraded telescopes in November 2011. The muon-analysis acts as a direct connection between the instrument calibration and the Monte-Carlo simulations. Therefore, the muon-analysis can be used to adjust major parameters in the simulations describing the point spread function (PSF) and the light collection efficiency. In this sense one can speak of the calibration of the Monte-Carlo simulations. The developed analysis and its results are presented here.

This chapter is organized as follows: First a brief description of the signal calibration is given. Then the Monte-Carlo production is addressed focusing on the effects of the optical PSF and the overall light collection efficiency. A short introduction is given on single muon events introducing the muon ring images. The use of muon rings, their parameterization and selection is explained in detail. The sensitivity of muon ring images on the PSF and the light collection efficiency is shown on MC simulations including a quantitative method to measure the difference in PSF and light collection. Finally, the muon analysis is applied to real data and the PSF and light collection efficiency of MI and MII are determined for data taken in February 2012. This chapter addresses only data taken after the upgrade of the read-out in both telescopes and the results can not be directly applied to older data. The scientific (gamma ray) data presented in this work have been taken before the upgrade and the here obtained results of the muon analysis do not apply there.

5.1 Signal calibration

The signal calibration is the conversion from arbitrary units in the read out electronics to photoelectrons. For this task each telescope is equipped with a calibration-box mounted in the center of the mirror dish. The calibration box illuminates the complete camera homogeneously with ~ 2 ns flashes of light. The F-factor method (Mirzoyan 1997) is used to calculate the conversion factor from counts in the read-out system to photoelectrons (phe). During observations a dedicated calibration run and pedestal run for each source is taken directly before the data taking to compensate for possible time and orientation dependencies in the telescope parameters. A pedestal event is an artificial triggered event and therefore includes no signal. Its purpose is to determine the baseline in the readout system induced from the light of the night sky and electronic noise. In addition, interleaved calibration and pedestal events are taken continuously during data taking, usually with a frequency of 25 Hz each. This allows for a constant monitoring of the baseline and the conversion factors which may change over time (i.e. due to temperature changes in the electronics or changes of the night sky conditions). A detailed description of the signal extraction and calibration can be found in Sitarek (2010).

5.2 Monte-Carlo Simulations and their calibration

Monte Carlo simulations play a major part in VHE gamma-ray astronomy and are the only way to identify the primary particle of an air shower (i.e., gamma or hadron). Furthermore, they are mandatory to determine absolute values of the physical parameters flux and energy. To achieve this, simulated events (with well known parameters) are compared to real measured events. The simulation software used in MAGIC consists of three programs: *Mmcs*, *Reflector*, and *Camera*.

Mmcs is based on the program *Corsika* and simulates the developments of air showers itself. This first step in the simulation chain deals only with the physics of the particle cascades and the subsequent Cherenkov light production. The biggest uncertainties here lie in the extrapolation of known cross sections to higher energies and the simulation of the atmosphere. For a detailed description see Heck et al. (1998) (see also http://www-ik.fzk.de/corsika/).

The second program, *Reflector*, simulates the mirror surface of the MAGIC telescopes and also accounts for absorption and scattering of the Cherenkov photons in the atmosphere. The underlying program is a ray-tracing algorithm following each single photon till it arrives on the camera plane. The optical parameters of the mirrors (i.e., reflection), as well as aberration effects are taken into account. A look up table including the position of each individual mirror is used to describe the overall shape of the mirror surface. The optical point-spread function of the reflector is introduced as the quadratic sum of the (mis-)aligned mirrors and their individual point spread function: $\mathrm{PSF} = \sqrt{(\mathrm{PSF_M})^2 + (\mathrm{PSF_A})^2}$. Here, PSF_M accounts for the individual mirrors and PSF_A for their alignment. Each value is estimated to be 5 mm.

The last step in the simulation chain is performed by the program *Camera*, where the complete response of the camera and the readout electronics is simulated. This includes the Quantum efficiency of the used PMTs, the reflectivity of the Winston cones, the trigger, the signal extraction algorithms, the light of the night sky, the electronic noise, and all other relevant parts of the system. *Camera* is also used to simulate calibration and pedestal events. The output files of *Camera* are the simulated equivalent to raw-files of real data. The obvious difference to real data is that the simulations contain only the kind of events (i.e., gammas, protons, muons) specified before.

Two of the most important parameters to be adjusted in the simulations are described below:

- The **Light collection efficiency (LCE)** is defined as the fraction of detected light over the Cherenkov light produced by an air shower. The produced Cherenkov light is strongly correlated to the energy of the primary particle which in turn strongly correlates with the size and shape of the induced air shower. The LCE can be adjusted in the Monte-Carlo simulations by the introduction of the mirror fraction (MF) parameter. The MF scales the total amount of light arriving at the camera plane and is applied in *Camera*. A difference of the LCE between data and MC will cause a bias of the energy reconstruction. The strong correlation between the produced light and shape of air showers will additionally spoil the event classification and therefore reduce the sensitivity. In addition, such differences will manifest in different trigger efficiencies and reconstruction efficiencies of Monte Carlo and real gamma rays. Ultimately, such a difference will produce wrongly estimated collection areas and therefore systematic uncertainties in the flux calculation.

- The **Optical point spread function (PSF)** has strong impact on the shape of the

recorded shower image. A too large value of PSF can smear out the image so that the reconstruction of the event becomes more challenging. To account for small changes in the PSF the light distribution arriving at the camera plane can be further smeared in the program *Camera*. This procedure saves CPU-time without loosing significant precision compared to re-running the program *Reflector*. Discrepancies between the real PSF and the one used in simulations will cause differences in the shower shapes and therefore have a similar effect than a difference in the LCE except for the bias in the energy reconstruction.

An accurate determination of the PSF and LCE is fundamental to achieve the maximum performance of the instrument. In MAGIC this is done in two ways. The first method is a direct measurement of the amount and shape of the reflected light of a single star on the camera plane. This method uses an SBIG CCD camera and has the advantage of a well defined and controlled experimental set up (Mirzoyan et al. 2007; Kellermann 2011). The main disadvantage of this method is that both the derived reflectivity and the PSF are obtained at optical wavelength and for the spectrum emitted by the used star. The Cherenkov spectrum is typically more dominated in the blue to UV regime. However, the use of blue stars (spectral types O and B) is a way to reduce this effect. Furthermore, during this method the telescope is focused to infinity (distance of the star) and during nominal data taking the telescopes are focused at a distance of ~ 10 km (the typical distance of showers). The second method is based on the analysis of single muon events and their comparison to MC simulations with different simulated PSF and MF values. In the framework of this thesis the muon calibration has been greatly refined and applied to both telescopes.

5.3 Calibration using muons

Muon events are induced by the Cherenkov light of single charged muons. Muons are produced as secondary particles in air showers induced by cosmic rays. While during the gamma ray analysis muons are rejected as background events, a specific subclass of muon showers can be used as probe to determine the LCE and the optical PSF of the instrument. This chapter deals only with a subclass of muon showers, the so called muon rings. Muon rings are produced by the Cherenkov light of single, relatively close (impact $\lesssim 12$ m) charged muons . The name *rings* arises from the ring like shape of the images produced by such events. Figure 5.1 show two real muon rings recorded with MAGIC II. Muons of higher impact appear usually as small dimm images and are less easy to distinguish from images produced by air showers.
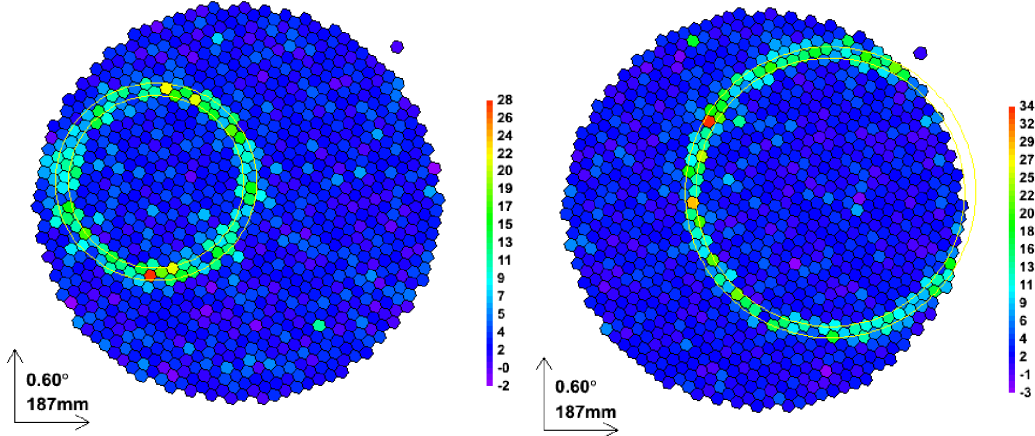
Figure 5.1: Example of two real muon events recorded with MAGIC II. The color scale is in arbitrary units and displays the amount of light detected by each pixel.

Muon rings   In a simplified model the ring image can be explained by the following example: Let a charged muon be created at several km above an IACT pointing to zenith. The muon travels to the ground till it hits the center of the IACT reflector. For simplicity it is assumed that Cherenkov light is only emitted at the constant Cherenkov angle of $1°$. For a 17 m diameter mirror the Cherenkov light hits the reflector below a distance of ≈ 490 m. From this distance the Cherenkov light is seen as a ring on the reflector till the muon passes the reflector. The reflector focuses all light emitted under a given angle (parallel light) at the same points in the camera plane. The resulting image is one ring of Cherenkov light with a radius of $1°$. This simplified explanation[1] of muon rings is illustrated in Fig. 5.2.

In reality the Cherenkov angle changes as a function of the refractive index of the air and therefore with the altitude. Furthermore, most of the close by muons are of relatively low energy (tens of GeV) and therefore the Cherenkov light production happens close to the threshold (≈ 5 GeV for muons). Therefore, both the angle and the wavelength of the emitted light show some energy dependence. In addition the light distribution within the detected ring is a function of inclination angle between telescope axis and velocity vector of the muon. Despite various parameters which have to be taken into account, the Cherenkov light production of single muons can be accurately calculated (see also Chapter 3).

---

[1]It has to be mentioned that in reality the individual rings of Cherenkov light hit the reflector and the camera almost simultaneously and usually not in the time order they where created. This can be explained by the fact that the muon travels faster in the atmosphere than the speed of light and therefore the later created Cherenkov light reaches the telescope earlier. However this also depends on the orientation of the shower/muon and the telescope and has no influence on the ring like shape. The radius of the muon ring is linearly connected to Cherenkov angle.

A single muon hitting the center of the reflector: (Cherenkov light)

μ+/-

1°

μ+/-

μ+/-

μ+/-

Time
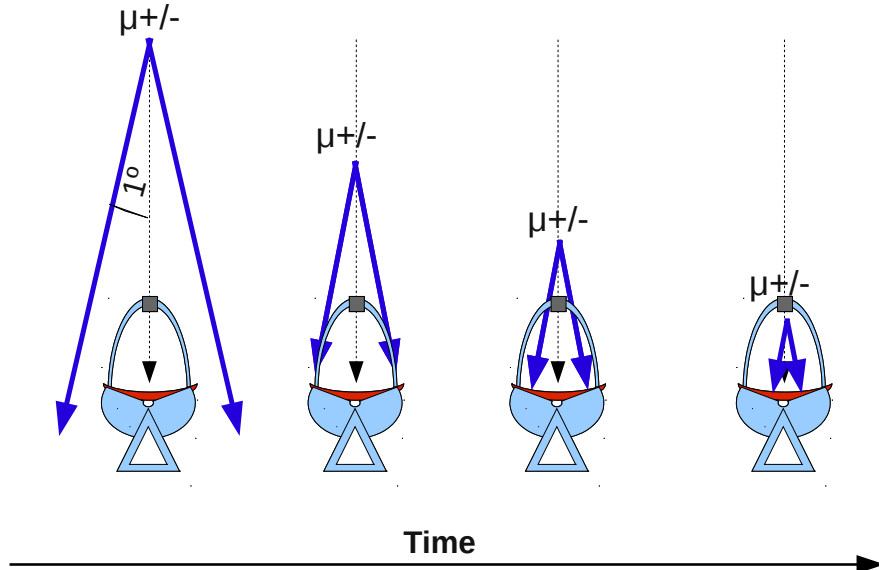
Seen from the top: (Cherenkov light , telescope reflector)
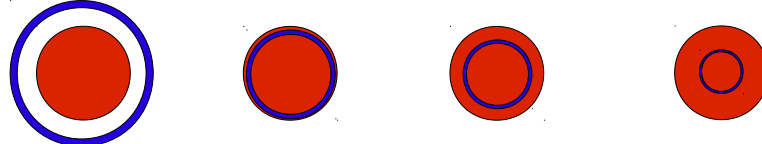
Seen from the camera plane: (integrated Cherenkov light)
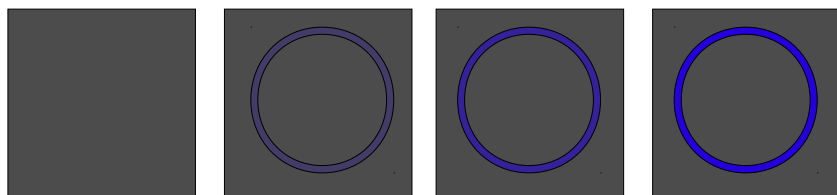
Figure 5.2: Illustration of a single muon event producing a muon ring image on the camera plane. For illustration and simplicity reasons the following assumptions have been made: The Cherenkov light (blue) is only and always emitted under the Cherenkov angle of 1°, and both, the muon and the created photons, are not scattered. The time evolution is illustrated from left to right in all panels. The individual panels show the scene from different perspectives: Top from the side, middle from above the reflector, and bottom as seen from the camera plane.

Vacanti et al. (1994) provided a detailed derivation of an analytical expression describing the light intensity along the ring image and the total light output of a single radiating muon. Following their description the light distribution for muon rings observed with the MAGIC telescopes is derived. The general gemoetry of the problem is shown in figure 5.3.
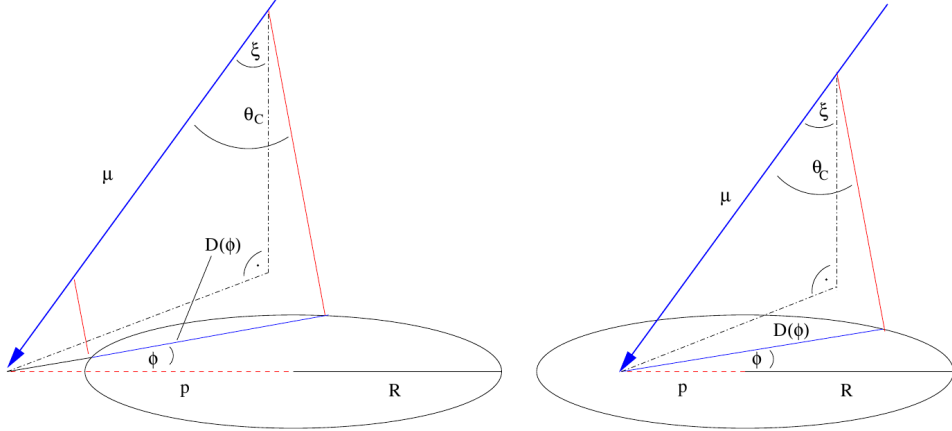
Figure 5.3: Geometry of the Cherenkov radiation produced by a single muon with impact inside (right) or outside the reflector (left). Here p is the impact parameter, R the mirror radius, ξ the inclination angle, and θ_c the Cherenkov angle. Picture taken from Meyer (2005).

The amount of photons emitted by a muon per unit path dh and unit azimuth angle $d\phi$ in the wavelength range $\lambda1$–$\lambda2$ which are reflected by the mirror is given as:

$$\frac{d^2N}{dhd\phi} = \alpha \int_{\lambda1}^{\lambda2} \frac{\psi(\lambda)}{\lambda^2} \left(1 - \frac{1}{\beta^2 n^2(\lambda)}\right) d\lambda \tag{5.1}$$

It is assumed that the energy of the muon is always above the Cherenkov threshold and that the muon does not decay in the time of interest. Furthermore, α is the fine structure constant, $\psi(\lambda)$ the light collection efficiency of the mirror, and $n(\lambda)$ the refractive index. Assuming that $n(\lambda) \approx$ constant, and using that $1/\beta^2 n^2(\lambda) = \cos\theta$ the equation can be simplified to:

$$\frac{d^2N}{dhd\phi} = \alpha \sin^2\theta \int_{\lambda1}^{\lambda2} \frac{\psi(\lambda)}{\lambda^2} d\lambda \tag{5.2}$$

Let

$$I \equiv \int_{\lambda1}^{\lambda2} \frac{\psi(\lambda)}{\lambda^2} d\lambda. \tag{5.3}$$

Note, that in the MC simulations the MF is introduced as a constant multiplying I' so that: $I = \mathrm{MF} \times I' = \mathrm{MF} \times \int_{\lambda1}^{\lambda2} \frac{\psi'(\lambda)}{\lambda^2} d\lambda$. Here $\psi'(\lambda)$ is the experimentally determined light collection efficiency of the mirror dish. The MF is introduced to correct for possible uncertainties in the determination of $\psi'(\lambda)$. The muon analysis is then used to determine empirically the value of MF. Expanding ξ to second order one obtains:

$$\frac{dN}{d\phi} = I \times \frac{\alpha}{2} \sin(2\theta) D(\phi). \tag{5.4}$$

Here $D(\phi)$ is the fraction of the emitted Cherenkov light hitting the reflector. Following Vacanti et al. (1994) one obtains

$$D(\phi) = 2R\sqrt{1 - (p/R)^2 \sin^2 \phi} \qquad \text{for } p/R > 1, \tag{5.5}$$

$$D(\phi) = R\left(\sqrt{1 - (p/R)^2 \sin^2 \phi} + (p/R)\cos\phi\right) \qquad \text{for } p/R \leq 1, \tag{5.6}$$

$$\tag{5.7}$$

where p is the impact distance of the muon on the plane perpendicular to the telescope pointing and R the radius of the mirror dish. Using that the argument of the square root must not be negative one obtains:

$$\sin^2 \phi \leq (R/p)^2 \equiv \sin^2 \phi_{max}. \tag{5.8}$$

For $p/R \leq 1$ the above condition is always fulfilled, allowing all possible azimuth angles ϕ and the possibility to observe full rings. However, the finite focal plane detector (camera), the finite light detection efficiency of it and, the not homogeneous light distribution along the ring, can lead to incomplete rings also for $p/R < 1$. In the case of $p/R > 1$, and thus an impact of the muon outside the mirror dish, only arcs of a maximum angular extend equal to $2\phi_{max}$ can form in the focal plane. Therefore full rings can only be produced if the muon impact lies within the mirror dish, for higher impacts less than half rings are formed at the camera plane. The total amount of photons in the camera plane is given as:

$$N = 2\alpha I \sin(2\theta) R \int_0^{\phi^\star} \sqrt{1 - \left(\frac{p}{R}\right)^2 \sin^2 \phi} \, d\phi \tag{5.9}$$

where

$$\phi^\star = \phi_{max} \qquad \text{for } p/R > 1, \tag{5.10}$$

$$= \pi/2 \qquad \text{for } p/R \leq 1 \tag{5.11}$$

Having the above description effects which broaden the derived light distribution are shortly discussed. A distinction is made between physical reasons of the broadening and technical reasons. The main physical reasons are:

- Changes of the refractive index.
  The refractive index of air depends on the altitude and the wavelength. In both cases the relative broadening of the muon ring image decreases with increasing energy of the muon. For energies above ~ 10 GeV the relative broadening $\Delta\theta/\theta \equiv \delta$ saturates in both cases. The change of the refractive index as a function of the height is $\delta_h \approx 3\%$, and the effect of the wavelength dependence is $\delta_\lambda \lesssim 2\%$.

- Ionization loss
  While the muon travels through the atmosphere it looses energy by ionization. As a result the Cherenkov angle decreases along the path of the muon. However the low energy loss of the muon makes this term by far the least important with $\delta_{ionization} < 1\%$.

- Multiple scattering
  Along its path the muon experiences coulomb scattering. Therefore, the photons arriving at the camera plane are scattered around the expected position in an approximately Gaussian distribution. Also this effect is decreasing with the energy of the muon and results in a broadening of $\delta_{ms} \approx 10\text{--}3$ % in the energy range 6–20 GeV.

Thus, intrinsically, one expects broader rings at lower muon energies. Besides the physical broadening, the observed muon rings are also affected by instrumental effects:

- Pixel size
  The discretization of the image in the camera caused by the finite pixel size, leads to an uncertainty in the determination of the radius. Due to the small pixels used in the MAGIC telescopes the relative broadening of a full ring is $\delta_{pixel} < 1\%$ and plays no significant role.

- Aberration
  The dominating effect for the MAGIC telescopes is the coma aberration raising from the parabolic shape of the reflector. The effect is almost independent of the muon energy and is with $\delta_{coma} \approx 5\%$ one of the dominant processes.

- The optical point spread function
  The PSF of the MAGIC telescopes is affected by the bending of the telescope structure. To conserve an optimal parabolic shape the individual mirror panels are adjusted by the AMC. A degradation of the PSF (not perfectly adjusted AMC) is observed as a broadening of all muon rings independent of their energy.

The only effect which can change over time (assuming constant atmospheric conditions) is the adjustment of the mirrors. Therefore any change in the broadness of the muon rings can be used to identify a change of the optical point spread function.

The simple identification of muon rings and their well understood physical properties allows to use them to calibrate basic properties of the system, the LCE and the reflector PSF. In case of the LCE/MF determination one uses the fact that the total amount of produced Cherenkov light for a muon of given energy can be very well determined. A comparison between the detected light of real data and simulated muons can therefore reveal the LCE and the needed value of the MF in the simulations. The PSF can be determined by the broadening of the muon ring due to the optical performance of the reflector.

From now on, throughout this chapter, muon(s) should be understood as muon ring(s) if not explicitly stated otherwise. Throughout this chapter both telescopes are treated as independent instruments. All data and all MC simulations used here are mono observations and therefore record all events triggered by each individual telescope. This is done for two reasons: First, the small light pool of muon showers will in most cases only trigger one telescope. In this sense the use of single telescope data significantly enlarges the muon statistics. Second, the request of a stereo trigger would introduce a correlation between the telescopes, but here one aims to determine the individual telescope parameters.

5.3.1 Muon Parameters

To characterize individual muon events (see Fig. 5.1 for an example) some basic parameters are defined:

- **Radius (R_μ)**
  is the radius of the measured ring and is correlated to the energy of the muon.

- **Arcphi**
  describes how *complete* the detected muon ring is and ranges between $0 - 360°$.

- **Arcwidth**
  is the parameter to describe the broadness of the ring and is defined as the sigma value of a Gaussian fit to the radial profile of the intensity distribution.

- **MuonSize**
  describes the total amount of charge in photoelectrons of the muon event.

To determine the above four parameters the first step in the reconstruction is a muon search algorithm. The muon search algorithm uses already cleaned[2] images to look for ring like structures. This is achieved by a ring fit which minimizes the following expression:

$$\sum_i S_i \times d_i^2 \tag{5.12}$$

where S_i is the charge per pixel and d_i the radial distance of the individual pixel to the closest part of the ring. The ring is defined by its center and radius which are both simultaneously varied during the fit procedure as shown in Figure 5.4
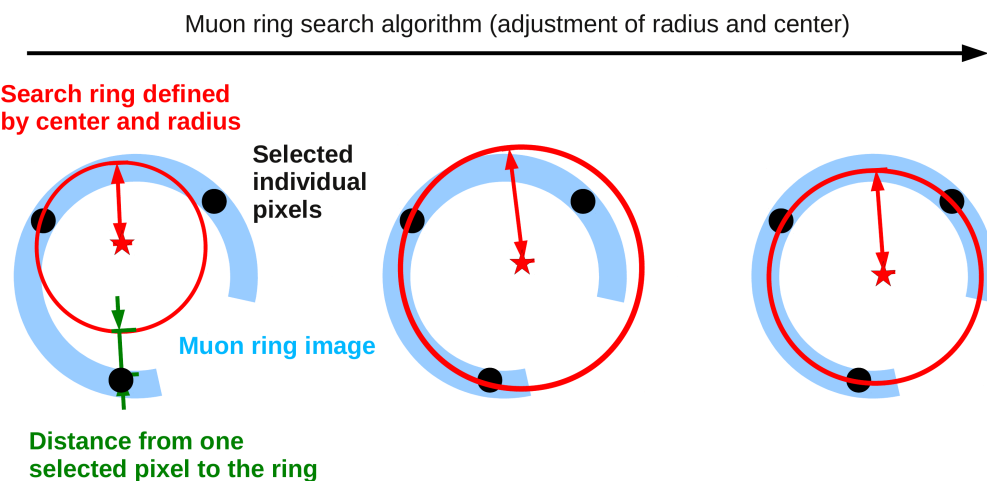
Figure 5.4: Illustration of the muon search algorithm.

---

[2]Cleaned images contain only pixels above a certain threshold

The calculation uses a two step algorithm where the first step determines the rough parameters. In the second step possible outliers are removed by allowing only pixels close to the first fit result to enter the second fit stage. The output of the muon search algorithm is the radius and center of the ring. Cleaned images make this procedure much more stable while both radius and center have no physical correlation to the pixel threshold. Only images with a radius within a given range ($0.6 - 1.35°$) and an RMS of the radial profile below $0.15°$ degrees are considered as possible muon rings and will be kept for the further analysis. For the remaining reconstruction all pixels are used independently of the amount of charge they contain. This approach allows for a precise determination of the detected light and its distribution in the camera. To remove remaining noise which does not belong to the shower a time-constrain is used. The time conserving parabolic shape of the MAGIC reflectors and high sampling frequency of the DAQ systems allow for very precise timing and make time-constraints powerful methods. In particular for small signals the time-constrain improves the separation between noise and real signals.

The time-constrain is defined as follows: the signal weighted arrival time distribution of all pixels, within a margin of $\pm 0.2°$ radial distance of the muon ring is fitted with a Gauss function. The time constrain allows only pixels to enter the further calculations which have an arrival time within 2 standard deviations of the fitted distribution. For more than 90% of all events this results in a time spread between the signals in individual pixels of less than one nanosecond, within expectations for real muon signals (Mirzoyan et al. 2006).

To determine the Arcphi, the azimuthal intensity distribution containing all pixels within a given margin around the radius (default: $\pm 0.2°$) is used. The edges of the ring are defined by an absolute threshold (default: 25 phe) of the charge contained in one azimuthal bin of $18°$ width. The Arcphi is defined as the number of connected bins above the threshold multiplied by the bin width. Arcphi is a powerful parameter to select muon events in the data, for the muon analysis itself it is not directly used.

The main two parameters used in the analysis are the Arcwidth and the MuonSize. The Arcwidth is defined as the sigma of a Gaussian fit to the radial profile of the intensity distribution. The resulting value of the Arcwidth is composed of an intrinsic broadening (scattering of the muon and the Cherenkov light) and the additional smearing effect arising from the optical PSF of the reflector.

The MuonSize is calculated as the sum of all signals in all individual pixels along the complete muon ring within a given margin (default: $\pm 0.2°$). Therefore the Muonsize contains the amount of detected light of a single muon event and can thus be used to connect the signal calibration to the amount of produced Cherenkov light.

5.3.2 Muon selection

As a part of this thesis the selection criteria for muon events have been redefined on the basis of a detailed comparison between data and MC. The muon selection is based on cuts of the muon parameters. Candidates of muon events are those events surviving the radius fit. For all candidates the muon parameters are subsequently calculated. The muon selection aims to achieve best possible agreement between the distributions of the muon parameters for data and MC.

To develop a muon selection some basic properties properties are recalled:

1. Muons are secondary particles of CR which arrive isotropic. In first order muons arrive also isotropic (for not too large zenith angles).

2. Muonrings are local events (few hundred meter above the Telescope).

3. Events in the form of ring-shapes are largely dominated by muons.

4. The R_μ and MuonSize distributions reflect the energy distribution of muons.

5. MuonSize is correlated with R_μ.

6. Cherenkov light from muons shows a very narrow spread in time (Mirzoyan et al. 2006).

Point 1 and 2 allow the assumption that the recorded muons and their parameter distributions do in first order not depend on the pointing position of the telescope. Furthermore, the fact that muon rings are caused by close by particles reduces significantly the effect of light scattering/absorption in the atmosphere due to the short travel distances. On the one hand, this is an advantage because it reduces the effect of the atmosphere, one of the largest systematic uncertainties in the simulations. On the other hand, it has the consequence that the detected Cherenkov light of muons will not show the same spectral properties as the detected Cherenkov light from air showers which travel much longer distances (~ 8 km) and are therefore much more effected by the atmosphere. Muons will produce strong Cherenkov light in the UV (below 300 nm) regime, which is absorbed in the case of air showers.

The typical ring-shapes of muon images allows a very efficient event classification via the Arcphi parameter. The connection between the energy distribution of muons and the radius originates from the Cherenkov angle dependence on the energy of the primary particle. Similarly the MuonSize distribution is connected to the energy distribution of muons by the Cherenkov light production as a function of the energy of the muon. Therefore the shape of both R_μ and MuonSize distributions agree between data and Monte-Carlo simulations if the muon spectrum is correctly simulated and the data sample contains only muons. A shift of the Muonsize distribution to higher or lower values can then be interpreted by a wrongly simulated light collection efficiency.

Most of the timing information has already been used in the calculation of the muon parameters itself. In addition, one can compare the arrival time distribution of the reconstructed muons with the one obtained from simulations and remove possible out layers.

In any selection process of a particular type of events the aim is to achieve the best possible agreement among the selected events in data and in MC. The ideal case would be a MC simulation which contains all possible events of a certain kind (here muons). To produce such a complete MC sample is a huge effort concerning the needed computational power. However, in many cases a complete simulation is not needed. In this case the muon analysis is only based on muon ring events, and therefore there is no need to simulate muon events which do not produce a ring (i.e. distant muons). Therefore the selection has to be understood not as a muon event selection, but as a selection of those muon rings which are contained in the simulations. Subsequently one has to be aware of the settings used to create MC muon sample.

Simulation settings and Monte Carlo muons In the case of the muon analysis the simulated muons have not been derived from first principles. Instead of simulating the CR spectrum itself to produce the secondary muon population a dedicated muon simulation has been used. This approach reduces the needed computational power (cpu time and storage) significantly. Furthermore, it avoids systematic uncertainties in the early phase of the simulation (i.e. atmosphere profile, cross sections, detailed CR spectrum). Following the work by Meyer (2005) the simulations have been carried out using the settings below. Muons are simulated from a starting altitude of ~ 1 km above the telescope randomly distributed in a cone of $1.5°$ around the vertical axis. The impact parameter was randomly chosen between 0 m and 12 m. The telescope was pointed to zenith and the muon spectra is taken from Motoki et al. (2003) and simulated in the range from 6 GeV to 80 GeV. The spectrum is described by a power law with different slopes:

$$dN/dE \propto \begin{cases} E^{-2.16} & \text{for } 6 - 10\,\text{GeV} \\ E^{-2.46} & \text{for } 10 - 20\,\text{GeV} \\ E^{-2.71} & \text{for } 20 - 80\,\text{GeV} \end{cases} \tag{5.13}$$
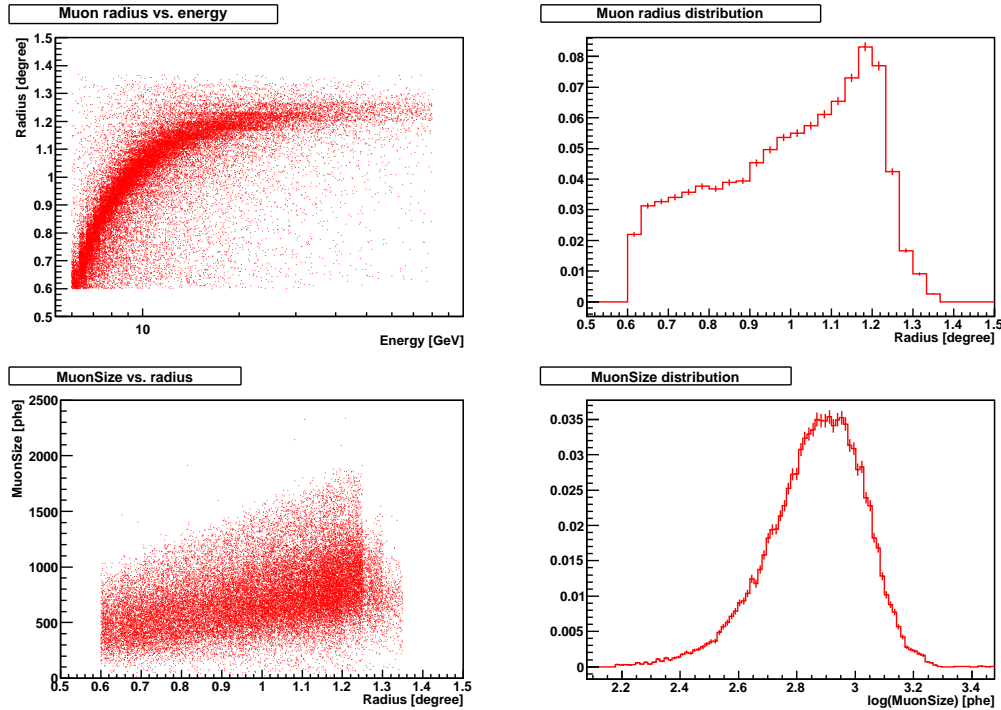
Figure 5.5: Selected parameter distributions of MC muons in MAGIC II. No selection cuts have been applied. The dependence of the Cherenkov angle close to the threshold can be seen in the radius vs. energy plot. Also a general tendency of higher MuonSize for higher R_μ is seen. Both the MuonSize and the radius distribution carry information about muon spectrum.

Fig 5.5 shows some selected distributions of simulated muons. In this example MII was simulated. No selection cuts have been applied. The radius vs. energy plot shows clearly the

correlation between the Cherenkov angle and the energy of the muon. The relatively large spread is mainly due to mis-reconstructed values of the radius. At around 20 GeV the muon is far above the Cherenkov light production threshold (≈ 5 GeV) and the angle (and here the radius) is no longer dependent on the energy but only determined by the refractive index of the medium. Furthermore, the MuonSize vs. radius plot shows that even though the correlation between radius and MuonSize is not very strict, a clear tendency of higher MuonSize with higher radii can be seen. In zero order approximation one would expect that the amount of light produced by a muon scales with the energy and therefore the radius. Strictly speaking the amount of produced Cherenkov light scales quadratically with the velocity of the particle divided by the speed of light (β^2). Thus, one expects a saturation effect in the MuonSize for energies far away from the threshold energy. Furthermore the MuonSize depends obviously on the completeness of the ring and therefore the Arcphi. In addition one sees that for any given radius a maximum size value exists; the full ring. The normalized radius and Muonsize distributions are shown on the right hand side of the figure. The higher abundance of large radii is explained in first order with the higher trigger efficiency of brighter events.

Muon selection criteria   After applying the muon-selection cuts to both, data and MC, the remaining events should show the same distributions of the parameters used to describe muons. In the case that all distributions agree between data and MC, the simulations are a good description of the data. However, there are two kinds of possible discrepancies which are directly connected to those parameters determined by the muon analysis itself. In this sense such mismatch would not be caused by wrong selection criteria, but by a not sufficiently well simulated instrument. Those are:

1. **The mirror fraction (MF)**, if not representing the real value of the instrument will cause a constant shift of the MuonSize distribution to larger or lower values.

2. **The PSF** if not representing the real value of the instrument will cause a shift of the Arcwidth distribution to larger or lower values.

In first order and for not too large changes of the MF and the PSF (roughly within $\pm 20\%$ of the real value) a not perfect value in the simulations will not produce any significant changes in the *selection distributions* except those mentioned above. How this systematic shifts will be used to determine the MF and the PSF will be described in section 5.3.3.

Muon selection cuts   As a first step a soft quality cut in the arrival time spread is applied. Since the muon parameters are calculated with a relative time constraint, false muon candidates can be sorted out by requiring a maximum absolute time spread derived from MC simulations. The empirically determined cuts are:

- TimeRMS < 0.6 ns
  The TimeRMS is the RMS obtained from the arrival time histogram of the charge (one value per pixel) around the ring (margin: $0.2°$).

- TimeSigma < 0.9 ns
  The TimeSigma is obtained from the charge weighted histogram of the arrival time and defined as the sigma of a Gaussian fit to the distribution.

TimeSigma and TimeRMS can differ because of noise effects and slightly different definitions. The TimeSigma parameter is much less effected by noise by allowing a free baseline in the fit and gives the more reliable value of the real physical time spread. The cuts are chosen to contain all simulated muon events up to $\sim 5\%$. The ring shape of the muon images allows a relatively simple selection criterion. In this work a set of only two cuts is used to select highly probable muon events out of all possible muon event candidates (surviving the ring fit) in the data. Those cuts are:

- Arcphi $> 180°$ (at least half rings)

- The *matching cut* allows only certain maximum MuonSize (M_S [phe]) per radius (R [°]):
  for MII: $M_S < 1308 \times R + 215.4$
  for MI: $M_S < 1308 \times R - 184.6$
  The physical meaning of this cut can be interpreted as the removal of all events of a given radius with more MuonSize than a complete ring would have. The cuts have been empirically defined from MC simulations.

Both cuts are only based on the property that a ring image is expected from close by muon events. The Arcphi cut has no physical influence on the MF and the PSF since it only chooses rings of a certain completeness. It should be noted, that a high value of the MF means more light arriving at the camera and due to threshold effects this can lead to slightly more complete rings. This will only result in a different efficiency of selected muons in MC and data, and not in a systematic difference of the selected events. The *matching cut* has no direct connection to the PSF but should be adjusted in the case that the MF is very far from the real value. The matching cut for MI allows a lower maximum MuonSize per radius because the overall light collection efficiency of MII is higher than the value of MI (i.e. due to a higher QE of the used PMT's).

Figure 5.7 illustrates the effect on both individual selection cuts and their combination on data (black) and MC muons (red) for MII. In Figure 5.8 the analog for MI is shown. The data used here have been taken in March 2012. For simplicity reasons the effect on only three distributions (MuonSize, MuonSize vs. radius, and Arcphi) are shown. For both telescopes same effects have been found, as expected. Without any further selection cut (see first column in Figures 5.7 and 5.8) the MuonSize distribution of the data differs drastically from the curve obtained from muon simulations. This is not surprising since most of the events in the data are hadronic showers while the MC only contain single muon events. The Arcphi distribution of the data shows a peak value of $\approx 60°$ significantly lower than the value found in the MC ($\approx 100°$). This is explained by the confusion of small (low MuonSize) showers. Small images from low energy (or distant) air showers can be easily confused with a small part of ring like image. By requiring a minimum of half a ring (Arcphi $> 180°$) this effect can be avoided. The agreement between data and MC in the Arcphi and MuonSize distribution after applying the Arcphi cut (second column in in Figures 5.7 and 5.8) impressively underlines the separation power of this cut. The Arcphi cut is sketched by the green line in the Arcwidth distribution.

In addition, the MuonSize vs. radius distribution shows that the Arcphi cut intrinsically performs a MuonSize cut. It is evident that to obtain at least half a ring image a certain minimum amount of light, and therefore MuonSize, is needed. After the Arcphi cut the Muonsize distribution is reasonably well matching except for a tail towards higher sizes which is only

seen in the data. From the MuonSize vs. radius distribution it can be seen that some events in the data have a much higher MuonSize for a given radius than what is expected from the MC simulations. The third column in Figures 5.7 and 5.8 shows how the *matching cut* removes all events of this kind in the data. The matching cut is sketched in the MuonSize vs. radius plot with the green line. Furthermore the MuonSize distribution after applying the matching cut shows that these events are responsible for the tail previously seen in the MuonSize distribution of the data. The last column shows a zoom to all three distributions after applying both selection cuts. Good agreement can be observed for all three distributions. The small shifts between the MuonSize distributions ($\approx 3\%$ less MuonSize in MC compared to data for MII; Fig. 5.7 and $\approx 15\%$ more MuonSize in MC compared to data in MI; Fig. 5.8) have been artificially introduced in this examples to show that a slight deviation in the MF parameter does not influence the muon selection. In the case of MI the too high MF in the simulations causes also the discrepancy in the Arcphi distribution; more light in the simulations causes the muon rings to be more complete compared to the data.

Before the two remaining parameters, radius and Arcwidth, of data and MC are compared it is worth to compare the MC distributions already shown in Fig. 5.5 before and after the applied selection cuts (see Fig. 5.6).
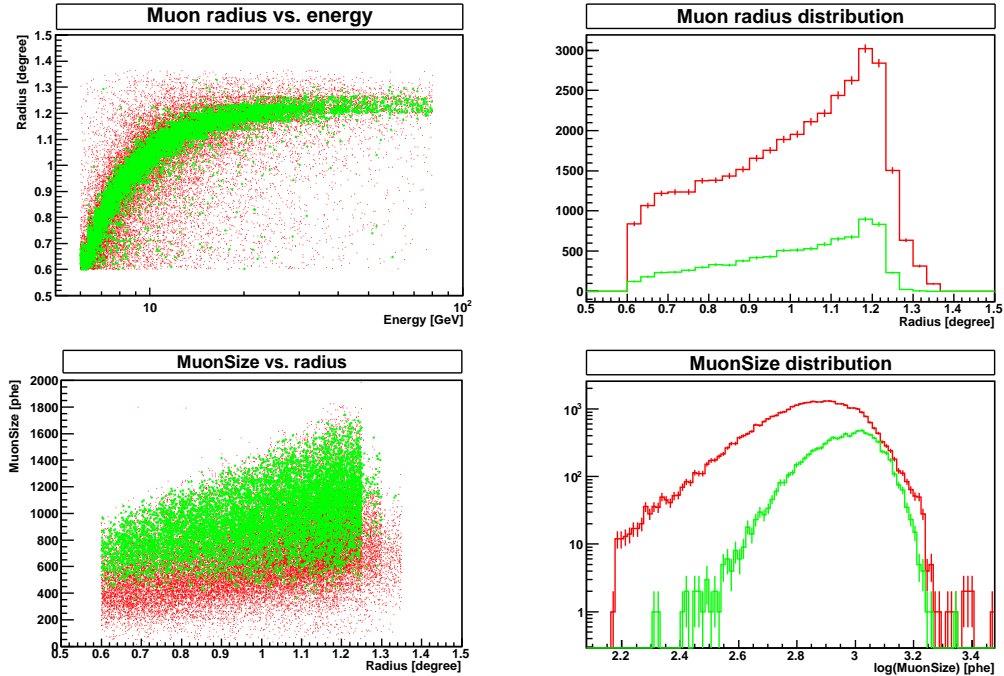
Figure 5.6: The same distributions as in Fig. 5.5 for MII Muon MC without selection cuts (red) and after applying the muon selection cuts (green). See text for details. It can be seen that the selection cuts do not prefer any specific radius of the muon.
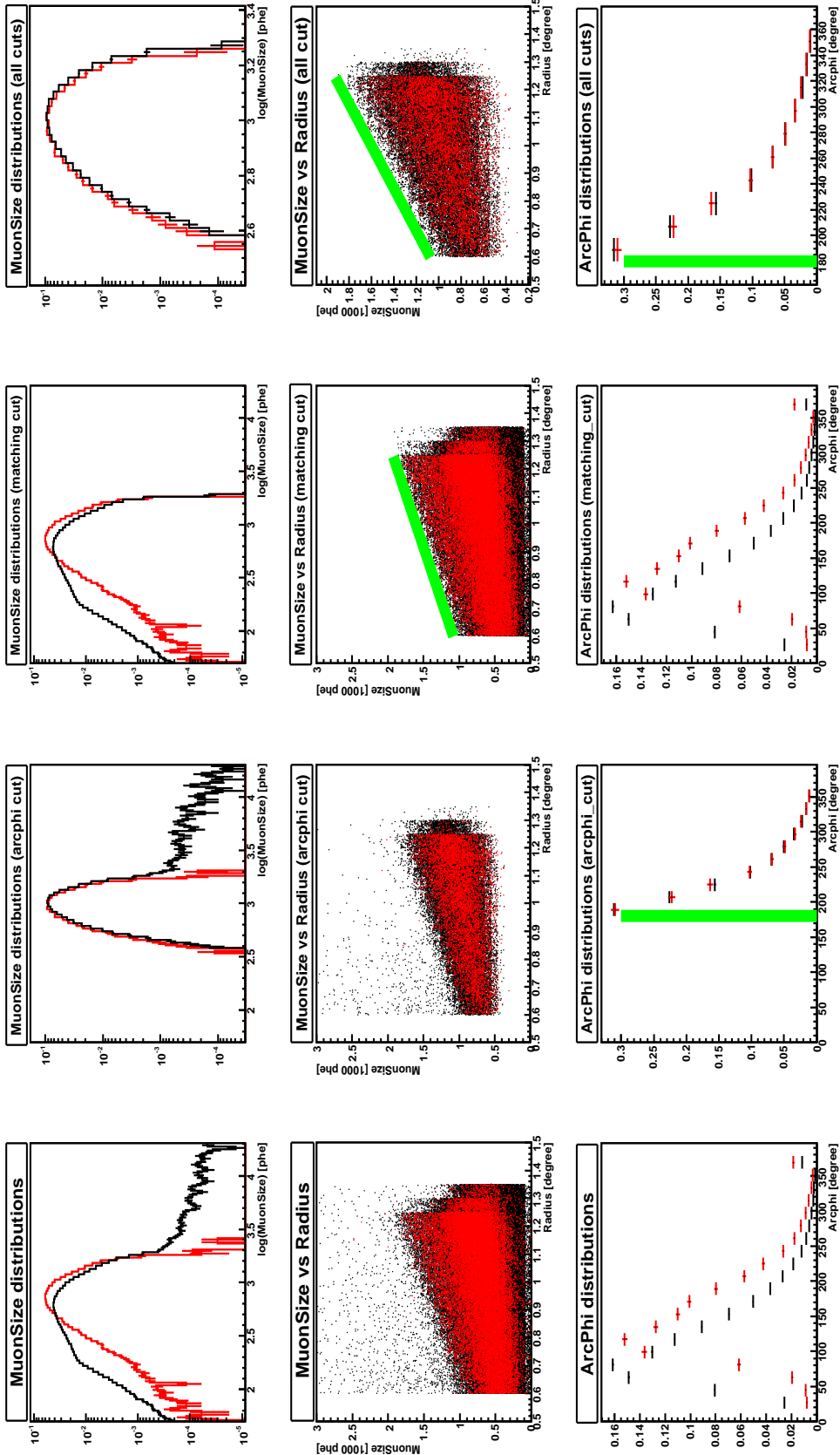
Figure 5.7: Example based on MII data (black) and MC (red) distributions to illustrate the effect of the muon selection cuts. In the first column no cuts have been applied. In the second column the arcphi cut is applied, in the third the *matching cut*. The fourth column shows a zoom of the distributions after both cuts have been applied. The individual cuts are sketched with green lines.
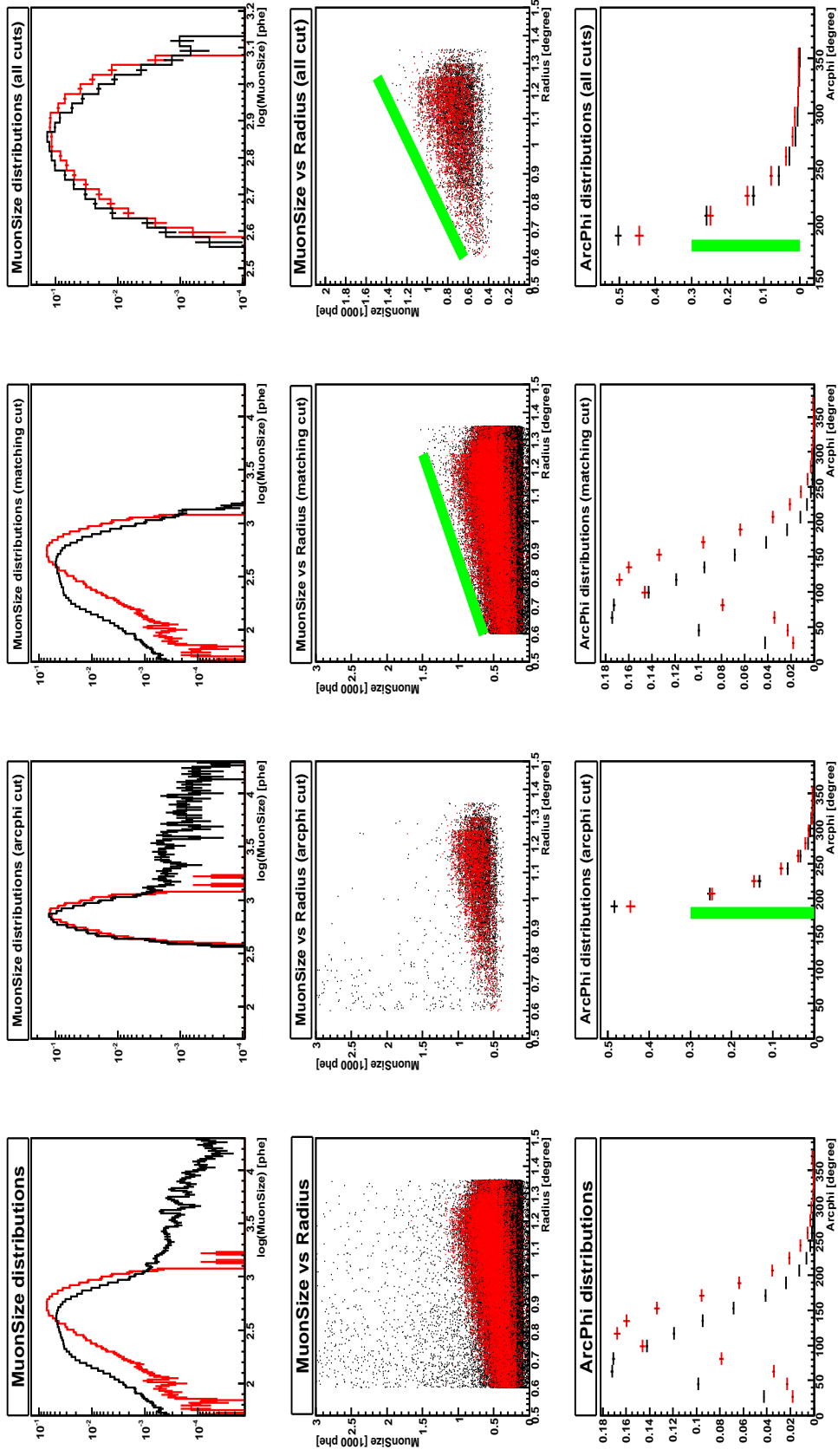
Figure 5.8: Example based on MI data (black) and MC (red) distributions to illustrate the effect of the muon selection cuts. In the first column no cuts have been applied. In the second column the arcphi cut is applied, in the third the *matching cut*. The fourth column shows a zoom of the distributions after both cuts have been applied. The individual cuts are sketched with green lines.

It can be seen that the selection cuts do not prefer any specific radius of the muon. The clear tendency of selecting events with a higher MuonSize arises from requirement to accept only half or more complete rings. The implicit MuonSize cut connected to this and its not trivial effect can be seen in the change of the MuonSize distribution. By choosing muon events in this way, one automatically chooses well reconstructed muons as seen by the much smaller spread in the energy as a function of the radius.

Figure 5.9 shows as an example the Muon Radius and Arcwidth distribution for MI data and MC.
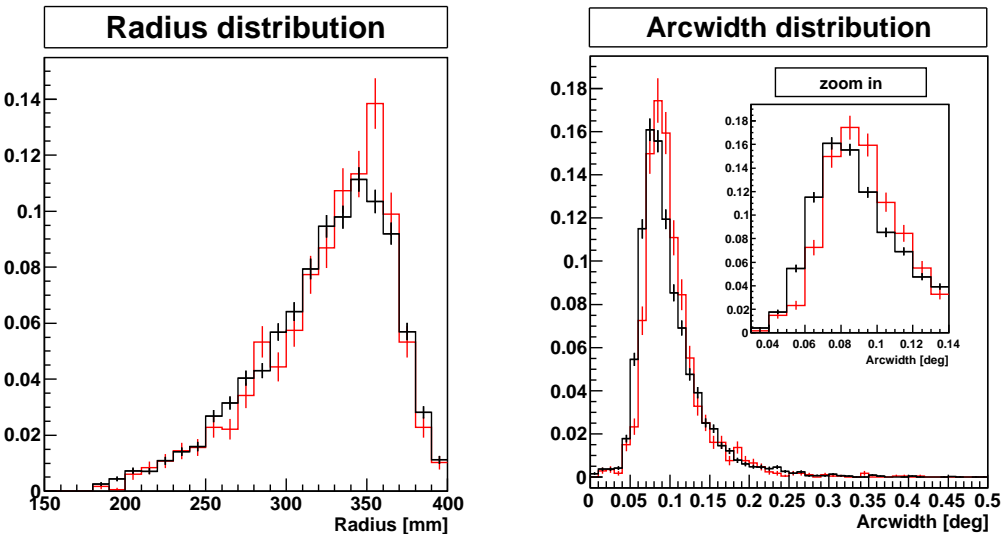
Figure 5.9: MI Arcwidth and R_μ distributions for data (black) and MC (red). The radius distributions agree reasonably well. The higher amount of muons with radii of $R_\mu \sim 360$ mm in the MC could be connected to the fact that in real data this events might be hidden in hadronic showers and are thus not reconstructed as a single muon event. The main discrepancy in the Arcwidth distribution can be described as a shift of the Monte Carlo distribution (red) towards higher values. While this shift has no effect for the muon selection it is a clear indication that the PSF used in the simulations was too large. This example has been explicitly chosen to show that the muon selection does not bias the later determination of the PSF.

The remaining tests to assure the validity of the muon selection cuts are based on the radius and Arcwidth distribution. The radius distribution reflects the energy spectrum of muons up to $R_\mu \sim 1.2$ where the Cherenkov angle saturates at the given altitude. A discrepancy between data and MC would either indicate that the simulated spectrum in the MC is not a valid assumption, or that the event selection allows to many non muon events in the data to survive. The later muon analysis will be performed as a function of the radius. In this way most of the energy dependence is removed from the analysis and small discrepancies in the radius distributions of data and MC will be compensated. The Arcwidth distribution is

strongly dependent on the PSF. Therefore, a difference in this distribution indicates mainly a not correct value for the PSF in the simulations and does not point to a caveat in the event selection. The PSF used in the simulations of the MC shown in Figure 5.9 was explicitly chosen to be larger than the expected value in the data to illustrate the resulting shift in the Arcwidth distribution due to a worse PSF.

To summarize: In the framework of this thesis a selection of muonrings in the data has been re-developed. The selection is based on only two cuts and founded on the basic principle that single, close by muons will create ring images. Images which can be described by at least a half complete ring (Arcwidth > 180°) and have a Muonsize value lower than the maximum value achievable for a full muon ring for a given radius are therefore selected as muonrings. The selection cuts produce reasonable agreement between data and simulations independent of the pointing position of the telescope (zenith: $0 - 50°$), the PSF (changes up to $\approx 30\%$), and the MF (changes up to $\approx 15\%$). Changes in the PSF and the MF will appear as shifts of the Arcwidth and MuonSize distribution, respectively.

5.3.3 Muon analysis

The muon analysis is the determination of the PSF and MF values which result in the best possible agreement between real (data) and simulated (MC) muons. In order to achieve this the MuonSize and Arcwidth of the selected muons in data and MC are compared as a function of the radius in bins of 0.05°. For the analysis only radii between 0.7° and 1.25° are used. The lower limit of the radius is applied to remove threshold effects. As can be seen in Figure 5.6 a radius of 0.7° translates into an energy of $6.5 - 7$ GeV. The minimum simulated energy was 6 GeV and thus the analysis is performed not to close to the minimum simulated value. The maximum allowed radius of 1.25° (370 mm) is chosen due to very poor statistics for higher values (see also Fig. 5.9) in both data and MC. In addition this restriction avoids to use events above the saturation of the Cherenkov angle. To determine the MF the profile of MuonSize/Radius as a function of the Radius is obtained for data and MC. This distribution describes the MuonSize for any given radius averaged over all Arcphi values. The advantage of the profile lies in the removal of the MuonSize ambiguity caused by rings of different completeness without loosing statistics. Following the same approach the PSF is determined using the profile of the Arcwidth/Radius as a function of the radius. A quantitative difference between data and MC is obtained by means of the ratio between data and MC simulations of the two profile plots. As the MF and the PSF are telescope intrinsic parameters they do not depend on the radius of the muons and therefore the ratio between data and MC is expected to be equal for all values of R_μ. To test the performance, the analysis has been performed first on MC only for both telescopes.

Effect of the mirror fraction (MF) The mirror fraction is a linear scaling factor and adjusts the total amount of light arriving at the camera. In first order one can expect a linear change of the MuonSize distribution. The effect of different MF values is shown in an example for MII. Two sets of muon MC have been produced which only differ in the MF. Figure 5.10 shows the muon paramters for both MC sets. Set one (red data) was simulated using a MF= 0.65 while for set two (black data) a MF= 0.75 was used. The MuonSize of the black data is therefore expected to be 11.5% above the value of the red data. None of the other muonparameters shows any significant difference.
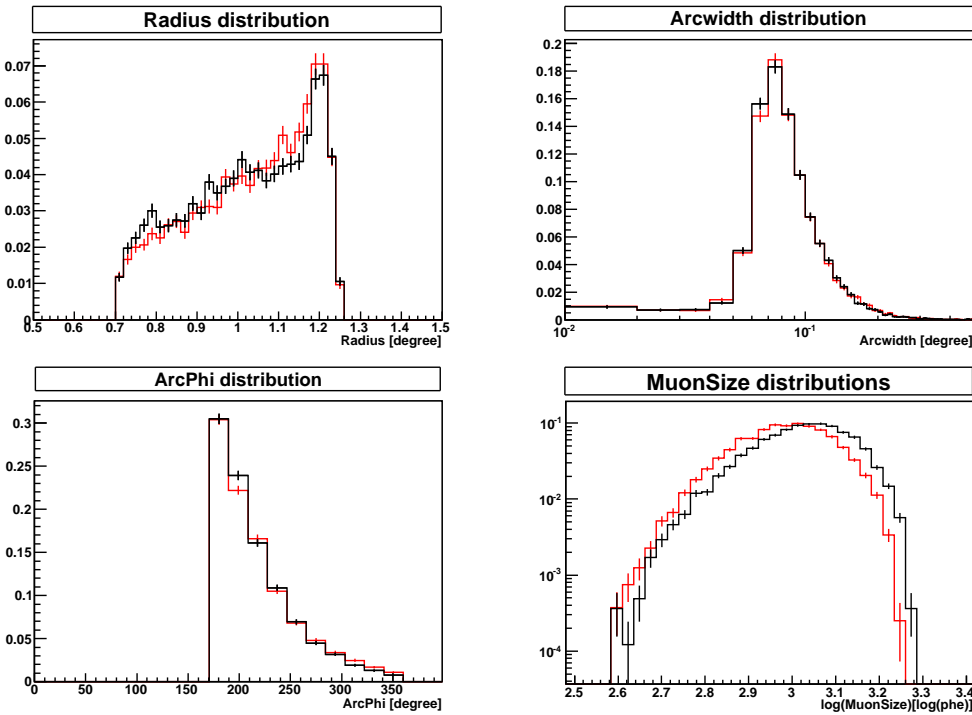
Figure 5.10: Shown are the muon parameter distributions, after muon selection cuts, for two different MC sets of MII. The sets differ only in the value of the MF. The MF= 0.75 was used to obtain the black data and a MF= 0.65 was used for the red data points. The only significant difference in the muon parameters appears in the MuonSize distribution where the black distribution is shifted to higher values as expected due to the higher MF.

To obtain quantitative values for the possible difference in PSF and MF the muon analysis is applied. The results are shown in Figure 5.11. The expected difference in the MuonSize/radius profiles can be easily seen. After fitting a constant to the ratio of the two data sets the resulting MuonSize difference is obtained as $10.9 \pm 0.4\%$ and agrees well with the expected value of 11.5%. As expected, the MuonSize and the MF show a straightforward connection and the ratio obtained for the MuonSize analysis can be directly translated in the difference of the MF. The accuracy of the analysis to determine the MF has been tested on MC simulations to be 1%.
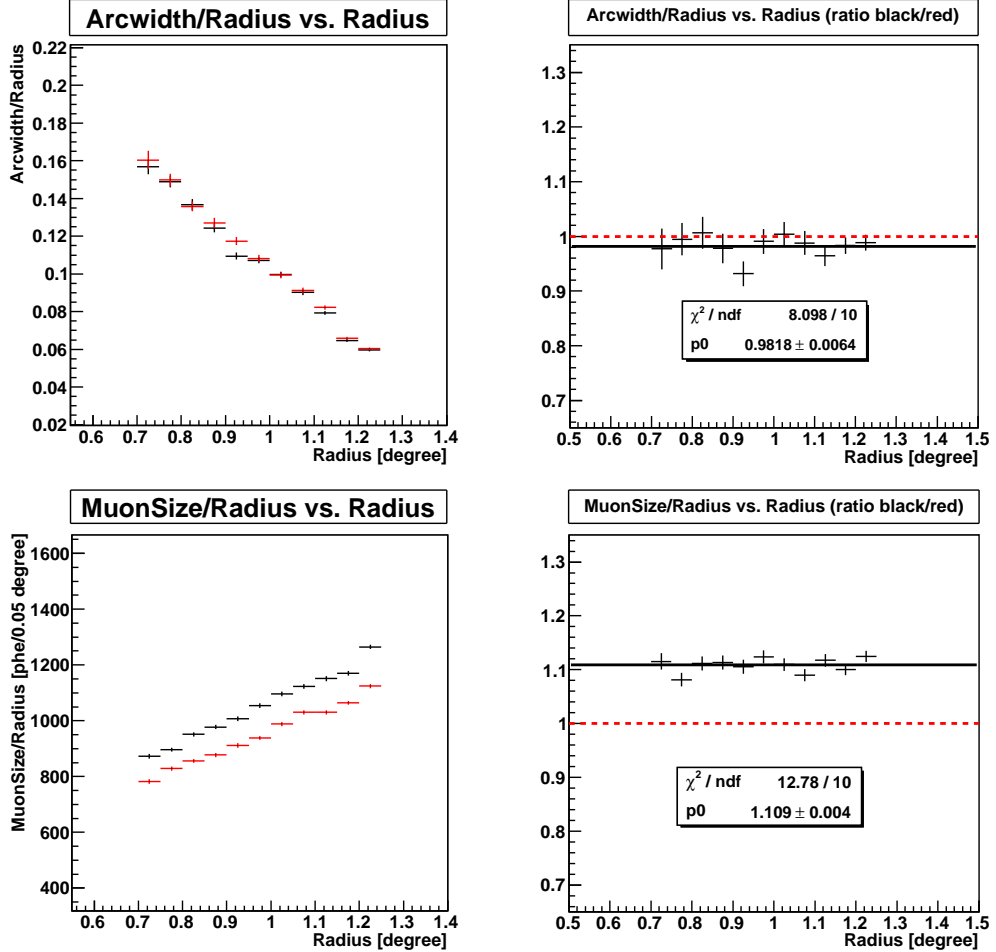
Figure 5.11: The muon analysis for the example of two different MF values (0.65 for red and 0.75 for black) used in MC simulations for MII. On the left hand the obtained profile plots for both sets are shown while on the right hand side the ratio between profile plots is shown. In the case of perfect agreement the ratio should be 1 indicated by the red-dotted line. The black line in the ratio plots is the result of fitting a constant p0 to the data. Besides the determined value of the constant and the statistical error also the χ^2 with the degrees of freedom of the performed fit are displayed. The obtained ratio of MuonSize/radius is $\approx 11\%$ and agrees well with the expected value of 11.5%. A small discrepancy in Arcwith/radius ratio $< 2\%$ is observed.

The ratio of both sets of the Arcwidth per radius as a function of the radius is used to determine differences in the PSF. In this case a small discrepancy $< 2\%$ is observed in this ratio even though there was no difference in the simulations concerning the PSF. This discrepancy depends on the MF difference and is mainly caused by threshold effects at the boundaries of the muon ring. In case of a smaller MF, the dimmer outer parts of the ring might not be detectable anymore which can change the determined Arcwidth. For changes in the MF in the order of 5% the effect on the PSF is $\approx 1\%$. This can be understood as the limitation

of the method to determine the real PSF. In the process of the muon analysis to estimate the real PSF and MF values which represent the data, the first step is to adjust the largest discrepancy.

Effect of the optical point spread function (PSF) The dependence of the Arcwidth on the PSF is similar as in the case of the MuonSize and the MF. A larger PSF value leads to a larger smearing of the photons which causes a broader muon ring and therefore a higher Arcwdith value. However, the translation of the ratio between two Arcwidth/radius profiles into a quantitative change of the PSF is not straightforward.
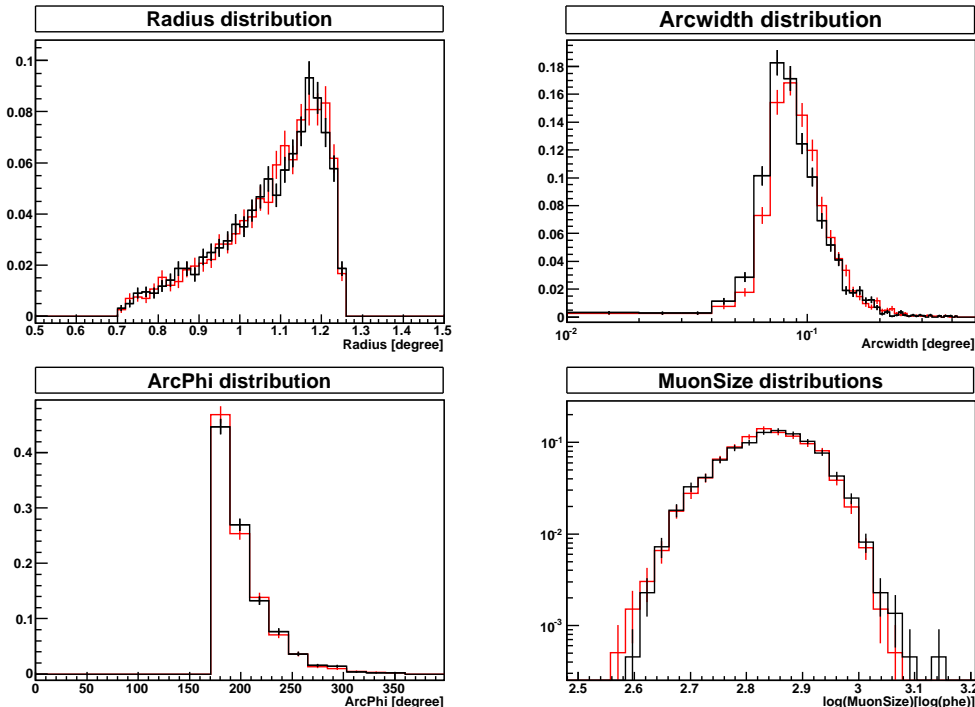
Figure 5.12: Shown are the muon parameter distributions, after muon selection cuts, for two different MC sets of MI. The sets differ only in the value of the PSF. The PSF= 8.0 mm was used to obtain the black data and a PSF= 9.5 mm was used for the red data points. The only significant difference in the muon parameters appears in the Arcwidth distribution where the red distribution is slightly shifted to higher values, as expected due to the higher PSF.

The shape of the PSF in both telescopes is described by a double Gaussian profile, motivated by direct measurements of the PSF from SBIG CCD pictures. The double Gaussian profile consists of one main Gaussian which contains most of the light and a broader second Gaussian. To simulate different values of the PSF the ratio of light in each Gaussian and the ratio between the widths is assumed to be constant. Then the profile is described by only one parameter, the width of the main Gaussian. To obtain the final value of the PSF one has to take into account that a minimum spread due to the individual mirror PSF and the (mis-)alignment of

the mirror panels is already taken into account in the simulations.
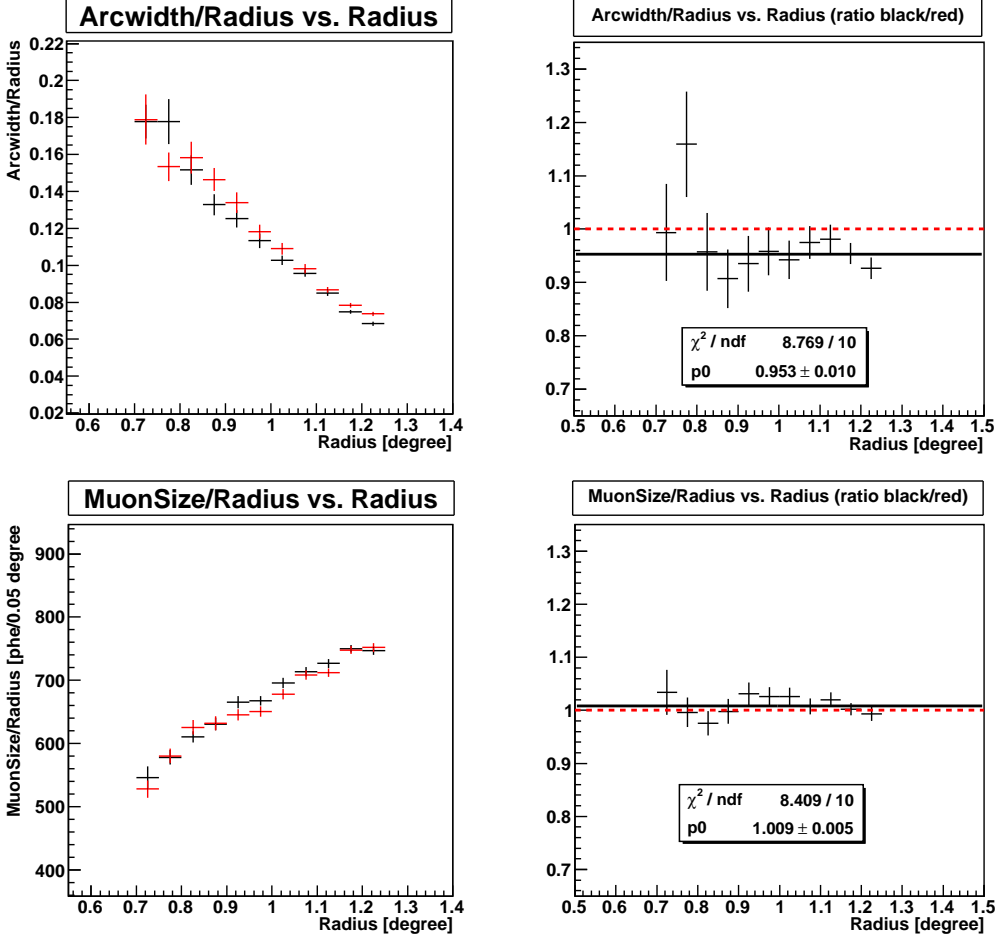
Figure 5.13: The muon analysis is shown for the example of two different PSF values (8.0mm for red and 9.5mm for black) used in MC simulations for MI. On the left the obtained profile plots for both sets are shown while on the right hand side the ratio between profile plots is shown. In the case of perfect agreement the ratio should be 1 indicated by the red-dotted line. The black line in the ratio plots is the result of fitting a constant $p0$ to the data. Besides the determined value of the constant and the statistical error also the χ^2 with the degrees of freedom of the performed fit are displayed. The obtained ratio of the Arcwidth/radius is ≈ 0.95. and agrees well with the empirical estimate of 0.94. A small discrepancy in MuonSize/radius ratio $< 1\%$ is observed.

It is worth to mention that the muon analysis is not very sensitive to the exact shape of the PSF and reasonable agreement between data and MC can be achieved for a double Gaussian as well as for a single Gaussian profile. However, direct measurements of the PSF, and PSF depended parameters (i.e., the width of gamma-ray showers) strongly indicate a double Gaussian profile. The effect of different values of the PSF is shown on an example of MC simulations for MI in

Figure 5.12. The individual PSFs are described by the sigma of the Gaussian $PSF\sigma_{main}$. For the black data points the $PSF\sigma_{main} = 8.0$ mm has been simulated and for the red simulation a $PSF\sigma_{main} = 9.5$ mm was chosen. No changes in the muon parameters are observed except for a small shift in the Arcwidth distribution.

It has been empirically obtained from MC simulations that a difference of 0.5 mm in the $PSF\sigma_{main}$ translates roughly linearly into an Arcwidth/radius ratio of ±0.02. As can be seen in Figure 5.13 the derived ratio is 0.953 ± 0.01 and lies therefore in the expected range. Similar to the MF effect on the PSF determination a small discrepancy of the MuonSize/Radius ratio is observed for different PSF values. Also here the discrepancy is $< 1\%$ and is a lower limit on the achievable accuracy of the muon analysis.

Performance of the muon analysis The muon analysis is a very sensitive tool to quantify the difference of the PSF and MF in two data sets. Due to not completely independent effects of the MF and the PSF the ratio of the Arcwidth/Radius and MuonSize/Radius can be obtained up to a precision of ±0.01. The uncertainty in the ratio of the MuonSize/Radius can be translated directly into an accuracy of ~ 1 % of the MF parameter. The PSF can be determined with a precision of $\Delta PSF\sigma_{main} \approx 0.25$ mm in case of a double Gaussian profile. This uncertainties represent the lower limit of the achievable accuracy. Note that these values have been obtained by comparing MC simulations where only one parameter (i.e. MF or $PSF\sigma_{main}$) has been changed. When comparing MC simulations with the real data it is not clear if all the parameters used in the simulations exactly represent the real conditions. The most important parts of the simulation which can affect the MF and the $PSF\sigma_{main}$ are listed below:

- Atmosphere (especially the density profile)
  - Cherenkov light production (intensity and spreading)
  - Scattering and absorption of Cherenkov light (on short distances this is a minor effect)
  - Scattering of the muon

- Optical characteristics of the instrument
  - Reflectivity (mirrors and Winston cones)
  - Total PSF (PSF of the mirrors and their focusing)

- Detector characteristics of the instrument
  - QE of the PMTs
  - Signal calibration

By construction the muon analysis uses the ratio between data and MC and is therefore a relative measurement. As long as the same parameter is used in both data and simulation its absolute value plays therefore no role for the uncertainty of the muon analysis. This is the major advantage of the muon analysis and makes the method very robust. All directly measurable parameters of the instrument (individual mirror reflectivity and PSF, reflectivity of the Winston cones, QE of the PMTs) do therefore only marginally affect the muon analysis.

For simplicity most of this parameters are not implemented individually for each mirror, Winston cone or PMT. Instead one average value is used in the simulations. The hereby introduced systematic uncertainty on the MF and PSF applies mainly for individual showers but is negligible by averaging over large shower samples (as done in the muon analysis).

The main systematic uncertainties arise from *a priori* unknown differences between real data and simulations. In case of the total PSF of the reflector one can obtain a direct measure from stars (Mirzoyan et al. 2007). This method has the advantage that it directly accesses the distribution of the reflected light on the camera plane and can therefore determine the shape of the PSF. In contrary, the muon analysis determines the effect of the PSF on the shower image, the Arcwidth. In this sense the muon analysis can not be used to determine the exact shape of the PSF. As the shape of the PSF is fixed in the simulations and only the spread is varied one can achieve a good matching between data and MC for different shapes of the PSF. This ambiguity mainly effects very bright showers where the light intensity is high enough such that the tails of the PSF become important. As the Cherenkov light intensity produced by a single particle saturates far above the threshold (~ 20 GeV) the muon analysis has a natural limit concerning the sensitivity to the tails of a given PSF.

By far the largest uncertainty arises from the atmosphere. The used atmosphere in the simulations determines both the Cherenkov angle and the light intensity. In addition, the scattering and absorption of the Cherenkov light, and the scattering of the muon itself in the atmosphere change both the MuonSize and the Arcwidth of a given muon event. Furthermore, the atmosphere changes on almost all timescales. Both, the MF and the PSFσ_{main} are applied at level of the camera plane thus have to be understood as parameters which include both, atmospheric effects and those of the optical characteristics of the instrument. This has the advantage that small discrepancies in the simulations of both, the atmosphere and reflector, can be absorbed by adjusting the values of MF and PSFσ_{main} in the simulations. The main remaining uncertainty arises from time depend effects and thus mainly from the changing atmospheric conditions. A restriction to high quality data (good weather conditions for gamma ray observations, see Chapter 6.1.3) will naturally reduce this kind of systematic errors.

To determine the overall systematic uncertainties in the determination of the MF and the PSFσ_{main}, the muon analysis has been applied by comparing data of different dates to one a priori defined reference data set. To assure no instrument intrinsic changes (which would cause a real change of the MF or the PSFσ_{main}) the measurements are spread over a conservatively short timescale of 9 days. Thus, the observed changes should be strongly dominated by day to day changes in the atmosphere. The results for both telescopes are displayed in Table 5.3.3. The following systematic uncertainties represent extreme conservative values as all statistical errors on the measurements have been neglected and all differences have been attribute to systematic uncertainties only. By averaging over all dates and both telescopes the systematic uncertainty of the MF parameter determination is estimated to be $\lesssim 0.3\%$. For the determination of the Arcwidth/R_μ ratio constant the systematic uncertainty is $\lesssim 1.1\%$. Both values are in the order of the above determined precision of the muon analysis.

Table 5.1: Shown are the determined constants of the Arcwidth/R_μ and MuonSize/R_μ ratios (date/reference) for each telescope compared to the reference date 2012/03/16. The spread in the values is used to estimate the systematic uncertainty of the muon analysis. Statistical errors of the measurement (in the order of the last shown digit) have been neglected and all differences are attributed to systematic uncertainties only. The individual dates cover the zenith angle up to 50° as well as different sky fields.

Date	MuonSize/R_μ ratio constant	Arcwidth/R_μ ratio constant
MI		
2012/03/16	:= 1	:= 1
2012/03/17	0.999	0.999
2012/03/24	0.999	0.997
2012/03/25	1.01	1.04
MII		
2012/03/16	:= 1	:= 1
2012/03/17	1.00	0.998
2012/03/24	1.002	1.01
2012/03/25	1.002	1.01

As a relative measurement the muon analysis is a precise tool to determine the MF and PSFσ_{main} parameter needed in the MC simulations to reproduce the conditions of real data. It should be stressed once more that the obtained values from the muon analysis represent a combination of the atmospheric and instrumental effects. If one aims to disentangle atmospheric effects from those of the reflector and thus derive absolute values for example of the reflectivity the uncertainties will be significantly larger. However, the small day to day variations presented here indicate that the main contribution arises from instrumental effects. Muon rings probe the atmospheric conditions only up to a height of ~ 0.5 km. In contrast, gamma ray and hadronic showers reach their maximum at a height of $\sim 6 - 12$ km (50 GeV – 10 TeV) above the telescope. Thus, the obtained value in the muon analysis might not represent the real values for hadronic and gamma ray showers. This leads to systematic uncertainties in the reconstruction of gamma rays. In Aleksić et al. (2012) these uncertainties have been estimated to be $\lesssim 10$ % on the energy scale and $\lesssim 10 - 15$ % on the flux normalization of a gamma ray signal.

5.3.4 Results and conclusions

In this section the MF and PSF for MI and MII are determined. The data used here have been taken simultaneously for both telescopes on the 16th, 17th, and 24th of March 2012. In total about 200 minutes of observations have been carried out for both telescopes. The data cover a zenith range between $15° - 50°$ and different sky fields. As shown above, the muon analysis shows no significant day to day fluctuations between these data sets.

MAGIC I

The best agreement between data and MC for MI is achieved for a PSFσ_{main} = 7.8mm and a MF= 0.58. The double Gaussian profile used in the simulations of M1 is described as:

$$DG_{M1} = \alpha \times G_1(\text{PSF}\sigma_{main}) + (1 - \alpha) \times G_2(\beta \times \text{PSF}\sigma_{main}) \qquad (5.14)$$

where $\alpha = 0.75$, $\beta = 3.5$, and $G_i(\sigma)$ are normalized Gauss functions of width σ.
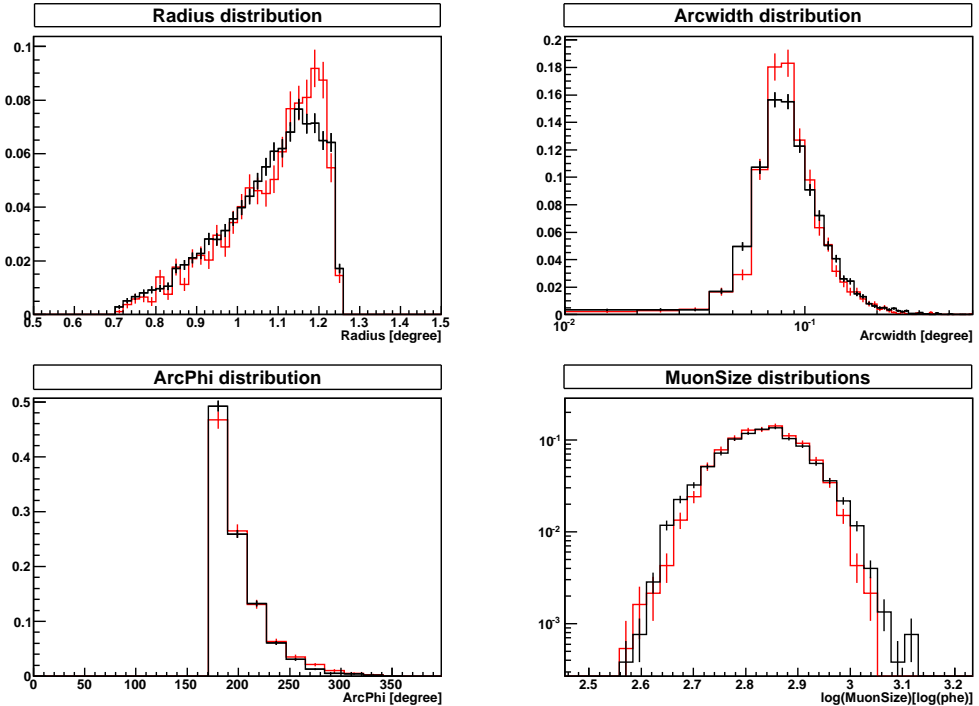
Figure 5.14: Overview of muon parameter distributions for MI data (black) and the best matching MC simulations (red). A general agreement is observed for all distributions, besides some caveats. The higher amount of high R_μ muons in the MC might be connected to the fact that in the data this events can be hidden in hadronic showers. This might also explain the small discrepancy for low and high values of the MuonSize by a possible small contamination of light from an accompanying hadronic shower. As the muon analysis is performed in bins of R_μ the obtained results are not affected by this. The Arcwidth distributions agree well in shape and peak position. The small remaining discrepancies might arise from single misaligned mirrors which would change slightly the shape of PSF.

Figure 5.14 shows the muon parameter distributions and the muon analysis plots comparing the data (black) with the above mentioned MC (red) set. All muon parameter distributions show good agreement between the data and the MC. The quantification of the MF and PSF is obtained from the muon analysis (see Fig. 5.15).
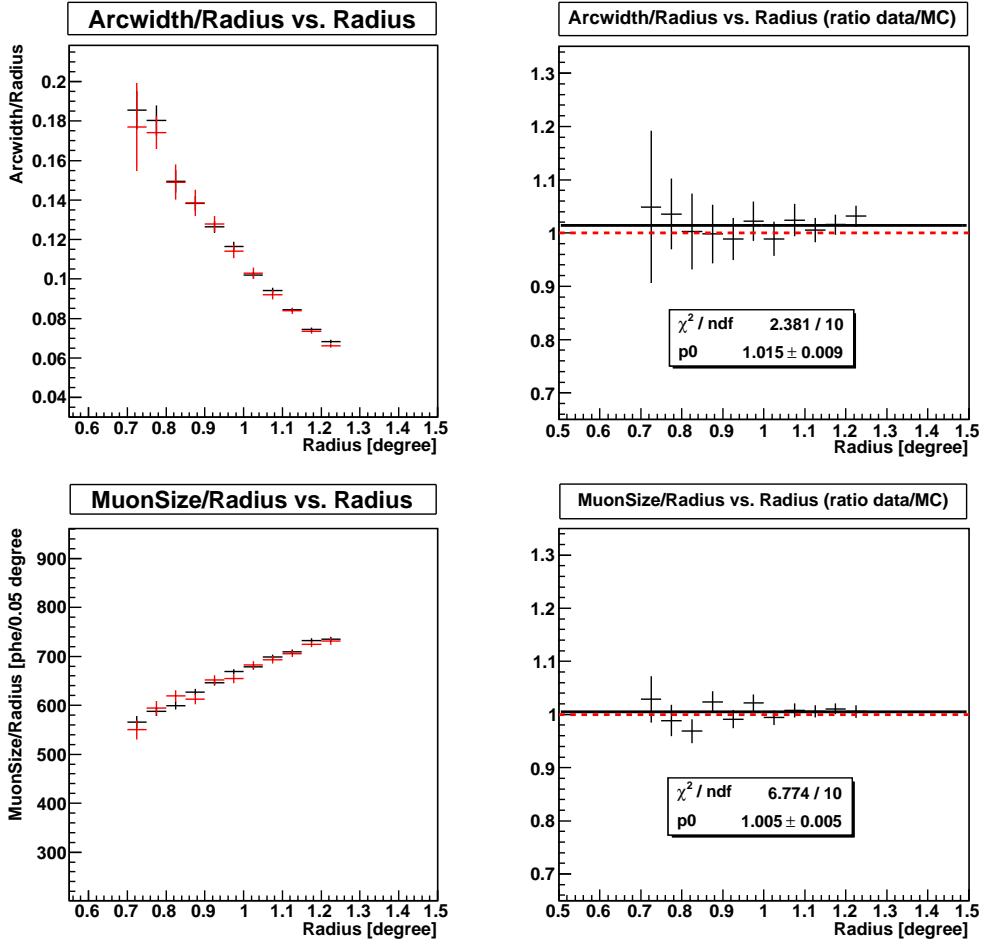
Figure 5.15: Muon analysis for MI data (black) and the best matching MC simulations (red). Both ratios are close to 1. All errors shown are statistically only. When taking the precision of the method ($\Delta ratio = \pm 0.01$) into account MC and data are compatible.

The Arcwidth/radius ratio between data and MC yields a value of: 1.015 ± 0.009. Taking into account the accuracy of the method the PSF of MI is compatible with the value used in the MC simulations. The translation of the ratio to a shift in the $PSF\sigma_{main}$ results in an absolute value of $PSF\sigma_{main} = 8.05 \pm 0.25_{stat} \pm 0.25_{acc}$ mm. Here, both, the statistical error on the obtained ratio and the error arising from the accuracy of the method, are indicated. The ratio obtained from the MuonSize/Radius profiles is: 1.005 ± 0.005. The MF used in the MC simulations agrees very well with the data. Using the direct dependence of the ratio on the MF the absolute value for the MF is: $0.575 \pm 0.006_{stat} \pm 0.006_{acc}$.

81

MAGIC II

The double Gaussian profile of the PSF used in MII has the following parameters:

$$DG_{M1} = \alpha \times G_1(\text{PSF}\sigma_{main}) + (1 - \alpha) \times G_2(\beta \times \text{PSF}\sigma_{main}) \qquad (5.15)$$

where $\alpha = 0.65$, $\beta = 2.7$, and $G_i(\sigma)$ are normalized Gaussian functions of width σ. In MII the best matching MC have a MF= 0.675 and a PSFσ_{main} = 7.5mm. The muon parameter distribution of data (black) and MC (red) are shown in Figure 5.16
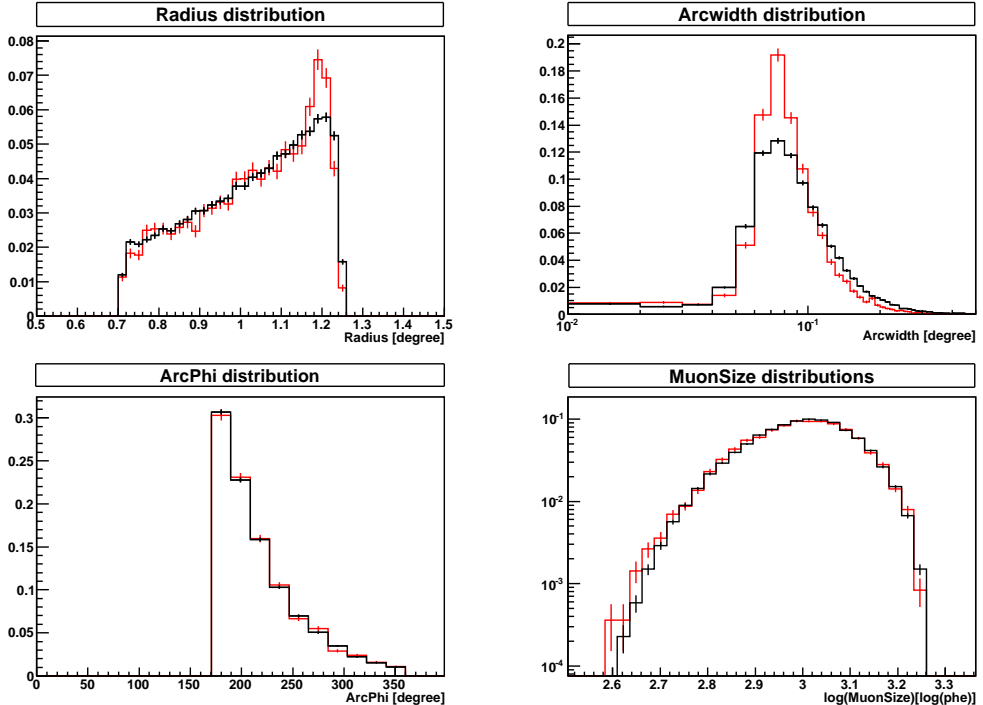
Figure 5.16: Overview of muon parameter distributions for MII data (black) and the best matching MC simulations (red). Reasonable good agreement is observed for all distributions except the Arcwidth distribution. Again, the larger amount of high R_μ in the data could be connected to the fact that these muons could be hidden in hadronic showers in the data. The tails of the Arcwidth distribution seen in the data are not reproduced by any of muon MC simulations used in this work independent of PSFσ_{main} and neither by simulating a simple gauss shaped PSF.

Good agreement between MC and data can be found for all parameter distributions (neglecting the known feature R_μ) except for Arcwidth. The data have a long tail towards higher values as well as a smaller tail which towards lower values which is not reproduced in the simulations. A change of the PSFσ_{main} value in the simulations has almost no influence on this tail but rather shifts the complete Arcwidth distribution. The tails in Arcwidth are seen in the data independent of the radius and appear as a generic feature in MII. The discrepancy between data and MC points clearly to a systematic difference. Caveats which could explain this effect are listed and discussed below:

- Treatment of different mirror types in MII
  In these simulations one averaged mirror type has been simulated. The glas mirrors in MII are known to have a broader individual PSF than the aluminum mirrors. However, a simple change in the $PSF\sigma_{main}$ mainly shifts the Arcwidth distribution instead of broadening it. This effect would imply a dramatic change in the shape of the PSF which is not observed by direct measurements.

- Incomplete simulations
  The simulation settings like impact, starting altitude and inclination angle have been adopted from previous MI simulations. As shown in Chapter 4.2 the trigger region of MII is almost twice as big as the one of MI and thus this settings might not achieve a complete enough muon sample. Highly inclined muons would produce a very asymmetric light intensity throughout the ring which would strongly peak in one half of the ring. Thus, the determined Arcwidth would stronger depend on the second, broader Gaussian which might result in a higher Arcwidth. However, it is not obvious that in such a case the remaining muon parameter distributions would match as good as they do here.

- Angular acceptance of the Winston cones
  If the Winston cones have a much higher reflection for photons arriving under large angles in reality than used in the simulations this could increase the effective Arcwidth. Such a scenario would be largely independent of the value of $PSF\sigma_{main}$ as each pixel in the camera would gain a larger field of view. However, direct measurements of the Winston cones do not support this scenario.

- Wavelength dependence of the PSF & MF
  The Cherenkov light in the UV regime emitted by muons is not strongly effected by absorption/scattering due to the short travel distance to the telescopes. If the PSF in MII is much broader in the UV regime compared to the simulations this would produce an effect on the Arcwidth distribution. The optical characteristics of the instrument in the UV regime are difficult to determine as the UV light from stars is almost completely absorbed in the atmosphere. The wavelength dependence of the reflectivity and the PSF could also be different for the different mirror types used in MII.

- Aberration effects
  Another possibility could be that optical distortions are underestimated in the simulations. At this point it seems unlikely that these effects are so much stronger in MII compared to MI.

- Misaligned mirrors or other effects in the data
  No indication of any not properly working subsystem during the observations has been found. Direct measurements of the PSF show that all mirrors were well aligned during the observations. A possible problem in the used data can be excluded.

New muon simulations are being prepared to determine the underlying reason(s).

Nonetheless, this MC set can still be used to get an estimate of the MF. All remaining muon parameters agree well between data and MC or their discrepancies plays no role for the muon analysis as in the case of the radius distributions. Especially the MuonSize distribution is very

well reproduced by the MC. Thus, it can be concluded that the MF can vary only marginally around the used value. An estimate of the PSF can found by restricting the analysis to a small region around the peak of the Arcwidth distribution. A change of the PSF mainly causes the Arcwidth distribution and especially the peak to shift (see also Fig. 5.12). In Figure 5.17 the muon parameter distributions after restricting the allowed Arcwidth to a narrow value around the peak value of the data $[0.06°, 0.09°]$ are shown.
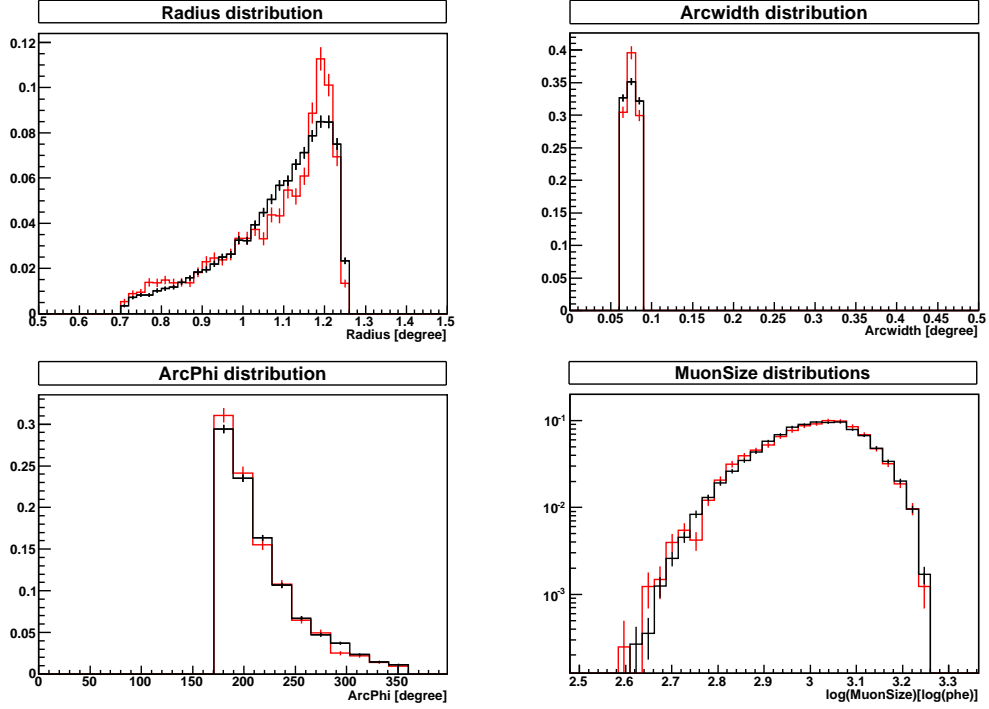

Figure 5.17: Overview of muon parameter distributions for MII data (black) and the best matching MC simulations (red) after allowing only events with an Arcwidth around the peak position of the data to enter the later analysis. All distributions show acceptable agreement except for the the Radius distribution. The exact shape of the distribution is not important for the muon analysis which uses differential bins in R_μ.

By reducing the allowed Arcwidth about 30% of the events in the data and about 50% of the MC events are kept. The effect of using only this narrow range has been estimated both on MC simulations and by applying the same cuts in the MI analysis. No additional introduced systematic in the determination of the MF has been found. In case of the PSF determination the reduction results in an additional uncertainty in the Arcwidth/radius ratio of ± 0.02. This translates into an additional uncertainty in the PSFσ_{main} of ± 0.5mm. The muon analysis based on the narrow range of allowed Arcwidth values is shown in Figure 5.18. The MF used in the simulations reproduces the data well. The MuonSize distribution agrees between data and MC independent of the Arcwidth restriction. No additional systematic effects on the MuonSize have been found connected to the Arcwidth distribution. Therefore, the derived value for MII is MF= $0675 \pm 0.014_{stat} \pm 0.07_{acc}$. For the PSF it was found that only the

Arcwidth restriction allows to achieve agreement between data and MC. This introduces an additional systematic error of 0.5 mm on the PSF determination. Furthermore, it should be noted that only 30% of all events in the data have been used to determine the PSFσ_{main}. As an estimation it has been obtained that for MII the PSFσ_{main}=7.50$\pm$0.1$_{stat}$$\pm$0.25$_{acc}$$\pm$0.5$_{sys}$ mm.
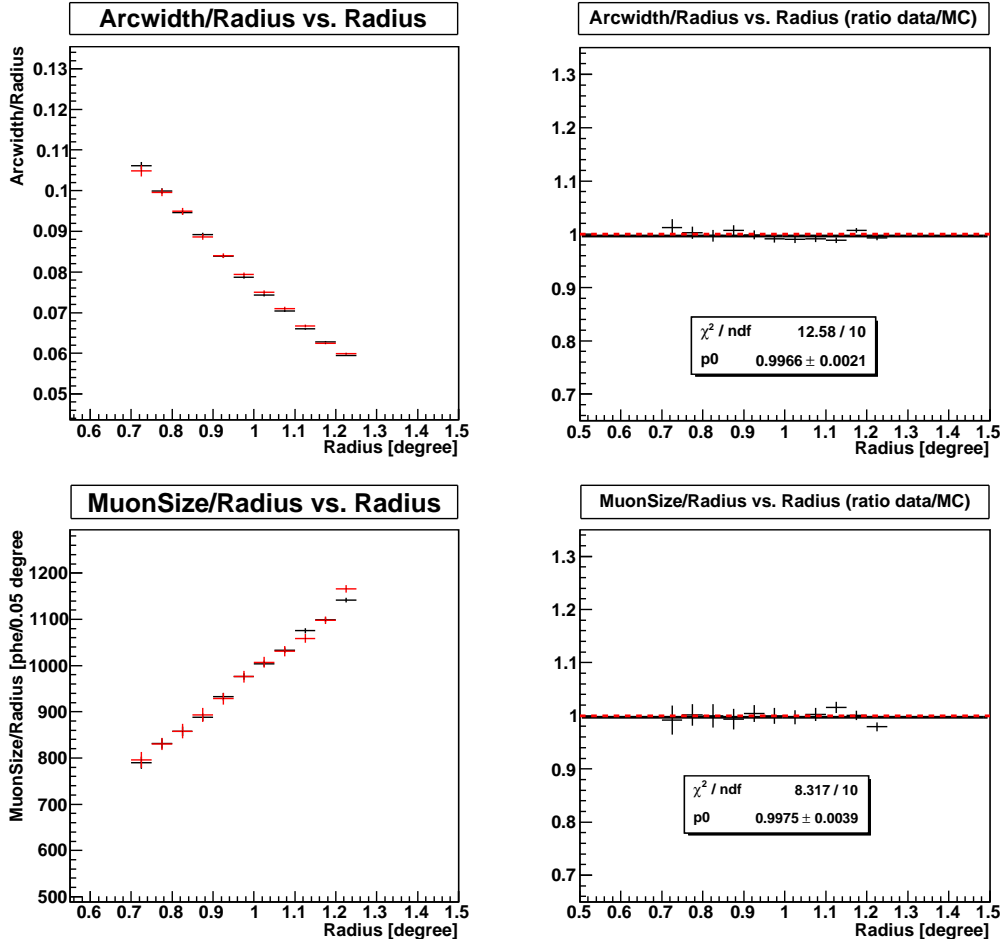
Figure 5.18: Muon analysis for MII data (black) and the best matching MC simulations (red). Only events with Arcwidth values around the peak position of the data distribution are kept $[0.06°, 0.09°]$. Both ratios are compatible with 1 taking the precision of the method and the statistical errors into account.

Summary and Future prospects

The muon analysis presented in this work acts as useful tool to adjust the light distribution and intensity arriving at the camera in the MC simulations. This is done by the two parameters MF and PSFσ_{main}. The method is based on a relative measurement using the ratio between data and MC, so many systematic uncertainties are removed with a typical precision of the obtained ratios of ~ 1 %.

In the case of MI very good agreement of all relevant parameter distributions and a precise

determination of the MF and the PSFσ_{main} have been performed. In the case of MII the situation is more complex. Here, a not reproduced tail in the Arcwidth distribution prevented a standard determination of the value of PSFσ_{main}. The finding of this discrepancy is important to further improve the simulations. By restricting the Arcwidth distribution in data and MC an estimate of the PSF could still be obtained by accepting a larger systematic uncertainty. For the determination of the MF in MII an additionally introduced systematic uncertainty due to this restriction could not be observed. The PSF obtained from the muon analysis is cross-checked with other methods and will be used to fix this parameter for other MC simulations (i.e. gamma-rays). To determine the MF the muon analysis is the only direct method to adjust this parameter as one can easily compare the detected light and with the expected light produced in muon events. Moreover, the effect of the lower atmosphere (scattering and absorption of Cherenkov light) is absorbed in the MF parameter.

Besides the improvement of the simulations to correctly reproduce the Arcwidth distribution found in MII data there are many future prospects of this work. Among these is the monitoring of the PSF and MF parameter over time. Here, preliminary work shows that the Arcwidth/radius distribution of MII data, and therefore the PSF, shows no significant changes between January and March 2012. In the case of M1 the same period was monitored and PSF changes due to commissioning work on the AMC could be clearly spotted. In addition, the MuonSize/radius distribution of both telescopes was monitored in the same period and clearly allowed to trace back expected changes during the commissioning work. This monitoring was done with dedicated muon runs (mono observations) and for the future it is planned to use muon events recorded in stereo mode to monitor the daily parameters during normal data taking.
In addition to the monitoring aspects a cross-calibration between MI and MII based on muons is planned. Such a calibration could also be useful for larger arrays of Cherenkov Telescopes, for example the CTA.

Chapter 6

Data analysis of the MAGIC Telescopes

This Chapter deals with the complete analysis chain of stereoscopic MAGIC data. For each detected air-shower one single event is stored. To extract physical information from the data the following key parameters have to be determined:

- Data quality

- Exposure time (effective observation time)

- Type of the primary for each event (i.e. gamma or hadron)

- Energy of the primary for each event

- Arrival direction of the primary for each event

- Arrival time of each event.

Determination of these parameters will be called *base-level-analysis*. In the *base-level-analysis* the general parameters of the observations (quality and duration) are determined and the event classification (type, energy, direction, time) is performed. This information is the basis to determine how many gamma-like events are observed from a certain direction in a given time, the *high-level-analysis*. To translate the results of the *high-level-analysis* into measurements of the absolute physical parameters (i.e, flux), the complete analysis is performed on an unbiased test sample of MC simulations. Starting with the observation settings and the determination of the data quality, the following sections describe the aspects of the event reconstruction and subsequent analysis of the data, up to the derivation of the measured physical parameters. The last section in this chapter describes two effects which have been addressed in the framework of this thesis. The first effect is based on the asymmetric acceptance of events in a system of two IACTs. As a major part of this work the background calculation in the signal extraction has been generalized to reduce systematic effects caused by this asymmetry. The last part of this Chapter addresses shortly systematic errors in flux calculation caused by imperfections in the MC simulations and shows how they can be reduced.

6.1 Observations and data taking

The standard data taking mode in MAGIC is the so called stereoscopic wobble observation. Stereoscopic indicates that only events which trigger both telescopes are recorded. Wobble stands for a specific pointing modus (Fomin et al. 1994). In wobble observations the telescopes do not point directly at the source but slightly away from it (default: 0.4°). Therefore the

source position is not located in the center of the camera but shifted to one side of the camera. This modus allows to observe the source and a source-free region (used for the background determination) simultaneously. To reduce possible systematics introduced by using one half of the camera for the signal and the other half for the background estimation the positions in the camera occupied by source and source-free region are regularly (default: 20 min) interchanged by switching the offset direction by 180°. During standard data taking the rate of recorded events (DAQ-rate) is ≈ 200 Hz. The gross of the recorded events are hadronic air showers induced by Cosmic rays (mainly protons) which represent the main background for IACT's. For comparison the rate of gamma-like events recorded from the Crab Nebula, one of the brightest known VHE-Gamma-ray sources, is in the order of 10 events per minute. This demonstrates the need for a very efficient background suppression. MAGIC collects light from the near UV to the visible wavelength regime, so a possible source of noise is caused by star light.

6.1.1 Light of the night sky and individual bright stars

Besides the electronic noise caused by the read-out and camera electronics the major source of noise in the PMT's is caused by the light of the night sky (LoNS). This includes all the light of the completely dark night (stars, air glow, reprocessed star light, and unresolved stars). The LoNS appears as a diffuse source of noise and adds up with the electronic noise to the baseline measured in each pixel. By taking so called pedestal events, which are events recorded at a given frequency (default: 25Hz) independent of the normal trigger decision, this baseline can be determined and subtracted from the signal. The fluctuations of this baseline define the individual pixel thresholds of the instrument. With the use of MC simulations this can be translated into the trigger threshold for gamma-rays in units of energy. This has been done in Aleksić et al. (2012) and was estimated to be 50 GeV for a gamma-ray spectrum following a power law with a spectral slope of −2.6. MAGIC can also operate under moderate moon or twilight conditions. The higher level of the background light causes higher fluctuation of the pedestal baseline leading to a higher trigger threshold under such conditions. All data presented here are taken in dark time.

Most of the stars seen by eye do not appear as single bright objects in the PMT cameras of the MAGIC telescopes. Particularly bright stars (magnitude ≲ 3) can, however, still have effects in the data taking procedure. If several pixels are affected by one star this can produce fake trigger signals. This is compensated by the individual pixel rate control which automatically adjusts the discriminator thresholds of the affected pixels to maintain the previously defined individual pixel rate. Nonetheless, these pixels will be occupied by the light of the star and could distort images of real showers. If possible, such bright stars are avoided by choosing the wobble positions (pointing positions) in such a way that the star is not longer in the field of view. If this is not possible the pixels have to be identified and treated carefully. For this purpose the algorithm to remove the effect of stars has been fine tuned as part of this work. To probe the noise caused by the star(s) the percentage of pedestal events which survive the image cleaning is calculated. The image cleaning will be described in detail in Chapter 6.2, for now this process should be understood as the removal of all pixels in the camera which do not contain any significant part of an air shower. Thus, pedestal events should not survive the cleaning. For pedestal events taken with a bright star in the field of view the affected pixels can however mimic a shower like image. The amount of surviving pedestal events depends

on the brightness of the star, the PSF, the pixel size, and the cleaning conditions. A star located in the bigger pixels of the outer part of the MI camera produces much less problems than the same star in the MII camera because here only smaller pixel sizes are used. To achieve a general treatment of the affected pixels independent of the star's magnitude, the number of stars, and the position of the star(s), the identification of affected pixels is based on the pedestal RMS. Based on interleaved pedestal events the average pedestal RMS over all pixels is calculated for every 20 seconds. For individual pixels the RMS value is calculated and compared to the average one. If the difference is larger than a constant times the average RMS, this pixel is marked as *unsuitable*. The signal in unsuitable pixels is interpolated from the neighboring pixels. If less than 3 neighboring pixels are suitable, the signal in the unsuitable pixel is set to zero. The minimum deviation required to set a pixel unsuitable is determined by minimizing the amount of surviving pedestal events and simultaneously maximizing the average efficiency among all affected pixels. The underlying assumption in this procedure is that pixels affected by the star will be marked much more efficiently than those which are marked by a too tight constrain. The minimization of the surviving pedestal events on the other hand ensures a minimum allowed deviation. The default setting for the algorithm has been obtained by comparing different star fields (one bright star, two bright stars, no stars). The resulting deviations from the average pedestal RMS was set to maximum of a factor 4.5 in the case MII and 5σ in the case of MI. Figure 6.1 shows an example of the pixels marked unsuitable in the camera of MII, due the star Zeta Tauri at about 1° distance to the Crab Nebula.
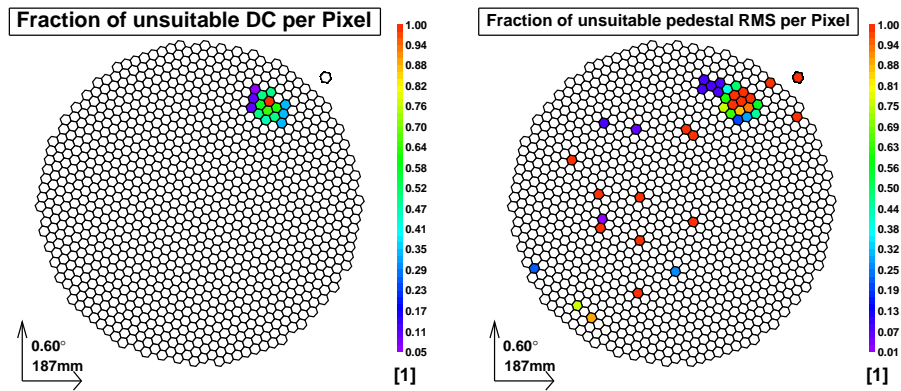
Figure 6.1: Example of the treatment of a bright star in the field of view for Zeta Tauri (magnitude (V) $\sim$ 3, spectral type Be) in MII. The left plot shows the pixels which show an unusual high output of the direct current (DC) and therefore trace the bright star. The right plot shows the pixels marked by the star-removing algorithm. The pixels affected by the star (top right) are precisely traced. Furthermore, it can be seen that not every pixel among those is affected equally strong by the star. In addition, one finds several single pixels being marked by the algorithm. These are either broken pixels (marked red) or noisy pixels (isolated pixels marked blue to yellow) The color scale in the plots gives the fraction of events where the pixel has been marked *unsuitable*.

6.1.2 Calibration and data preparation

During the first steps of the data processing the individual telescopes are treated separately. MAGIC data are divided into runs (pointing/wobble positions) and sub-runs. Each sub-run is one data-file. The length of each file is limited by the physical size of the data file and results in ~ 2 minutes observation time for one MI star-file and ~ 1 minute per MII star-file. The shorter observation time per sub-run in MII results from the roughly double amount of pixels in the MII camera compared to MI. The calibration of the data is performed automatically by the ONSITE analysis (OSA) on a daily basis. This process includes not only the calibration in phe but also merges the reports of all subsystems (pointing, weather station, cameras, DAQ's, trigger) into the data stream and changes the raw data format to files in *root-format*. The MAGIC analysis and reconstruction software (MARS, see Moralejo et al. 2009 for details) is based on the C++ framework *root* (http://root.cern.ch) . From calibrated files on, all further steps of the analysis deal with files in the *root-format*. The centralized handling of raw data ensures on the one hand a high quality of the calibration, on the other hand the ONSITE computer facilities can easily deal with the large amount of physical space needed to handle raw data. In a ~ 7 hours night, the system accumulates ~ 1.3 TB of raw data. The calibrated files use only about 10% of the same hard-disc space and are therefore much easier to handle. The next step in the analysis is the image cleaning and event parameterization. In this step each event is checked to be a possible shower image and the individual signals of all pixels belonging to the shower are used to characterize the event. This task is performed by the program STAR which also includes the star removing algorithm. A description of this will be given below in Chapter 6.2. At this stage it is important to know that the total amount of charge contained in each event (SIZE) measured in phe is one of the calculated parameters. STAR files still contain all the information of the subsystems but do not longer contain individual pixel information. They occupy only $\sim 5\%$ of the hard-disc space used for calibrated files. Since all settings used in STAR rarely need changes of the user (exceptions are observations under strong moonlight/twilight), the onsite analysis performs automatically the *starification* of all data with the standard settings. The standard user starts the data analysis with STAR files which reduces the CPU time for each analysis and the individually needed storage to ~ 0.9 GB per hour of data.

6.1.3 Data quality

The first step in the data analysis is the check of the data quality. Every user has several options to determine the data quality. The three major sources are:

- The runbook
  (a documentation during the data taking, provided every night by the shift crew)

- The daily-check
  (a number of standardized test-runs on a daily basis over all data taken the night before)

- The data themselves

The information in the runbooks covers technical problems occurred during the observations as well as regularly updated information about the weather conditions and the trigger rates. This information is used to determine the general conditions during data taking and to identify

possible problems. The daily-check is executed off-line after OSA finished by the daily-checker on the calibrated/*starified* data and the results are provided to the collaboration. A series of pre-defined tests are performed for each telescope to ensure the correct functionality of all subsystems and the signal calibration. The main use of the daily-check is the fast spotting and identification of possible technical problems in the system. The quality of any given subsample of data can be checked by using the information inside the data themselves. Even though the data is taken as stereoscopic data the quality check has to be performed on both telescopes individually. One tool used in the collaboration to test the data quality and select between good or bad runs has been developed over the last years in the Max-Planck-Institute for Physics. A part of this work was dedicated to the upgrade and further development of this tool. The experience of many people, who have been working on many different sources over years allowed for a broad coverage of parameters and their possible dependence on the quality of the data. The final tool is based on a simple *root*-macro which operates on STAR files. In a first step the macro visualizes selected subsystem reports over the duration of the observations on a daily scale. In Figure 6.2 a typical output is shown.
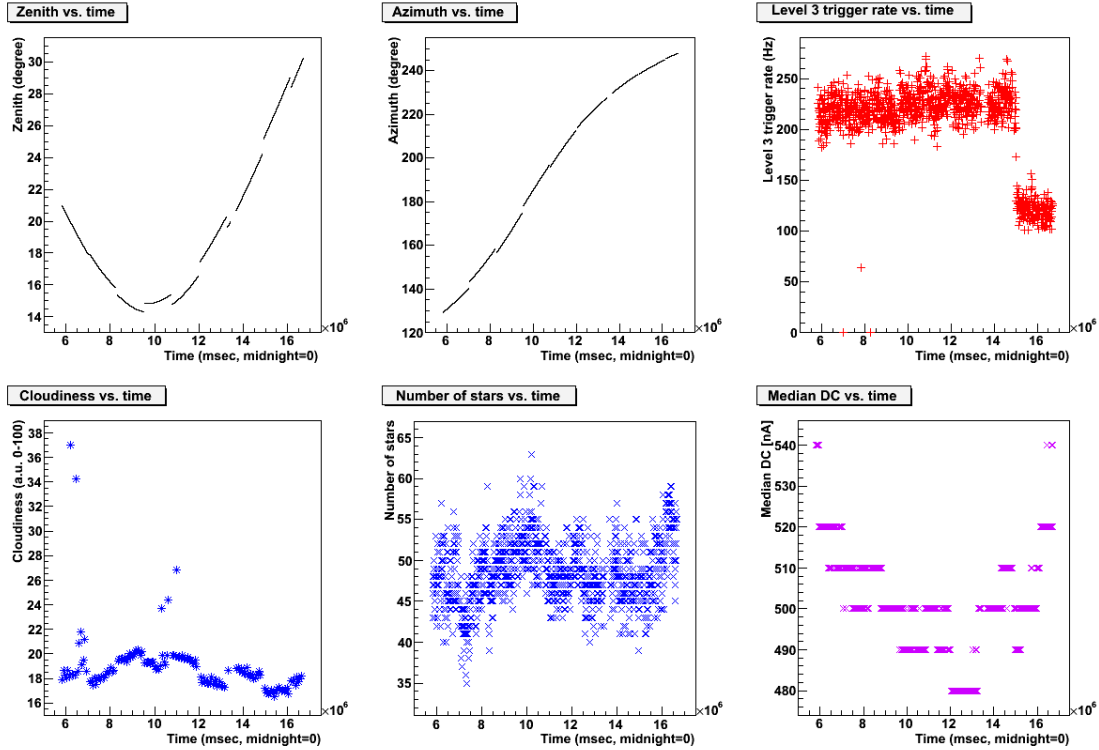
Figure 6.2: Example of a first look into the data to determine the data quality. Displayed are several subsystem reports as a function of the observation time. The data shown ($\sim$ 170 min. recorded with MII) was taken during June 2010 on the object W51 close to the Sagittarius arm of the Milky Way. The drop in the level 3 trigger rate seen at the end of the observation was caused by a technical problem connected to the receivers.

The displayed parameters are:

- pointing position in zenith (Zd) and azimuth (Az) over time

- Level 3 trigger rate

- Cloudiness,
  a measurement of the night sky temperature, calibrated to trace clouds and normalized to values between 0 (no clouds) and 100 (full cloud coverage).

- Number of stars,
  traced by a camera monitoring the field of view and calibrated with a bright star catalog.

- Median direct current (DC),
  of the anode in each PMT, averaged over the inner pixel ($\sim$ trigger region) of the camera.

Every subsystem sends one report at least every 30 seconds. These plots allow the analyzer to obtain a first impression of a given data set, like the Zd/AZ range, the stability and value of the trigger rate, an estimate of the weather conditions (cloudiness and number of stars), and information about the sky brightness (median DC) during the observations. The data selection is based on the time averaged parameters per sub-run.

Observation conditions For the judgement about the data quality one has to first determine the observation conditions between dark or moon/twilight data. Since the high voltage settings used for the PMT's of the camera(s) are constant from day to day, the median DC value can be used to determine the brightness of the night sky. It should be noted that the median DC can vary depending on the star field or the weather conditions. However, in case of dark nights with reasonable weather conditions the DC values are below 1000nA and 800nA for MI and MII, respectively. All data in this work are taken under dark conditions defined by this limits.

Weather conditions The MAGIC weather stations monitors the humidity, temperature, wind-speed, and cloudiness during the data taking. Both, wind speed and humidity, determine mainly the limits under which safe observations are possible. If data have been taken the main interest of the analyzer is to know if the sky was clear or cloudy. A cloudy sky will absorb/scatter great parts of the produced Cherenkov light and therefore shift the energy threshold to higher values and cause a shift in the detected light versus produced light distribution. In the worst case of strong clouds almost no Cherenkov light is observed at ground. The Cloudiness parameter is used as a first indication. This parameter is based on a temperature measurement of the night sky using a pyrometer. An empirical formula is applied to translate the measured temperature in the Cloudiness parameter which ranges between 0 and 100. In general, Cloudiness values above ~ 50 indicate a not absolute clear sky while values above $\sim 60 - 70$ are only found in very cloudy nights. In addition to the Cloudiness parameter the amount of identified stars in field of view is also a strong indicator for a clear sky. Here both Telescopes are equipped with a star-guider-camera, monitoring the field of view. The main purpose of the star-guider-camera is the monitoring of the pointing position by the use of cross-correlations between the observed star-field and the absolute star

positions taken from catalogs. However, the amount of stars can also indicate clouds. The absolute number of stars depends strongly on the observed star-field and here the number of stars should be compared to high quality observations of the same field of view. A minimum of ~ 30 stars for a field of view in the galactic plane should be observed in any case.

Data selection The final selection should provide data of constant and high quality. The selection criteria used throughout this work are based only on dark data. A minimum of 30 visible stars and a maximum cloudiness of 60 are required. Both cuts on the weather parameters have been chosen very loose. To guarantee a high quality of the selected sub-runs the main selection is based on the trigger rate of events with a minimum SIZE of 50 phe (rate50). Additionally, the L3 trigger rate has been required to be $\approx 200-250$Hz. The amount of accidentals in the trigger rate is however not constant due to the DT changes of the IPRC. The rate50 instead contains the information about how many real showers above a given SIZE are recorded and is therefore not affected by accidentals which would not survive the image cleaning. This cut on the rates is based on the principle that the recorded background rate should be constant to warranty the same observing conditions. A constant background rate is expected because the main background is due to CR induced air showers. The CR flux can be assumed to be fully isotropic and constant. As described in Chapter 2.1 the CR spectrum can be well described by a power law of the form $\sim E^{-2.7}$, where E is the energy of the particle. A change in the observing conditions (i.e., by clouds) will produce a shift in the threshold and thus lead to a lower rate of recorded background showers. The minimum SIZE above which the rate is calculated was chosen to be 50 phe as this will also be the minimum allowed SIZE for the later analysis. Lower SIZE events are more strongly affected by any kind of systematic uncertainties (i.e., different star field, Zenith, temperature of the electronics, small changes in the weather conditions). As an additional test the rate100 has been also checked, in any of the data used in this work the changes seen in the rate50 are also seen in the rate100. The rate50 cut is also very sensitivity to possible technical problems.

Throughout this work the allowed rate50 margin was $\approx 90-120$ Hz. In case of MII the allowed rate is slightly lower due to the 10% dead-time in DRS2 read-out system, not existing in MUX read-out. More than 95% of all rejected data in this work have been rejected based on the rate50 cut. As an example the selection cuts have been applied to the data set above and the graphical output of the data-check-macro is shown in Figure 6.3. The break down of the rate50 for the highest runs was connected to a technical problem connected to the receivers. Besides the graphical output the macro also provides some information about the total amount of selected/non-selected runs and observation times. The user can choose between different cut criteria (level 3 trigger rate, rate50, rate100, cloudiness, stars, DC). The above described quality selection is performed for both telescopes individually on a daily basis. All files surviving these criteria are kept for the further analysis.
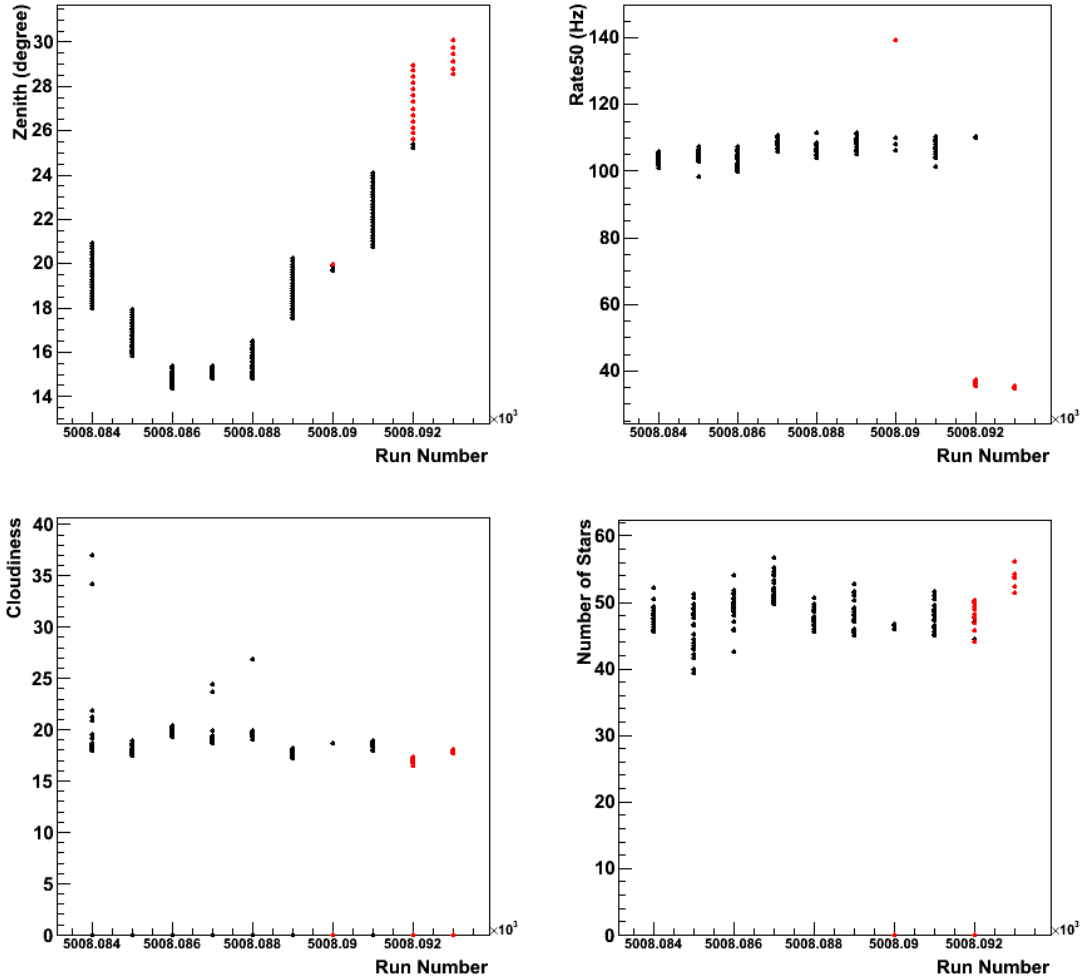
Figure 6.3: Example of the graphical output of the data-check-macro after applying selection cuts. The same data as in Figure 6.2 were used. Every data point is obtained as the average value per sub-run. Several subruns appear as a line perpendicular to the run-number axis. Black data points have been accepted, sub-runs with red data points will be removed from the sample.

6.2 Event parameterization

After the data calibration the next step in the analysis is the so called image cleaning. Here pixels which belong to a shower image are separated from those which contain only noise. Only pixels which contain signal connected to the shower image are kept, all others are removed from the further analysis. Figure 6.4 illustrates different aspects of the image cleaning from the raw signal to the cleaned image.

RAW IMAGE

CLEANING LEVELS

ARRIVAL TIME

CLEANED IMAGE
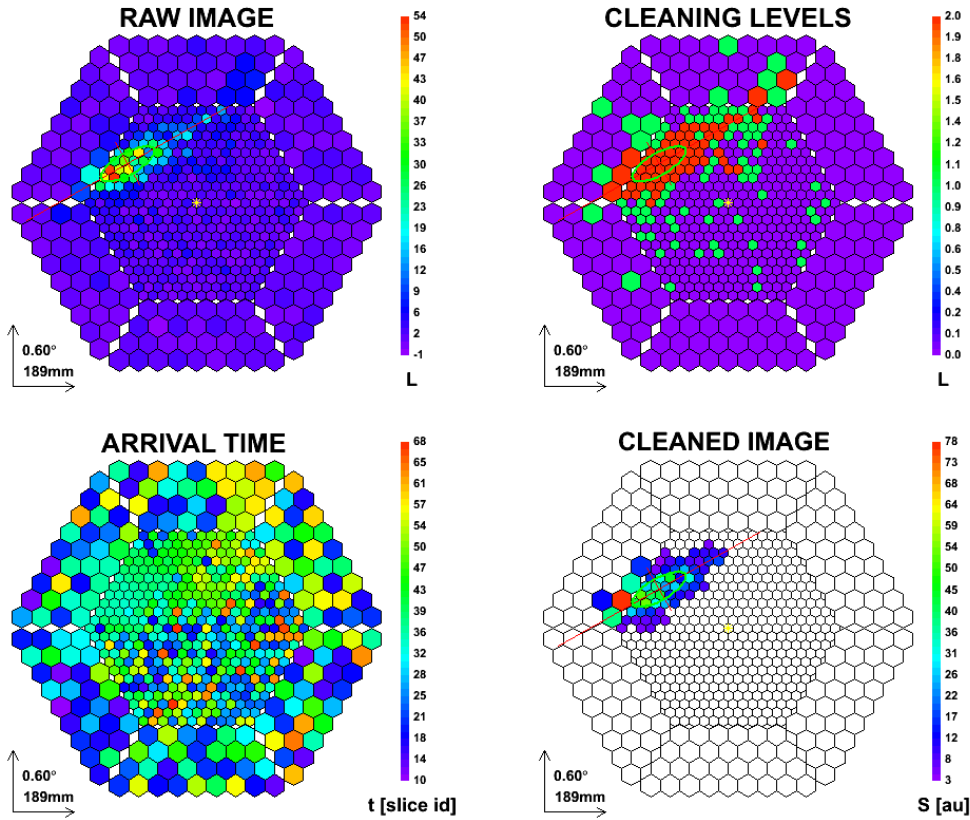
Figure 6.4: Example of the standard image cleaning on an example event in MI. Top: The left plot shows signal in each pixel. On the right the pixels which are above the cleaning thresholds are shown. Pixels above the level-1 threshold are marked in red, pixels above the level-2 threshold appear in green. Bottom: The Arrival time distribution is shown on the left. The resulting cleaned image is displayed in the lower right. The minor and major axis are indicated by the red lines. The Hillas ellipse is indicated in green.

The standard cleaning in MAGIC is a two-level cleaning including the arrival time information for each individual pixel. Two absolute thresholds level-1/level-2 in units of phe are defined: 6/3 for MI and 9/4.5 for MII[1]. First, all pixels above the thresholds are determined. Any pixel which is above the level-1/level-2 threshold is a *core/boundary-pixel-candidate*, respectively. A pixel which survives the cleaning is a *core-pixel* if the contained signal is above the level-1 threshold, it has at least one neighboring *core-pixel*, and its arrival time is not more than 4.5 ns off from the average arrival time of all *core-pixels-candidates*. To survive as a *boundary-pixel* the pixel has to be above the level-2 threshold, the pixel has at least one neighboring *core-pixel*, and the arrival time difference to the average arrival time of all neighboring *core-pixels* is less than 1.5 ns. Events without any surviving pixel after the image-cleaning will be completely removed. The cleaning can be understood as both, the search for shower images

---

[1]The higher cleaning levels in MII arise from the higher light collection efficiency and thus also a higher level of background light

and a first level of characterization for the possible shower.

SUM-cleaning   A new cleaning algorithm dedicated to improve the low-energy analysis is currently in the commissioning phase. The method is called SUM-cleaning and was presented to the community in 2011 by Lombardi et al. (2011). In this method the signal of every pixel is clipped above a certain maximum. For every 2NN, 3NN, or 4NN combination of pixels the sum of the clipped signals within a sharp time constrain (~ 1 ns) has to overcome a predefined threshold. As an example the conditions for 3NN combinations are: Every pixel is clipped above 1.365 phe, for a valid combination the sum of three neighboring pixels has to be above 3.9 phe within a maximal arrival time difference of 1.2 ns. Only pixels which are part of at least one valid combination will be kept. After the SUM-cleaning the standard cleaning is applied on all remaining pixels with reduced threshold levels (preliminary default: 4/3 for MI and 7/4 for MII). SUM-cleaning shows better performance at the lowest energies ($< \sim 150$ GeV) and compatible performance at all other energies. At this stage the improvement due to SUM-cleaning is clear below 100 GeV Zanin (2011). In this work SUM-cleaning was used to analyze the data of HESS J1857+026.

6.2.1 Single telescope parameters

The remaining images after the cleaning are used to calculate the image parameters for the individual telescopes. All images are parameterized by means of an ellipse, following greatly but not exclusively the definition by Hillas (1985). In the subsequent analysis all images are only described by their parameters. Both, cleaning and the image parameter calculation, is performed by the MARS executable *Star*. Additionally, the zenith and azimuth angles (Zd, Az) of the telescopes and arrival-times are obtained. The main ones are illustrated in Figure 6.5 and all single telescope parameters used in the analysis are listed below:
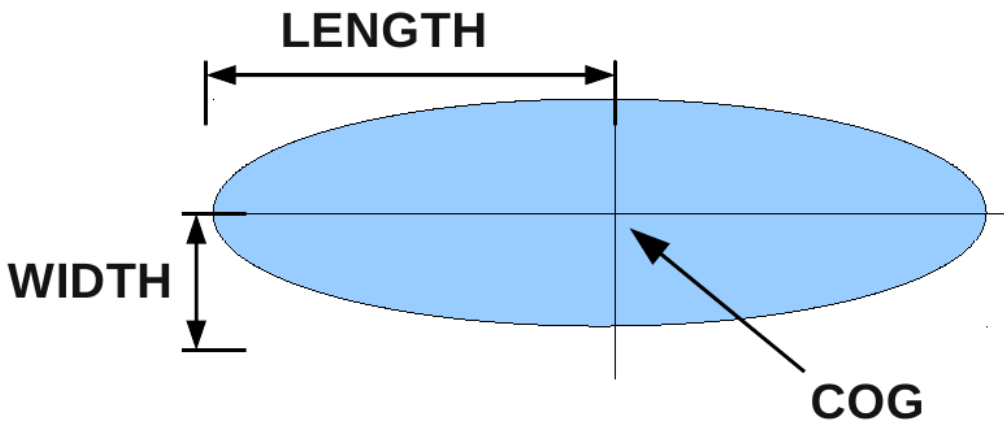
Figure 6.5: Illustration of the Hillas ellipse and the shower parameters: WIDTH, LENGTH and Center of Gravity (COG).

- SIZE
  total amount of charge (phe) contained in the image. This parameter is strongly corre-
  lated to the energy of the shower and therefore also to many other image parameters.

- WIDTH
  second moment of the charge distribution along the minor axis

- LENGTH
  second moment of the charge distribution along the major axis

- COG
  Center of gravity of the image

- ISLANDS
  number of isolated clusters in one image

- TIME-GRADIENT
  The arrival time distribution is projected on the major axis of the event and fitted by a
  first order polynomial. The slope of the function is defined as the TIME-GRADIENT.

- LEAKAGE (1,2)
  Is defined as the amount of signal contained in the outer most (two outer most) pixel
  ring(s) of the camera, divided by SIZE of the image. The parameters allow to estimate
  if the complete image was contained in the camera or not.

6.2.2 Stereoscopic parameters
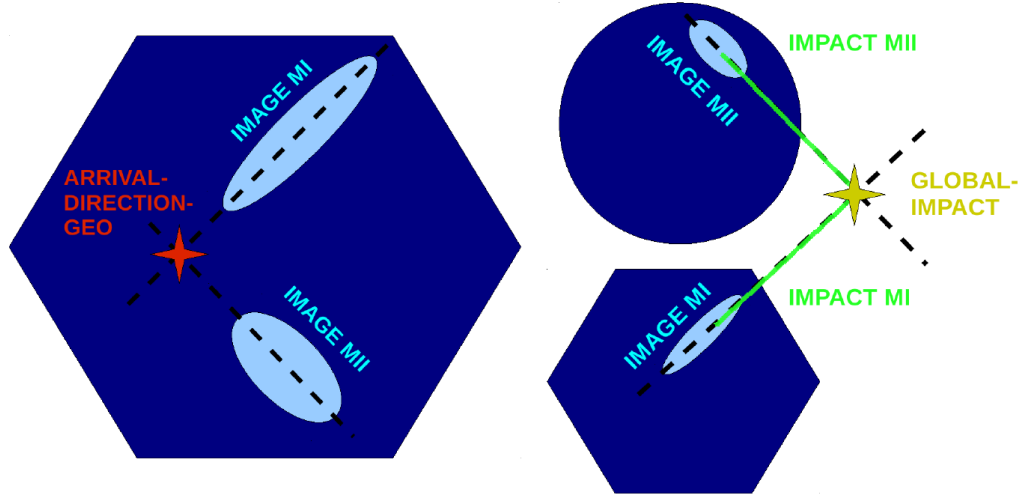
Figure 6.6: Illustration of the geometrical reconstruction of the stereoscopic parameters
GLOBAL-IMPACT and ARRIVAL-DIRECTION.

The next step is the combination of the individual telescope information and the calculation
of the stereoscopic parameters. For this purpose the program *Superstar* is used. Every event

holds a unique stereo trigger number to trace associated events. *Superstar* combines the information of both telescopes for each stereo trigger number. Events which appear in only one telescope (i.e., due to dead-time reasons or removed sub-runs in the data selection) are removed from the further analysis. The information of all individual sub-runs is combined to one output file per run (~ 20 minutes of observations, one pointing/wobble position). The stereo parameters calculated in *Superstar* are obtained based on pure geometrical considerations and are listed below:

- ARRIVAL-DIRECTION
  The reconstructed arrival direction obtained from crossing the major axis of the individual shower images

- GLOBAL-IMPACT
  crossing point of the shower-axis in the plane perpendicular to the pointing direction. It describes the virtual impact point of the primary in the plane perpendicular to the pointing direction.

- IMPACT
  Distance from the telescope to the impact point of the shower in the plane perpendicular to the pointing direction.

- HMAX
  Height of the shower maximum above the Telescopes

- CHERENKOV-RADIUS
  The radius of the Cherenkov light emitted by an 86 MeV electron at the shower maximum measured in the Cherenkov light plane perpendicular to the telescope pointing direction at ground level.

- CHERENKOV-DENSITY
  The photon density on ground in the CHERENKOV-RADIUS produced by a single 86 MeV electron at HMAX.

6.3 Event reconstruction

After *Superstar* every image of every event is described by its single telescope (each parameter twice, one for each telescope) and stereoscopic (stereo from now on) image parameters. The further determination of the physical event characteristics (type, energy, and arrival direction of the primary) is based on these image parameters. At this part of the analysis the use of MC simulations is needed to access the expected image parameters of gamma-rays and their dependence on the energy and arrival direction. In addition, one also needs MC simulations of CRs (from now on hadrons) since their shower development and therefore the resulting images and their parameters can significantly vary from those of gamma-ray showers. Indeed, to determine some basic characteristics of the instrument like the energy threshold hadronic simulations have to be taken into account. In the standard analysis however, such simulations are not used for two reasons:

1. Hadronic simulations are not necessarily needed in the γ-ray analysis; as most of the recorded events are CR's and represent therefore a direct measurement of hadronic showers.

2. The simulation of hadronic showers is much more challenging and time consuming due to the much higher multiplicity of the possible interactions. The relatively high transverse momentum can develop sub-showers which are detectable even if the impact of the main shower is several km away and therefore simulations to large distances and extremely high energies are needed to produce a representative sample of hadronic MC. In addition, the systematic uncertainties of the cross-sections and branching ratios increase with increasing energy.

Since the aim of the final analysis is to determine the properties of γ-ray-sources the first step of the event reconstruction is the identification of the primary particle. In this step a new parameter called *hadronness* will be assigned to each single event.

6.3.1 Identification of the primary particle
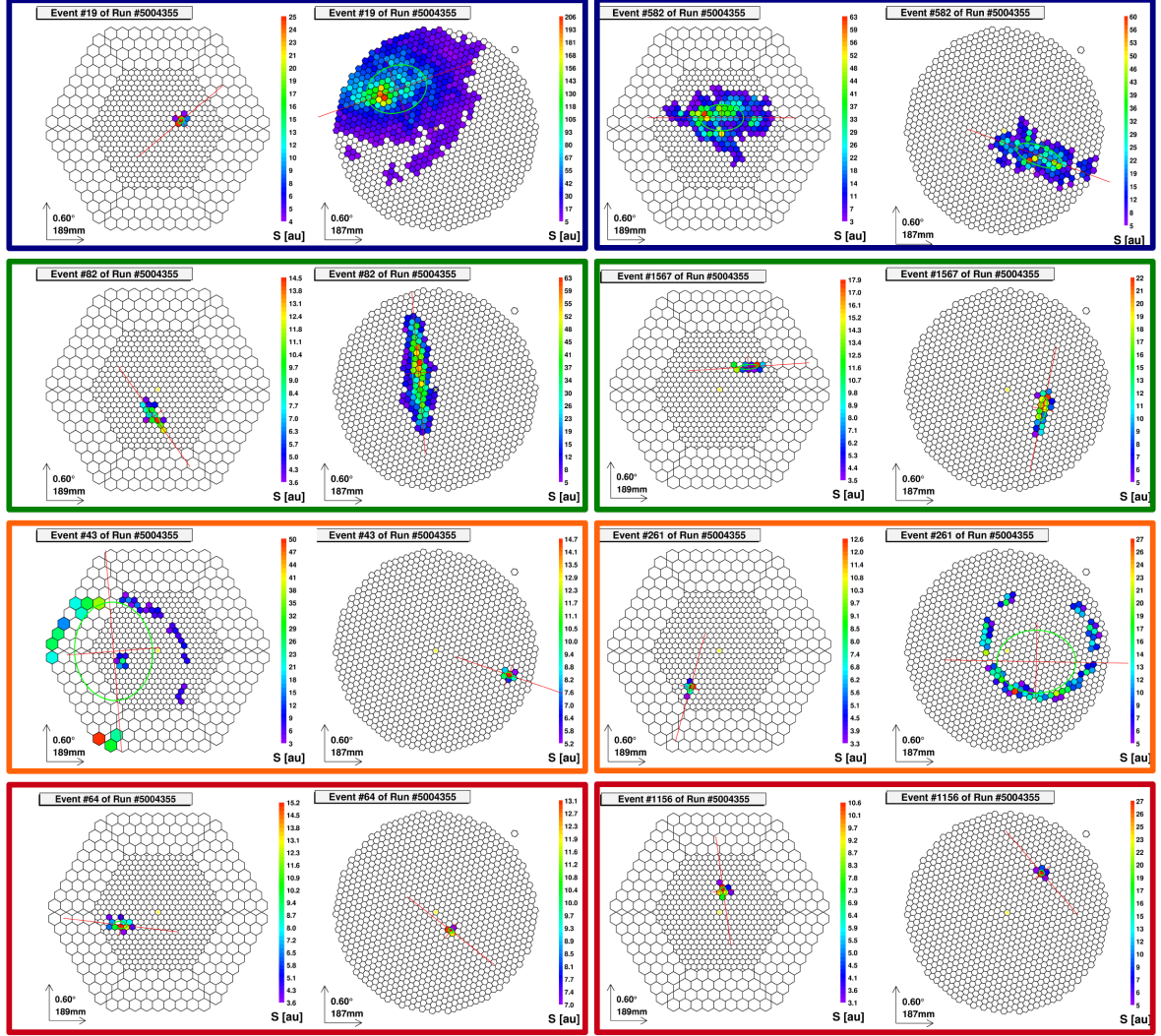
Figure 6.7: Selected examples of real stereo events, recorded with MAGIC seen by the individual telescopes. The blue framed events are hadronic candidates, the green ones are gamma-candidates, the orange ones are muon-candidates, and the red framed events represent events where the identification is not obvious. The events have been hand selected and classified by eye.

Figure 6.7 shows eight selected examples of real stereo events recorded with MAGIC. The events can be divided in four classes from top to bottom: hadron-candidates, gamma-candidates, muon-candidates, and *unknown*-candidates. The main characteristics of the individual shower classes can be described as follows:

- **gamma-rays**
  Gamma-ray showers are almost purely dominated by the electromagnetic interactions

of electron-positron pair creation and Bremsstrahlung. Since both interactions are two-body processes and the mass of the electron is negligible, a high transverse momentum is suppressed by the law of momentum conservation. This results in a very regular and elliptical shape of gamma-ray showers and their images.

In the left example (see green framed events in Fig. 6.7) of a gamma-ray shower the elliptical and regular shape can be easily recognized in the image of MII. The MI image is much smaller indicating an IMPACT of the shower much closer to MII, still the elongated shape of the image can be suspected. The images of the right hand example show a regular elliptical shape in both cases. The similar SIZE indicates an similar IMPACT to both telescopes. Especially for small images (low energy or high impact) it is however not trivial to determine regularity of elongation of a given image.

- **muons**
  As described in Chapter 5.3, close-by muons appear as ring shaped images in the camera. Far away muons will however, not produce rings but small arc-like images. For muons already several tens of meter impact have to be considered as *far away*.
  The two examples of stereo muons (see orange framed events in Fig. 6.7) show that if a muon produces a ring in one telescope it is already so far away from the second telescope that it here will appear only as a very small event. For the remaining analysis muons will not be treated individually from all other kind of **hadrons**.

- **hadrons**
  The high transverse momentum of hadronic interactions can produce sub-showers (similar to jets in particle physics). This is seen as an irregular image shape or an image containing multiple islands. If an irregular shape of the image and/or multiple islands are observed the event is most likely of hadronic nature. However, the observed shape of an image depends on the orientation of the shower to the telescope, the energy and impact of the shower, as well as the individual shower itself. In particular, hadronic showers suffer from strong shower to shower fluctuations caused by the high multiplicity of the possible interactions. In addition, hadronic showers can develop purely electro-magnetic sub-showers over the production and subsequent decay of π^0-particles. In case only this sub-shower is observed by both telescopes a separation from real γ-ray showers is highly challenging.
  The right hand example of the hadronic shower (see blue framed events in Fig. 6.7) is a good example of the irregular image shape. The dependence of the irregularity on the observing angle and impact can be seen as the different appearance of the image in the individual telescopes. For example in MII the image shows two islands while in MI only one island is observed.
  The left hand example can be explained in the sense that a hadronic shower impacted close to the MII telescope but far away from MI. Here MI observes only a tiny sub-shower while in MII the observed shower fills half of the camera.

- ***unknown*** The last class of events are those where an obvious classification is not possible. For this cases a classification can only be achieved by means of statistical methods. In most cases the event classification is difficult due to the extremely small SIZE of the images. In such cases the shape of the images is difficult to define because the amount of detected light was so low that only very few pixels contribute to the image. Here,

one has to consider that the image could appear irregular simply because of statistical fluctuations in the light detection or because the shower really showed intrinsic irregularities.

The red framed images in Figure 6.7 show two examples of such events. Both events could be far away muons, small hadronic showers, small sub-showers of a larger hadronic shower, or small SIZE gamma shower. It should be mentioned that for extremely high SIZE showers similar problems appear if the images are not well contained in both cameras.

It is noted that most of the events show a similar SIZE in both telescopes and the above selected events are only examples and do not represent all possible images. However, the examples have been choosen to show some generic features of the individual shower classes. In addition, the selected examples (especially the left hadron-candidate, the left γ-candidate and the μ-candidates) show how important the stereoscopic observation can be for the event classification.

γ-hadron separation

For the standard analysis one of the main questions is: *Is the event a gamma or not, and how sure is the classification?* This step is called: gamma-hadron separation. In one hour of data, MAGIC accumulates around 4×10^5 events which survive the image cleaning. Already the amount of recorded events requires a numerical tool for the gamma-hadron separation. In addition, the classification is not always obvious, as shown above, and has to be achieved using a statistical approach. In MAGIC the gamma-hadron separation is performed using the random forest (RF) method (Albert et al. 2008). The RF is a mathematical tool to separate two distinct populations based on randomly chosen cut-parameters but optimized cut-values.

Figure 6.8 illustrates the working principle of one tree of a random forest. Each tree starts with two samples of events. The samples contain only events of type-a or type-b. The events are described by a series of parameters. In each node n parameters are choosen randomly (number of trials). For each of the parameters a optimum cut value is determined. The optimum cut value is defined by maximizing the separation of different types of the events. This is achieved by minimizing the so called GINI-index (Q_{GINI}). The mathematical definition is given by:

$$Q_{GINI} = 4 \cdot \frac{N_\gamma}{N} \cdot \frac{N_H}{N} = 4 \cdot \frac{N_\gamma \cdot (N - N_\gamma)}{N} \tag{6.1}$$

where $N = \#$ events, $N_\gamma = \#$ gammas, $N_H = \#$ hadrons. Only the cut with the minimum Q_{GINI} is applied. The procedure is repeated till only pure samples remain or a minimum allowed number of events (final node-size) is reached in each node. Strictly speaking the Q_{GINI} index is only a valid measure of the separation power in the case of uncorrelated parameters. In case of correlations it can be used as an approximation, however, the average GINI-index determined over one tree for each parameter does not directly reflect the separation power of this parameter. It does more give an estimate of the separation power for each parameter in combination with all other parameters.
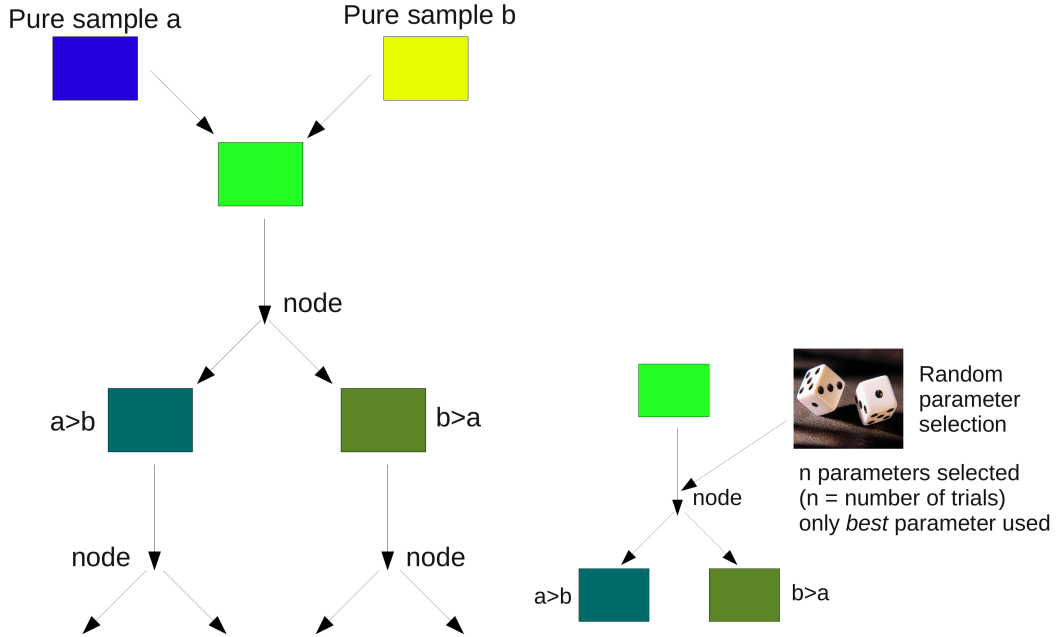
Figure 6.8: Schematic view of one RF tree. Two samples of events, one only containing type-a events and one only containing type-b events are mixed. Every event is described by a series of parameters. At each node n of the available parameters are randomly selected. For each parameters the cut value with the highest separation power is determined. The *best* separating parameter is chosen and the sample is divided according to the previously determined cut. The procedure is repeated till only pure samples remain or a minimum allowed number of events (final node-size) in each node is reached.

For every final tree a number is assigned to each final node: 1 if only events of type-a are found in this node, 0 in the case of only type-b events and for a mixture of events the average value is calculated (i.e., two type-a events and one type-b event would give 2/3). The forest originates by growing multiple trees (default: 100). The creation of the RF is the so called *training*. Later the RF is applied to the data (and MC). The *hadronness* is defined for each event by the average number obtained from all final nodes which contained the event. A hadronness of 1/0 is obtained if the event always ended in a pure hadron/gamma final node. By averaging over multiple trees (and final node-size values > 1) the hadronness ranges between 0 and 1.

The training is performed using so called train samples. To avoid a bias they will not be used in the further analysis. The train samples consist of MC gamma simulations and of source free real data (either taken on a dedicated dark patch or from observations where no signal has been found in a previous analysis). The real data are strongly dominated by hadronic showers and therefore represent a hadronic sample.

The following parameters are the standard parameters used in the RF to separate γ's from hadrons:

- $SIZE_{1,2}$ (one per telescope)

- $LENGTH_{1,2}$

- $WIDTH_{1,2}$

- $TIME-GRADIENT_{1,2}$

- $IMPACT_{1,2}$

- HMAX

- Zd

Not all of this parameters have the same separation power. For example SIZE and Zd do not have any separation power. SIZE is in first order an estimation of the energy of the primary and Zd is one of the parameters describing the pointing position of the telescope. However, both parameters can have strong effects on all other image parameters: For example a high SIZE image will have a larger WIDTH and LENGTH than a small SIZE image. Under high Zd observations the air shower has to travel longer distances through the atmosphere and the image is therefore stronger affected by absorption and scattering of the Cherenkov light. To account for this effects, SIZE and Zd have been included in the RF. To avoid systematic differences in the train samples caused by the use of this parameters (i.e., not the same Zenith distribution of data and MC) the train samples are re-sampled in average SIZE and zenith to start with two equal distributions. To account for never perfectly continuously agreeing distributions both parameters are used in binned quantities. To optimize the result of the training some pre-cuts on the samples are applied to remove noise events, events where the classification is clear, and events where the classification is extremely difficult. The pre-cuts used in this chapter[2] are:

- $SIZE_{1,2} > 50$

- $SIZE_{1,2} < 50000$

- $ISLANDS_{1,2} = 1$

- $LEAKAGE2_{1,2} < 0.2$

All events with a very low SIZE and a high LEAKAGE (extremely difficult to reconstruct), a very high SIZE (mostly rare artificial events), or containing multiple ISLANDS (hadronic showers) are from here on removed from the analysis. These pre-cuts remove about 68% of all events in the data and about 26% of all events in the MC. The gross of the removed events are those of very low SIZE and those with multiple ISLANDS. The default settings of the RF

---

[2]Note that due to the different size of the outer pixels in MI and MII the same cut translates into a tighter constrain for MII. However this will only slightly reduce the statistics at the highest energies. The analysis of the scientific data in this thesis was adopted for this feature and uses constrains of $LEAKAGE1_2 < 0.3$ and a $LEAKAGE1_1 < 0.15$.

training uses 100 trees, a final node-size of 5 events, and a number of trials equals 3. The final node-size of 5 events accounts for a possible contamination of the hadronic sample (i.e. rare diffuse gamma events) and small possible imperfections in the MC simulations of gammas, which both could bias the training. A trial number of three (out of possible 12 parameters) is chosen as a compromise between a random selection and the possibility to pick the best separating parameter. It has been empirically found (Albert et al. 2008) that the optimal number of trials is given by #trials = $\sqrt{\#\text{parameters}}$. The hadronness distribution obtained by applying the RF to a new set of MC (test-sample) and data is shown in Figure 6.9.
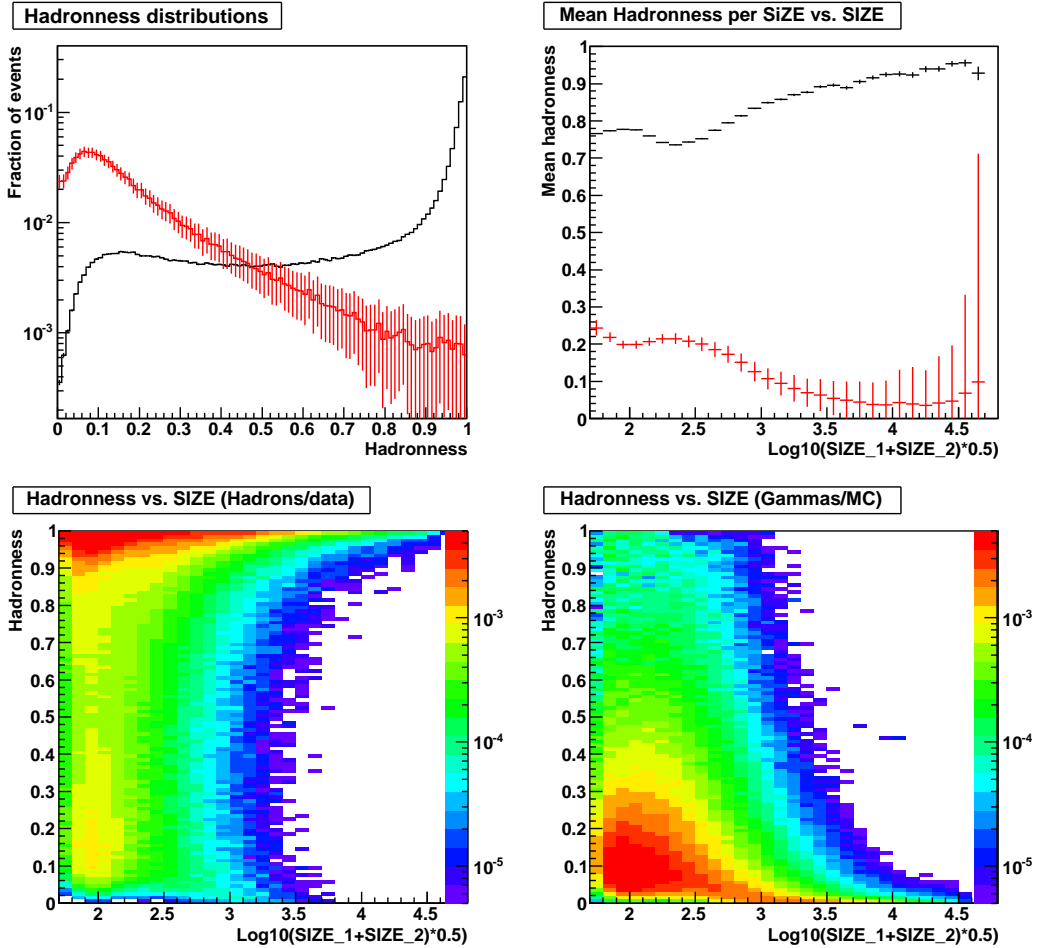
Figure 6.9: Top: Left the hadronness distribution of all events for real data/hadrons (black) and MC-γ's (red) is shown. The distribution is strongly dominated by low energy events ~ 100 GeV (the MC simulation has a slope of -2.6). On the right side the mean hadronness value as a function of mean SIZE is shown. The dip around Log10(mean SIZE)=2 is connected to the high muon rejection power of the HMAX-parameter. Bottom: Shown are the hadronness distributions for data/hadrons (left) and MC-γ's (right) as a function of the mean SIZE. Both distributions have their maximum close to 1/0, but (depending on the SIZE) show significant tails towards each other.

Even in the integrated distribution (see Fig 6.9 top left) dominated by low SIZES most of the hadronic events ($> 95\%$) are classified with a hadronness> 0.5 while most of the γ's ($> 95\%$) are classified as with a hadronness< 0.5. The mean hadronness per SIZE shows that the populations are distinct up to the highest SIZE. A clear dependence on the separation as a function of the SIZE can be observed. Even though the distributions are clearly distinct for all SIZES it should be noted that for typical gamma-ray source the amount of recorded gamma-candidate events is usually 3 to 5 orders of magnitude lower than the amount of recorded hadron-candidates. Therefore, only a small fraction of mis-classified events can have strong impact on the final sensitivity of the instrument. Besides the gamma-hadron separation, the strongest tool to suppress the background is the angular resolution, which allows to determine how many events arrive from a given position in the sky.

6.3.2 Arrival direction estimation of the primary

For simple geometrical reasons one knows that the arrival direction of the primary lies on the major axis of the image. By crossing the major axis of the images in both telescopes (projected in the same camera coordinates) one therefore obtains a reasonable estimate of the arrival direction (see Fig. 6.6). This method has two disadvantages. The first is given in the case of nearly parallel major axes of the images. In such a case a small change of the angle between the two major axes will have a large effect on the reconstructed arrival position. The second disadvantage arises from the fact that the major axis is difficult to determine in case of small images. In the geometrical reconstruction one mis-reconstructed major axis can have a large effect on the estimated arrival direction. To overcome these uncertainties MAGIC uses the so called DISP-method (Domingo-Santamaria et al. 2005). DISP is defined as the angular distance between the COG of the image and the reconstructed arrival direction along the major axis (see Fig 6.10). It can be derived as a function of the image and stereo parameters. Depending on the elongation (LENGTH/WIDTH), IMPACT, TIME-GRADIENT, and HMAX of the image the angular distance between the COG of the image and the arrival direction can vary. The determination of the DISP is again performed by using the random forest method and is therefore also called DISP-RF. Similar to the case of the γ-hadron separation the SIZE and Zenith is also included in the RF. In contrast to the RF training explained in the last section in this case only MC-γ's are used to train the DISP-RF. One DISP-RF is trained individually for each telescope. To improve the reconstruction each DISP-RF uses also image parameters from the other telescope and stereo parameters in the training. The parameters used in the training for telecospe j are:

- $\text{SIZE}_{1,2}$
- $\text{TIME} - \text{GRADIENT}_{1,2}$
- $\text{IMPACT}_{1,2}$
- HMAX
- Zenith
- LENGTH_j
- WIDTH_j
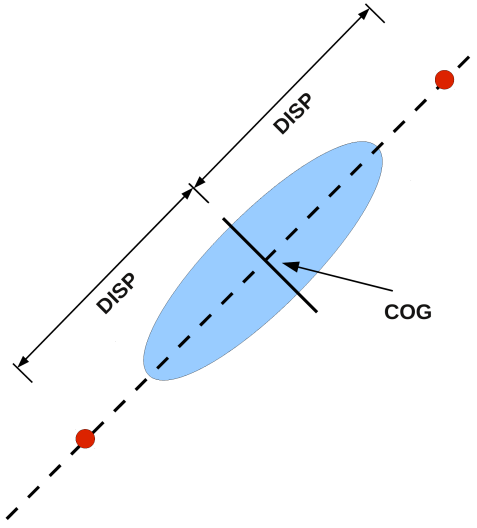
Figure 6.10: Sketch of the DISP parameter which is defined as the angular distance between the COG of the image and the reconstructed source position along the major axis of the image. As can be seen the parameter offers two symmetrical solutions around the COG of the image for the reconstructed source position.

The training uses the same pre-cuts and RF settings as in the case for the γ-hadron separation. As it can be seen in Figure 6.10, the algorithm provides two symmetric solutions per telescope for each image. This results in a total of four possible arrival directions for each event. For each of the possible 4 combinations the angular distance between the reconstructed positions is calculated. The combination with the minimum distance is chosen if the discrepancy is smaller than 0.05°. Events where no combination fulfills this criterion are marked as non valid reconstructed and will be removed from the further analysis. Since the training was performed on and is therefore optimized for MC-γ's the method results more often in a valid reconstruction for γ's than for hadrons. In addition, for hadronic showers it can happen that each telescope sees a different part of the shower (i.e., main shower and sub-shower or two different sub-showers) which would result in two different reconstructed positions. Therefore, a non valid Disp reconstruction can point to a hadronic event.

The final reconstructed source position is calculated by the weighted average of the selected combination. As weight the amount of pixels contained in each of the two individual image is used. The achieved angular resolution using this method ranges from $\sim 0.1°$ to $\sim 0.05°$ between 100 and 1000 GeV and is shown in Figure 4.8. In the framework of the arrival direction reconstruction in the DISP method also the IMPACT parameters are recalculated. The newly obtained values will be used in the energy reconstruction.

6.3.3 Energy estimation of the primary

The energy reconstruction is based on look-up-tables (LUT's) produced from MC γ's. These LUTs are based on a simplified analytical description of the air shower. Below the critical

energy $\epsilon_{\text{critical}} = 86$ MeV of an electron/positron the energy losses are dominated by ionization and not anymore Bremsstrahlung. Thus, the maximum amount of particles in a given shower is reached when all electrons/positrons reached the critical energy and can be estimated as $N_{\text{particles}} \propto E/\epsilon_{\text{critical}}$. Following this description the energy of the primary γ can be parameterized assuming that all the Cherenkov radiation is produced from 86 MeV electrons at the shower maximum. The energy estimation can therefore be understood as the *effective* amount of 86 MeV particles N_{eff}^{86} needed to produce an image of a given SIZE. The correlation between the image SIZE and the physical distance between the air shower and the telescope is decoupled in following steps:

- The IMPACT parameter is divided by the CHERENKOV-RADIUS to account for the physical distance of the shower (I/R).

- The SIZE is corrected for a possible LEAKAGE of the image outside of the camera.

- The corrected SIZE (SIZE$_{\text{corrected}}$) is divided by the CHERENKOV-DENSITY (S_c/C).

The final LUTs for the energy estimation are obtained by dividing a sample of γ-MC with known energy E_{true} in bins of (S_c/C) and (I/R). The mean in E_{true} of each bin gives the estimated energy E_{est} with the uncertainty given by the RMS of the distribution in each bin. The derived value is later corrected for different absorptions in the atmosphere depending on the zenith angle by an empirically determined correction factor. For each telescope one LUT is created. The final estimated energy is obtained by a weighted mean, where the weight is given by the uncertainty of each individual reconstruction. Energy resolution and bias produced by this method is shown in Figure 4.7.

6.4 Signal determination and flux calculation

The data and MC used for the training of the γ-hadron separation, the DISP estimation, and the energy reconstruction are only used for the *base-level-analysis* and are now removed from the further *high-level-analysis*. The obtained RFs and LUTs are applied to the data and to a yet unused set of MC, the so called test-sample. This is preformed by the MARS executable *melibea*. The output files (so called *melibea*-files) contain all the information of a *superstar*-file but in addition the hadronness, estimated energy, and reconstructed arrival direction for each event. For the signal determination cuts connected to all these three parameters are applied. The signal determination can divided in two sub-tasks:

- **Signal detection**
  is the pure search for a significant signal. A signal is defined as significant and a detection is announced if the signal shows a least 5σ, following the definition of Li & Ma (1983) equation 17, in two independent analyses.

- **Signal characterization**
  After a signal is detected the signal characterization determines the physical parameters like flux, differential energy spectrum, possible extension etc.

First, the signal detection will be described. There are two different methods used for the signal detection. One method can be interpreted as an imaging technique. Here, the arrival

directions of all selected events are used to build exposure maps of the field of view. After subtracting the background the resulting *skymap* can be interpreted as an image of the gamma-ray source. This method allows a fast scan of the complete field of view and also morphological studies of the emission. A more detailed description will be given later in this chapter in section 6.4.2. The more classical approach of a signal search uses an angular cut around a predefined (assumed) source position to determine the events arriving from the source region. A source free region of equal acceptance is used to determine the amount of expected background events. By building the difference of the two numbers a possible excess can de determined. This method is based on the so-called θ^2-plot.

6.4.1 θ^2 plots

θ is defined as the angular distance between the reconstructed source position and the real (or assumed) source position (see Fig 6.11). A restriction in θ is therefore the maximum allowed angular distance between the arrival direction of every event and a predefined position in the sky. The cut value is given by the angular resolution of the instrument and the extension of the source.
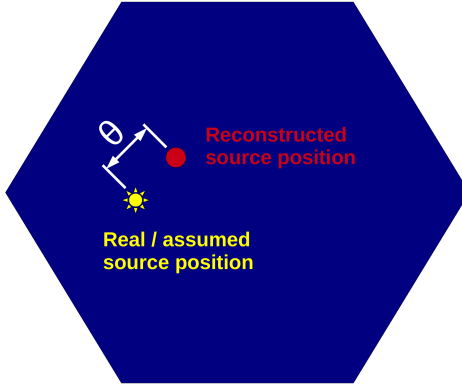
Figure 6.11: Sketch of the definition of θ as the angular distance between the reconstructed and assumed source position.

θ^2 is proportional to the integration area and therefore the background distribution as a function of θ^2 is flat in first order. The so called θ^2-plot shows the amount of selected events as a function of the θ^2-value with respect to the assumed source position. This will be called ON distribution. In addition, the same distribution is calculated for a known source free position in the sky showing the same effective acceptance (equal observation time, equal observation conditions, and equal trigger efficiency). This will be called OFF distribution. How to correctly choose the source free position for the OFF distribution was studied in detail as part of this thesis. A full description will be given in section 6.6.3. An example for a θ^2-plot obtained from data of the Crab Nebula is shown in Figure 6.12.
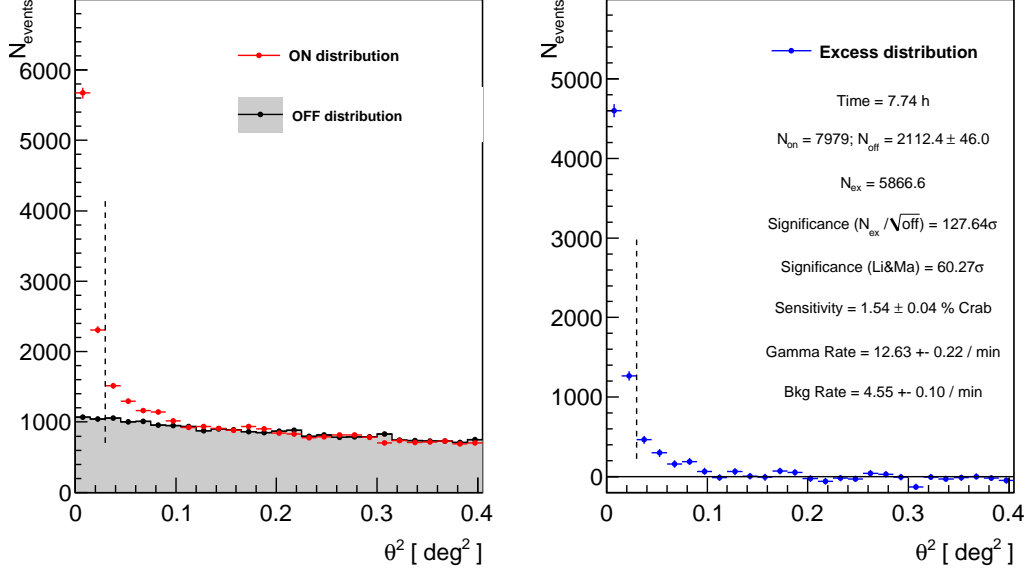
Figure 6.12: On the left hand side the ON and OFF distributions of the θ^2 for the Crab Nebula are shown. In addition, the right-hand side shows the excess distribution and some statistical properties within the signal region. The signal region is defined by a maximum allowed θ^2 and marked with the vertical dotted line. It should be noted that the agreement between the ON and OFF distributions for large values of θ^2 (away from the source) is mandatory as long as no other real gamma-ray source exists in the data set. Here $\sim$ 8h of data from the Crab Nebula have been used. The plots have been obtained by applying the reference analysis developed in this work (See Chapter 6.5). Besides the pre-cuts a hadronness-cut of 0.3 has been applied. An integration radius of $\theta^2 = 0.03 \text{deg}^2$ has been used. The energy threshold of the analysis is $\sim$ 100 GeV.

A clear increase of the excess towards small θ^2 values and therefore towards the source position can be seen. The shape of the excess is determined by the angular resolution of the instrument and the intrinsic extension of the source. In case of the Crab Nebula the source extension is much smaller than the angular resolution and therefore negligible. For larger θ^2 values the ON and OFF distributions agree as in both cases the distribution is completely dominated by isotropic background events. Using the background rate in the source region and comparing it to the rate50 of about 100 Hz the total amount of background in this analysis is reduced by a factor $\sim$ 1300. The advantage of the θ^2-plot as a tool to detect signals is based on a simple and fast algorithm which reduces an originally two dimensional problem to only one dimension. In addition the signal determination depends only on the number of ON and OFF events within the signal region and not on the shape of the distributions. The disadvantage lies in the need for an assumed source position, which is not always obvious (i.e., for extended sources, scans, or serendipidious discoveries). Furthermore possible morphological features of the source might be washed out by the reduction to one dimension. For the purposes of an unknown source position or morphological studies skymaps are used.

6.4.2 Skymaps

In MARS this task is performed by the program *caspar*. The reconstructed arrival directions of all selected events (after hadronness cut and a possible restriction to a range in estimated energy) are binned in sky coordinates (default: RA [h], DEC[°]). The result is the so called *exposure-map* and represents the ON (background+signal) distribution of the complete field of view. There are two methods implemented in *caspar* to estimate the background. In both cases two exposure maps are created by dividing the camera into two parts.[3].

- **Blind-map**
  is a background estimation where no assumption about the source position is needed. The two exposure maps are compared in each bin of sky coordinates and the bin with the lower content is used for the background estimation (OFF) the other for the ON. Since the lower of two gaussian distributed variables is biased by $-\sqrt{(\sigma_1^2 + \sigma_2^2)/2\pi}$ (half of the expectation value of the half-normal distribution that describes the absolute differences of the two bin entries), an upward correction is applied to each selected bin. It should be noted that in the case of a strong signal the bias-correction is wrong, as the lower entry is not biased anymore but simply not the entry containing signal and background. This results in a reduced sensitivity of this method

- **Wobble-map**
  is an algorithm where the half of the camera containing the expected signal is predefined. Usually the half containing the center of observations (coo) is defined as the ON and the remaining half will be used for the background estimation (OFF). The wobble-map method is the more sensitive skymap around the center of observations but is not useful for sources far away from the coo. For sources deviating less from the coo than the wobble distance (default: $0.4°$) there is no influence. In the case of much higher distances the blind map should be used.

Independent of the method to determine the background (wobble- or blind-map) the chosen events are used to build a background model. For each event in the ON distribution 200 events of the OFF distribution are randomly selected. This oversampling reduces statistical fluctuations caused by very low event numbers arising from the splitting the data in many bins. In addition, the oversampling removes fluctuations by averaging over many shower positions in the camera plane. The background model is obtained by re-normalizing the over-sampled distribution. This is first done by the known number of entries and afterwards by a direct normalization between the ON exposure map and the background model. Especially in the case of a strong signal the ON exposure map and the background model can show imperfections in the normalization. Since most bins do not contain a signal the distribution of $\log \frac{N_{ON}}{N_{background}}$ over all bins in the skymap is expected to peak at 0. The normalization value for the background model is given by means of Gaussian fit to the peak position. To account for systematic differences in the acceptance (see the section 6.6.3 in this chapter for details) the complete algorithm operates in bins of $\cos Dec \times Ha$ (where Ha is the hour angle). During the usual data analysis the blind map option is used as first analysis step to determine the

---

[3]This method relies on the wobble observation mode and a full sky coverage of the same field of view by both camera parts. This is usually achieved by using two wobble positions symmetrically separated by $180°$ around the center of observations. For more details see Chapter 6.6.3

possible source location. The final analysis is usually done with the wobble map option. An example for an ON, background, and excess map (using wobble map) is shown in Figure 6.13.
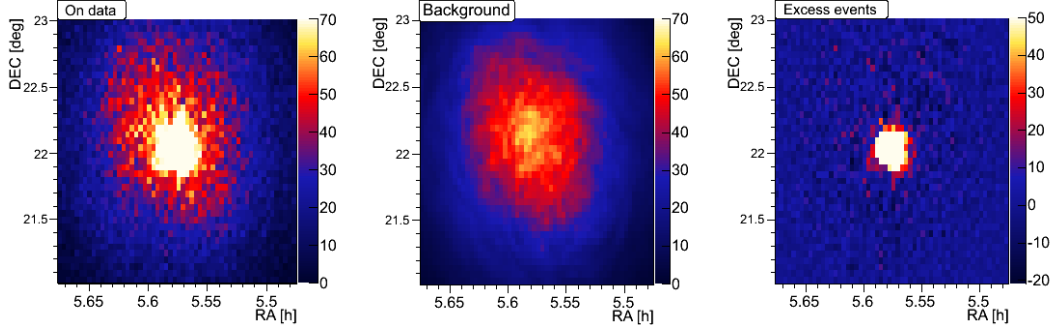
Figure 6.13: ON, Background, and excess maps obtained from the Crab Nebula. All three maps are binned maps and no smearing has been applied. A bin size of $0.05° \times 0.05°$ has been used. The same analysis cuts as in the θ^2-plot example have been used (Figure 6.12). For illustration purposes the ON map has been cutted at 70 events (real maximum value is around 500 events). The smaller fluctuations of the background map compared to the ON map are due to the oversampling of the OFF distribution. While the overall shape and structure of the exposure are conserved small fluctuations are washed out by the oversampling. The elliptic shape of the exposure is typical for wobble observations with two pointing positions. The resulting excess map shows a clear excess arising from the Crab Nebula. Also here the maximum of the map has been cutted for illustration purposes (real maximum is around 450 events).

The final skymap is obtained by applying a smearing according to the angular resolution of the instrument (and the possible extension of the source) to the obtained maps. This smearing uses a Gaussian kernel of a certain sigma. In some sense the smearing can be understood as the analogy to the θ^2-cut; it defines the size of a possible signal region. The significance of any given excess is estimated by using the so called test statistics (TS). The TS are obtained by applying Li & Ma (1983) equation 17 to the smeared excess and the smeared background model. The correlation between individual sky regions caused by the applied smearing as well as the oversampling used in the background modeling lead to the fact that TS values do not represent real significance values. The null hypothesis obtained from the TS mostly resembles a Gaussian function but in general can have a somewhat different shape or width. The correlation between TS value and significance value depends on the individual case and analysis. In general the TS value is somewhat above the real significance value, mainly caused by the oversampling of the background.

To investigate the morphology of the source one has to correct for the unequal exposure of all positions in the camera field of view. This is achieved by the relative flux map. The relative flux map is defined as the excess map divided by the background per constant area, and therefore uses the background as an exposure correction. For all physical discussions the relative flux map is used. From now on skymap refers to a relative flux map if not explicitly stated differently. Figure 6.14 shows a skymap obtained for the Crab Nebula.
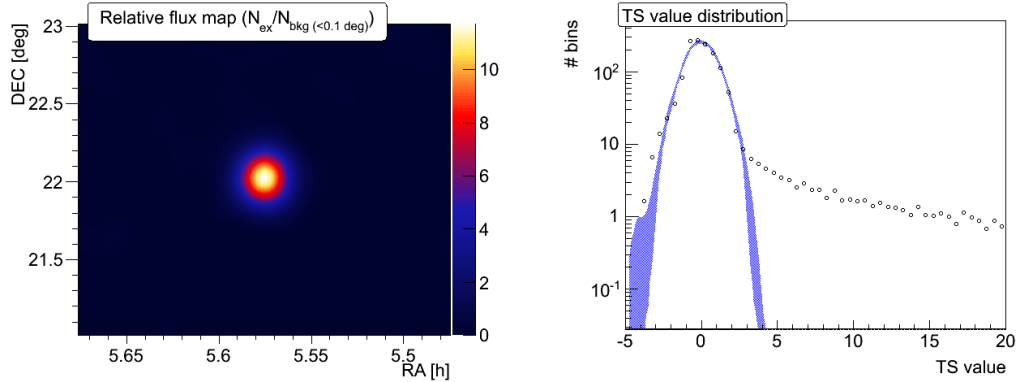
Figure 6.14: Left: The skymap obtained for the Crab Nebula analysis above 100 GeV as already shown before. The map has been smeared with a Gaussian kernel of $\sigma = 0.14°$. The emission arising from the Crab Nebula is clearly visible in the center of the skymap. Right: The obtained TS distribution (cut at 20, maximum ~ 100) shows clearly a deviation from the null hypothesis (blue) obtained from the background model. A clear similarity of the null hypothesis to a Gaussian function is visible.

In most cases the skymap is shown with contours defined by the TS-values overlaid to simultaneously show the morpholgy (defined by the skymap colors) of the source and an indication of the reliability on the structure. The TS contours can not be directly translated into significance values as they are obtained by applying a point-like measurement on the smeared structure of the source. Therefore, a TS contour $< x$ will always be found around a real source with a maximum TS value above x caused by the shape of the source and the finite angular resolution of the instrument. To estimate the reliability of the structure one uses the fact that the null hypothesis of the TS distribution is symmetric around zero in the case of a source-free map. The lowest trustful TS contour is determined by the absolute TS value of the strongest negative fluctuation. From this definition it automatically follows that the TS distribution has to show a clear deviation from the null hypothesis, otherwise all structures in the obtained map are only statistical fluctuations.

6.4.3 Physical parameters: energy threshold, flux, and spectra

To translate the obtained excess in physical parameters, MC simulations are needed. To do so the MC test sample is used. The test sample undergoes the same analysis (RF's, DISP-RF, LUT's) and analysis cuts (all pre-cuts, hadronness-cut, estimated energy-cut, θ^2) as the real data. There are three main quantities obtained from the test sample:

- **Energy threshold of the analysis**
  The energy threshold is a defined quantity which describes the low energy threshold of an analysis as the peak of the true energy distribution. This quantity is used to specify the most probable energy of the detected excess events and obviously depends on the spectral properties of the signal.

- **Effective area**
  is the estimate of the effective detector area. It is defined as the area of a 100% efficient detector. It is calculated by multiplying the simulated area of the detector (given by the maximum detectable impact around the telescopes) with the gamma detection efficiency. The gamma detection efficiency is given by the ratio of γ-MC events surviving the analysis ($N_{\gamma\,eff}$) and the amount of simulated events ($N_{\gamma\,sim}$).

- **Migration matrix**
  is the relation between reconstructed and true energy after applying the complete analysis. In the last step of the standard analysis the migration matrix is used in an unfolding algorithm to correct for the finite energy resolution and a possible bias.

Energy threshold In this section the energy threshold for a given analysis is determined. As an example the threshold of the analysis shown in Figure 6.12 is determined and shown in Figure 6.15. The peak of the true energy distribution of the MC test sample is determined by means of a Gaussian fit. The obtained peak value is defined as the energy threshold, here 98 ± 1 GeV. The energy threshold of a given analysis is affected by many individual aspects. The most important are: The trigger threshold of the instrument, the energy depended fraction of events surviving the analysis, and the spectrum of source itself.
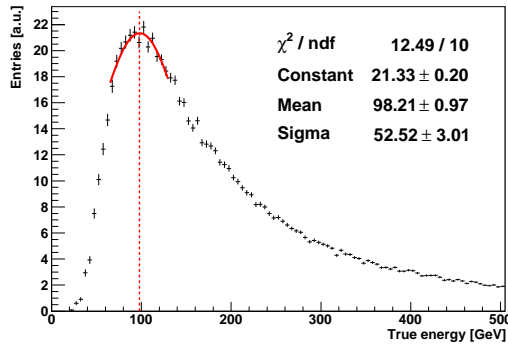
Figure 6.15: True energy distribution obtained from MC $\gamma's$ after applying the same analysis and cuts as in Figure 6.12. The peak of the distribution, obtained by means of a Gaussian fit, is defined as the energy threshold of the analysis. The fit (red solid) and the resulting parameters are displayed in the figure. In addition, the red dotted line illustrates the obtained energy threshold of 98 ± 1 GeV. For the simulated γ's a spectral slope of -2.6 was used.

Being defined as the peak of the true energy distribution the energy threshold is not a sharp threshold but the most probable energy of a single event in the selection. This obviously also allows to extract a differential excess in an energy range below the obtained threshold.

Effective area, flux and spectrum The flux (F) (or differential flux: dF/dE) of a source can be decomposed into the excess (N_γ), the effective time (T_{eff}), and the effective area (A_{eff}):

$$F = \frac{N_\gamma}{T_{eff} \times A_{eff}} \quad [\text{\# gammas cm}^{-2}\ \text{s}^{-1}] \tag{6.2}$$

$$dF/dE = \frac{dN_\gamma}{T_{eff} \times A_{eff} \times dE} \quad [\# \text{ gammas cm}^{-2} \text{ s}^{-1} \text{ TeV}^{-1}] \tag{6.3}$$

The effective time is the effective observation time corrected for the dead time of the instrument. Due to the Poissonian distribution of the cosmic events in time, the time difference of consecutive events follows a exponential function. The slope λ of the exponential represents the effective rate of recorded events. Therefore, the effective time is given by: $T_{eff} = \frac{N}{\lambda}$ where N is the total amount of recorded events (see Wittek 2002 for a detailed discussion on the effective time determination in MAGIC).

As already indicated above, the effective area is strongly dependent on the energy. Among others the most important influences are: The trigger efficiency, the analysis efficiency, and for the integral collection area the spectrum of the source. All influences on the effective area are themselves functions of the energy what causes the strong energy dependence of the effective area. In a first step the effective area is calculated in bins of estimated energy as this is the only energy parameter accessible for both MC and data. A typical example of an effective area is shown in Figure 6.16.
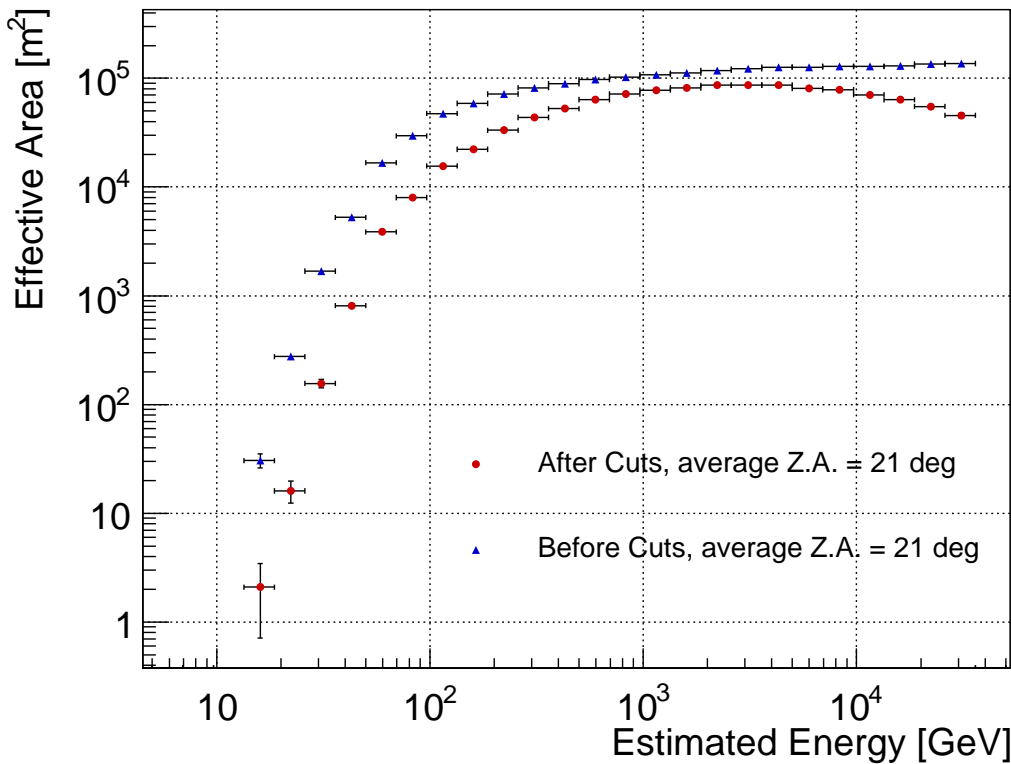
Figure 6.16: Effective area after the image cleaning (blue) and after applying all analysis cuts (red). The zenith angle range used here is 5-42 degrees with and average zenith angle (Z.A.) of 21 degrees.

The blue points represent the theoretically possible effective area obtained from all events in the MC simulations which triggered the telescopes and survived the image cleaning. Af-

ter applying all steps of the analysis (pre-cuts, hadronness-cuts, and θ^2-cuts) the surviving events build the real effective area of the given analysis. Here, the reference analysis with an hadronness cut efficiency for MC-$\gamma's$ of 90% was applied (for details see Chapter 6.6.4). The effect of the analysis lowers the total amount of surviving γ-candidate events and therefore the effective area. At energies below $\sim$ 100 GeV the main effect arises from the pre-cut of SIZE> 50 phe while at energies above few tens of TeV the main reduction is caused by the pre-cut on the LEAKAGE. In addition, the hadronness cuts and the applied θ^2 cuts in each bin of estimated energy reduce the effective area. Furthermore, the collection area is also a function of the zenith angle. The maximum effective area for low energies ($<$ 100 GeV) is reached in low Zd ($<$ 30°) observations. For low zenith angles the Cherenkov light has to travel a shorter distance in the atmosphere and is therefore less affected by absorption and scattering. The effective area for showers with medium and high energies ($>$ 300 GeV) on the other hand increases as a function of the Zd. This arises from the fact that showers arriving under larger zenith angles are further away from the telescopes and therefore produce a larger Cherenkov cone at the telescope site (see also Zanin (2011) for more details). In the case of high energetic showers the larger amount of produced Cherenkov light ensures that enough light reaches the camera although it suffers from stronger absorption/scattering.

The preliminary spectrum is obtained by combining the effective time, the excess, and effective area found in each bin of estimated energy. It is labeled as preliminary here because the spectrum obtained in such a way is given in units of estimated energy not true energy. To correct for the finite energy resolution and a possible bias in the energy reconstruction the preliminary spectrum needs to be unfolded.

Migration matrix and unfolding   The final step in each MAGIC analysis is the unfolding (see Albert et al. (2007a) for details). The measured spectrum in estimated energy ($S_{obs}(E_{est})$) represents the real source spectrum in true energy ($S_{true}(E_{true})$) folded by the energy resolution $M(E_{est}, E_{true})$ of the instrument:

$$S_{obs}(E_{est}) = \int S_{true}(E_{true})M(E_{est}, E_{true})dE_{true} \qquad (6.4)$$

The unfolding of the observed spectrum by inverting the above equation is in general analytically not solvable. By discretization the above equation can be rewritten in Matrix notation as:

$$S_{obs} = S_{true} \otimes M(E_{est}, E_{true}) \qquad (6.5)$$

In this form the problem can be solved numerically. Here, $M(E_{est}, E_{true})$ is the so called migration matrix which translates the true energy in estimated energy on the basis of MC simulations. As the binning in both quantities is not necessary the same (with usually less bins in true energy) the matrix is in general not quadratic. An example for a migration matrix is shown in Figure 6.17.
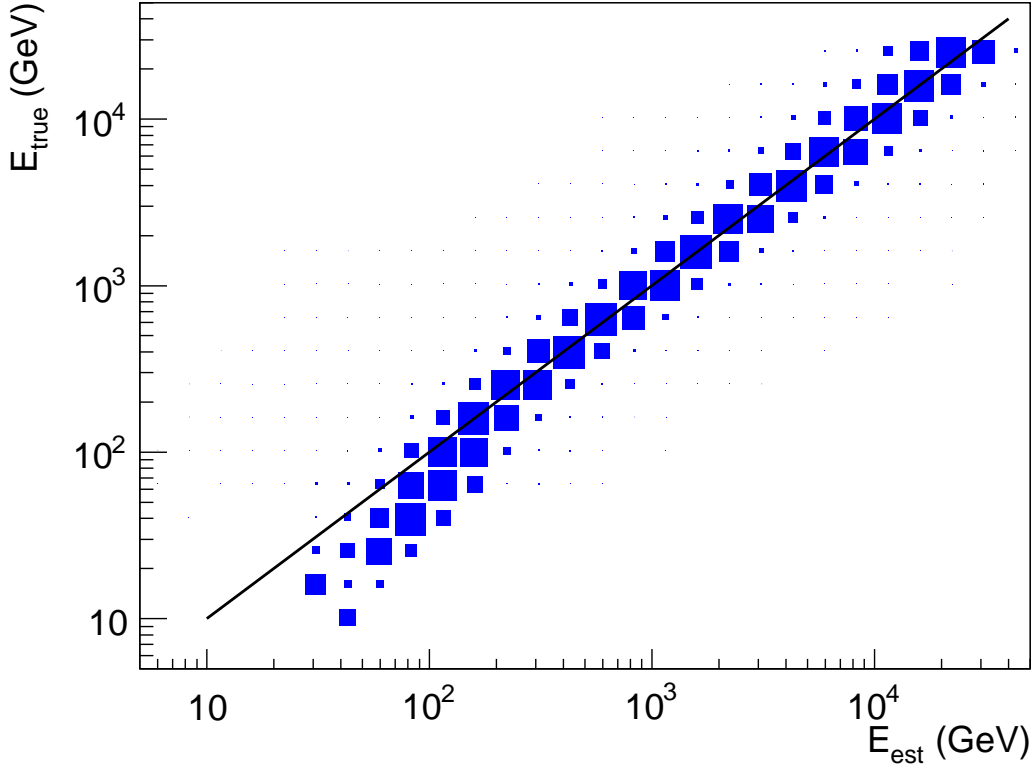
Figure 6.17: Example of a migration matrix. For illustration purposes the black line indicates the symmetry axis where estimated energy equals the true energy. The bending of the migration axis below $\sim 100\,\text{GeV}$ is due to the bias in the energy reconstruction at such low energies. Besides the energy resolution also the bias is corrected in the unfolding algorithm.

6.5 Reference analysis

As a part of this thesis a reference analysis was developed. This reference analysis is composed of an RF for the γ-hadron separation, two RFs for the DISP estimation, and two LUTs for the energy estimation. The aims of this analysis chain are to have a well tested analysis which is applicable over a wide range of conditions. The main purpose of the reference analysis is to allow a first and fast analysis of the data and/or to cross-check the results of another more specified analysis. It should be understood that the overall performance of a general analysis can not achieve the same quality than an analysis especially dedicated to a given problem. The reference analysis presented here is a compromise between best performance and universality for all energies and zenith angles up to $50°$. All the analysis plots shown above make use of this reference analysis. More specifically the analysis has been produced using the following settings:

- Pre-cuts:
    - $\text{SIZE}_{1,2} > 50$

- $- \text{SIZE}_{1,2} < 50000$
    - $\text{ISLANDS}_{1,2} = 1$
    - $\text{LEAKAGE2}_{1,2} < 0.2$

- Re-distributing data and MC to achieve the same Zenith/SIZE distribution:
    - 90 bins in $\log(\text{SIZE}_1 + \text{SIZE}_2)$ from 1 to 5.5
    - 11 bins in $\cos(zd)$ from $0°$ to $50°$ (bin width in $\cos(zd) \approx 0.0333$)

- Data used as OFF/hadrons:
    - ≈ 30 hours ($> 10^7$ events after pre-cuts)
    - Data taken between November 2009 and November 2010

- Used for the training:
    - γ-hadron separation training: $\sim 4 \times 10^5$ gammas and $\sim 4 \times 10^5$ hadrons
    - DISP RF and LUT training: $\sim 4.5 \times 10^5$ events

- Random forest settings:
    - Number of trees: 100
    - Number of trials: 3
    - Final nodesize: 5
    - Amount of decission nodes used per tree in each training:
      $\sim 4 \times 10^4$ for γ-hadron separation
      $\sim 10^5$ for DISP training(s)

It should be noted that in the process of assimilating the Zenith/SIZE distribution first the distribution for MC and data is obtained independently. In each bin the lower content between data and MC sets the desirable amount of events. Then events from the higher populated set are randomly chosen until the desired amount is reached. The much larger OFF sample in this case ensures an averaged OFF distribution over the complete period between 2009 and 2010. In the case of variations in the telescope performance over time a more specific analysis should use OFF data taken as close as possible compared to the data of interest. Except for ~ 1 month of a worse optical point spread function compared to usual no strong variations in the above period have been observed. Data from the mentioned month were not included as OFF data for the training. Furthermore, by allowing a larger time span to enter the OFF calculation one can access naturally more appropriate data and therefore enhance the statistics in the training. As there were no major changes in the system the analysis is applicable for data taken between November 2009 and June 2011. From the amount of decision nodes used in an RF one can estimate the average amount of successive cuts used following individual events to reach the final node in each tree. In case of the γ-hadron separation the average amount is ≈ 15.3 successive separation cuts per tree. For the DISP estimation an average of ≈ 16.7 classifications was used. In the following, few examples will be shown to demonstrate the performance of this analysis.

Crab and performance In addition to the already shown examples from the Crab Nebula, Figure 6.18 shows the spectrum of the Crab Nebula obtained by applying the reference analysis. The spectrum has been unfolded with the Bertero method (see Albert et al. (2007a) and references therein for more details). Furthermore, the sensitivity of the analysis settings used to obtain this spectrum is displayed on the right hand side of the figure.
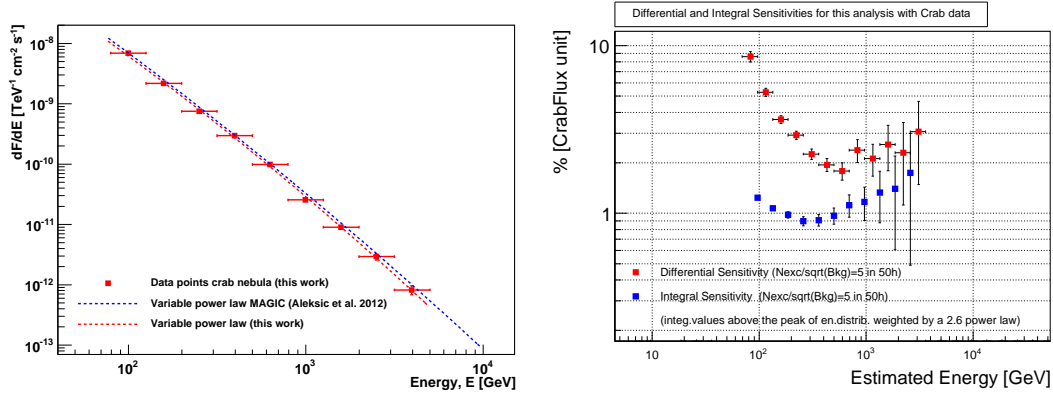
Figure 6.18: Application of the reference analysis with a hadronness cut of 95% efficiency on a ~ 8 hours Crab Nebula sample covering a zenith range between 5° and 40°. Left: The obtained spectral points (red) and the resulting variable power law from a fit to the data. In comparison the obtained fit from Aleksić et al. (2012) is shown in blue. Right: Shown is the differential and integral sensitivity computed from the cuts to obtain the spectrum. All errors are statistical only.

The spectrum of the Crab Nebula is described by a power law of variable index:

$$\frac{dF}{dE} = f_0 \times 10^{-11} \left(\frac{E}{TeV} \right)^{a+b\times\log\frac{E}{TeV}} [TeV^{-1}cm^{-2}s^{-1}], \qquad (6.6)$$

where $f_0 = 2.88 \pm 0.08$, $a = -2.50 \pm 0.04$, and $b = -0.17 \pm 0.05$. All errors are statistical only. The here obtained spectrum is $\approx 13\%$ lower than the one obtained in Aleksić et al. (2012). The results are compatible within the systematic uncertainty of the instrument (Aleksić et al. 2012). However, this discrepancy indicates the limitations of the reference analysis which is build as a multi purpose analysis and might therefore not achieve the same accuracy as a dedicated analysis. The here obtained sensitivity is, with a maximum integral sensitivity of $\approx 0.9\%$ crab units above 300 GeV, very close to the optimal sensitivity of $\approx 0.8\%$. It should be mentioned that the applied cuts have not been optimized for sensitivity but simply use a hadronness cut which contains 95% of the Monte Carlo gamma rays.

On-site analysis (OSA) The on-site analysis (OSA) does not only calibrate the data and performs the image cleaning and parameterization but produces some first preliminary high-level-output. This ensures the detection of high flux states for strongly variable sources as fast as on the morning after the observations. While also a rough real-time analysis is carried out during the data taking, the analysis by the OSA is much more sensitive and precise. In the OSA the analysis is applied to all data automatically. A set of standardized detection

cuts is applied to the data produced by the OSA. Figure 6.19 shows the results as produced by the OSA for the object MRK-421 in January 2011.
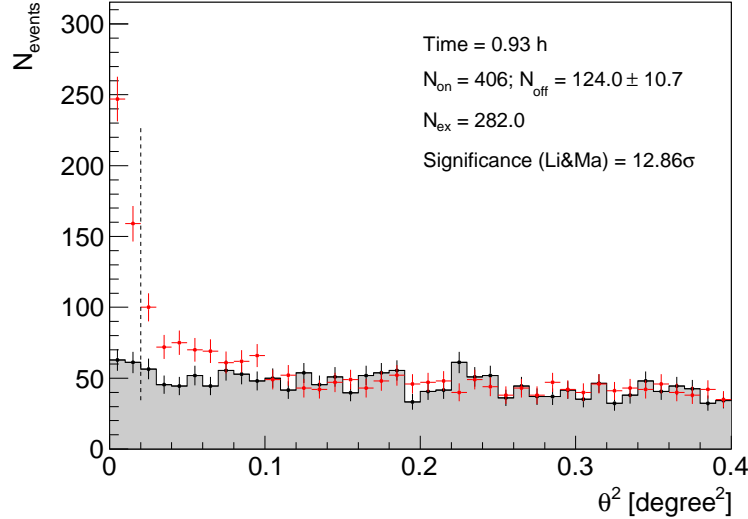
Figure 6.19: MRK-421 in January 2011, analysis automatically performed by the OSA using the here presented analysis. The energy threshold of the analysis is ~ 100 GeV.

Summary The analysis files and an appropriate test sample of MC are accessible for every member of the MAGIC collaboration. Besides the use in the OSA the here presented analysis serves as a test analysis. In addition, it offers a fast excess to MAGIC data and is therefore a helpful tool also for new members of the collaboration. In order to reach the maximum performance and accuracy of the instrument a dedicated analysis for each source (i.e., training data from the same time or a priori restriction to a given zenith range) is not substitutable by the here presented work.

6.6 High level analysis details: Effects of the background

As part of this work a generalization of the background calculation has been developed and implemented in the standard MAGIC analysis. This method is called *OFF from wobble partner* (OfWP) and is especially important for serendipitous discoveries of sources, scans, and extended sources. In addition, the development of this method has led to a change of the standard observation modus which allows the use of multiple OFF positions without introducing additional systematic uncertainties. This section is organized as follows: First, the different observation set ups are introduced. Then the natural asymmetry arising in stereo observations of two telescopes is discussed. It is shown how this asymmetry is canceled in standard wobble observations in the case of one OFF position and how *OFF from wobble partner* is a generalized version of this approach. Finally, the advantage of using four pointings is discussed and it is shown how this allows the use of three independent and equally valid OFF positions. The last part of the section addresses the impact of the background uncertainties for the sensitivity and excess accuracy. Finally systematic effects connected to the background and not perfect MC simulations will be discussed.

6.6.1 Pointing modes and their effect for the trigger efficiency

As most gamma ray sources have relatively low fluxes the signal to noise ratio is rather low. Therefore, an accurate determination of the background is fundamental to ensure a high sensitivity of the instrument and a precise determination of the excess. Especially in the low energy regime (< 200 GeV) the challenging gamma hadron separation and the high background flux produce a high irreducible background level (Sobczynska 2007). Only the angular resolution allows a clear determination of a signal by comparing the surviving events from the expected source direction with the isotropic background from a source free direction. Due to a never perfectly constant acceptance of events throughout the field of view (and within the camera plane) a background region has to be chosen which is not affected by these uncertainties. There are several ways to obtain such a region and therefore to directly measure the background. The next sections will describe the underlying effects and their reasons. First the observation modes and the general principles of the background determination are introduced to access the understand the underlying effects.

Observation modes

Before the different observation modes are discussed it is important to know how individual gamma ray showers of a point-like source are distributed in the camera plane. This is illustrated in Figure 6.20.
Gamma ray showers are distributed radially around the source position. Therefore, and connected to the impact parameter distribution of the images, which reflect the light pool of gamma ray showers, the COG distribution for a point like source has a donut like shape. It should be noted that the spatial size of the image for low energy events is rather compact around the COG position. Therefore, the size of the trigger region should be at least as large to cover the COG distribution, up to the desired impact parameter. For higher energetic events and therefore larger images the size of the trigger region is less important as in most case a significant fraction of the image falls inside the trigger region independent of the COG position.

A smaller trigger region will, however, cut high energy showers at large impact parameters. The limited size of the trigger region causes a radial dependence in the trigger efficiency as a function of the distance of the source from the camera center. For obvious reasons this dependence is especially strong for small SIZE showers and therefore low energies.
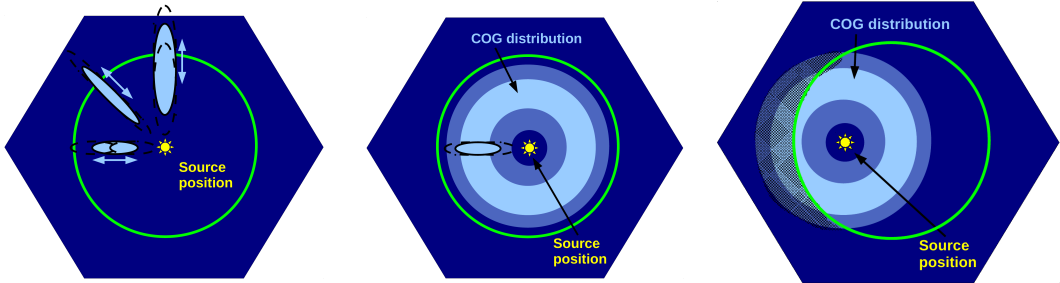
Figure 6.20: Illustration of the center of gravity (COG) distribution of gamma ray showers in the camera plane assuming a point like source in the case of single telescope observations. In all pictures the green circle marks the size of the trigger region. Left: Shown are images of gamma ray showers of three different energies. All events point to the source position, while the distance of the COG to the source position (DISP) of each image (for a given energy) is mainly determined by the impact parameter. For close impacts the DISP is smaller than for larger impacts. Middle: By plotting the COG of many events a donut like shape around the source position can be seen. Here, the COG distribution of low energy events is shown. Right: Here, the case is shown if the source position is not at the center of the camera but slightly shifted to one side. As can be seen in the illustration this results in a reduced trigger efficiency for low energy events as a part of the COG distribution (shaded area) is outside the trigger region resulting in a non spherical COG distribution of the recorder events.

A similar behavior is expected for background events. In contrast to the case of a gamma ray source, the background flux is isotropic. One can approximate the background as a superposition of equally strong point sources equally distributed over the sky. Due to the isotropic flux of CRs and the different light distribution on ground of hadronic showers the COG distribution of the background is more a flat disk than a donut. However, the finite size of the trigger region will affect the background in a very similar way than the gamma ray showers and therefore also the background acceptance for any assumed source position will decrease towards the outside of the camera.

It should be noted that a larger trigger region would partially solve the above mentioned problem. However, the always finite size of the camera and therefore also the limited field of view will always produce this kind of effect at some critical distance from the camera center. To understand the observation modes and the later determination of background and signal this radial dependence is of fundamental importance. In particular it means that the sensitivity of the observations (the acceptance of events) is not independent of the source position in the camera plane. This has to be taken into account in the observation strategy. There are two main observation modes used by IACTs:

- **ON - OFF observations** The most simple way to determine the background is to use in addition to ON observations (pointing at the source), dedicated OFF observations (pointing at a source free region). For both observations the amount of events pointing towards the camera center are determined by means of a θ^2 plot. By putting the source in the center of the camera the great advantage of this method is that it uses the maximum trigger efficiency. Another advantage of this method is that the source (ON) position and background (OFF) position in the camera is the same in both cases (namely the center of the camera). Therefore possible differences in the camera (e.g. different PMTs) are canceled by construction. The disadvantage of this method is first of all that dedicated OFF observations are needed which reduce the total amount of available observation time. In addition, as ON and OFF are not taken simultaneously, it can be challenging to maintain the same observation conditions (e.g. weather, day to day fluctuations, etc.).

- **Wobble observations** Nowadays the wobble (Fomin et al. 1994) observations are the standard observation mode in ground based gamma ray astronomy. Here one points not directly towards the source, but at a given angular offset (MAGIC default: 0.4°) next to the source. In this case the source position is not at the center of the camera but shifted by this offset away from it. Now the position mirrored at the camera center can be used to simultaneously measure the background. It should be noted that the distance from the camera center towards the source and background position has to be the same as the acceptance of the camera degrades radially towards the outside. The main disadvantage of this method is the reduced trigger efficiency as the source is not longer located at the center of the camera. In addition, the ON and OFF position in the camera is by definition not the same. This can introduce systematic acceptance differences caused by intrinsic inhomogeneities in the camera (e.g. slightly different QEs of the PMTs). To avoid this effect the pointing position is regularly switched (default: every 20 minutes) such that the source position in the camera changes by 180° around the camera center. Each pointing position is called one wobble position and defined by the distance of the source to the camera center (so called wobble distance, default: 0.4°) and its rotation angle with respect to the Declination axis (default: 0° and 180°). By combining the same amount of time in two wobble positions possible systematic affects are canceled as both the ON and the OFF position spend the same time in the same parts of the camera. It should be noted that the source position in the camera plane rotates around the camera center over time due to the ALT/AZ mounting used by Cherenkov Telescopes. This movement is in the order of 0.05°/20min (except for culmination) and therefore usually smaller than the size of an individual pixel. As this movement is properly taken into account in the analysis software and for the sake of simplicity the effect will be neglected in large parts of the further discussion.

Even though ON observations offer the optimal trigger efficiency, the need for extra OFF observations significantly enhances the time needed to finish a given observation compared to the use of Wobble observations. The additional problematics in avoiding possible systematic differences between the individual ON and OFF observations were another reason that all currently operating IACTs use mainly Wobble observations[4]. In addition, Wobble obser-

---

[4] Recently the VERITAS collaboration is developing the so called *orbit-mode* observations where the pointing

vations offer the possibility to use multiple OFF positions simultaneously and therefore can reduce the statistical errors on the background measurements significantly without the need to spend huge amounts of time in dedicated OFF observations. Before the use of multiple OFF positions is discussed, the effects of Wobble observations in a stereoscopic system are introduced.

Asymmetries introduced by stereoscopic observations

Besides the advantages of stereoscopic observations there are also some newly introduced challenges. By requiring that each event triggers both telescopes the azimuthal symmetry around a single telescope is broken, as the overlap of the viewing angles of both telescopes is located between them. In addition, the different sizes of the trigger region in MI and MII make the overlap region shift towards the telescope with smaller trigger region. This effect is illustrated in Figure 6.21. Due to the not completely overlapping view cones of the trigger region at the height of the showers (~ 10 km) one side of each individual camera is effectively more sensitive than the other. This leads to an asymmetric COG distribution of the isotropic background, which is called the level-3-blob. The COG distribution of the background data is shown for events > 100 GeV in Figure 6.22. Before the hadronness cut this distribution is strongly dominated by hadronic, most likely muon, events (top panel). As many of these events appear very close (~ 2 km) above the telescopes (see also Aleksić et al. (2012) and references therein) the level-3-blob has a very strong effect. After applying the hadronness cut (see lower panel) the COG distribution is much more homogeneous. However it should be noted that the COG distribution is not located in the center of the cameras but shifted towards the other telescope.

---

is performed in an *orbit* around the source position, yielding as fast rotation of the source around the camera center and thus an homogeneous use of the camera plane (Finnegan & for the VERITAS Collaboration 2011)
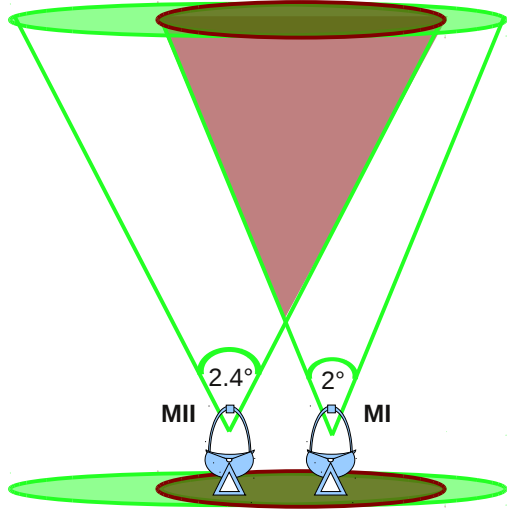
Figure 6.21: Shown are the viewing angles of the trigger regions in MI and MII, respectively (green lines). The overlapping area (red) illustrates the *active* area during stereoscopic operation. As the individual showers are extended objects, only a part large enough to cause a trigger has to occur inside the *active* area.
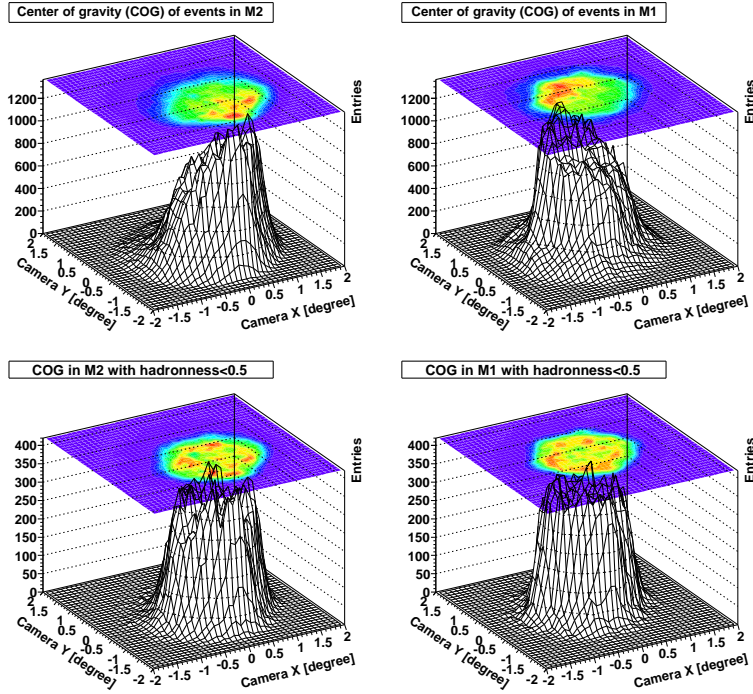
Figure 6.22: The COG distribution of real background events (SIZE> 50) in camera coordinates of each telescope. Top: The level-3-blob is clearly seen as an enhancement of the COG distribution towards the second telescope. Bottom: The applied hadronness cut removes most low altitude hadronic events, resulting in a flatter COG distribution. Note however that the COG distribution is not centered at the camera center but shifted towards the direction of the second telescope.

As the size and direction of the overlapping region depends strongly on the projected base-line between the telescopes and their distance to the shower the level-3-blob shows a strong dependence both on the Azimuth and the Zenith of the observations. It should be noted that the COG distribution shows only a simplified picture as the light distribution of the shower is an extended object in the camera plane. Therefore, it is sufficient if a fraction of the shower, large enough to cause a trigger, falls inside the region of the level-3-blob. Therefore, the effect of this asymmetry becomes more important for small SIZE showers.

The most important consequence of the level-3-blob is connected to the question how a non uniform acceptance as a function of the shower location in the cameras influences the trigger probabilities for showers of a given direction. In other words, does the trigger probability and therefore the sensitivity depend on the source location in the camera plane? Figure 6.23 illustrates the COG distribution for low energies of a point like gamma-ray source in both cameras during stereo observation. Here, the left figure illustrates the case of first wobble position and the right figure shows the case of the second wobble position where the source position has been rotated by 180° around the camera center.
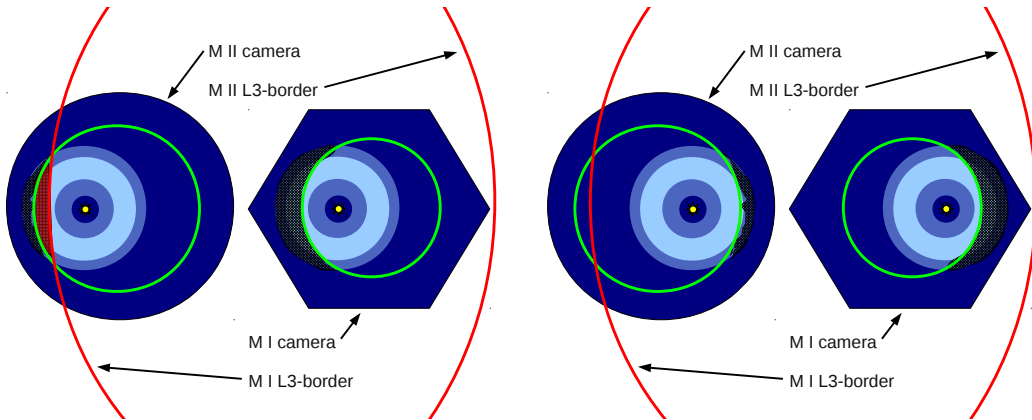
Figure 6.23: COG distribution (light blue area) of a point like source in both cameras during stereoscopic wobble observations. The green circle represents the size of the trigger region in both telescopes, while the red lines represent the edges of the common viewing angle. The source position (yellow star) is located on one side of the camera in each wobble position. It can be seen that the level-3-blob cuts a part of the COG distribution in MII in the case of left wobble position (left). In the second wobble position the COG distribution is unaffected by the level-3-blob in both cameras. This shows that depending on the source position in the camera(s) with respect to the level-3-blob the trigger efficiency and therefore the acceptance can change.

From this figure it is clear that the source position in the camera with respect to the level-3-blob can significantly change the amount of triggered events for a given gamma ray source. For the background the situation is similar as the COG of the background events around a given position has a disk like shape and is therefore similar to that of a gamma ray source. It is noted that the reconstruction quality of the arrival direction for a given shower is not affected here. Instead, the acceptance of events arriving from a given point in the sky depends on the

location of this point in the camera plane. This translates into a non uniform exposure of the field of view (both for the background and the signal). Figure 6.24 illustrates the asymmetric exposure around the camera center (pointing position) for each individual wobble observation. The data used here showed no significant gamma ray signal and therefore represent a pure background sample.
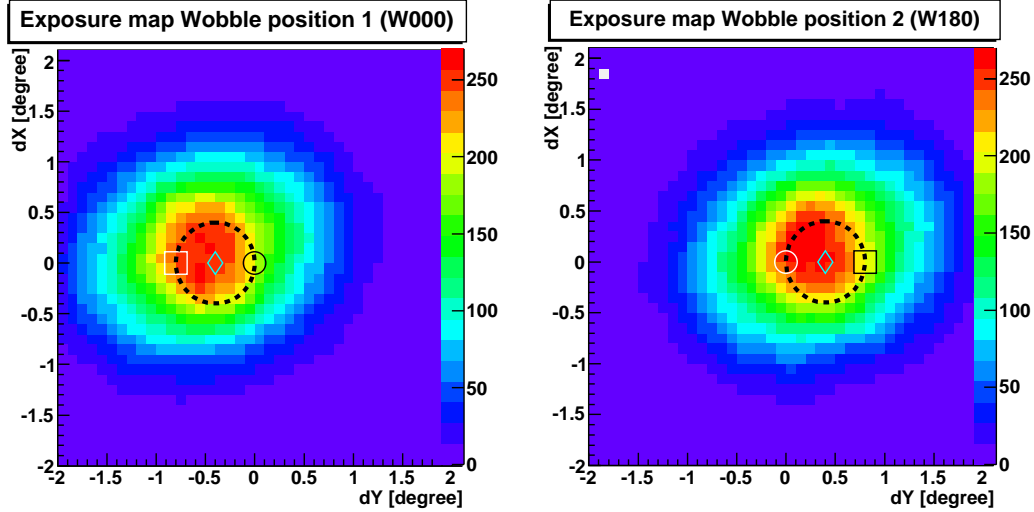
Figure 6.24: Exposure maps in stereo observations (> 100 GeV) of a source free observation for each of the two used wobble positions. The color scale presents the amount of events arriving within an area of $0.0025^{\circ 2}$. dX and dY represent the angular distance to the center of observations in an arbitrarily chosen coordinate system representing the field of view. The center of the maps represent the center of the observations, whereas the pointing (blue diamond) in each wobble position has been $\pm 0.4^{\circ}$ along the y-axis, respectively. The pointing position marks the center of the camera during each wobble position. A general radial dependence of the acceptance can be observed in each of the wobble positions. The elliptic shape arises from shape of overlapping view cones (the projected baseline connecting the two telescopes defines the major axis of this elliptic shape). On top of this radial dependence one can observe an asymmetric behavior, best seen in the shift of the red area in both maps away from the pointing positions towards the upper left. To highlight this effect a 0.4° circle (black dotted) has been drawn around the pointing positions. This shift is caused by the level-3-blob. The circle marks an assumed source position, while the squares mark the regions used to determine the OFF distribution.

As the exposure shows a general radial dependence from the camera center the background regions have been chosen to have the same distance to the center as the source position. If one compares the amount of events at the source position and the background position within one wobble position one observes a significant difference ($\sim 20\%$). However, by comparing the exposure at the source and background position in both wobble positions it can be seen that by the interchange of their positions in the camera plane(s) this systematic difference

is canceled. Both, the source and the background position, are once in a region of higher exposure (white symbols) and once in a region with lower exposure (black symbols). Even though the exposure shows a highly asymmetric behavior it has been shown in Figure 6.24 that due to the use of multiple wobble positions this systematic effects can be canceled by the use of OFF positions which show the same effective exposure as the assumed source position.

6.6.2 Standard Wobble Background determination
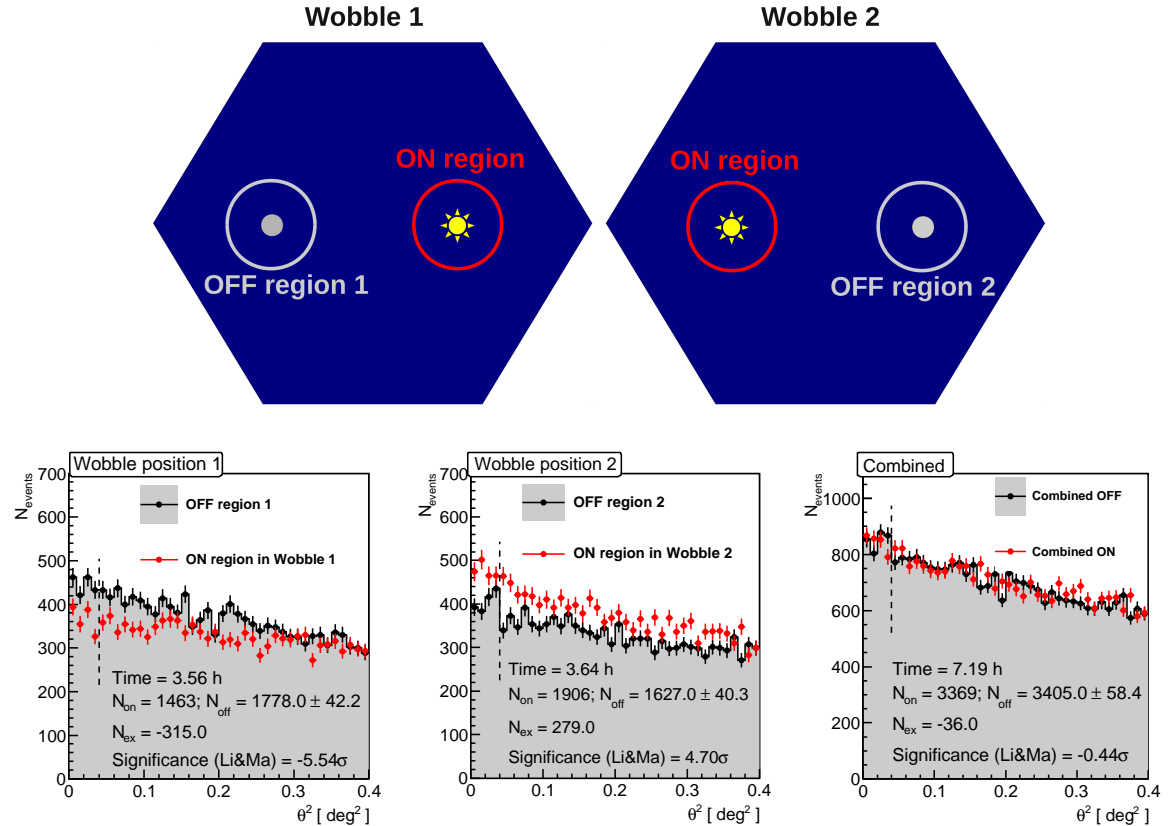
Figure 6.25: Standard determination of the ON and OFF distribution in observations with two wobble positions where the source has the same distance to the camera center in each wobble position. The wobble positions are chosen in such a way that the source is located at the opposites site of the camera with respect to the other Wobble position. The observational set up is illustrated in the top panel. Bottom: Shown are the obtained ON and OFF distributions within each Wobble position (left and middle) and the combined distributions of both Wobble positions of a source free region. Inserted in the plot are the amount of ON, OFF, and excess events within a signal region of a point like source (black dotted line).

The standard background determination in Wobble observations obtains the background at the same radial distance from the camera as the source position but from the opposite site of the camera(s). This OFF position is also commonly named as *180 OFF* as it reflects a 180°

rotation of the source position in the camera. By choosing the Wobble positions in such a way that ON and OFF regions interchange their positions, systematic differences of the acceptance at individual position in the cameras are compensated. The observational set up as well as the obtained ON and OFF distributions are shown in Figure 6.25. The θ^2-plots shown here have been obtained from a source free data sample with an analysis threshold of ~ 100 GeV. The non uniform acceptance in the camera plane is seen as a global mismatch of the ON and OFF distributions within the individual Wobble positions.

It should be noted that a simple normalization of the OFF distribution to match the ON distribution within one Wobble position is very challenging. A normalization of the OFF distribution is based on the assumption that ON and OFF should agree in a signal free region, i.e., large values of θ^2 (typical range: 0.2 to 0.4). As can be seen in the figure the major difficulties of this approach arise from the fact that ON and OFF distribution in one Wobble position show different shapes as a function of θ^2. By combining the data of both Wobble positions the ON and OFF distributions show very good agreement for all values of θ^2 and no significant excess is found. At this stage also the shapes of the distributions agree and a small mismatch could be solved by applying a normalization factor to the OFF distribution. However, the need for a normalization always indicates residual systematic effects and should be used with care.

At this point it should be noted that the here shown example(s) do not allow for a general quantitative statement about the non uniform acceptance caused by the level-3-blob. The effect shows strong dependence on the individual observational settings (Zenith, Azimuth, source location in the camera planes) as well as on the investigated energy range. Therefore, the magnitude of the effect changes from observation to observation and as function of energy. Qualitatively one can say the effect is largest for the lowest energies and observations performed under the lowest zenith angles. But even in this case the exact position of the source in the cameras plays a crucial role. Independent of the magnitude of the effect, a cancellation of the systematically introduced mismatch between the ON and OFF distributions can be achieved by the combination of data from both Wobble positions.

However, the use of the 180 OFF position has two major caveats:

1. **The need for a priori known source position**
   The symmetry between the location of the source position and the 180-OFF-position in the camera plane (i.e., their interchange between the two wobble positions) is only given for one particular position in the field of view. Therefore, the observational set up has to be chosen in such a way that this position is equivalent to the source position itself. This requires an a priori knowledge of the source position, as it invokes a wobble set up around this sky coordinates. While for example in the observations of an active galactic nuclei the source position is usually known a priori, this is not the case for the observation of extended objects like supernova remnants.

2. **Equal net exposures in each wobble position**
   To warranty the cancellation of the systematic differences the amount of data in each Wobble position has to be the same. In addition the quality and observational settings has to be as equal as possible (i.e., Zenith/Azimuth coverage, and same data quality).

6.6.3 OFF from Wobble partner

To overcome these caveats a generalization of the background determination has been developed as part of this thesis. The main idea behind this method is determining the background (OFF) from the same position in the camera plane as the ON. As for one given wobble position this position is occupied by the source, the background will be determined from the same camera position but in the second wobble position. Therefore, the method is called **OFF from Wobble Partner** (OfWP). As the OFF for a given ON is not determined from the same Wobble position they are not taken simultaneously anymore. However, as has been shown above the strictly simultaneous OFF shows in general a systematic difference in the exposure (see Fig. 6.25). To account for possible differences in the effective observation time of each wobble position the background is scaled by the observation time ratio of the Wobble position used to extract the ON and the one used to extract the OFF. The major aspects of OfWP are:

- For any given source position the OFF will be determined from the same position in the camera plane as the ON.

- Possible differences in the observation times of each wobble position will be taken into account by scaling the OFF accordingly.

- OfWP is a generalization from the standard 180 OFF calculation to arbitrary source positions and non equal observation times in the individual wobble positions.

Each ON-OFF combination is taken from two different wobble positions. With respect to the example shown in Figure 6.25 this means that the ON from wobble 1 is combined with the OFF from wobble two and vice versa. In addition the OFF is scaled to the time ratio between the two positions accordingly ($\sim \pm 2\%$ in this example). The final θ^2 plot is then obtained by combining the individual ON/OFF combinations. The resulting θ^2 plots are shown in Figure 6.26.

The overall excess found with OfWP agrees with the one obtained from the standard 180 OFF calculation (see right plot in Figure 6.25 and 6.26). In addition, the previously observed mismatch in the individual wobble positions has vanished and the excess found in each wobble position became accessible. The method does not reduce exactly to the standard calculation, even in the case of exact the same observation in both wobble positions. This is due to the real time difference between the observations of two consecutive wobble positions. In the standard duration of one wobble position (default: 20 min.) the source position rotates around the camera while zenith and azimuth angle change during the tracking. In practice this leads to a marginal difference between the OFF positions used in OfWP and in the standard 180 case. However this effect is negligible compared to the statistical errors of the background. Therefore OfWP gives an equivalent measure of the background as the standard method but is applicable for a much broader range of possible situations. Especially in the case of different observation durations for each wobble position, OfWP provides a much less systematically affected background. An additional ON-OFF normalization in a signal free region is much more reliable as the shape of ON and OFF is the same in each OfWP combination. Even though such a normalization is in most cases not needed (and by default not applied) there are few cases where it is an useful additional tool to overcome small background variations (e.g.,

if the observing conditions change significantly between the individual wobble positions). As mentioned above the need of a normalization factor always indicates systematic problems. Therefore, it should be used with care, especially if the normalization factor significantly changes the results.
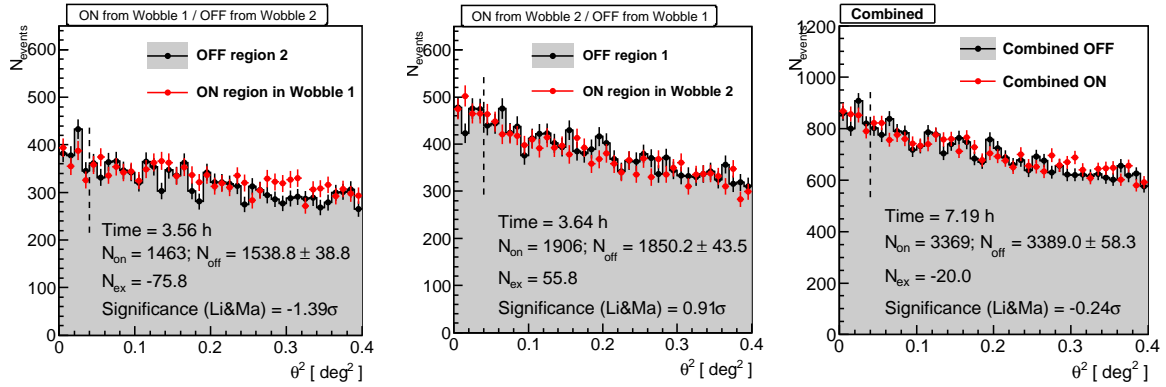
Figure 6.26: θ^2 plots obtained with OfWP for the same example of a source free region as already shown in Figure 6.25. The left and middle plot show the individual ON distributions combined with the time weighted OFF distributions from the wobble partner. The time in each plot represents the effective time of the ON distribution. Minimal residual mismatches (e.g., left hand plot around $\theta^2 \sim$ 0.3) arise from the never perfectly matching Az/Zd distribution in both wobble positions and the real time difference between the observations. The right hand plot shows the combination of both ON and OFF distributions. By using OfWP, the previously observed mismatch in the individual wobble positions is canceled. Therefore, the excess within each wobble position can be accessed in addition to the combined excess. In all cases the results show no significant signal. The overall excess of -20 ± 82.3 agrees within 0.2 sigma of that obtained from the standard 180 OFF calculation.

Arbitrary source positions

One of the main reasons to develop OfWP was the need of a reliable background determination for arbitrary source positions within the field of view. As mentioned above the standard 180 OFF calculation provides only an interchange of ON and OFF positions in the camera plane for one particular point in the field of view. OfWP determines the OFF position in such a way that this symmetry is kept for all possible source positions. Figure 6.27 illustrates the case of an arbitrary source position in the field of view. As can be seen in this example, the standard 180 OFF positions (round, green surrounded) do not reflect the same camera positions as the source (green star). Therefore, systematic differences are not canceled but can even add up. It should be noted that this behavior is true for all possible source positions except one (the yellow star in this example). This means that the standard OFF calculation can be severely affected if one is interested in an emission arising from any other point in the field of view. Therefore, OfWP is an essential tool if the source is not at the previously assumed source position, another source appears to be within the field of view of an already

taken observation, or one is interested to investigate individual regions of an extended source. As an example of such a case the MAGIC discovery of the extragalactic object IC 310 (Aleksić et al. 2010) will be used. In the work of Aleksić et al. (2010) an early version of the OfWP method has been used to validate the signal. It should be noted that this work does neither aim to provide any physical discussion of this object, nor a detailed analysis of this object. The only reason to use IC 310 is its particular location within the field of view during the observations of NGC 1275 (Aleksić et al. 2012a). The situation is similar to the one shown in Figure 6.27; IC 310 is located $\sim 0.25°$ away from the camera center in one of the Wobble positions and in the other one the distance is $\sim 1°$. In the work of Aleksić et al. (2010) the excess was determined from the closer wobble position only.
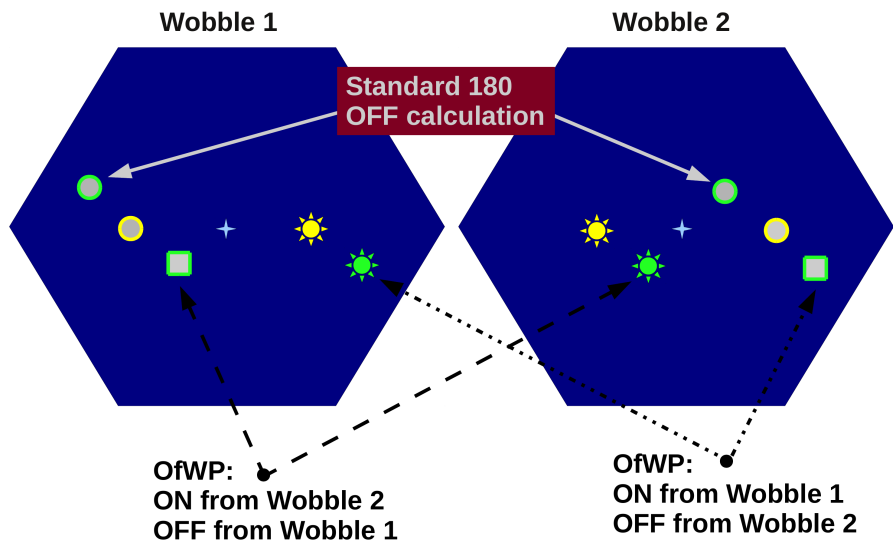
Figure 6.27: Illustration of an arbitrary source position. The assumed source position and center of the observations is marked by the yellow star. The wobble positions have been chosen to lie $0.4°$ *left* and *right* of this position (blue cross, camera center). The round yellow surrounded regions mark the 180 OFF positions for the assumed source position. For this source position the standard 180 OFF and OfWP OFF positions are equivalent. The green star represents the *real* source position. The round green surrounded regions show the 180 OFF positions for the green source. It is clear that this OFF positions do not occupy the same parts in the camera plane as the source. Instead this OFF positions are always located on the opposite half of the camera as the source itself. In this case systematic differences would most probably add up between the two Wobble positions instead of being canceled. The quadratic green surrounded OFF positions show those positions in the camera plane which are also occupied by the source and used by OfWP.

Due to the radial dependence of the acceptance one can expect a higher amount of excess in the position where the source is closer to the camera center. The results obtained with OfWP

for this source are shown in Figure 6.28.
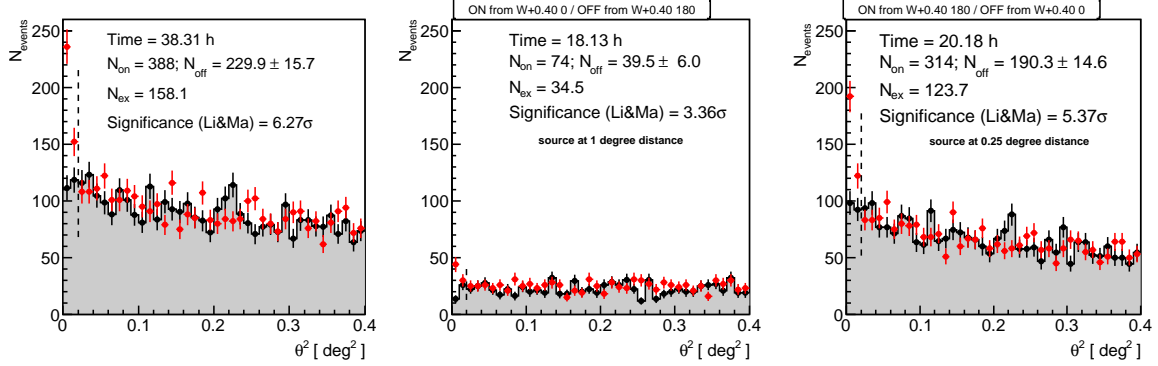
Figure 6.28: θ^2 plots obtained with OfWP from the object IC 310 above an energy threshold of ~ 400 GeV. IC 310 was located within the field of view during the observations of the source NGC 1275 and appears in one wobble positions (W+0.4 0) at a distance of $\sim 1°$ to the camera center and in the other wobble position (W+0.4 180) at a distance of $\sim 0.25°$. The plots show the combined θ^2 plot (left) as well as the individual θ^2 plots (middle and right). The effect of the radial decrease in the acceptance is clearly reflected in different amounts of events found for each Wobble position. The source is significantly detected with more than 5σ and its emission is seen in both Wobble positions. A very good agreement between the ON and OFF distributions for large values of θ^2 can be seen in all cases. No direct ON-OFF normalization has been applied, only observation time scaling.

This example illustrates the capability of OfWP to extract the correct OFF in the case of an arbitrary source position. It should be emphasized that no kind of ON-OFF normalization was used for the results shown in Fig. 6.28 and the very good matching arises only from the symmetric exposure between the ON and OFF positions. To stress the importance of this, Figure 6.29 shows the results obtained with the standard 180 OFF method. Shown are two plots, one without ON -OFF normalization (left) and one where the OFF has been normalized to match the ON. Due to the reduced background the amount of excess events increases by 28% compared to the non-normalized plot. Both plots do not provide a correct background determination. The non-normalized plot (left) shows a clear mismatch between ON and OFF in the signal free region, which implies a wrong determined background. Therefore, one can not draw conclusions on the validity of the background within the signal region. The normalized plot has been obtained under the assumption that the ON and OFF distributions have the same shape, which is not correct as they have been obtained from different parts of the cameras. The large difference between the two results clearly indicates strong systematic effects. This case demonstrates on the one hand that the OFF has to be obtained from the same positions in the cameras as the ON. On the other hand, an OFF normalization can even introduce additional errors in the background determination if used under the wrong circumstances. For completeness it should be mentioned that if one forces an ON-OFF normalization in the results obtained with OfWP the resulting excess of 155 ± 25 agrees perfectly with the one obtained without normalization of 158 ± 25. This result is, however, not a surprise as the

ON and OFF distributions in OfWP show no significant mismatch and therefore the applied normalization factors are very close to 1.
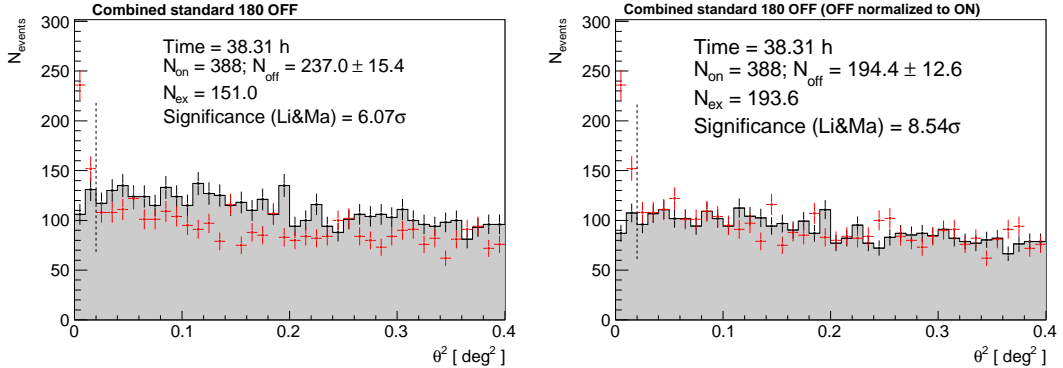
Figure 6.29: Resulting θ^2 plots obtained with the standard 180 OFF method. Both plots show the combined plot of both wobble positions. The left plot shows the result obtained without ON-OFF normalization. A clear mismatch between the ON and OFF distributions at large values of θ^2 is observed. Naively one might interpret this as an over prediction of the background. Following this interpretation the OFF distribution has been normalized to match the ON distribution in the region from $\theta^2 = 0.15$ to $\theta^2 = 0.4$. This scaled down the background by 18%. The result is shown in the right hand plot. The results obtained with and without normalization differ by more than 20%. The reason that the background did not match is that the used OFF positions do not have the same exposures as the ON position (see also Fig. 6.27). A simple normalization is not an appropriate solution as the ON and OFF distributions show different shapes. None of the two plots represent a reliable background determination.

Multiple OFF positions

The major advantage of wobble observations is the potential use of multiple OFF positions. This means that for each ON position more than one OFF position is used to determine the background. The final OFF measurement is then given by the average of the individual OFF positions. In this sense one can obtain a background measurement which is equivalent to a higher observation time as the ON measurement. Therefore, one reduces the statistical error of the background measurement and subsequently enhances the sensitivity of the instrument. The case of three OFF positions is sketched in Figure 6.30. The limitation of the number of OFF positions is given by the size of one ON/OFF region (the angular resolution plus source extension) and the circumference of the ring at the wobble distance around the camera center. The statistical error on the background is reduced by a factor of $\sqrt{\#\text{OFF}_{\text{pos}}}$, as long as all OFF positions are independent. For example the significance of 60 excess events over 100 background events in case of one OFF position is $4.3\,\sigma$. When using three OFF positions, the resulting significance increases to $5.3\,\sigma$.

The problem in using multiple OFF positions with MAGIC arises from the non uniform acceptance around the camera plane. As shown above this problem can be overcome by

using the same camera coordinates to extract the ON and the OFF, by OfWP. However, this means that the additional OFF positions (OFF 90 and OFF 270 in Figure 6.30) will have a systematically different exposure than the OFF position used by OfWP.
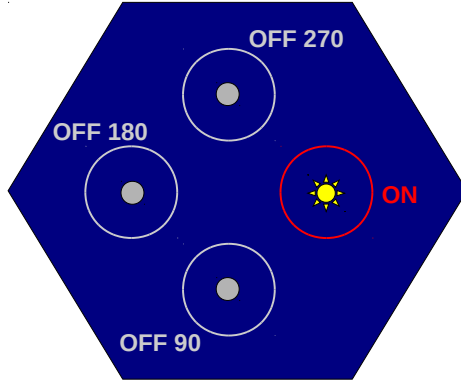
Figure 6.30: Illustration of the use of multiple OFF positions in Wobble observations. The source position is marked with the yellow star, the OFF positions with the grey disks. The red and grey rings mark the size of the ON and OFF regions respectively. Here the example of three OFF positions is shown. The naming convention of the OFF positions follows the needed rotation around the camera center in degrees to move the source position to the individual OFF positions.

Therefore, the use of multiple OFF positions can create a strong systematic effect in the background. The signal to noise ratio at low energies is usually lower than at the high energies resulting. In addition the stronger level-3-blob effect for small SIZE events leads to the strongest effects of the systematics in the background determination at the lowest energies. However, as shown in the example of IC 310, the use of inappropriate OFF positions can also cause severe problems at higher energies.

Even though the idea of multiple OFF positions is not strictly related to the OfWP method, the development of this method has triggered a change of the standard observational setting from 2 Wobble positions to the use of 4 wobble positions. By generalization of OfWP to an arbitrary amount of wobble positions (N_W) it is possible to obtain $N_W - 1$ equally valid OFF positions for any assumed source position within the field of view. This is shown in an example in Figure 6.31. Each used OFF position covers an equivalent location in camera coordinates as the ON position. The exact location of the Wobble positions does not play any role as long as all resulting OFF regions are independent within the integration region. Thus, an observational set up should be chosen, which maximizes the distance between the individual Wobble positions. The maximum possible distances is given by the set up of one Wobble position every 90° around the assumed source position. This set up is the standard observation mode in MAGIC since 2011. By using four Wobble positions and OfWP the use of 3 independent OFF regions is always possible without introducing additional systematic effects in the background determination. Hereby each ON-OFF combination (12 in total, three OFF regions for each ON obtained from one of the wobble positions) is corrected for

possible effective time differences. The ON in each wobble position is summed to give the combined ON distribution. In case of the background all 12 individually time re-weighted OFF distributions are summed. The resulting OFF is scaled down by a factor of three to account for the three times higher observation time. The resulting statistical error of the background is reduced by a factor $\sqrt{3} \approx 1.73$ compared to the case of 2 Wobble positions. It should be noted that the resulting reduction of the background error depends also on the applied time scalings and $\sqrt{3}$ is the best possible case where the time in all Wobble positions is identical. In first order one can estimate the real reduction factor (B_r) to be given by:

$$B_r \approx \frac{\sqrt{3}}{\sqrt{t_{max}/t_{min}}}. \tag{6.7}$$

Here t_{max} and t_{min} are the longest and shortest observation times of the involved Wobble positions. Therefore, one can conclude that the use of 4 wobble positions only reduces the statistical error of the background if the largest ratio of time differences is smaller than 3. However, usually the time differences are smaller than 20% and therefore the statistical error on the background is reduced by at least a factor of ~ 1.6.
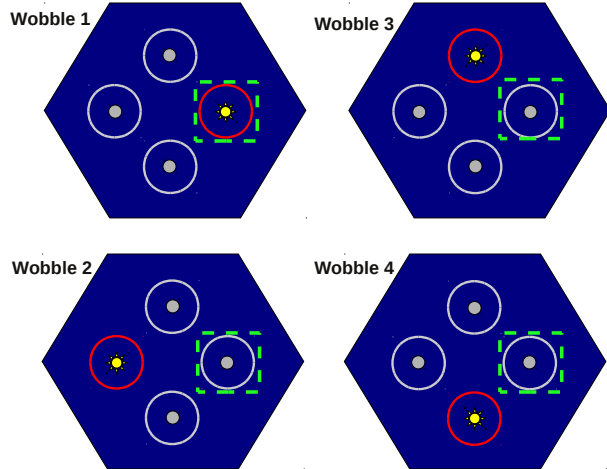
Figure 6.31: Illustration of 4 wobble observations. The source is marked as the yellow star in all wobble positions. The grey points show the used OFF positions. Red/grey circles mark the ON and OFF regions. The green dotted squares mark the OFF positions for all possible OfWP combination for the also marked ON region in Wobble 1

Compared to observations with two wobble positions, the use of four pointings requires two more telescope pointings to complete one full cycle (four wobble positions). The repositioning in MAGIC takes $\lesssim 1$ minute. Thus to complete one cycle and be able to make use of three OFF positions one needs $4 \times (20 + 1)$ minutes. Here, the observation time in each wobble position is 20 minutes. In contrast one cycle of two wobble positions takes only half the time. To achieve optimal conditions one aims to observe every night only complete cycles. Therefore, the observation with four wobble positions is more challenging concerning the scheduling. As

long as the overall observation times in each wobble position are similar ($\lesssim 20\%$) and their distribution among the observing dates also, small differences play no major role.

In case the source position is a priori known, the four wobble positions are distributed every 90° rotation around the source position, and all wobble positions show the same effective time the combined OfWP OFF distribution reduces to an equivalent background determination compared to using the three OFF positions 180, 90, and 270.

Summary

OfWP is a generalization of the background determination in the sense that the OFF positions are chosen in such a way that systematic differences of the exposure throughout the camera plane are automatically canceled. The method takes into account possible differences in the observation times and works for all possible positions within the field of view. The amount of valid OFF positions is one less than the amount of used wobble positions. By default no ON-OFF scaling is applied, and therefore all distributions reflect direct measurements (only corrected for possible time corrections). The development of OfWP has lead to a major change in the observing settings which allows the use of multiple OFF positions and therefore significantly improved the sensitivity of MAGIC. This method is fully implemented in the standard analysis software of MAGIC. The remaining systematic uncertainty (arising mainly from never perfectly equal observing conditions in the individual wobble positions) is difficult to estimate. In Aleksić et al. (2012) the uncertainty is estimated to be $\lesssim 2\%$ in case of the standard 180 OFF calculation and an a priori known source position. With OfWP and therefore the correction for different observation times in each wobble position the remaining systematic effect is at least reduced to $\lesssim 1.5\%$.

Table 6.1: Shown are the background and γ rates (within the signal region) for the individual OfWP combinations obtained from the Crab Nebula above different energies. Combination 1 represents the case where the ON has been extracted in W1 and the OFF in W2 and vice versa. It can be seen that the differences between the OfWP combinations decrease with increasing energy. At the highest energies the statistical errors do not allow a clear conclusion. As long as the ratio of the background rate significantly differs from unity, OfWP is mandatory to achieve a highly accurate background determination.

	OfWP combination 1	OfWP combination 2	ratio 2/1
> 100 GeV			
γ rate [#/min]	10.8 ± 0.3	14.5 ± 0.3	1.35 ± 0.05
background rate[#/min]	4.1 ± 0.1	5 ± 0.2	1.24 ± 0.05
> 500 GeV			
γ rate [#/min]	2.1 ± 0.1	2.4 ± 0.1	1.15 ± 0.07
background rate[#/min]	0.03 ± 0.01	0.04 ± 0.01	1.3 ± 0.6
> 1000 GeV			
γ rate [#/min]	0.09 ± 0.01	0.1 ± 0.01	1.11 ± 0.13
background rate[#/min]	0.013 ± 0.009	0.013 ± 0.009	1 ± 0.98

For high energies the larger physical extend of the showers reduces the effect significantly.

More correctly the physical extension of the detectable light of an shower determines the strength of the effect. For a given Zenith angle this translates into the investigated energy range. Table 6.6.3 shows the γ and background rate above three different energies in case of the Crab Nebula (~ 8 hours of data). It can be seen that for higher energies the differences in the individual combinations get smaller and become compatible to the statistical error of the measurement.

In addition, one can use the well understood background determined with OfWP to test the validity of the background model used in skymaps. While the excess calculation of each individual point via θ^2 plots is not very efficient concerning the needed CPU time (~ 1 week of CPU time per skymap) it offers an completely independent and very well controlled background calculation. Such skymaps have been produced for few selected objects. In all cases the OfWP map confirms the normal skymap and therefore validates the high quality of the background determination.

6.6.4 The effect of background systematics

Following the last section about a proper background determination it should be mentioned that a large signal to noise ratio ($S_N \equiv N_{ON}/N_{OFF}$) naturally reduces the net effect of background induced systematic uncertainties in the determined excess. For example if the excess shows a $S_N - 1$ of 300% even a 5% systematic uncertainty in the background would only lead to an additional systematic error in the excess of about 1.5%. On the other hand if the excess shows only a $S_N - 1$ of about 10% the same systematic uncertainty would lead to a systematic error of 50% in the excess.

The S_N depends on the flux of the source, its spectrum and the background suppression. As flux and spectrum of a source are fixed parameters, the background suppression is the only way to change the S_N, via usage of strong hadronness and θ^2 cuts with small gamma efficiency. However especially for extended sources the θ^2 cut depends on the source extension itself. In addition, the θ^2 is limited by the angular resolution of the instrument. As shown in Figure 6.9 the background suppression is stronger for higher energies. For most cases the S_N increases as a function of energy (if the spectrum is not particular steep). However, as the total amount of background events at high energies is very low (e.g. $\lesssim 0.01$ events/min for energies > 1 TeV for an integration region of point like source) the statistical errors on the background strongly dominate over the systematic uncertainties even for long observation times. For a systematic uncertainty in the background of 1.5% the size of the systematic error becomes compatible to the statistical error for ≈ 1500 background events (3 OFF positions used). As the background flux is much higher at low energies due to the higher flux of CRs and the worse background suppression, the background at low energies is dominated by systematic effects. This means that the background uncertainty for an analysis threshold of ~ 100 GeV (which implies a background rate of ~ 5 events/min) in any observation longer than ~ 10 h is dominated by systematic effects.

The implications of the background uncertainty on the signal are twofold:

1. **Detection**
   The significance of the excess is calculated from the statistical error of the background.

2. **Spectral information**
   The uncertainty of the excess determines the precision of the spectral points.

Detection of a signal   As discussed in Chapter 6.4, a significant signal is detected if the excess is $\geq 5\sigma$ of the statistical background uncertainty (Li & Ma 1983). Additionally if the systematic error is compatible to the statistical error of the background one requires the signal to be 5% higher than the background. This is a conservative limit which assures that a systematic effect can not cause a false detection. In other words the signal has to be > 3.3 times higher than the systematic background uncertainty. Note that in Aleksić et al. (2012) the same limit of the $S_N - 1$ is translated into a less constraining limit due to the slightly higher systematic uncertainty of the background in the standard 180 OFF calculation. In practice this means that independent of the statistical significance, and therefore the amount of data, the S_N sets a lower limit on the detectability of gamma ray source.

Spectral calculation   In case of a quantification of the excess (i.e., spectral information) the situation is slightly different. In this case one is interested in the precision of the number of excess events (ΔN_{ex}). This number is given as a combination of the statistical uncertainties in the ON and OFF distributions plus the systematic uncertainty of the background:

$$\Delta N_{ex} = \sqrt{\Delta_{stat}(N_{ON})^2 + \Delta_{stat}(N_{OFF})^2 + \Delta_{sys}(B)^2}. \tag{6.8}$$

Here, N_{ON} is the number of ON events, N_{OFF} the number of OFF events, and $\Delta_{sys}(B)$ is the systematic uncertainty of the background in absolute numbers. In the ideal case of three OFF positions, the introduction of the signal to noise as S_N [ratio ON/OFF], and a systematic background uncertainty of 1.5% the above equation can be re-written as:

$$\Delta N_{ex} = \sqrt{S_N \times N_{OFF} + 1/3 \times N_{OFF} + 0.00025 \times N_{OFF}^2}. \tag{6.9}$$

As $S_N > 1$ for any given signal by definition, this formula shows that for low background levels (i.e., small N_{OFF}) the absolute error on the excess is dominated by the signal to noise ratio. As the contribution of the systematic error in the background grows quadratically with the number of background events for any given S_N, there is a certain background level N_{OFF} for which the systematic errors dominate. More than the absolute error of the signal one is interested in the relative error:

$$\frac{\Delta N_{ex}}{N_{ex}} = \frac{\sqrt{S_N \times N_{OFF} + 1/3 \times N_{OFF} + 0.00025 \times N_{OFF}^2}}{N_{OFF}(S_N - 1)} \tag{6.10}$$

Here, N_{ex} is the number of excess events. In the limit of large statistics (long enough observations) this expression reduces to:

$$\frac{\Delta N_{ex}}{N_{ex}}_{\lim N_{OFF} \to \infty} = \frac{0.015}{S_N - 1} \tag{6.11}$$

This result has two major consequences: The relative error of the excess (i.e., the flux) can not be determined with a higher accuracy as given by the systematic uncertainties independent of the amount of data. For example, the excess of a source at the detection limit $S_N - 1 = 5\%$

can never be determined with more than 30% accuracy. Note that this is only a lower limit for the spectral uncertainty as other systematic effects are not yet taken into account. The second consequence is that to improve the spectral measurements the only way is to increase the S_N.

It was shown that the remaining systematic uncertainties in the background determination limit both, the detection capability and the precision of the excess (flux) determination. The most simple way to impose a stronger background suppression is by applying a tighter cut in the hadronness parameter. For a very strong background suppression, very large S_N, equation 6.10 reduces to:

$$\frac{\Delta N_{ex}}{N_{ex}}_{\lim S_N \to \infty} = \frac{1}{\sqrt{N_{ex}}} \qquad (6.12)$$

As the excess grows linear in observation time (assuming a constant source) this equation shows that the precision of the excess, and therefore also the detection capability, has no intrinsic limit in the case of a high S_N. This shows that theoretically the systematic uncertainty in the background determination can be overcome for the case of a very strong background suppression. In reality this approach has two caveats:

- **Separation capability** A tighter hadronness cut does not remove only hadrons but also a fraction of gamma rays and therefore excess events. As for high S_N the amount of excess events is the dominant contribution for the accuracy, this means that due to the loss of excess events the accuracy will shrink.

- **Accuracy of the Monte Carlo simulations** A tight hadronness cut can be translated as the selection of gamma rays most consistent with MC simulations. As the hadronness parameter is trained based on Monte Carlo simulations of gamma rays (see Chapter 6.3.1) this requires highly accurate simulations.

The first point plays a significant role only for extremely large S_N values. Such high values of S_N are only reached for high energies (> 1 TeV, $S_N \approx 80$ for the Crab Nebula) or with long observations. The accuracy and detection capabilities are then limited by the amount of excess. In this case too tight gamma ray selection might not improve the results. For most sources (except very steep spectra) the maximum achievable energy in a given observation therefore only depends on the observation time.

For low energies the situation is different. Here, the limiting factor is not the amount of events but the background suppression. Therefore, one aims to reach the best possible S_N by applying tight hadronness cuts, even though one might sacrifice some excess events too.

Figure 6.32 shows the normalized excess and background as well as the S_N as a function of the applied hadronness cut. Here, a Crab Nebula data sample has been used to simulate a 50 hour observation of a source with a flux of 2% of that of the Crab Nebula. The analysis has an energy threshold of 100 GeV and uses three OFF positions.
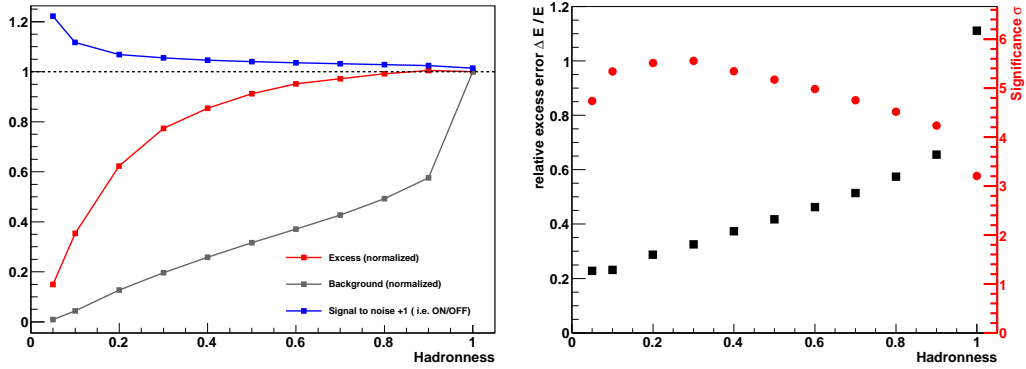
Figure 6.32: Real data model of a 50 hour observation of a source with the same spectral shape as the Crab Nebula but only 2% of the flux. The energy threshold is ~ 100 GeV. Left: Shown is the normalized excess and background as a function of the hadronness cut. In addition, the signal to noise S_N is displayed. Right: The relative error ($\Delta N_{ex}/N_{ex}$ as defined in equation 6.10) on the obtained excess as well as the significance (using 3 OFF positions) of the signal is shown for different values of the hadronness cut. It can be seen that a tighter hadronness cut increases the S_N and simultaneously improves the accuracy of the signal. The significance, however, has its maximum for a hadronness cut of ~ 0.3.

The observed difference between the best hadronness cut for a high significance and the best cut for a maximal precision in the excess determination has two reasons. The significance calculation is defined as the probability that a background fluctuation produces a measured excess, where the intrinsic error of the excess is not directly taken into account. In addition, the excess uncertainty $\Delta N_{ex}/N_{ex}$ (equation 6.10) additionally includes the systematic background uncertainty. Figure 6.33 shows the individual contributions to the total $\Delta N_{ex}/N_{ex}$ for the above assumed scenario.
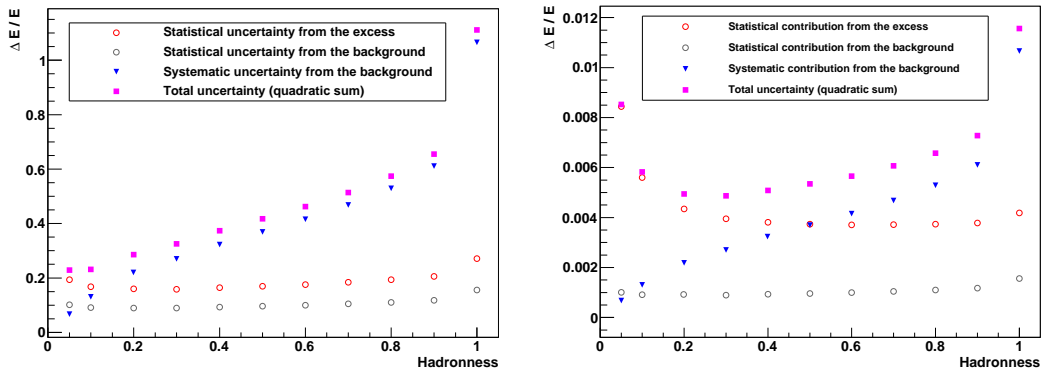
Figure 6.33: Shown are the individual contributions to the uncertainty of the excess above an energy threshold of ~ 100 GeV for different hadronness cuts. The left panel shows the case of a weak source (flux = 2% of the Crab Nebula) and the right plot shows the case of a very strong source (flux = 200% of the Crab Nebula).

Here, the three summands of equation 6.10 correspond to: excess statistics, background statistics, and background systematics. For comparison the individual contributions are also shown for the same analysis but assuming a source twice as strong as the Crab Nebula. In case of the weak source the highest contribution arises from the systematic uncertainty of the background determination. Here, the case of equation 6.11 applies. However it can be seen that for very tight hadronness cuts this contribution can be suppressed below the uncertainty from the excess itself which is equivalent to the case shown in equation 6.12. In the case of a 200 times stronger source this transition happens for much softer cuts. It can be seen that for very tight cuts in hadronness the reduction of the excess causes an increase of the excess uncertainty. The precision of the differential energy spectrum (or the integrated flux) and the uncertainty in the excess are linearly correlated (see also equation 6.3). Additional statistical errors of the observation time or the effective area are negligible. Not negligible is the systematic uncertainty of the effective area. As this parameter can only be determined by Monte Carlo simulations, one is faced with rather large uncertainties. In Aleksić et al. (2012) the systematic uncertainty in the flux level (neglecting a possible shift in the energy scale) due to Monte Carlo simulations is estimated to be $11 - 19\%$ (depending on the energy range). This has a severe effect for the gamma hadron separation. It might happen that the derived separation cuts inside the random forest reflect the best possible separation between gammas and hadrons only for simulated but not for real gammas. The importance of such a difference naturally increases the tighter the chosen hadronness cut is. For cuts which remove $\sim 25\%$ of the simulated gamma rays the imperfections of the Monte Carlo simulations lead to systematic effects of $\sim 15\%$ at low to medium energies (below 1 TeV) and $\sim 30\%$ at high energies (above 1 TeV). This was tested on real data of the Crab Nebula and MrK 421 where the S_N is naturally so high that a spectrum without hadronness cuts can be derived with good precision. For tighter cuts the consequently induced systematic uncertainty grows further. To minimize the systematic uncertainties down to $\lesssim 10\%$ one has to soften the cuts in the hadronness parameter to keep at least 90% of the simulated gamma rays. Depending on the individual analysis this value might reach up to 95%. For the sensitivity and accuracy of the results this restriction leads mainly to a loss at medium to low energies. Throughout this work a hadronness cut of $90 - 95\%$ MC efficiency is used which corresponds to hadronness values of $\sim 0.3 - 0.5$ at low to medium energies and $\sim 0.2 - 0.3$ at high energies. Future improvements of the Monte Carlo accuracy, for example by the study of muon rings (see Chapter 5), will allow to use tighter selection cuts and therefore a more accurate flux determination and a more sensitive analysis.

Chapter 7

The supernova remnant W51C
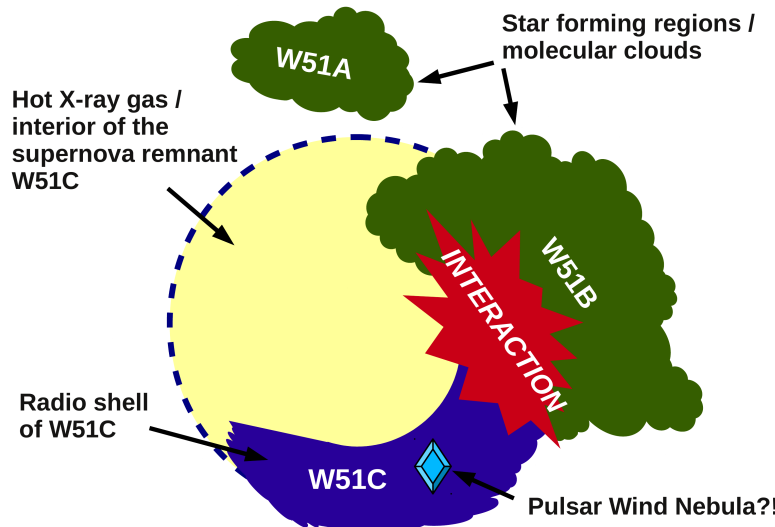
Figure 7.1: Illustration of the W51 region. Seen are the supernova remnant W51C, the star forming regions W51A and W51B, and the Pulsar wind nebula candidate CXO J192318.5+140305. As indicated, the shell of the remnant interacts with the molecular cloud of the star forming region W51B.

This Chapter contains the observational results and their interpretation of the region W51. The system hosts a middle-age supernova remnant (W51C), two large star forming regions (W51A & W51B), and the pulsar wind nebula candidate CXO J192318.5+140305. The shock wave of W51C collides with the molecular and atomic material of W51B. An illustration of the region is shown in Figure 7.1. All observational results obtained with the MAGIC telescopes shown in this chapter have been obtained during this work and represent the major part of this thesis. As leader of this project I was heavily involved in the physical interpretation of the results and responsible for the publication of the results. I presented the first preliminary results (obtained from the first ~ 30 h of data) during a talk at the Fermi Symposium 2011 (Krause et al. 2011). A detailed article has been published in the journal Astronomy & Astrophysics (Aleksić et al. 2012b). This chapter largely reflects the published results, but comprehends some additional information, partially based on newly available multi-wavelength data and recent theoretical developments.

7.1 Introduction

Located at the tangential point ($l = 49°$) of the Sagittarius arm of the Galaxy, the W51 region lies at a distance of ~ 5.5 kpc (Sato et al. 2010). The three main components consisting of the star forming regions W51A and W51B and the supernova remnant W51C (see also Fig. 7.1) are identified according to radio continuum observations. The age of W51C is estimated to be 30 kyrs (Koo et al. 1995a). Several observations provide evidence that the shock wave of W51C collides with the star forming region W51B. Crucial of them are the existence of two 1720 MHz OH masers (Green et al. 1997) and the detection of about 10^3 solar mass atomic gas at a velocity between 20 and $120 \, \mathrm{km \, s^{-1}}$ with respect to its ambient medium (Koo & Moon 1997a). The high-velocity atomic gas exhibits a counterpart in high density molecular gas clumps (Koo & Moon 1997b) sharing the same location and velocity shift. Koo & Moon showed that the shocked gas is displayed in a thin layer in the interface between the SNR shell, as delimited by the X-ray image from *ROSAT* and the *unshocked* molecular gas. This can be taken as the existence of a J-type shock penetrating the dense gas in a particular region of W51B(Koo & Moon 1997b), whereas in the location of the 1720 MHz OH masers the shock should be continuous (C-type). Moreover, recent measurements (Ceccarelli et al. 2011) showed an unusually high ionization of the gas in W51B in certain locations close to W51C coinciding with the shocked gas. They conclude this excess in ionization implies the existence of an intense flow of freshly accelerated cosmic rays (CRs) that, through proton-proton collisions, ionize the hydrogen in the adjacent cloud. Furthermore, ~ 0.2 degrees South-East to the shocked gas region, a hard X-ray source CXO J192318.5+140305 is detected. This object was first resolved by *ASCA* (Koo et al. 2002) and later confirmed by *Chandra* (Koo et al. 2005). Its X-ray spectrum, together with its morphology, suggests that it is a possible pulsar wind nebula (PWN) associated with the SNR. Therefore, the presence of CXO J192318.5+140305 plays a role in the interpretation of the gamma-ray emission from the W51 region. An extended source of gamma rays was first detected by the H.E.S.S. telescopes with an integral flux above 1 TeV of about 3% of the Crab Nebula flux (Fiasson et al. 2009). However, the presented morphological and spectral information was not enough to attribute the origin of the emission to any particular object in the field of view. Also, the Large Area Telescope on board the *Fermi* satellite detected an extended source between 200 MeV and 50 GeV in coincidence with the H.E.S.S. source (Abdo et al. 2009c). Moreover, the reanalysis of the archival MILAGRO data after the release of the first *Fermi* catalog revealed a 3.4σ excess with median energy of 10 TeV coinciding with the *Fermi*/LAT source (Abdo et al. 2009d).

Figure 7.2 shows the W51 region in a multi-wavelength view highlighting some of the main properties. Note that the radio continuum emission contains both thermal and non-thermal emission and the x-ray flux is of thermal nature. Only non-thermal emission is produced by relativistic particles, however also thermal emission can yield important information, for example, concerning the density of the ambient interstellar medium. Thus information from thermal emission can significantly reduce the allowed parameter space concerning the modeling of the non-thermal emission. The main goal in very high energy gamma astronomy is to derive information about the relativistic particle distribution, so the natural focus lies on the modeling of the non thermal emission. Therefore all multi wavelength data, used directly in the modeling, is of non thermal nature.
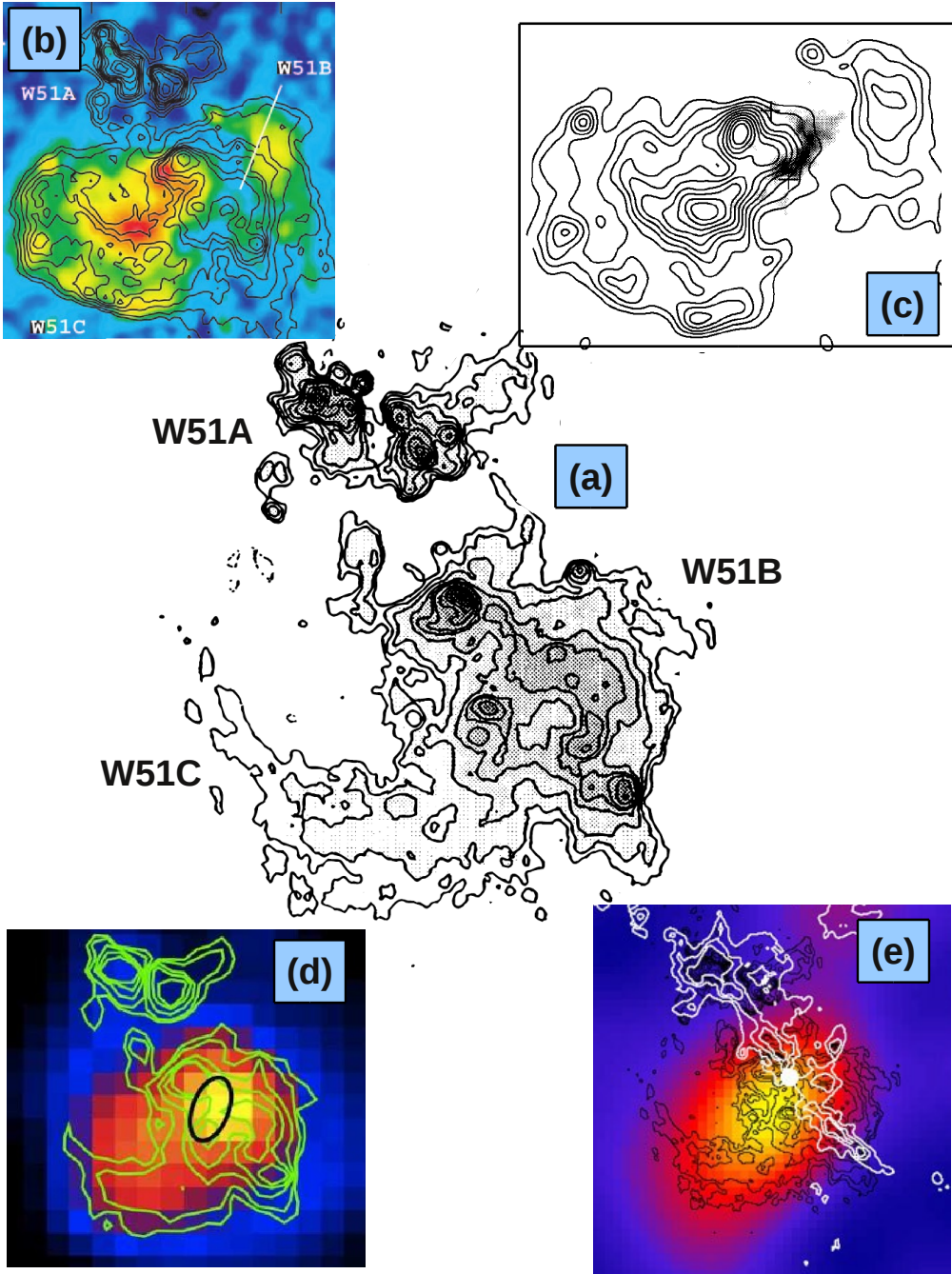
Figure 7.2: The W51 region seen in different wavelength: (a) The radio continuum (21 cm) image clearly shows the three major components (Koo & Moon 1997a). (b) The X-ray image in the range $0.7 - 2.5$ keV reveals the hot x-ray gas filling the remnant. Contours represent radio continuum (330 MHz) (Koo et al. 2002). (c) Contours show the x-ray image, the grey shaded area represents shocked (velocity shifted) atomic gas at the edge of the x-ray emission. (Koo & Moon 1997a). (d) Gamma ray emission $2 - 10$ GeV, overlaid to the radio continuum contours (Uchiyama & et al. 2011). (e) Gamma ray emission > 1 TeV, overlaid are radio continuum contours in black and CO-contours (white) (Fiasson et al. 2009).

At radio wavelengths, synchrotron radiation due to ambient magnetic field explains the emission detected from W51C. At higher energies, there are several processes that yield emission of gamma rays: inverse Compton scattering of electrons on seed photons (cosmic microwave background, starlight), non-thermal bremsstrahlung of electrons on charged target, and decay of neutral pions created in flight from a proton-nucleon collision. The modeling done by (Abdo et al. 2009c) of the spectral energy distribution (SED) of W51C disfavors leptonic models and suggests a hadronic origin for the emission. Further support for the hadronic origin of the emission arises from the unusually high CR ionization.

For the hadronic channel, two main (non-exclusive) mechanisms are to be considered: molecular cloud illumination by cosmic rays that escaped the shock (Gabici et al. 2009b; Ohira et al. 2011) or emission from clouds that are being overtaken by the SNR blast wave (Uchiyama et al. 2010; Fang & Zhang 2010). It is well known that $\approx 10\%$ of the energy released by the supernova explosions in the Galaxy can account for the energy budget of the CR spectrum up to energies close to the *knee* ($\sim 10^{15}$ eV). Nevertheless, the evidence that SNRs can accelerate particles up to such high energies is still missing. Since W51C is one of the most luminous Galactic sources at *Fermi*/LAT energies, observation of gamma rays up to several TeV would have serious implications regarding the SNR contribution to the Galactic CRs: such an observation would show that SNRs are not only capable to provide a sufficient flux, but could also shed light on the question of the maximum energy of CR's still achievable in such a medium age SNR.

For these reasons, W51C represents an interesting case for the study of the acceleration of particles to very high energies (VHE) and their interaction with the interstellar medium. The object from which the gamma rays originate has not yet been identified within the W51 field, and the gamma-ray spectrum has so far been precisely measured only up to some tens of GeV. In what follows, observations with the MAGIC telescopes are reported, which will help to address some of the remaining questions on the gamma-ray source in the W51 region, both regarding its precise location and the physical processes needed to explain the observations. In section 7.2 the performed observations are shown; section 7.3 will focus on the observed morphology and spectral properties; and, finally, in section 7.4 a theoretical framework is applied that can explain the detected gamma-ray emission. After concluding about W51 in section 7.5 this results will be put in a broader context concerning the origin of galactic cosmic rays in section 7.6.

7.2 Observations

MAGIC observed W51 in 2010 and 2011. In the first period of observations between May 17th and August 19th 2010 about 31 hours effective time remained after quality cuts. Between May 3 and June 13 2011 additional 22 effective hours of data were taken, resulting in a total amount of 53 h effective dark time data and covering the zenith angle range from 14 to 35 degrees. The observations were carried out in the so-called wobble mode around the center of the *Fermi*/LAT source W51C (RA = 19.385 h, DEC = 14.19°). All data were taken in stereoscopic mode, recording only events which triggered both telescopes. To minimize systematic effects in the exposure and to optimize the coverage for an unknown extension of the emission a total of six pointing positions ($n_{\text{point}} = 6$), were used. In all pointing positions the wobble distance (offset from the central position) was 0.4°, as it is regularly done in

MAGIC observations.

The analysis of the data was performed using the MARS analysis framework (Moralejo et al. 2009) including the latest standard routines for stereoscopic analysis (Lombardi et al. 2011). A detailed description of the analysis is given in chapter 6. The used analysis has been set up explicitly to match the observing conditions of this source in terms of the zenith angle distribution. The training conditions as described in Chapter 6.5 have been used. To account for the different pixel size in the outer camera between MII and MI the used LEAKAGE2 cuts are 0.3 and 0.15, respectively. The used analysis has been tested on Crab Nebula data and showed the same performance as described in Chapter 4.4. In addition the obtained results have been cross checked by two independent analysis showing no significant deviations. The background estimation uses the *OFF from Wobble partner* algorithm developed in this work (see chapter 6.6.3). In a first step of the analysis a blind map (see Chapter 6.4.2) of the region was produced above an energy threshold of 150 GeV. Figure 7.3 shows the results together with the used pointing positions (W1-W6). In addition the integration region (red dashed circle) and the background regions (dotted circles) used in the θ^2 analysis are marked.
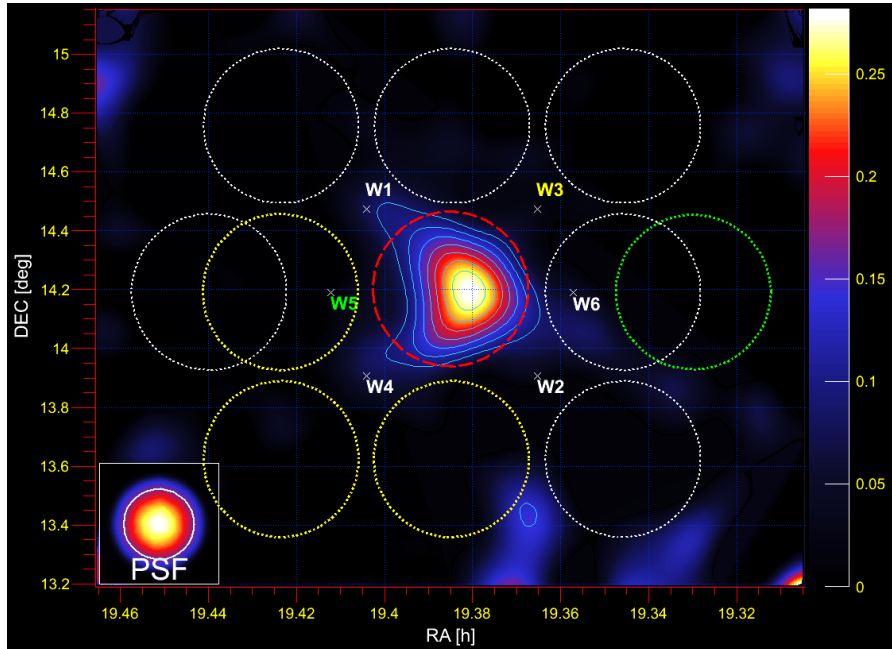
Figure 7.3: Relative flux map (blind mode) above an energy threshold of 150 GeV. In addition the pointing positions (W1-W6), the integration region (red dashed circle) and the sky regions used for the background determination by means of θ^2 plots are used. For W5/W6 only one OFF region has been used (the background region for W5 is marked in green as an example). For the pointing positions W1-W4 the background was estimated from the corresponding three OFF regions determined by OfWP. The used background regions for W3 are marked in yellow. For more details see text. Contours levels represent TS values starting at 3 and increasing by one per contour.

A sophisticated scheme for the background estimation was in this thesis developed (see chapter

xx). The aim of this method is to fully account for systematic shifts in the camera response which otherwise would lead to wrong background estimations. The detailed description of all relevant factors on the camera response are in general described in chapter 6.6.3 while here I will focus on the W51 specific observations. All used OFF regions are well separated from the ON region. Even though some OFF regions overlap or even share the same sky coordinates (for example, the region between W2 and W4 represents an OFF region observed during both pointing positions) they are statistically independent. Even though the same sky regions are observed, the data taking is performed at different times, in different pointing positions and are also located at different coordinates in the camera plane. For each pointing position, the ON sample is compared to an OFF sample obtained from the combination of the $n_{\mathrm{point}}-1$ OFF regions observed at the same focal plane coordinates but from the complementary pointing positions. Four of the pointing positions (W1-W4) have an observation time of the order of $\sim$ 12 hours each. Therefore, three background samples per pointing can be averaged. Exemplary, the background regions used for W3 (extracted in W1, W2, and W4) are highlighted in yellow (Fig. 7.3). The remaining two positions have an observation time around 2 hours each and, in this case, the background was estimated from one sample only. As an example the used background region for W5 (obtained in W6) is marked in green (Fig. 7.3). This method ensures a maximum usage of symmetrical OFF positions without introducing big scaling factors due to differences in the observation times. The significance of the excess is determined from the combined θ^2 distribution of all individual pointing positions using equation 17 in Li & Ma (1983) (Li&Ma significance hereafter).

7.3 Results

7.3.1 Detection

Figure 7.4 shows a close-up of the relative flux map[1] above an energy threshold of 150 GeV around the center of the observations. The angular resolution of MAGIC for this analysis is $0.085°$ defined as one sigma of a two dimensional Gaussian distribution, see Aleksić et al. (2012) for details. The map was smeared with a two-dimensional Gaussian kernel with a sigma equivalent to that of the angular resolution[2]. Contours represent isocurves of test statistics (TS) evaluated from the excess of gamma-like events over the derived background model. The signal region is defined within $0.265°$ radius around the *Fermi*/LAT position. This radius is selected in order to include most of the emission ($\gtrsim 90\%$) observed in the relative flux map. We compute an excess of 1371.7 ± 122.5 events inside the signal region, yielding a statistical significance of 11.4 standard deviations. The centroid of the emission (black dot in Fig. 7.4, statistical errors are represented by the ellipse) has been derived by fitting a 2 dimensional Gaussian function to the map, prior to the smearing. The centroid coordinates found are:

$$\mathrm{RA} = 19.382 \pm 0.001\,\mathrm{h} \qquad \mathrm{DEC} = 14.191 \pm 0.015\,°$$

This deviates by $0.04°$ from the position reported by *Fermi*/LAT, marked as the center of the sky map (green cross) (see Fig. 7.4). To determine the extension of the source the distribution

---

[1]Relative flux means excess events over background events. This quantity accounts for acceptance differences between different parts of the camera. See Chapter 6.4.2 for details

[2]The PSF shown in all skymaps is the sum in quadrature of the instrumental angular resolution and the applied smearing.

of the squared angular distance θ^2 between the arrival direction of the gamma-like events and the centroid of the MAGIC source (see Fig.7.5) was computed, both for the integration area represented in Fig. 7.4 and for a combination of signal-free regions, as described above, to estimate the background.
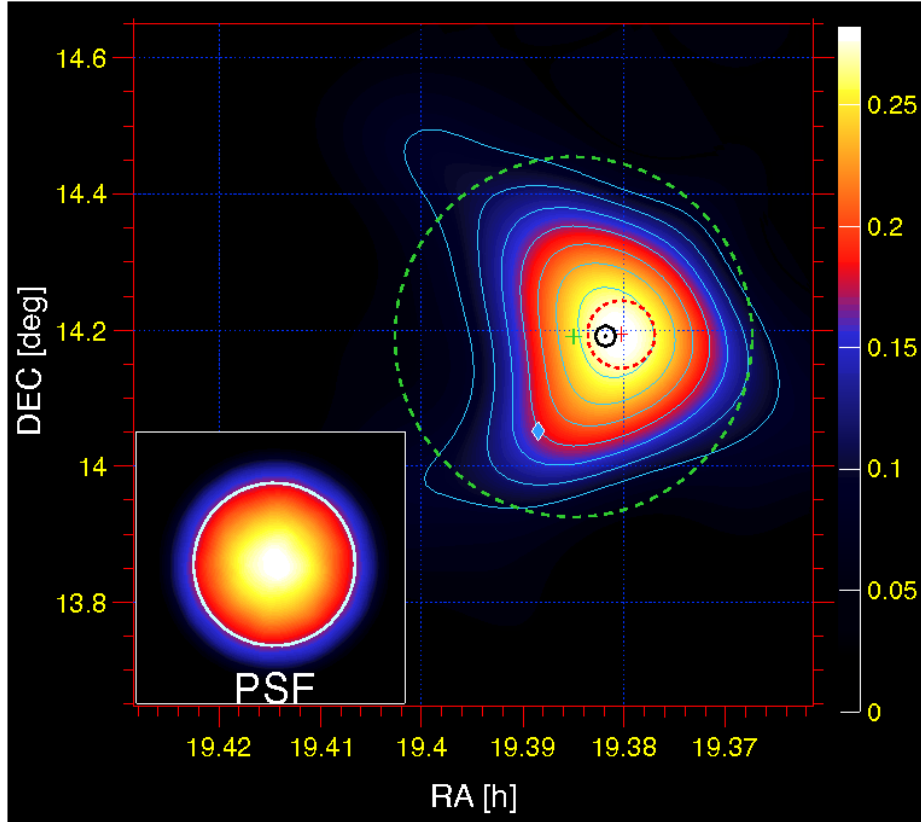
Figure 7.4: Relative flux (excess/background) map above $150\,\mathrm{GeV}$ around W51. Overlaid are contour levels from test statistics starting at 3 and increasing by one per contour. The map was smoothed with a Gaussian kernel of 0.085°. The green cross shows the center of the observations, while the green dashed circle represents the integration area. The black dot is the determined position of the centroid with the statistical uncertainties shown by the surrounding black ellipse. The region of shocked atomic and molecular gas (Koo & Moon 1997b,a) is represented by the red dashed ellipse. The blue diamond shows the position of the possible PWN CXO J192318.5+140305. In the left lower corner the gaussian sigma of a point-like source (PSF) after the applied smearing is shown.

An exponential function (corresponding to a Gaussian-shape source) is fitted to the difference between ON and OFF θ^2 distributions. For illustration, the shape of a point source with the same excess was calculated from Monte-Carlo simulations and is shown for comparison (red

curve) to the fit to the data (blue curve). After correcting for the angular resolution (0.085 degrees $> 150\,\mathrm{GeV}$) of the instrument the intrinsic extension of the source is determined to be: $0.12 \pm 0.02_{\mathrm{stat}} \pm 0.02_{\mathrm{syst}}$ degrees.
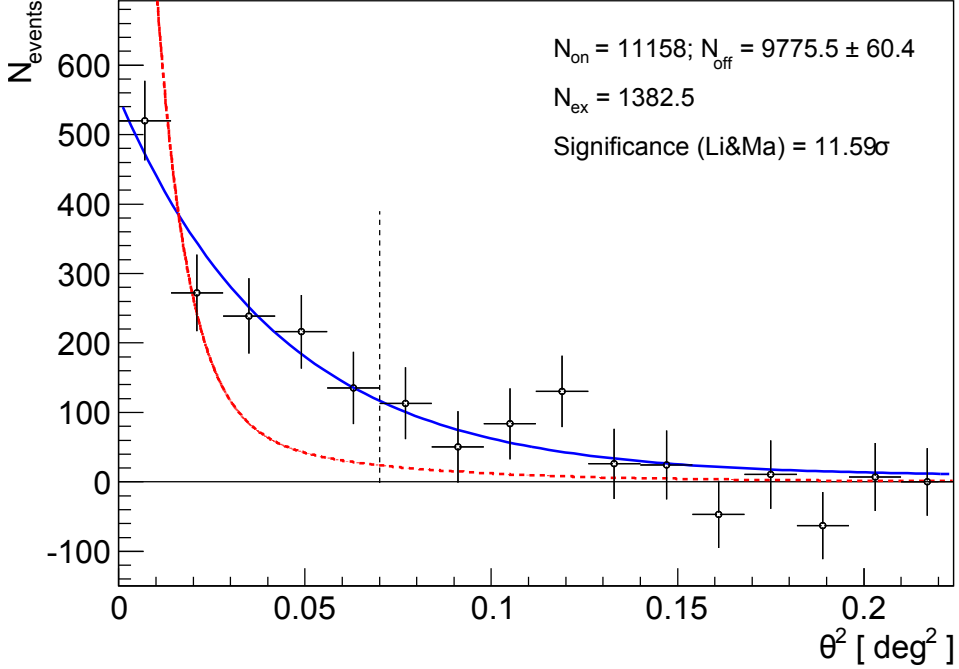
Figure 7.5: θ^2 distribution of the excess events towards the centroid of the emission determined from figure 7.4, showing a clear and extended signal. The excess has been fitted by an exponential (blue curve) to determine the extension. For comparison the shape of a point-like source with the same excess, determined from Monte-Carlo simulations, is shown (red curve).

7.3.2 Spectrum

In what follows the energy spectrum of the gamma-ray emission is extracted. The effective area was estimated using a Monte-Carlo data set with photons simulated uniformly on a ring of $0.15°$ to $0.55°$ distance to the camera center. This should account for variations of the acceptance across the area of the source. The effect of using this ring Monte-Carlo compared to standard point-like ones turns out to lie well within the statistical uncertainties. The spectrum needs to be unfolded in order to take into account the finite energy resolution and the energy bias of the instrument (Albert et al. 2007a). The unfolded spectrum shown in Fig. 7.6 starts at $75\,\mathrm{GeV}$ and is well described ($\chi^2/\mathrm{NDF} = 5.26/6$) by a simple power law of the form:

$$\frac{dN}{dE} = N_0 \left(\frac{E}{1\,\mathrm{TeV}} \right)^{-\Gamma} \tag{7.1}$$

with a photon index of $\Gamma = 2.58 \pm 0.07_{\mathrm{stat}} \pm 0.22_{\mathrm{syst}}$, and a normalization constant at $1\,\mathrm{TeV}$ of $N_0 = (9.7 \pm 1.0_{\mathrm{stat}}) \times 10^{-13} \mathrm{cm}^{-2}\mathrm{s}^{-1}\mathrm{TeV}^{-1}$. This is the first time that the differential energy spectrum for this source at VHE is measured. The energy threshold of MAGIC allows almost

to connect the spectrum to the *Fermi*/LAT points (Abdo et al. 2009c). The systematic error on the flux normalization is 15%, which includes the systematic uncertainties of the effective area (11%) and the background calculation. In addition, the systematic uncertainty in the energy scale is estimated to be 17 % at low ($\sim 100\,\mathrm{GeV}$) and 15 % at medium ($\sim 250\,\mathrm{GeV}$) energies. The integrated flux above $1\,\mathrm{TeV}$ is equivalent to $\sim 3\%$ of the flux of the Crab Nebula above the same energy, and therefore agrees with the previous flux measurement by the H.E.S.S collaboration (Fiasson et al. 2009). The spectral index measured by MAGIC agrees well with the one measured by *Fermi*/LAT above 10 GeV (Paneque et al. 2011) of $\Gamma = 2.50 \pm 0.18_{\mathrm{stat}}$. Thus the emission from W51 can be described by a single power law between $10\,\mathrm{GeV}$ and $5.5\,\mathrm{TeV}$.
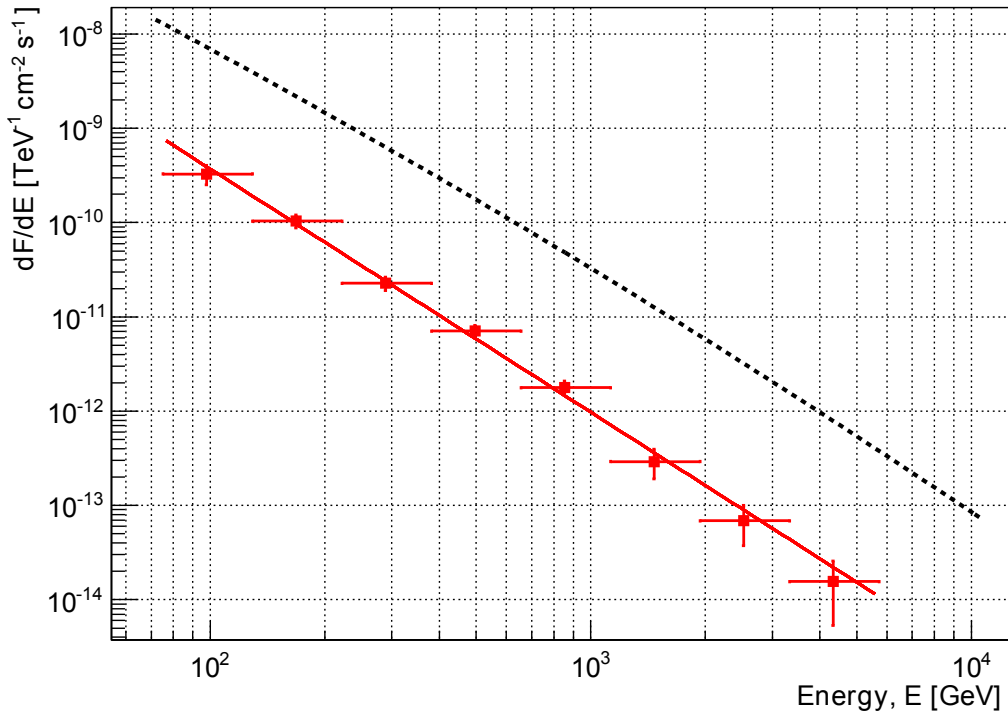
Figure 7.6: Differential energy spectrum of W51 obtained by MAGIC. The red points represent the differential flux points after unfolding. The red line represents a power law fit to the data. The error bars represent the statistical errors. For comparison, the dotted line represents the spectrum of the Crab Nebula as shown in Aleksić et al. (2012).

7.3.3 Detailed morphology

MAGIC reaches its best sensitivity in the energy range from $\sim$300 to $\sim$1000 GeV. At energies of $300\,\mathrm{GeV}$ the angular resolution of MAGIC is $0.075°$ and it improves until reaching the saturation value of $0.054°$ at energies above $1\,\mathrm{TeV}$. We investigate sky maps in two energy ranges. The first map covers the estimated energy range from 300 to $1000\,\mathrm{GeV}$, and the second the energies above $1000\,\mathrm{GeV}$. Both maps were smeared with a Gaussian kernel of a width equal to the angular resolution of the instrument in the corresponding energy range.
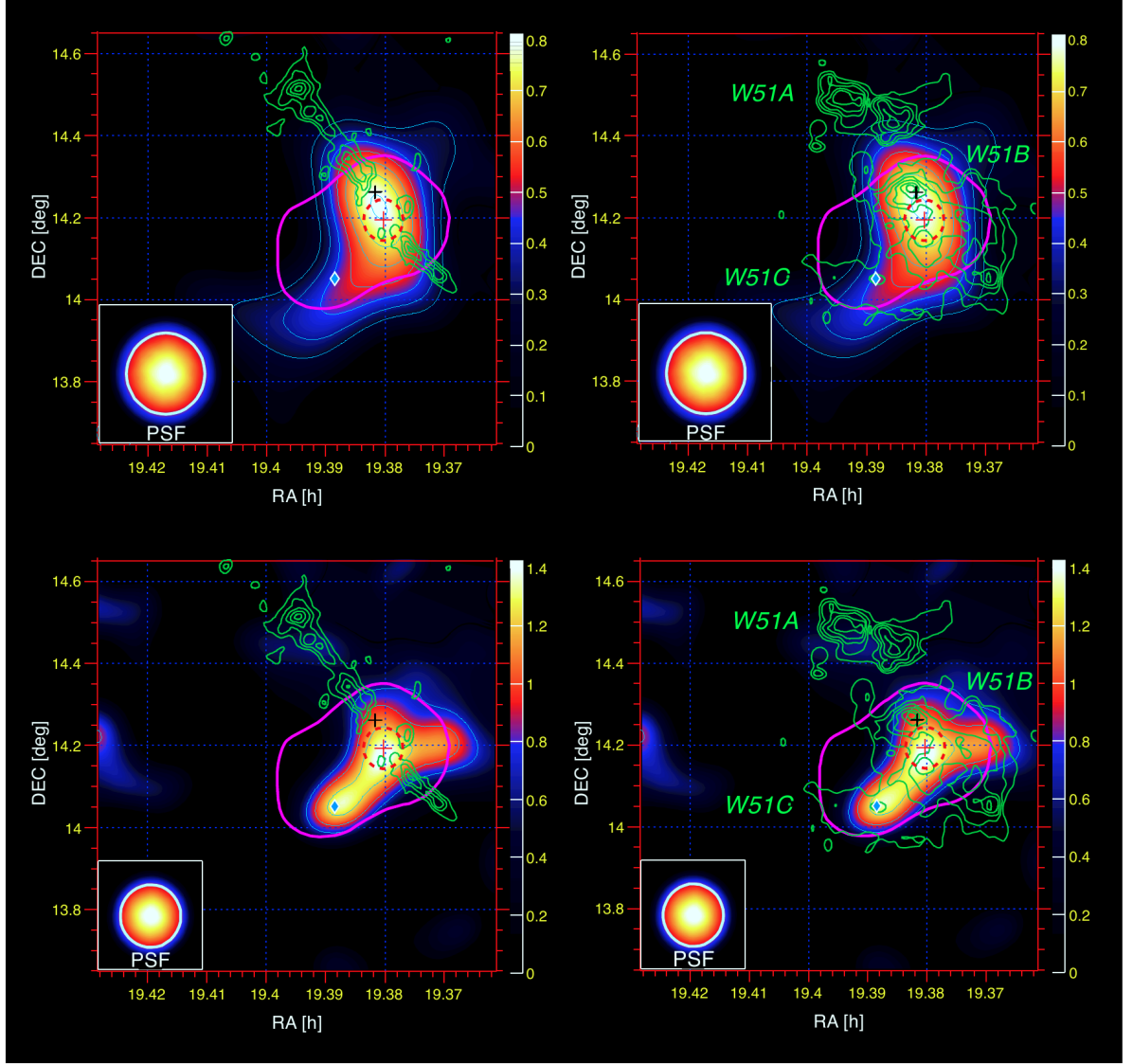
Figure 7.7: Relative flux maps: From $300\,\text{GeV}$ to $1000\,\text{GeV}$ (top) and $>$ $1000\,\text{GeV}$ (bottom). On the left the MAGIC data are combined with the ^{13}CO (J=1-0) intensity maps from the Galactic Ring Survey (see http://www.bu.edu/galacticring/new_index.html), integrated between 63 and $72\,\text{km}\,\text{s}^{-1}$ and shown as green contours. On the right the green contours represent the 21 cm radio continuum emission is shown from (Koo & Moon 1997a). In all maps the blue diamond marks the position of CXO J192318.5+140305 and the black cross the position of the OH maser emission (Koo et al. 2005; Green et al. 1997). The red dashed ellipse represents the region of shocked atomic and molecular gas (Koo & Moon 1997b,a). The 3 counts contour above $1\,\text{GeV}$ determined by *Fermi*/LAT is displayed by the pink contour. In each picture the gaussian sigma of a point-like source (PSF) after the applied smearing is shown. The color scale (blue to red) shows the relative flux as measured with MAGIC. In addition the TS contours (cyan) are shown starting at 3 and increasing by one per contour.

In Fig. 7.7 (top panels) the relative flux map between 300 and 1000 GeV is shown. The overall shape of the emission appears to be elongated showing a tail towards the lower left. The maximum of the emission coincides with the shocked-gas region, represented by the red dashed circle, where the lack of molecular material at the systemic velocity is clear (top left panel). The determined centroid and extension agree within statistical errors with those found above 150 GeV.

Above 1000 GeV (Fig. 7.7, bottom panels) the centroid and the extension of the emission are in agreement with those obtained at lower energies. The South-Eastern tail of the source, evident in the 300 to 1000 GeV map, becomes a prominent feature coincident with the possible PWN CXO J192318.5+140305 at energies above 1 TeV. However, the main part of the emission is still coincident with the shocked gas region.

While the centroid of the emission is consistent with the position of the shocked gas, in addition a tail towards the PWN candidate is seen. Note that, in any case, the VHE emission does not strictly follow the SNR shell shape (as seen from the 21 cm continuum emission shown by green contours in the right panels), nor does it follow the molecular gas with the velocity expected due to Galactic rotation, as traced by the ^{13}CO (green contours, left panels). The tail seen towards the PWN rises the question of a possible substructure in the emission.

Projections

In order to investigate the source for underlying structures, the unsmeared excess distribution of the source has been projected along a line. The line is 2° long divided in 40 bins with 0.05° width. The orientation of the line is defined by the position of the PWN candidate and the centroid of the shocked clouds identified by Koo & Moon (RA = 19.380 h, DEC = 14.19°). Events within a distance of 2 gaussian sigma of the instrumental PSF to the line were projected. Since the angular resolution is energy dependent, the width of the projected rectangle is 0.3° and 0.216° for the energy ranges from 300 to 1000 GeV and above 1000 GeV, respectively. OFF events were estimated from the background model. The number of projected excess events is not the same as in the spectral calculation, where a circular region of 0.265° radius around the center of the observations was used. Therefore, the projected excess does not allow for direct determination of the fluxes from specific regions of the map. The projection has been carried out in both energy ranges independently on the unsmeared excess distribution and is shown in Fig. 7.8.

The projection is fitted alternatively using one and two Gaussian functions. χ^2/d.o.f. values are 28/17 (one Gaussian) and 18/14 (two Gaussians) for the medium-energy range and 16/17 (one Gaussian) versus 12/14 (two Gaussians) for the high-energy events. The data are very well described with the two Gaussian functions, where the centroid of the individual functions coincides within statistical errors with the position of the shocked gas and the PWN. The tail-like feature towards the possible PWN is more peaked in the energy range above 1000 GeV.

The statistics are not sufficient to clearly discriminate between an extended source of Gaussian excess, an extended source of a more complicated shape, or two individual sources. However, the fact that there is no region of dense gas close to the PWN makes it difficult to explain the TeV emission in this area under the assumption of uniform CR density. A possible scenario of two emission regions could manifest itself in different spectral behaviors.
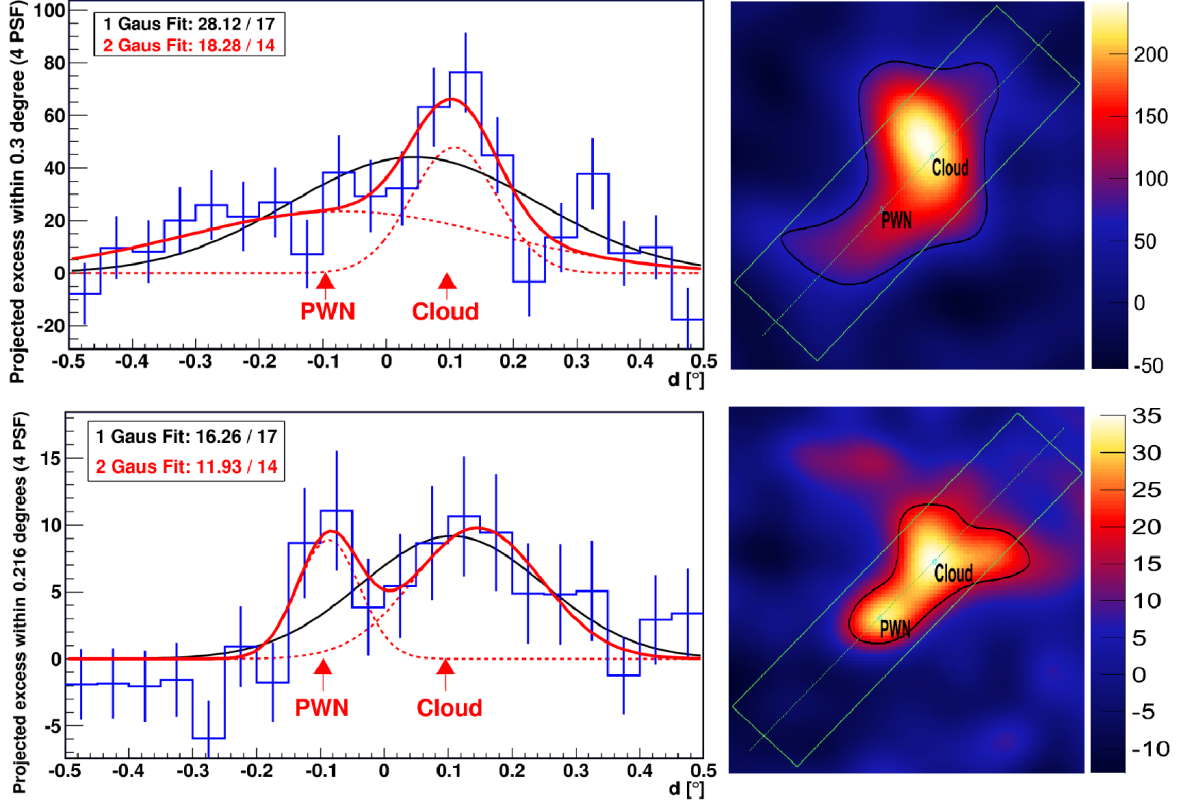
Figure 7.8: Projection of the excess inside the marked box in both differential sky maps: 300 GeV to 1000 GeV (top) and above 1000 GeV (bottom) along the line connecting the PWN and the shocked-gas region described in Koo & Moon (1997a,b). The projection is done with the unsmeared distribution. The excess is fitted with one (black) and two (red) Gaussian curves. The positions of the shocked gas and the PWN are marked with red arrows. On the right sketches of the skymaps in both energy ranges are shown to illustrate the projected areas, as well as the position of the cloud and the PWN, respectively. The projected box has a length of $1°$ and a width of 4 gaussian sigma of the instrumental PSF. The sky maps show the smeared excess (for comparison with Fig. 7.7) with the black contour representing the 3 TS contour.

Energy spectra of individual regions

To quantify the results obtained from the projections in more detail the spectral properties of the detected signal were investigated. Two individual regions within the source are analyzed separately. One was defined to cover the shocked cloud region with centroid at $RA = 19.380\,h, DEC = 14.19°$; hereafter this will be called the *cloud* region. The second one was defined by the position of CXO J192318.5+140305 and hereafter will be called the *PWN* region. To avoid contamination from the surrounding emission, and their possible spread due to the worse angular resolution at lower energies, an integration radius of $0.1°$ was used. The same analysis was performed on data of the Crab Nebula showing that such a region contains

at least 70% of the excess from a point-like source above 300 GeV. For an easier comparison, the integration radii were chosen to be the same. The distance between the chosen positions is 0.19°. There is an area of overlap of only 1.7% compared with the integration area of each region, therefore they can be treated as independent. The combined areas of both regions represent about 30% of the area used to determine the overall spectrum. The small distance between the regions and a very similar average distance to the camera center allows one to assume the same acceptance of gamma-like events for both regions, at least within 5%.

For each individual region the amount of excess events above three different energies was determined. From this the contribution to the overall excess was computed. The resulting values are shown in Table 7.1. Excesses used to calculate these ratios show a significance of at least 2.9σ. Both regions show significant emission above 300 GeV with 5.6σ and 7.9σ for the *PWN*- and *cloud*-region, respectively.

Table 7.1: Number of excess events determined for the *PWN*-region and the *cloud*-region and their contribution to the overall emission. Within the statistical errors we do not detect a significant energy dependence on their contributions to the overall excess.

E [GeV]	*cloud*	*PWN*	*cloud*/all [%]	*PWN*/all [%]
> 300	200 ± 30	132 ± 25	30 ± 5	19 ± 4
> 500	116 ± 17	79 ± 17	32 ± 6	22 ± 5
> 1000	48 ± 10	27 ± 10	43 ± 12	24 ± 10

The excess contribution arising from the cloud region is about 30% and shows no dependence on energy. For the *PWN* region the contribution is about 20% neither showing a dependence on energy. A spectral analysis for both region was performed above 350 GeV assuming a point source (see Fig. 7.9). Note that this assumption is probably correct for the *PWN*-region, if proven to be independent, but probably not for the *cloud*-region. The assumption is made for simplicity reasons, and an easier comparison between the two spectra. The main purpose of this analysis was to look for spectral difference between the emission arising from the individual regions and is not affected by this assumption. For both regions the emission can be well described by a simple power law. The normalization constants at 1 TeV are

$$N_{\mathrm{cloud}} = (4.3 \pm 0.9_{\mathrm{stat}}) \times 10^{-13} \mathrm{cm}^{-2}\mathrm{s}^{-1}\mathrm{TeV}^{-1}$$

$$N_{PWN} = (2.3 \pm 0.8_{\mathrm{stat}}) \times 10^{-13} \mathrm{cm}^{-2}\mathrm{s}^{-1}\mathrm{TeV}^{-1},$$

respectively. The spectral index of the cloud emission is $-2.4 \pm 0.5_{\mathrm{stat}}$. For the *PWN*-region an index of $-2.5 \pm 0.6_{\mathrm{stat}}$ is obtained. This translates into an integrated flux above 350 GeV of 1.2% for the *cloud*-region and 0.7% for the *PWN*-region compared to that of the Crab Nebula above the same energy. The large statistical uncertainties arising from the low fluxes of the individual regions do not allow detailed constraints on their flux levels or the spectral shapes. However the emission arising from the *cloud*-region appears to be more luminous at all energies. The excess contribution of each of the regions reflects the same behavior and shows no dependence on energy, suggesting no intrinsic morphological changes in the energy ranges investigated here. This is in agreement with the spectra, with the differential maps,

and with the projections of the excess distribution. It should be noted that the number of excess events within the *PWN* region and the *cloud* region (Table 7.1) agrees within statistical errors with the projected excess (Fig. 7.8) found within ±0.1 degree from the PWN and the cloud positions, respectively. By looking at the skymaps (Fig. 7.8) only, the emission around the PWN seems to be more intense above 1 TeV. However this can be explained by the worse angular resolution at lower energies and by a much higher signal-to-noise ratio at the higher energies.
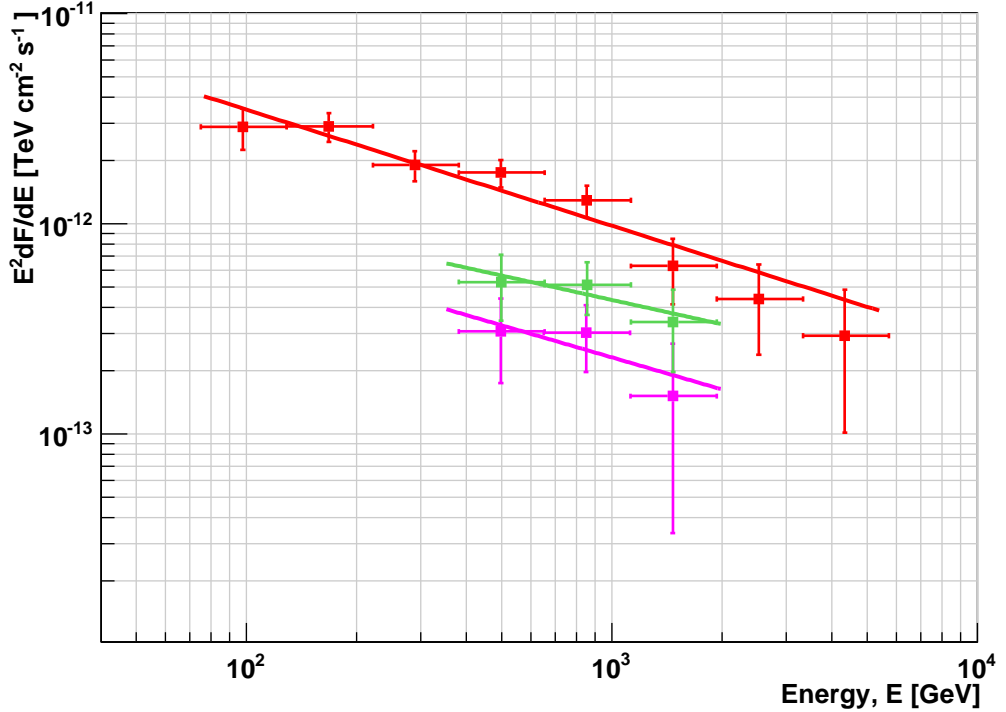
Figure 7.9: Unfolded spectral energy distributions for the overall emission (red), the *cloud*-region (green) and the *PWN*-region (pink) in comparison. In addition a power law fit to the data of each region is shown. The sum of the individual spectra do not add to the overall flux, caused but the not complete coverage of the emission overall emission by the *PWN* and the *cloud* region.

7.4 Discussion

Before modeling the multi-wavelength emission the possibility that the PWN alone is the source of all the emission is shortly addressed. Followed by a qualitative discussion on the possibility of contribution of the PWN to the overall emission and the justification of the approach using a one-zone model (i.e. one homogeneous emission region filled with one particle distribution per species) to investigate the processes underlying the emission.

First, recall that no spectral difference or morphological energy dependence has been found. In order to assess whether the VHE emission can be originated only by the PWN candidate, we consider the estimated rate of rotational energy loss $\dot{E}= 1.5 \times 10^{36}\,\mathrm{erg\,s}^{-1}$ estimated by

Koo et al. (2005) with the empirical relation from Seward & Wang (1988). Given the observed luminosity of the order of $\sim 10^{36}\,\mathrm{erg\,s^{-1}}$ reported in Abdo et al. (2009c), it seems unlikely that the PWN alone is the source of all gamma-ray emission since, it would require an extremely high efficiency in the conversion from rotational energy into gamma rays. In addition the maximum emission coincides with the high density region of the shock cloud interaction. In this sense the observed emission should be caused by Bremsstrahlung in the dense medium of relativistic electrons accelerated in the pulsar wind. In addition there is no obvious explanation why these emission should be spatially coincident with the shock cloud interaction instead of the in general dense regions of W51B. At the location of the PWN candidate itself the low density should lead to a gamma ray spectrum dominated by Inverse Compton scattering of the same electron population on the ambient photon fields. In this scenario, the emission arising from the *cloud*-region is expected to be softer by $\approx E^{-0.7}$, which despite the large errors on the individual spectra, seems unlikely. Thus, both, from morphological and energetic reasons, a scenario attributing the overall emission to the PWN candidate is disfavored.

Second, the possibility of a two-zone model is considered. The *PWN* region can account for the $\sim 20\%$ of the gamma-ray emission confined in a point-like source, however the brightest part is the *cloud* region. This scenario would require an $\dot{E}$ conversion into gamma rays of the order of 10%, in agreement with the generally accepted value. A possible contribution of PWN candidate has also been estimated by Abdo et al. (2009c), who obtain a value of $\sim 10\%$ similar to the here derived value.

With the current statistics and resolution, it cannot be established if there is a spectral difference between the *cloud* and the *PWN* region, but the contribution of the *PWN*, is in any case small. For the reasons above, the simplest approach is to assume one overall particle distribution underlying the emission we observe.

This assumption introduces an error in the flux normalization of about 20% in case part of the emission originates from the PWN candidate; this uncertainty lies within the statistical and systematic errors of the MAGIC measurement.

7.4.1 Model description

The SNR is modeled as a sphere homogeneously filled with hydrogen, helium and electrons, with respective average number densities n_{H}, n_{He} and n_{e^-}. For the relative abundances of helium the cosmic abundance ratio $n_{\mathrm{He}} = 0.1\,n_{\mathrm{H}}$ is assumed. Full ionization of the medium is assumed, such that $n_{e^-} = 1.2\,n_{\mathrm{H}}$ yields for the electron ratio. The magnetic field B is assumed to be homogeneous inside the sphere; Koo et al. (2010) derived an upper limit for it of $B_{\parallel} < 150\,\mu$G, but Brogan et al. (2000) measured a local magnetic field as high as 1.5–1.9 mG towards the maser sites.

The geometric model of the SNR and molecular cloud interaction region as proposed by Koo & Moon (1997a), describes a scenario in which the spherical blast wave of the supernova explosion interacts with part of the cylindrical molecular cloud contained inside the SNR volume. Carpenter & Sanders (1998) estimated the total mass of the molecular cloud to be $m_{\mathrm{cloud}} = 1.9 \times 10^5$ M$_\odot$. From the radio measurements in Moon & Koo (1994) the angular extent of the partial radio shell of the SNR is known to be $\theta \approx 30'$. A clear displacement between the morphology presented here and the center of the spherical extended SNR as seen in thermal X-ray emission (Koo et al. 1995b) is observed. The maximum of the emission is located at the interaction region of remnant and the molecular cloud. Therefore it is concluded

that the size of the remnant is not directly physically related to the size of the VHE emission region. The intrinsic extension determined in this work is adopted to determine the radius of a spherical emission zone. Assuming a distance to W51C of 5.5 kpc, as measured by Sato et al. (2010) and Moisés et al. (2011), the radius of the sphere is estimated to be 24 pc.

The kinetic energy released by the supernova to the SNR has been estimated in Koo et al. (1995b) as $E_{SN} \approx 3.6 \times 10^{51}$ erg, using both a Sedov and an evaporative model to derive the parameters of the SNR. This value will be compared with the one obtained from the integral of our initial spectra, after fixing the normalization constants, to determine how much of the initial explosion energy of the supernova has been converted into particles (W_e, W_p). The different parameters of the supernova, of the SNR, and of the molecular cloud are summarized in Table 7.2.

Table 7.2: Parameters of the W51C supernova, supernova remnant and molecular cloud.

Parameter	Value	Reference
age	$\approx 30\ 000$ yr	Koo et al. (1995b)
E_{SN}	$\approx 3.6 \times 10^{51}$ erg	Koo et al. (1995b)
d	5.5 kpc	Sato et al. (2010)
		Moisés et al. (2011)
θ (radio)	$\approx 30'$	Moon & Koo (1994)
$B_{\parallel}$	$< 150\ \mu$G	Koo et al. (2010)
B (at masers)	1.5–1.9 mG	Brogan et al. (2000)
α_r	≈ -0.26	Moon & Koo (1994)
m_{cloud}	$1.9 \times 10^5\ \mathrm{M}_\odot$	Carpenter & Sanders (1998)

The spectral energy distribution is modeled folding input spectra of accelerated particles with cross sections of processes yielding photons; this includes synchrotron radiation, inverse Compton scattering (IC), non-thermal bremsstrahlung and π^0 decay (Blumenthal & Gould 1970; Baring et al. 1999; Kelner et al. 2006).

For IC, three seed photon fields are considered: the cosmic microwave background ($kT_{CMB} = 2.3 \times 10^{-4}$ eV, $u_{CMB} = 0.26$ eV cm^{-3}), infrared ($kT_{IR} = 3 \times 10^{-3}$ eV, $u_{IR} = 0.90$ eV cm^{-3}) and optical ($kT_{OPT} = 0.25$ eV, $u_{OPT} = 0.84$ eV cm^{-3}), with temperatures and energy densities for the infrared and optical components adopted from Abdo et al. (2009c). Bremsstrahlung is computed on a target of electrons and ions. For the π^0 production cross section, the parametrization of Kelner & Aharonian (2006) is adopted with a constant nuclear enhancement factor of 1.85 (Mori 2009).

The multi-wavelength data considered here include radio continuum measurements (Moon & Koo 1994), high-energy observations by the *Fermi*/LAT (Abdo et al. 2009c) and the new VHE data taken with MAGIC, presented in this work. Included is also one data point by MILAGRO (Abdo et al. 2009d). Note that the lowest energy radio data point may be affected by free-free absorption, see Moon & Koo (1994) or Copetti & Schmidt (1991), which is not considered here. However, this single point does not affect the fitting of the radio data. The radio measurements in Moon & Koo (1994) indicate a spectral index of $\alpha_r \approx -0.26$ (as defined by $S_\nu \propto \nu^{\alpha_r}$). This can be attributed to electrons emitting synchrotron radiation and fixes the initial power-law index of the electron spectrum to $s \approx 1.5$. For simplicity this value is adopted both for electrons and protons.

As a conservative upper limit for the non-thermal X-ray emission the integrated thermal X-ray flux of the whole remnant as measured by *ROSAT* (Koo et al. 1995b) converted into a differential flux in the sub-keV range is used. The thermal emission observed by Chandra from CXOJ192318.5+140305 is used accordingly as an upper limit to the non-thermal emission of the possible PWN. The MILAGRO measurement has a significance of 3.4 σ, was derived assuming a gamma-spectrum $\propto E^{-2.6}$ without a cut-off and is given at an energy of 35 TeV. For details see Abdo et al. (2009d). Very recently *Agile* (Guiliano et al. 2013) reported an upper limit (UL) on the gamma ray emission around 100 MeV.

Separate scenarios are considered in which one of the following emission processes dominates over the others, pion decay, inverse Compton, or Bremsstrahlung. The models discussed here are obtained using as equilibrium particle spectra a broken power law with an exponential cut-off, both for electrons and protons, of the form:

$$\frac{dN_{e,p}}{dE_{e,p}} = K_{e,p} \left(\frac{E_{e,p}}{E_0}\right)^{-s} \left[1 + \left(\frac{E_{e,p}}{E_{\mathrm{br}}}\right)^{\Delta s}\right]^{-1} \exp\left[-\left(\frac{E_{e,p}}{E_{\mathrm{cut},e,p}}\right)\right] \tag{7.2}$$

The spectral index changes here from s to $s + \Delta s$ at an energy E_{br} with a smooth transition. The exponential cut-off at $E_{\mathrm{cut},e,p}$ reflects the roll-off of the particle spectrum near the maximum energy, arising from the acceleration and confinement mechanism, as well as energy losses.

The break energy E_{br} is fixed from the *Fermi*/LAT data, while the new MAGIC data allows to fix the spectral break Δs. A spectral break in the particle spectrum at these energies is traditionally thought to be inconsistent with both standard or non-linear diffusive shock acceleration theory, see Malkov & O'C Drury (2001b) and references therein. However, Malkov et al. (2012a) have recently proposed a mechanism which can also explain a spectral break in the cosmic ray spectrum of $\Delta s = 1$ by strong ion-neutral collisions in the surroundings of a SNR, leading to a weakening in the confinement of the accelerated particles. The spectral break that was derived here is $\Delta s = 1.2$, not far off this prediction, giving a hint that this mechanism might be responsible for the observed break. Note also that other authors have proposed scenarios in which the CR spectrum, and consequently the gamma-ray spectrum, can show one or more spectral breaks, for example due to finite-size acceleration or emission region (Ohira et al. 2011) or energy dependent diffusion of run-away CRs from the remnant (Gabici et al. 2009b; Aharonian & Atoyan 1996).

The luminosity of W51C in the energy range 0.25 GeV – 5.0 TeV, which is roughly the energy range of the *Fermi* and MAGIC data, is $L_\gamma \approx 1 \times 10^{36}\ \mathrm{erg\,s^{-1}}$, assuming a distance of 5.5 kpc, which is one of the highest compared to other SNRs.

7.4.2 Adjustment of model parameters

First leptonic scenarios are considered. The same problems already reported by Abdo et al. (2009c) appear, namely that it cannot reproduce the radio and gamma-ray data simultaneously. Note that the parameters in the leptonic models are not unique, however they share the same problems in explaining the observed emission. An Inverse Compton (IC) dominated scenario is shown in figure 7.10, top. The total kinetic energy in electrons is very high, approximately 39 % of the explosion energy of the supernova. A similar amount of kinetic energy is expected in relativistic protons, severely challenging the energy budget of the system. The

volume averaged hydrogen density has to be very low, which does not seem reasonable given the dense environment of the molecular cloud. Also the electron to proton ratio is very high and the magnetic field rather low, of the order of the average Galactic magnetic field. For the parameters used in this model see table 7.3.
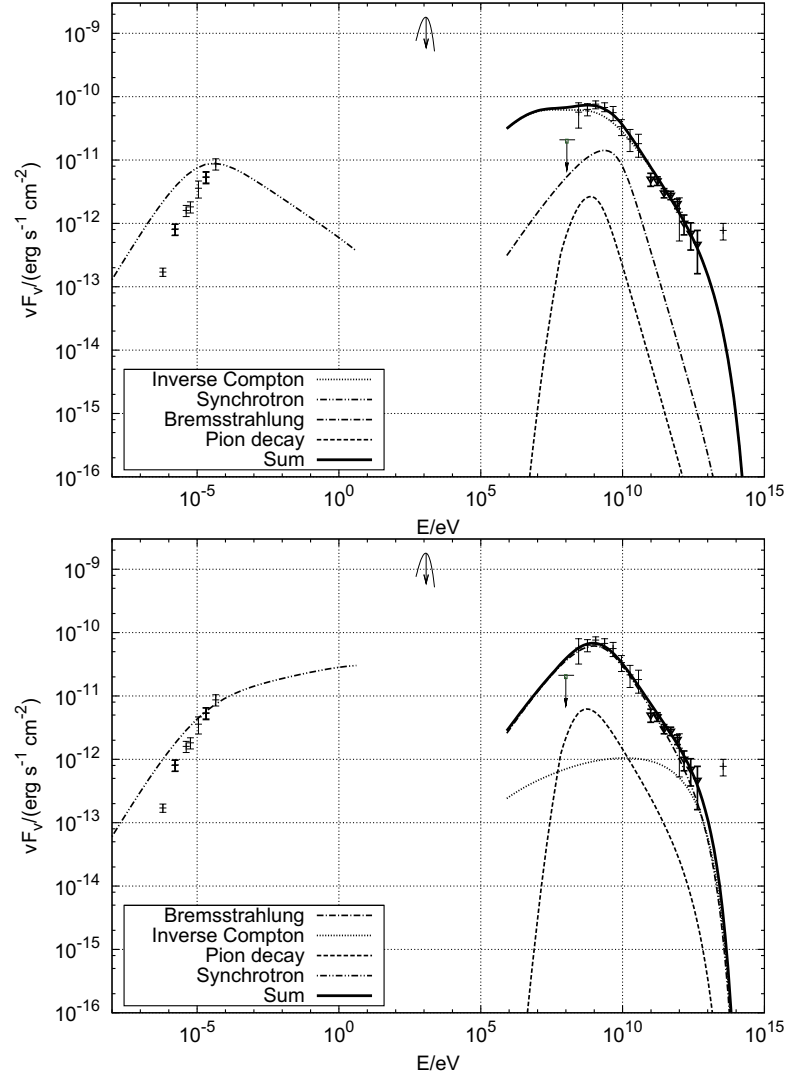
Figure 7.10: The dashes with error bars are 21cm radio continuum, circles represent *Fermi*/LAT data, squares are the data obtained in this work and the star represent the MILAGRO data point. The upper limit in the X-ray regime is obtained from *ROSAT* data, the upper limit at ~ 100 MeV was obtained by *Agile*. Top panel: a scenario in which the gamma-ray emission is dominated by Inverse Compton processes, bottom panel a scenario of Bremsstrahlung dominated gamma ray emission.

Moreover it is not obvious why the centroid of the emission should be located in a dense environment of the shock cloud interaction zone if the emission is dominated by a process not

related to the matter density. Thus, such a scenario appears unlikely.

Even though a Bremsstrahlung dominated scenario (Brems) would be able to explain the observed morphology, similar problems are found when trying to describe the broad band spectrum, see figure 7.10 bottom. It is not possible to reproduce both radio and gamma emission simultaneously. Furthermore, an electron to proton ratio in the order of one is needed to suppress the hadronic contribution. Due to the different injection efficiencies of electrons and protons into the shock acceleration process one usually expects an electron to proton ratio much smaller unity.

The recently presented, preliminary, UL of the Agile collaboration at ~ 100 MeV adds very helpful information (Guiliano et al. 2013). At this energy the different Models (Brems, IC, and also hadronic models) start to diverge and thus a measurement in this region allows one to distinguish between them. Note, that all models presented here have been produced before the reported UL was available. The reported UL lies a factor ~ 4 below the emission predicted in an IC scenario ruling out this possibility. The Bremsstrahlung dominated model in figure 7.10 also predicts emission higher than allowed by the UL. As the index before the break is fixed by the radio emission and the index after the break by the MAGIC emission, the only way to fulfill the flux requirement imposed by the UL is to shift the break to higher energies. However in such a scenario the model largely over-predicts the very high energy emission, as shown in figure 7.11.
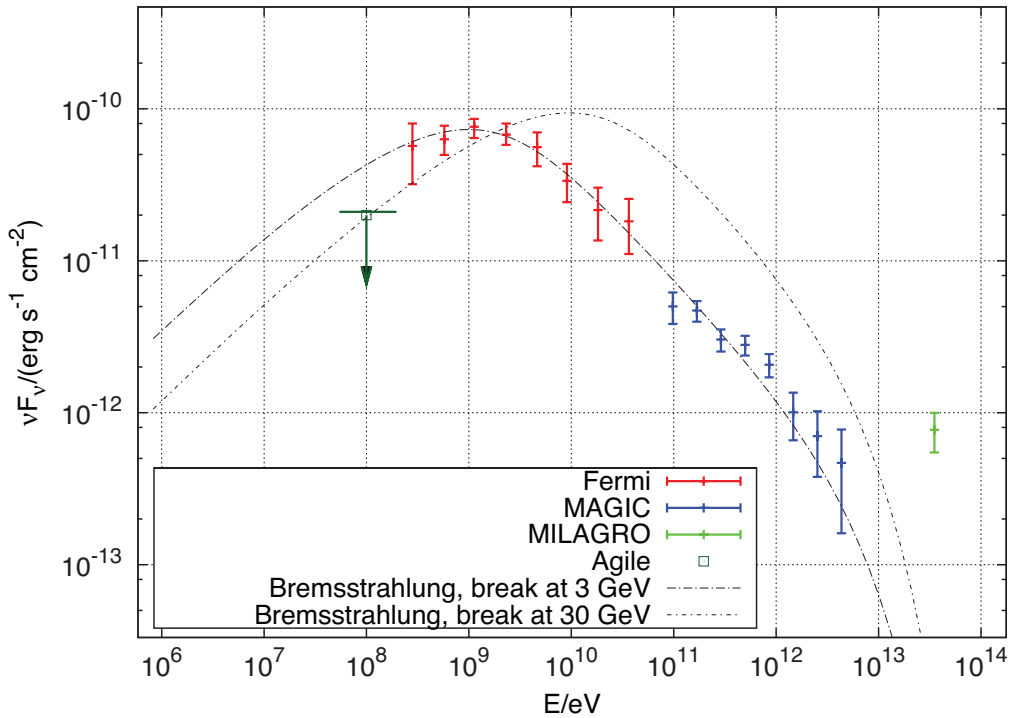

Figure 7.11: Gamma ray data together with the predicted emission of Bremsstrahlung. The only difference in the model parameters is the break energy. None of the models is able to explain the data.

It is concluded that the observed broad band spectrum can not be explained by any simple

one-zone leptonic model. Note, that even in a multi-zone Bremsstrahlung model, allowing for the possibility to adjust the spectral shape before the brake, the inferred spectrum of electrons would have to be significantly harder than $E^{-1.5}$, which is hardly possible in the framework of shock acceleration.

When the emission is modeled with pion decay as the dominant process, both radio and gamma-ray emission can be reasonably reproduced, as shown in Fig. 7.12. A hadronic scenario is particularly interesting, as the shock-cloud interaction naturally favors a CR-matter interaction mechanism. Moreover, the parameters used in this model, see table 7.3, are a reasonable description of the interstellar medium around W51. The low flux imposed by the Agile UL is not in conflict with the model and might be understood as the signature of the pion production threshold.
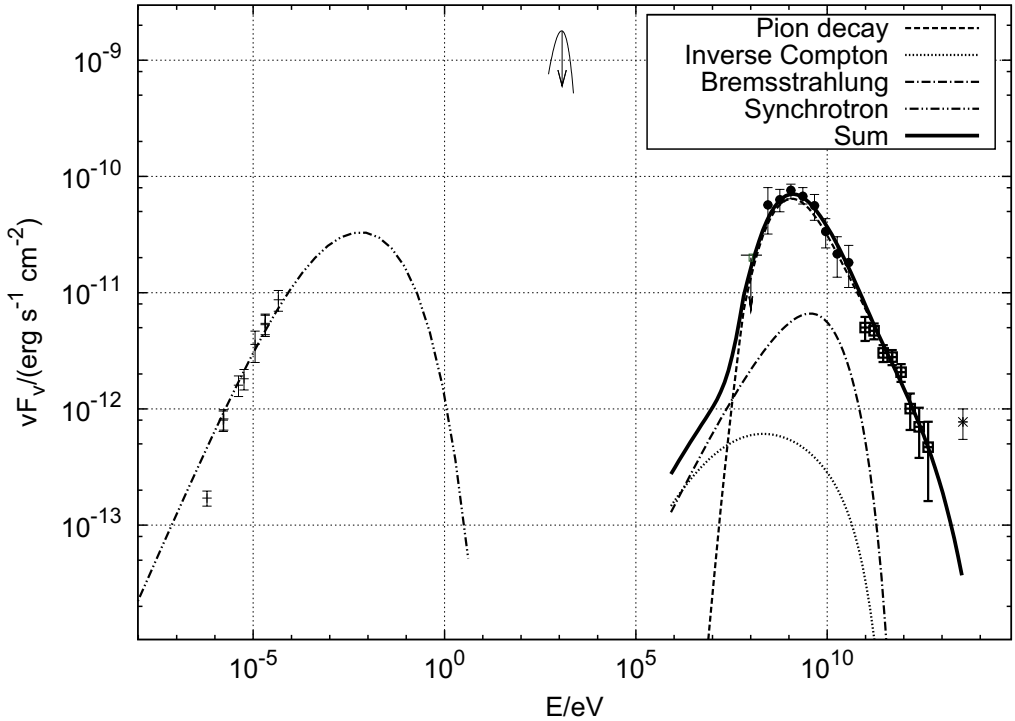
Figure 7.12: Model of the multi-wavelength SED in the hadronic-dominated scenario. The MILAGRO measurement can not be explained in any of the considered models. An additional component or a strong hardening of the particle distribution would be needed to explain the MILAGRO hint. Same data as in Fig. 7.10

Compared to the hadronic model suggested in the work of Abdo et al. (2009c), the main difference is the index of the particle distribution after the break. The spectrum after the break is more precisely determined by the data presented here. The index obtained here is harder, allowing for the explanation of all the gamma-ray data up to the end of the MAGIC spectrum. A detailed view of the high energy and VHE region is shown in Fig. 7.13. It shows that the index above the break is clearly determined by the data presented here. In addition, the hadronic model by Abdo et al. (2009c) is displayed. Besides the good agreement between the model and the data, the clear improvement of the determination of the underlying particle

distribution at high energies is visible. In this scenario a cut-off energy of $E_{\mathrm{cut},p} \geq 50$ TeV is needed to fit the MAGIC data, indicating the existence of protons at least to this energy.
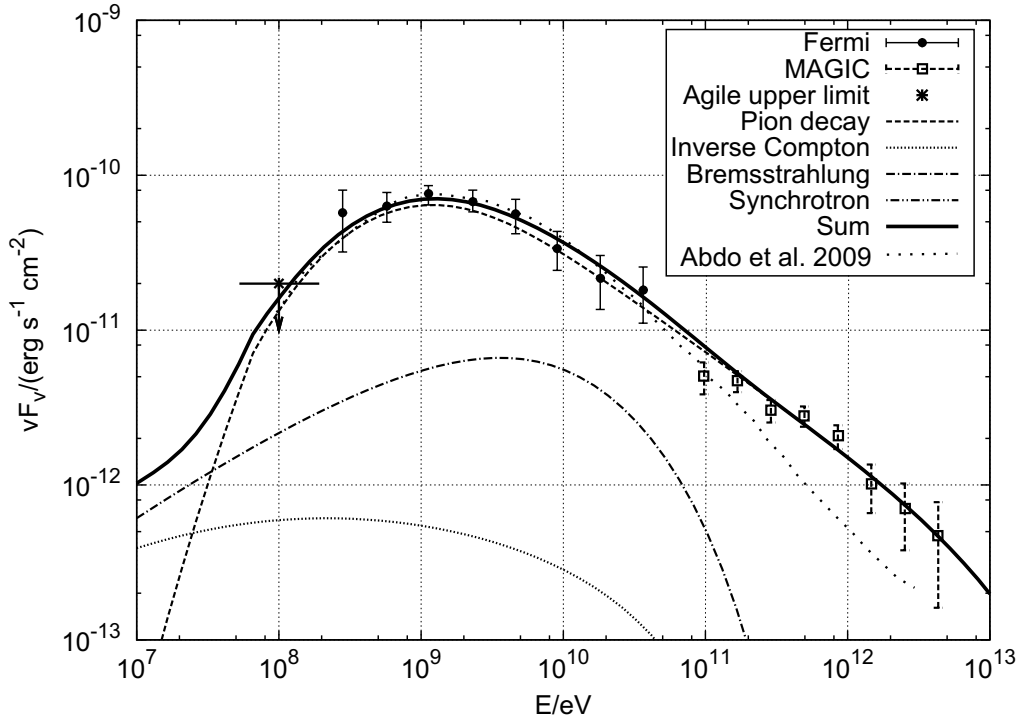
Figure 7.13: Detailed view of the hadronic model in the high energy and VHE region. For comparison to the hadronic model by Abdo et al. (2009c), shown as long dotted line. This models ends at the highest energy shown in that publication. The major difference between this model and that of Abdo et al. (2009c) is the harder particle spectrum above ∼100 GeV, which is now precisely constrained by the measurements presented here.

Table 7.3: Parameters used in the modeling of the multi-wavelength spectral energy distribution for the different scenarios. The power-law index before the break is $s = 1.5$ for both protons and electrons. $E_0 = 10$ GeV. The total kinetic energy of the particles was integrated for $E_{\mathrm{kin}} > 100$ MeV both for electrons and protons.

Parameter	Pion decay	Inverse Compton	Bremsstrahlung
K_e/K_p	1/80	1/1	1/1
Δs	1.2	2.1	1.3
E_{br} [GeV]	10	10	3
$E_{\mathrm{cut},e}$ [TeV]	0.1	50	12
$E_{\mathrm{cut},p}$ [TeV]	120	50	12
B [μG]	53	2.7	38
n [cm^{-3}]	10.0	0.1	50
W_e [10^{50} erg]	0.069	14	0.15
W_p [10^{50} erg]	5.8	13	0.14

The precise cut-off energy of the electron spectrum $E_{\mathrm{cut},e}$ is not well constrained, since the synchrotron peak is not resolved. Therefore, the energy $E_{\mathrm{cut},e}$ used here is only a lower limit, as enforced with the radio data. However, a 1 TeV electron in a magnetic field of $50\,\mu$G has a lifetime of about 4700 years, determined by synchrotron losses. This value is much lower than the age of the remnant, suggesting that for such high energies the electron spectrum should develop a break, with the consequent spectral steepening at higher energies. Assuming constant electron injection over time, the electron spectrum steepens at 100 GeV by a factor $1/E$. This yields a very similar gamma-ray emission as in the hadronic model presented here, even for a higher value of $E_{\mathrm{cut},e}$.

7.4.3 Implications of the models

It is discussed what general conclusions can be drawn from the hadronic model explaining the data.

The volume-averaged hydrogen density is a fit parameter and left free to vary. From that, the volume filling factor f is computed, which is the fraction of the mass of the clumpy molecular cloud that is contained inside the SNR interaction volume (defined as the volume of the emission zone) as $f = n_{\mathrm{H}} V \left(m_{\mathrm{H}}^{\mathrm{atom}} + 0.1 m_{\mathrm{He}}^{\mathrm{atom}}\right)/m_{\mathrm{cloud}} \approx 0.11^3$. Here m_{cloud} is the total mass of the molecular cloud, V is the volume of the radiation sphere and $m_{\mathrm{H}}^{\mathrm{atom}}$, $m_{\mathrm{He}}^{\mathrm{atom}}$ are the masses of a hydrogen and helium atom, respectively. This would imply that around 11 % of the mass of the molecular cloud is contained in the emission volume and is interacting with the SNR. This value is consistent with the filling factors of around 8–20 % for other SNRs interacting with molecular clouds (Uchiyama et al. 2010).

The total amount of kinetic energy in electrons and protons is about 16 % of the explosion energy of the supernova. This fraction is just slightly higher than the value normally assumed, of around 10 %, of the explosion energy converted into CRs to maintain the observed flux of Galactic CRs (Hillas 2005). The proton to electron ratio in CRs is not far from value observed at earth of $K_p/K_e \approx 50$, see for example Simpson (1983b).

Since the hadronic gamma-ray emission is proportional to the product of the kinetic energy in protons and the density of the medium, these parameters are strictly correlated. Assuming that the complete mass of the molecular cloud acts as target material (f=1) would imply a density of n=100 cm^{-3}. Therefore the lower limit of the energy in relativistic protons is about 1.6 % of the explosion energy of the supernova. Note that such a scenario would need either a higher magnetic field ($B \sim 150\,\mu$G) or a much lower electron to proton ratio ($K_e/K_p \sim 1/800$) to still reproduce the broadband emission. In addition, the morphology presented in this work shows that only a fraction of the molecular cloud is emitting VHE gamma emission (see Fig. 7.7). Therefore one can conclude that the amount of kinetic energy in protons is clearly above this lower limit and in the order of 10–20%.

In the scenario investigated here all of the gamma-ray emission was attributed to π^0 decay. It was not possible to model the broad-band emission with a purely leptonic scenario. The radio data could not be fitted and the model parameters were not physically reasonable (too low density n_{H}, too high energy content W_e in electrons, too low magnetic field B, electron to proton ratio of 1). These discrepancies could be caused by a too many simplifications in the model such as assuming a homogeneous medium and magnetic field. However, the

---

[3] The primordial ratio He/H ratio of 0.1 was assumed as usually done in the literature

preliminary upper limit presented by the *Agile*-collaboration is difficult to account for in a leptonic scenario. Thus it is concluded that most likely the *Fermi*/LAT data and the MAGIC data can be interpreted in terms of hadronic interactions of high-energy protons with the molecular cloud and subsequent decay of neutral pions. With the current data it is not possible to decide what process causes the excess of emission observed by MILAGRO which, if confirmed at this flux level, would require the introduction of an additional component at the highest energies.

7.4.4 Discussion on the acceleration process

Following the result of the modeling the observed gamma-ray emission is assumed to be of hadronic origin. As mentioned in Section 7.1, there are two main possible scenarios: a cloud illuminated by runaway CRs or acceleration of CRs in the shock wave propagating through the cloud.

In the first case, CRs escaping the SNR will homogeneously fill a sphere with a radius $R_d \sim \sqrt{4D\,t}$ where D is the diffusion coefficient and t is the time since particles are diffusing (Gabici et al. 2010). For 10 TeV protons, responsible for gamma-ray emission of 1 TeV, the radius of this sphere would be about 350 pc, assuming the average Galactic CR diffusion coefficient at 10 TeV to be $\sim 3 \times 10^{29} \mathrm{cm}^2$ s. Here it was assumed that the high-energy particles escape the SNR early enough such that the diffusion time can be approximated to be the age of the SNR. The distance between the maximum of the emission measured by MAGIC above 1 TeV and the assumed center of the SNR (RA=19.384 h, DEC=14.11°) is about 8 pc (for a distance of 5.5 kpc). The distance to other parts of the SNR/cloud complex W51C/B is of similar order. This implies that the complete cloud should be uniformly illuminated by CRs. As can be seen in Fig. 7.7 the complete W51B/C complex is not detected at energies above 1 TeV (lower right skymap): parts of the outer regions, both on the side towards the SNR and on the opposite side, do not emit gamma radiation. In the scenario of runaway CRs, one would expect diffusion from the SNR to W51A (northern region in the 21cm emission); no significant emission from W51A is detected. However, the distance of the regions A and B is measured with an error of the order of hundreds of parsecs, which means that the relative distance between the two could be high enough to explain the lack of diffusion from one to the other. The scenario of runaway CRs also can not explain the incomplete illumination of W51B/C, especially towards the outer regions. Even in a scenario of highly anisotropic escape, it appears unlikely that the centroid of the emission appears by chance coincident with the cloud shock region.

Concerning the acceleration of CRs in the shocked cloud region, the gamma radiation should originate very close to the acceleration site of the radiating particles due to the high density of the surrounding medium. This is in agreement with the morphology described in this work. The unusually high ionization reported by Ceccarelli et al. (2011) close to the maximum VHE emission region indicates the presence of freshly accelerated low-energy protons, supporting this interpretation. The missing emission towards the edges of the cloud could be explained with a lower diffusion coefficient in the shocked cloud region, or with a shielding effect, either of which is possible in a surrounding medium of high density.

Assuming the possible PWN is not responsible for the observed tail emission, possibilities to account for this feature in a hadronic emission scenario are explored. As argued before, the absence of an enhanced matter density at the location of the observed tail, requires and

enhanced density of CRs in this region. Thus, the idea of a homogeneous and isotropic CR distribution has to be dropped. It is stressed that the overall flux and spectral shape of the CR spectrum derived above represent the parameters of the complete (spatially integrated) CR distribution. Thus, the above derived results do not depend on the specific shape of the assumed emission and are therefore unaffected by the following discussion.

From the theory of DSA there is no physical argument requiring a spherical symmetry for the CR distribution. In fact, even for a spherical symmetric supernova shock waves the expected CR distribution is located in a thin shell around the shock front (see (Drury 1983) and references therein). Furthermore Völk et al. (2003), showed that the injection of thermal particles into the acceleration mechanism, and thus the parts of the SNR where CRs are efficiently produced is not constant over the shock surface. In their work a strong dependence of the injection efficiency with respect to the magnetic field orientation to the shock normal was found, suppressing the injection for oblique shocks. Strong observational support for this theory (Berezhko et al. 2012b) was found in supernova remnant SN 1006, where radio, x-ray, and gamma-ray emission (Acero et al. 2010; Rothenflug et al. 2004; Reynolds & Gilmore 1986) shows a clearly bipolar structure located at the magnetic pools of the shell. Moreover, Giacinti et al. (2012) showed that CRs released from a point like source do not diffuse in a spherical symmetric way. Instead they showed that, even in a random magnetic field, CRs diffuse highly anisotropic building large scale structures around their sources. Only for large time scales the anisotropies are washed out and the assumption of a homogeneously filled, spherically symmetric CR halo around the source holds. The characteristic time scale above which the asymmetry is washed out, was estimated to be $\sim 10^4$ years for PeV protons increasing with decreasing energy. Even though, this estimate may vary significantly caused by the large uncertainties of the assumed parameters an anisotropic TeV gamma ray halo around middle age remnants appears plausible. Based on this works it is concluded that the simplified assumption of a homogeneous and isotropic CR distribution is unlikely to be realized in nature. More realistic appears a highly structured CR distribution, in particular of the escaping CRs. Giacinti et al. (2012) showed that this structures can extend over sizes of few tens of pc and are reflected in the gamma-ray emission. Thus, the possibility to observe such structures is within the capabilities of the angular resolution of current Cherenkov telescopes (given a close enough source). It is noted that the actual size of such structures depends strongly on diffusion coefficient and the surrounding medium and can vary significantly for different cases. Gabici et al. (2010) showed also that the diffusion can be suppressed by turbulences induced from the relativistic particles themselves. Figure 7.14 illustrates how a scenario of anisotropic escape or of an inhomogeneous acceleration along the shell could apply for the here presented morphology of W51.

Wing like structures of the escaping CR distribution (see right panel of figure 7.14) have been found in the simulations of Giacinti et al. (2012). These structures appear as the escaping CRs diffuse preferred along the global magnetic field orientation (see also Nava & Gabici 2012). An explanation where the complete emission is attributed to CRs accelerated in the interaction between the SNR W51C and the molecular cloud W51B is therefore possible in scenario of anisotropic escaping CRs.

Another plausible possibility would be that the tail emission traces a part of the shock wave where efficient acceleration is still taking place. As seen in the example of SN 1006, not the complete shell has to show the same CR acceleration efficiency and some parts can even appear dark in gamma rays. Such a behavior could be explained by the dependence of the

injection efficiency on the magnetic field orientation with respect to the shock front (Gargaté & Spitkovsky 2012). In this scenario the inferred globular magnetic field orientation would have to be almost perpendicular to the direction suggested by the scenario of asymmetric escape.

Both the morphology at TeV energies and the measured high ionization indicate in all discussed scenarios at least partially ongoing acceleration. This suggests that the particle distribution, whose gamma emission is observed, may represent the source spectrum of cosmic rays currently being produced in W51. However, the differentiation between ongoing acceleration of particles in the shocked region or reacceleration of already existing CRs, like in the *crushed cloud* scenario (Uchiyama et al. 2010), in the same region is not obvious and is not addressed in this work.
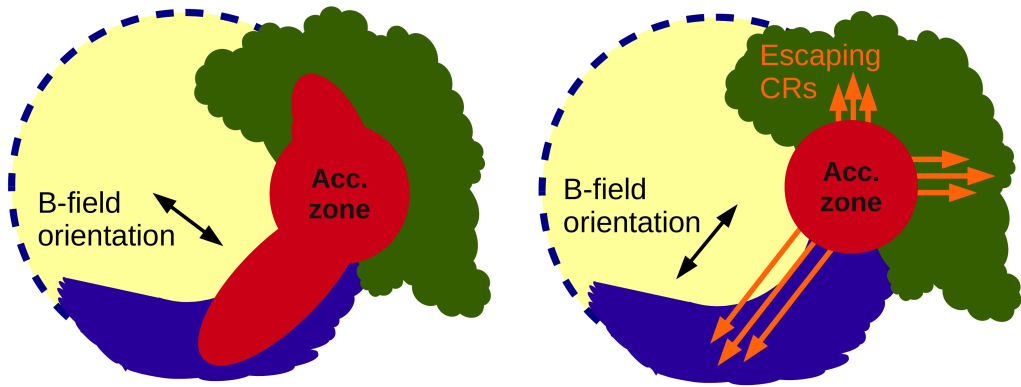

Figure 7.14: Possible explanations of the observed morphology, neglecting a possible contribution of the putative PWN. Left hand side: Illustration of an resolved acceleration zone (red region) along the shell of the remnant. The almost perpendicular magnetic field orientation with respect to the shock normal suppresses injection of particles on the lower left part of the shell. Right hand side: Illustration of how an unresolved accelerator (red region) located at the shock cloud interaction could be responsible for the observed morphology. Arrows indicate the possible anisotropic escape of CRs from the acceleration zone. The molecular cloud suppresses escape towards the cloud, while CRs escaping away from the cloud diffuse along the global magnetic field orientation.

7.5 Conclusions

MAGIC has performed a deep observation of a complex Galactic field containing the star-forming regions W51A and W51B, the SNR W51C and the possible PWN CXO J192318.5+140305. As a result of this observation, emission of gamma rays above 150 GeV has been detected with 11 σ statistical significance. The spectrum of this emission has been measured between 75 GeV and 5.5 TeV. Spectral points are well fitted with a power law with a photon index of 2.6, compatible with the *Fermi*/LAT measurement between 2 and 40 GeV. The spectrum measured by MAGIC allows for the first time a precise determination of the spectral slope of the underlying particle distribution above the spectral break measured at around a few GeV by *Fermi*/LAT.

The MAGIC source spatially coincides with those previously reported by H.E.S.S. and *Fermi*/LAT. The main emission region is restricted to the zone where W51C interacts with W51B and, in particular, to the region where shocked gas is observed. This clearly pinpoints the origin of the emission to the interaction between the remnant and the molecular cloud.

Non-thermal X-ray emission which could help to trace the relativistic electron distribution was found only from a compact region around the position of the possible PWN (Koo et al. 2005). The MAGIC source exhibits a morphological feature extending towards CXO J192318.5+140305, more prominent in the image at higher energies.

The projection of the gamma-like events on the line connecting the putative PWN and the centroid of the shocked clouds shows a hint of an underlying distribution that may be described as the sum of two Gaussian functions. However, the existence of two independent, resolved sources could not be statistically established. The contribution to the total excess of two regions of 0.1° radius centered on the *cloud* region and the *PWN* region has been obtained. It was found that the regions contribute about 30% and 20% of the total emission, respectively, and the contribution is not energy dependent within the uncertainties. Spectra of the individual regions above 350 GeV could be obtained, but do not allow for detailed conclusions due to the weak individual fluxes. Given the low possible contribution of the PWN candidate in the energies investigated in this work, it is very unlikely that the main conclusion drawn here will be significantly affected even if the PWN contribution can be established. Scenarios in which the tail emission is explained in context of the supernova remnant W51C are as well theoretically possible.

The MAGIC observations extend the spectral energy distribution of W51 by more than one order of magnitude in energy with almost no gap to the spectrum obtained by *Fermi*/LAT. A physically plausible model of the emission of the SNR has been proposed by considering a spherical geometry and uniform distribution of the ambient material. Note that this system is clearly anisotropic (as seen in the multi-wavelength data), and more detailed modeling may achieve a better description of the source. It was found that the VHE emission from W51C cannot be explained by any of the considered leptonic models. The emission is best described when neutral pion decay is the dominant gamma-ray production mechanism. In the proposed model, the SNR has converted about 16% of the explosion energy into kinetic energy for proton acceleration and the emission zone engulfs 10% of a molecular cloud of 10^5 solar masses, which provides the target material. In this scenario, protons are required to reach at least an energy of the order of 50 TeV to produce the observed emission.

The morphology of the source cannot be explained by CRs diffusing from the SNR to the cloud. It can instead be qualitatively explained with VHE gamma-ray emission being produced at the acceleration site of CRs. This involves ongoing acceleration of CRs or re-acceleration of already existing CRs at the shocked cloud region. Given the high luminosity of this source and its very likely hadronic origin, it is concluded that W51C is a prime candidate cosmic ray source in the Galaxy.

The detection of neutrinos from this source would be the final proof about the hadronic nature of the emission. But, according to the calculations by Yuan et al. (2011), the chances for detection are low. Very recently new upper limits of the AMANDA-Icecube detector on the neutrino flux have been presented (IceCube collaboration et al. 2012). In this work W51 is one of the six most promising preselected point source candidates for neutrino emission. Even though the derived upper limit on the neutrino emission of W51 is the most stringent one to date, it does not constrain the here presented hadronic model.

To reveal the morphology and the possible emission of the PWN, more data at energies above 1 TeV are necessary. Extension of the spectrum towards higher energies would constrain the maximum achievable energy in the system and might shed light on the meaning of the MILA-GRO measurement, which cannot be accommodated in the theoretical framework proposed here. A determination of the spatial distribution of the CR ionization rate in the system might in addition help to separate between locations of acceleration (high CR ionization) and locations illuminated by escaping CRs (low CR ionization).

7.6 W51C in the context of galactic cosmic ray origin

The question of the origin of galactic cosmic rays, that is now one century old, is still an unsolved issue. However, recent theoretical and observational results strongly support the common believe that SNRs are indeed the major sources of galactic cosmic rays. Among all SNRs detected in the gamma ray regime, only very few clearly favor a hadronic nature of the observed emission. The most prominent cases are the remnants: Tycho, W44, W28, IC443 and now also W51C. Of these remnants only Tycho belongs to the class of young supernova remnants which were originally thought as the best objects to study the origin of galactic cosmic rays. However, their low luminosity, low number, and the potential leptonic dominated emission render the class of young SNRs not longer as the best objects to study the origin of cosmic rays. Instead middle age remnants (all of the above listed but Tycho) start to become a more and more important class to address question of the origin of galactic cosmic rays and to reveal the underlying physical processes. This section addresses the impact of the observed high and very high gamma ray emission from middle age remnants to our understanding of cosmic ray acceleration and escape with a particular focus on the results derived in this thesis. First the reader is reminded of two major aspects in the framework of linear and non linear diffusive shock acceleration (DSA): the spectral shape of the accelerated particle distribution and the maximum achievable energy. In the simple test particle solution (assuming a strong shock i.e., compression ratio equals 4) one obtains a spectrum described by a power-law in momentum[4] (Drury 1983)

$$f(p) = C \left(\frac{p}{p_0} \right)^{-4} , \tag{7.3}$$

where C is the normalization constant, p_0 the minimum momentum where the solution holds. In the more sophisticated non linear theory (taking into account the feedback of the accelerated particles on the acceleration mechanism) the spectrum develops a concave shape getting harder at higher energies (Caprioli et al. 2010). The end of the spectrum is determined by the maximum achievable energy of the accelerator. As the speed of the supernova shock wave slows down the maximum energy reachable is decreasing over time (Ptuskin & Zirakashvili 2005; Lagage & Cesarsky 1983). Note, that the observed spectrum at earth is described by a power-law in energy of $\sim E^{-2.7}$ up to energies of $\sim 3 \times 10^{15}$ eV. The steepening of the spectrum during the CR diffusion in space is assumed to be $\sim E^{-0.3}$. Thus, the source spectrum needed to explain the observed CR spectrum at earth is $\sim E^{-2.4}$ and needs to extend at least until 3 PeV. This spectrum is significantly softer than predicted by diffusive shock acceleration

---

[4]Note that under the usually assumed isotropic momentum distribution the spectrum can be rewritten as a power-law of energy with a spectral index of -2 for highly relativistic particles.

and the requirement on the maximum energy are at the limit of those theoretical possible (Caprioli 2012). However, the sensitivity of the current instruments for gamma rays at ~ 300 TeV is not sufficient to verify if SNRs can indeed accelerate particles up to the knee. But as the maximum energy is decreasing as a function of the age of the sources, the putative cut-off produced by the lower achievable maximum energy in older accelerators should be observable. In addition, the higher luminosity and number of middle age SNRs offer both, the possibility of detailed individual observations and a first look into this population of sources.

First the spectral properties of the most prominent objects of this class (W51C, W28, IC 443, and W44) are compared. Here, W44 is a very particular case as *Agile* (Giuliani et al. 2011b) resolved the low energy cut off in the gamma ray spectrum, interpreted as caused by the threshold of the π^0 production (~ 280 MeV). This is one of the clearest cases of hadron acceleration in SNRs. Furthermore the spectrum undergoes a steepening with a spectral break at few GeV. The steep spectrum (slope ~ -3.0) above the break prevented a detection at energies above 100 GeV till now. For the other three objects a similar break has been observed, however the spectral slope above the break is significantly harder with a slopes similar to -2.7. All objects are of similar age (few 10000 years) and are interacting with the surrounding molecular clouds. Both the morphology and the modeling of the multi wavelength data suggest a hadronic origin of the emission. All objects show a similar spectral behavior as summarized in Table 7.4.

Table 7.4: Summary of the spectral properties of the four most prominent SNR-molecular cloud associations. Slope1 gives the power law index before the break while slope2 the value after the break. The break is given in units of GeV.

Object	slope1	break	slope2	Maximum observed gamma ray energy
W51C	-1.5	10	-2.7	~ 5 TeV (Aleksić et al. 2012b)
IC443	-1.9	3	-2.6	~ 2 TeV (Albert et al. 2007b; Acciari et al. 2009)
W28	-1.7	2	-2.7	~ 3 TeV (Aharonian et al. 2008b)
W44	-1.7	6	-3.0	~ 100 GeV (Abdo et al. 2010c)

The persistent feature of CR spectra described by broken power-laws in all these objects is not explainable by standard DSA. In addition, the soft spectra after the break contradicts the expectations of a harder concave spectrum predicted by non linear DSA. If the inferred CR spectra from these observations do represent the source spectrum of CRs released into space, then the observed spectra at earth ($> 100 GeV$) should be as steep as E^{-3}, due to the further steepening of the CR spectrum caused by the propagation. Moreover, the expected maximum energy of protons still reachable in these systems is $\lesssim 10$ TeV, thus predicting a cut-off in the gamma-ray spectrum around $\lesssim 1$ TeV (Ptuskin & Zirakashvili 2005; Zirakashvili & Ptuskin 2011). None of these objects discovered in TeV energies show any significant indication of a high energy cut-off. In particular, here obtained indications of ongoing proton acceleration in W51C up to at least 50 TeV challenge the theoretical expectations.

However, recently several authors proposed mechanisms which can explain the observed behavior in the framework of a modified DSA. A possible explanation of the brake in the CR spectrum observed in W44 (and maybe in others too), was recently presented by Malkov et al.

(2012a). In this scenario the damping of Alfven waves by neutral particles in the molecular cloud leads to a break down of the CR confinement above the break energy and subsequently a steepening of the observed gamma ray spectrum. Thus the observed break, followed by the steep spectrum, can be interpreted as a signature of a collective escape of CRs from their accelerator. Another explanation was put forward by Malkov et al. (2012b), in which the self excited magneto-hydrodynamic waves in the vicinity of the shock front produced by escaping CRs can account for the steep spectrum observed. In both such scenarios the broad band escape of CRs might significantly alter the former scenario of a sharp cut-off at the maximum energy. Recently, Caprioli (2012) provided a theoretical framework of DSA where the relative velocities of the scattering centers with respect to the upstream and downstream plasma are taken into account. In this work the author finds that a more efficient acceleration leads to a steeper spectra and also a higher maximum energy. This model successfully explains the emission observed from the young SNR Tycho (Morlino & Caprioli 2012), which also shows a spectrum as steep as $E^{-2.2}$. This scenario does not explain the observed spectral break, which however, may be an effect of the molecular cloud interaction as suggested in Malkov et al. (2012a); Ohira et al. (2011). In the framework of Caprioli (2012) the steep spectra of W51C, the extension of the spectrum to high energies, the morphology, and the high CR ionization rate might be interpreted as efficient CR acceleration, in the interaction zone of remnant and molecular cloud. On the other hand an interpretation following the work of Malkov et al. (2012a,b) would imply a broad band escaping CR spectrum. Both scenarios do not have to exist exclusively and also an intermediate state might be possible. In the case of W51C the high CR ionization rate and the morphology favor a scenario where acceleration is still ongoing. The even steeper spectrum of W44 and the recently discovered harder gamma ray emission surrounding the remnant Uchiyama et al. (2012), favor a scenario of efficient escape for this remnant. Here the surrounding emission is interpreted as escaping CRs illuminating the surrounding molecular material. In the case of W28 (Giuliani et al. 2010; Aharonian et al. 2008b; Abdo et al. 2010b) emission is seen both from a molecular cloud interacting with the remnant and from several clouds in its surrounding. The similarity of the spectra from all TeV emitting regions might indicate ongoing acceleration and simultaneous escape of CRs from the acceleration site. In the case of IC443 (Albert et al. 2007b; Acciari et al. 2009; Tavani et al. 2010; Abdo et al. 2010d) both scenarios or a mixture are possible.

Therefore, W51 might represent an earlier evolutionary state, where efficient acceleration is still ongoing. IC 443 and W28 would then represent an intermediate state, where escape becomes compatible to acceleration, while W44 would present the final stage where most of the remaining CRs are released into outer space. Clearly, this is only a qualitative argumentation. However, the idea of an observable evolution of cosmic ray accelerators has many attractive features and would allow to access the dynamics of CR acceleration and escape.

In any case the discovery of GeV and TeV emission of middle age supernova remnants has already triggered many developments in the theory of particle acceleration and escape. The continuously all sky monitoring in the GeV band (*Fermi*/LAT and *Agile*) and deep observations of the Cherenkov Telescopes (MAGIC, H.E.S.S., VERITAS, and in the future CTA) will reveal more sources and more precise spectral and morphological properties of possible GCR accelerators.

Chapter 8

The unidentified source HESS J1857+026
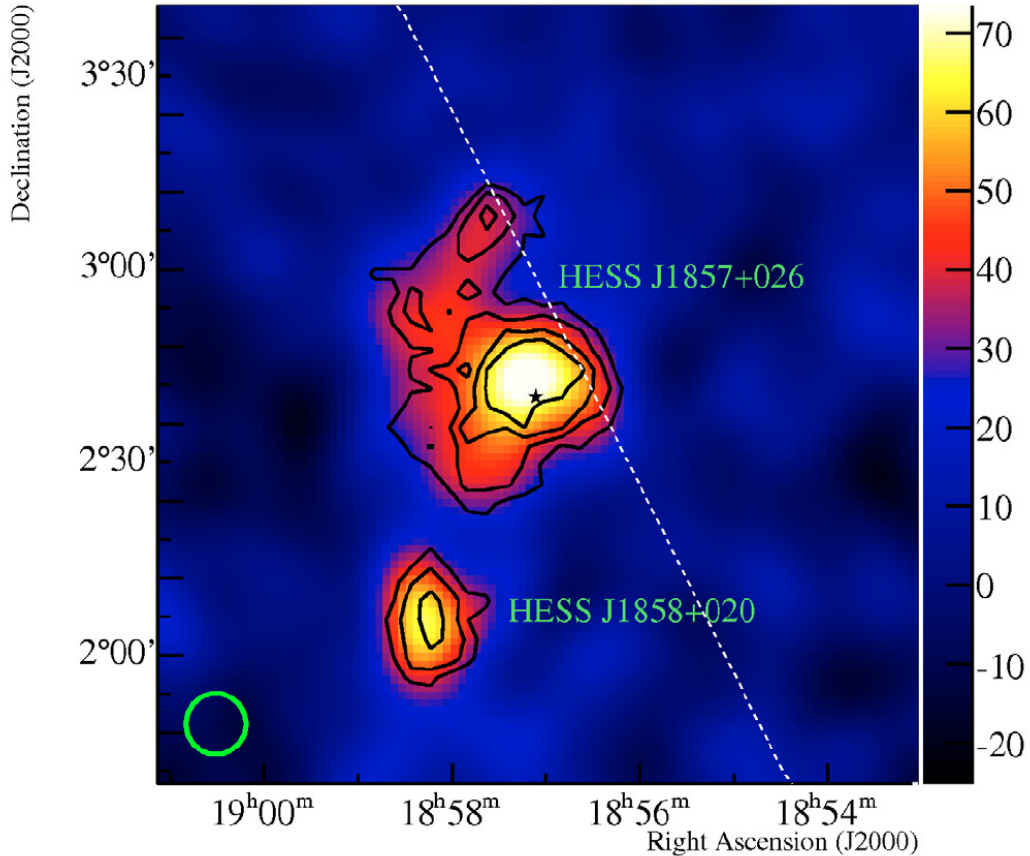
Figure 8.1: Gamma-ray skymap obtained by HESS (above ~ 1 TeV) showing the sources HESS J1857+026 and HESS J1858+020. The excess events are presented by the color bar. The green circle shows the PSF, the white dashed line indicates the galactic plane. Significance contours start from 4 and increase by one per contour. Picture adopted from (Aharonian et al. 2008a).

8.1 Introduction

The TeV source HESS J1857+026, see figure 8.1 was discovered during the galactic plane scan by H.E.S.S. (Aharonian et al. 2008a). No clear counterparts in other wavelengths could be

found. The source shows a significant extension[1] of $(0.11 \pm 0.08)° \times (0.08 \pm 0.03)°$ and a tail like structure in the North. The spectrum can be fitted by a power law with a spectral index of 2.39 ± 0.08 in the energy range between 800 GeV and 45 TeV. The reported flux of the source is $\sim 15\%$ of the Crab Nebula. The discovery was confirmed by VERITAS (Ong et al. 2009).

Shortly after the discovery of the TeV source an energetic Vela-like pulsar (PSR J1856+0245) was discovered in the vicinity of HESS J1857+026 by Hessels et al. (2008). They report a period of 81 ms and a characteristic age of ~ 21 kyr based on data of the Arecibo PALFA survey. The authors use the pulsar dispersion measure of 622 ± 2 cm^3 pc and the NE2001 model of the distribution of free electrons in the galaxy (Cordes & Lazio 2002) to obtain a distance estimate of 9 kpc. However, this method has an uncertainty of a factor 2–3. At the same time the source appeared in the list of hard fermi sources (Paneque et al. 2011) with an integrated flux above 10 GeV and an index of -1.30 ± 0.28, indicating a hardening at lower energies. Rousseau et al. (2012) showed the first GeV spectrum of the source which confirmed the hard index in the energy range 1–100 GeV. No significant pulsation has been found at GeV energies using three years of *Fermi*/LAT data (Rousseau et al. 2012). A detection of a significant signal above 100 GeV using *Fermi*/LAT data was first reported by Neronov & Semikoz (2010). The nearby energetic pulsar and the spectral turnover might be indications that the source can be explained by a pulsar wind nebula scenario. Rousseau et al. (2012) showed that both a leptonic and a hadronic model of the gamma ray emission are plausible based on data from *Fermi*/LAT, MAGIC (preliminary results) (Klepser 2011), HESS and Chandra. The Chandra data are upper limits obtained from a 6 arcmin region around the HESS position (Rousseau et al. 2012).

The motivation to observe this source with MAGIC was twofold: The low energy threshold of MAGIC allows to close the gap between the *Fermi*/LAT and HESS data. The determination of the spectral turnover can add important information to address the nature of this object. Moreover the northern tail of the emission might indicate a second component which will be investigated by means of morphological studies.

In the vicinity a second source was discovered; HESS J1858+020 (Aharonian et al. 2008a). Paron & Giacani (2010) identified the source as a SNR possibly interacting with the surrounding molecular clouds. Although this source was not the major target and is thus located at the edge of the FOV (resulting in a significantly reduced exposure) we can use the data to gain more information about this source.

In addition, the known extension and the relatively high flux of the source allows one to test the capabilities of the instrument concerning extended sources.

Preliminary results from this work have been presented at international conferences (Klepser 2011) and a detailed publication is in preparation. This chapter is organized as follows: first the observational setup is introduced and the general results are presented. Section 8.3.1 is devoted to the detailed morphological results obtained from this object. A summary and a discussion of the results are presented in section 8.4.

---

[1]The extension is defined as the sigmas of a two dimensional Gaussian function

8.2 Data and Analysis

HESS J1857+026 was observed with MAGIC between July and October 2010 at zenith angles between 25° and 36°. After quality cuts a total of $\sim$ 29 h effective observation time has been obtained. The source was observed in Wobble mode using a total of 8 pointing positions (W1–W8), half of them with an offset of 0.4° and 0.5°, each. This setup was chosen to optimize the exposure for the extension of the source. The effective time in the positions W1 and W2 is $\sim$ 1h, each. For the remaining positions 4–5h have been accumulated, each. The analysis of the data was performed using the MARS analysis framework (Moralejo et al. 2009) including the latest standard routines for stereoscopic analysis (Lombardi et al. 2011). A detailed description of the analysis is given in chapter 6. The analysis employed here was tuned to match the observing conditions of this source in terms of the zenith angle distribution. For the training diffuse Monte Carlo gamma rays have been used to optimize the reconstruction of off-axis events. An analysis using point-like Monte Carlo simulations was also performed as a cross-check. Both results agree within statistical and systematic errors.
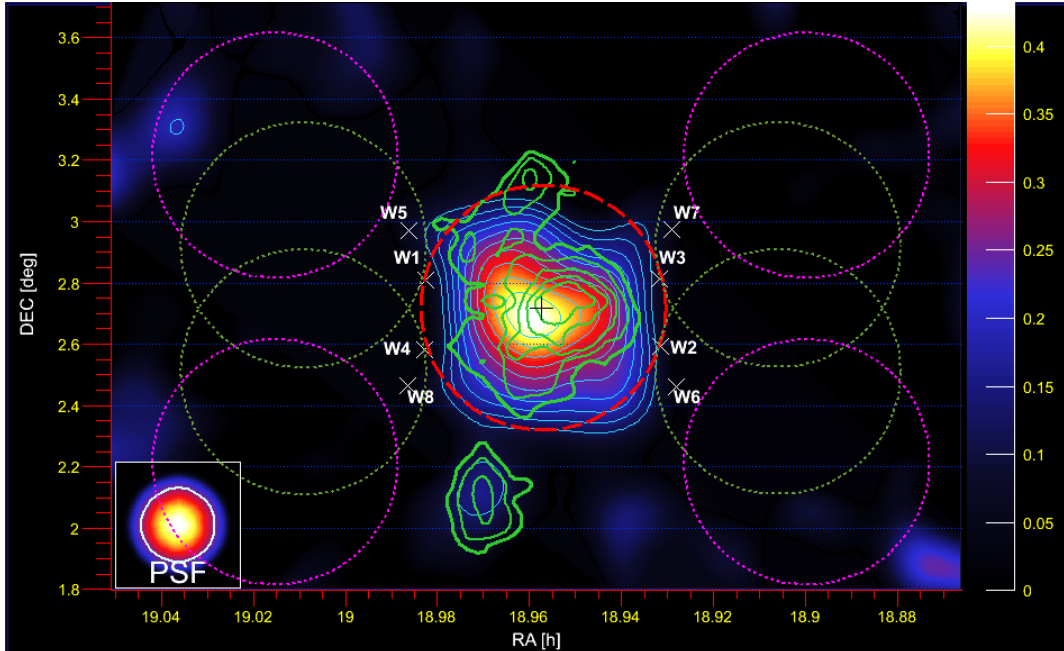

Figure 8.2: MAGIC gamma-ray flux map in arbitrary units above an energy threshold of $\sim$ 150 GeV. The blue contours represent test statistics (TS) starting at 3 and increasing by one per contour. The red dashed circle illustrates the integration region around the center of the observations (black cross). W1–W4 (W5–W8) mark the 0.4° (0.5°) offset pointing positions and the green (magenta) dotted circles their OFF regions. The skymap has been smeared by a Gaussian kernel of width 0.12°. The size of a point like source is indicated in the lower left (PSF). Overlaid are the significance contours obtained by HESS above $\sim$ 1 TeV (in green starting from 4 and increasing by one per contour.)

Furthermore the SUM-cleaning algorithm (Lombardi et al. 2011) was used, which provides

higher performance at energies $\lesssim 200$ GeV. The background estimation uses the *OFF from Wobble partner* (OfWP) algorithm developed in this work (see chapter 6.6.3). Figure 8.2 shows a skymap (> 150 GeV) obtained by MAGIC, where also the measurement of HESS is overlaid.

The individual pointing positions (W1–W8), the OFF regions (dotted circles), and the ON region (red dashed circle), later used for the θ^2-analysis, are shown in Fig. 8.2. The OFF regions (inferred from OfWP) are well separated from both sources in the field of view. The integration region for the θ^2-analysis was chosen to cover the entire emission region and has a radius of $0.4°$ around the center of observations (RA: 18.9575h, Dec=2.7167°). Note that this is also the maximum possible integration radius for the $0.4°$ offset pointings, as for larger values the ON and OFF regions start to overlap. This analysis uses only 1 OFF region per pointing to avoid a signal contamination of the background. Figure 8.3 shows the obtained θ^2 plot (ON and OFF distributions in the top panel and excess distribution in the bottom panel). A clear excess is found with a significance of 12.7σ.
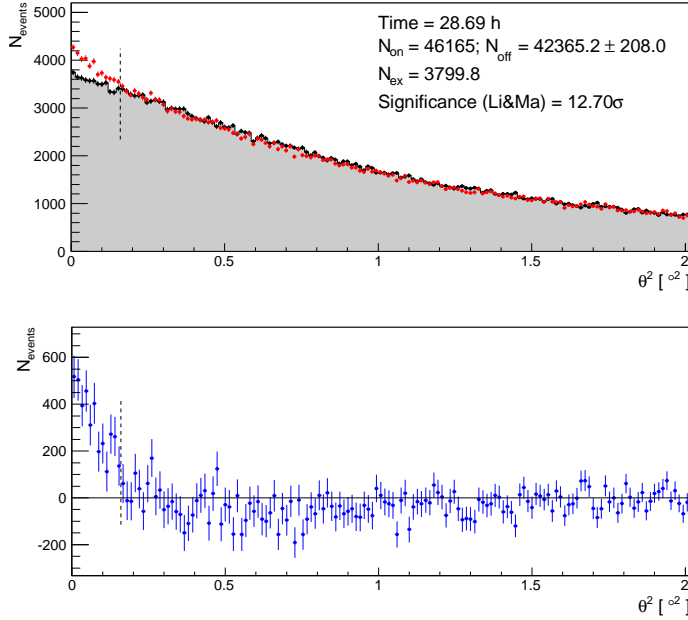

Figure 8.3: θ^2-plots towards HESS J1857+026 (around the center of observations, RA: 18.9575h, Dec=2.7167°). The applied θ^2-cut is $0.16^{\circ 2}$ (vertical black dashed line). ~ 3800 excess events are found showing a statistical significance of 12.7σ. Top: Shown are the ON (red) and OFF distribution (grey) for the combined data of all individual pointings. Bottom: The excess distribution (blue) is shown. In both panels the excess is clearly visible.

A significant emission is clearly visible within the used θ^2-cut of $0.16^{\circ 2}$. The negative excess in the θ^2-range from 0.16 to 0.8 is caused by the fact that in this range the source contaminates the OFF regions. The OFF regions for W1–W4 are $0.8°$ away from the center of the observations, thus for the θ^2-range between 0.16 and 0.64 this OFF regions overlap with the ON region. Such OFF contamination is expected for θ^2 between 0.25 and 0.81 in the positions

W5–W8. By combining all the data tone expects to see such a *negative excess*. For θ^2-values above this region no significant deviation is found, consistent with the reliable background determination. Taking into account the systematic uncertainty of the background (Section 6.6.4) the total excess is $3800 \pm 298_{\text{stat.}} \pm 636_{\text{syst.}}$.

8.3 Results

Figure 8.4 shows the region around the detected emission above 150 GeV together with the position of the Pulsar (PSR J1856+0245), the HESS significance contours and the position of HESS J1858+020. As can be seen from the skymap the emission is clearly extended.
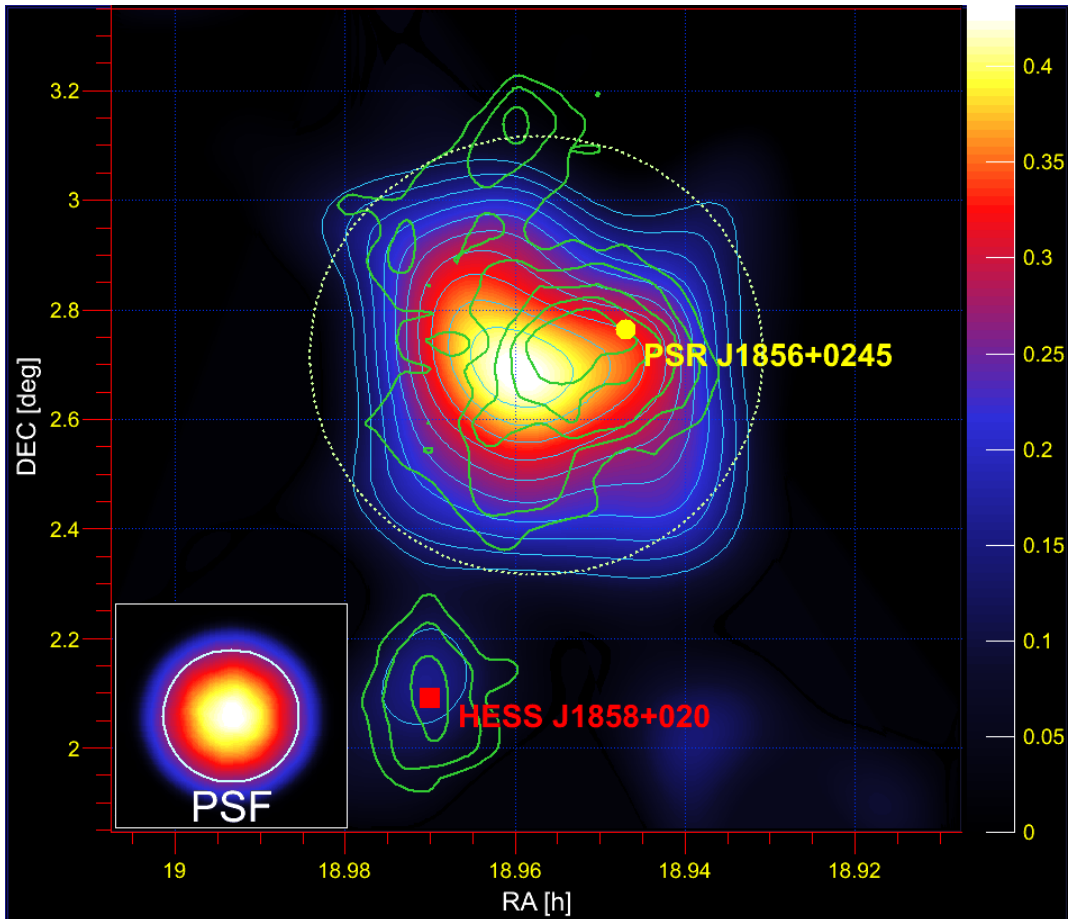

Figure 8.4: Zoom into the relative flux map above 150 GeV (same as Fig. 8.2, integration region marked as green dotted circle). The center of the MAGIC emission is clearly displaced with respect to the pulsar PSR J1856+0245. No emission is seen towards the northern feature of the HESS source.

To determine the centroid and the extension of the emission a two dimensional Gaussian function is fitted to the skymap (before the smearing is applied). The obtained centroid of the emission is:

$$\text{RA} = (18.957 \pm 0.001_{\text{stat.}})\,\text{h} \ \ \text{and} \ \ \text{DEC} = (2.69 \pm 0.02_{\text{stat.}})^\circ$$

which agrees well with the HESS centroid position as well as the one obtained from *Fermi*/LAT by Rousseau et al. (2012). The obtained centroid is clearly misplaced with respect to the pulsar position.

The intrinsic source extension, described by a two dimensional Gauss, is found to be

$$\sigma_{Ra*} = (0.2 \pm 0.02)^\circ$$

$$\sigma_{Dec*} = (0.27 \pm 0.03)^\circ$$

Angle : $(32 \pm 11)^\circ$ (counterlockwise with respect to Ra).

The extension is given as the sigma of the fitted Gauss function where σ_{Ra*} and σ_{Dec*} are the extensions along the right ascension an declination axis for an angle of zero. For Angles different from zero the, both orientations are rotated counterclockwise with respect to the right ascension axis. The here derived extension is larger than the one obtained by HESS in their respective energy range. Rousseau et al. (2012) find no significant extension with *Fermi/LAT* above 10 GeV. Compared to the HESS contours no clear emission is found at the northern tail, in agreement with the results above 10 GeV presented by Rousseau et al. (2012). These discrepancies might indicate a source intrinsic morphological change from GeV to TeV energies.

A spectrum is derived, which is then unfolded to account for the finite energy resolution and bias. The effective area is determined by using a Monte Carlo data set with gammas simulated in a ring with inner radius of 0.25° and the outer radius of 0.65° to account for the differences in the acceptance across the camera plane. The obtained spectrum covers the energy range from ~ 70 GeV to ~ 30 TeV and is shown in figure 8.5. It is well described $(\chi^2/\text{NDF} = 18.81/11)$ by a simple power law of the form:

$$\frac{dN}{dE} = N_0 \left(\frac{E}{1\,\text{TeV}}\right)^{-\Gamma} \tag{8.1}$$

with a photon index of $\Gamma = 2.30 \pm 0.06_{\text{stat}} \pm 0.2_{\text{syst}}$, and a normalization constant at $1\,\text{TeV}$ of $N_0 = (4.3 \pm 0.3_{\text{stat}}) \times 10^{-12} \text{cm}^{-2}\text{s}^{-1}\text{TeV}^{-1}$. The systematic error on the flux normalization is 30%, which includes the systematic uncertainties of the effective area (11%) and the background calculation. In addition, the systematic uncertainty in the energy scale is estimated to be 17 % at low ($\sim 100\,\text{GeV}$) and 15 % at medium ($\sim 250\,\text{GeV}$) energies. The spectral slope agrees very well with the value of -2.39 ± 0.08 obtained previously by HESS. The here obtained results close the gap between between the HESS and the *Fermi*/Lat measurements, overlapping with both of them. By combining the data from high and very high energy gamma rays (see Fig. 8.6) it is clear that the spectrum has a break around 100 GeV. A potential flat emission between ~ 100 GeV and ~ 1 TeV and further steepening at higher energies, which seems to appear in Fig. 8.6, can not be statistically established.
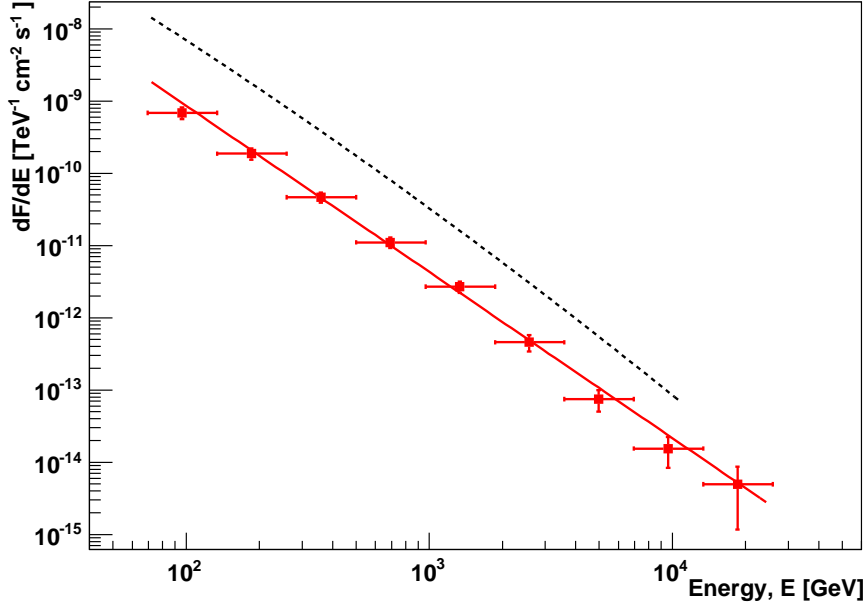
Figure 8.5: Unfolded spectrum obtained for HESS J1857+026 (red points) together with a power-law obtained from forward unfolding (red line). The error bars represent statistical errors only. For comparison, the dotted line represents the spectrum of the Crab Nebula as shown in Aleksić et al. (2012).
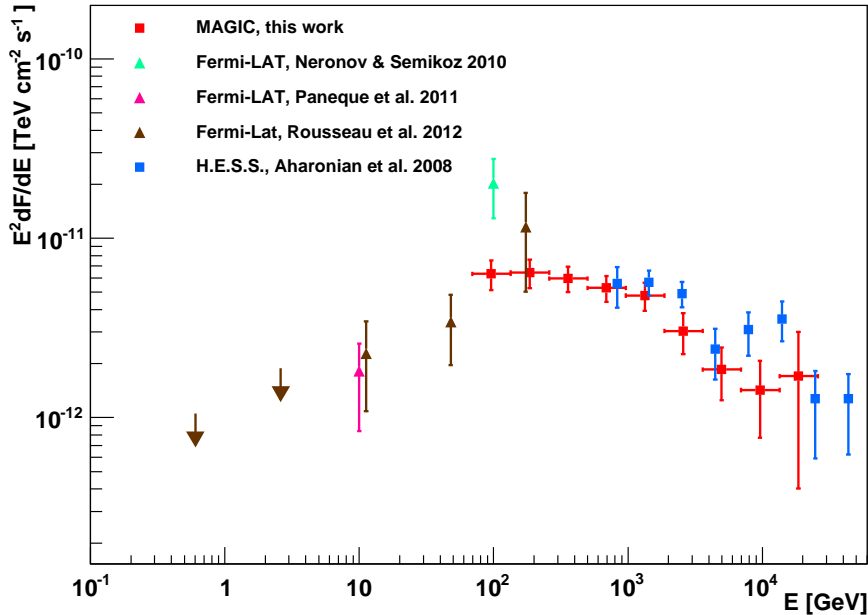

Figure 8.6: Sepctral energy density from HESS J1857+026 obtained by different authors and from different experiments. The slope undergoes a steepening around 100 GeV.

8.3.1 Morphology

To further investigate the possible energy dependence of the morphology, two differential skymaps are produced. They cover the energy range 300-1000 GeV and above 1000 GeV. The lower energy map covers the energy range, where MAGIC reaches its maximum sensitivity, the high energy map is in the range where the best angular resolution is obtained. Note that the angular resolution (defined as one sigma of a 2D Gauss function) is $0.075°$ above ~ 300 GeV and it improves until reaching the saturation value of $0.054°$ at energies above $1\,\mathrm{TeV}$. The total Gaussian smearing applied are $0.11°$ and $0.076°$, respectively. The obtained maps are shown in figure 8.7.
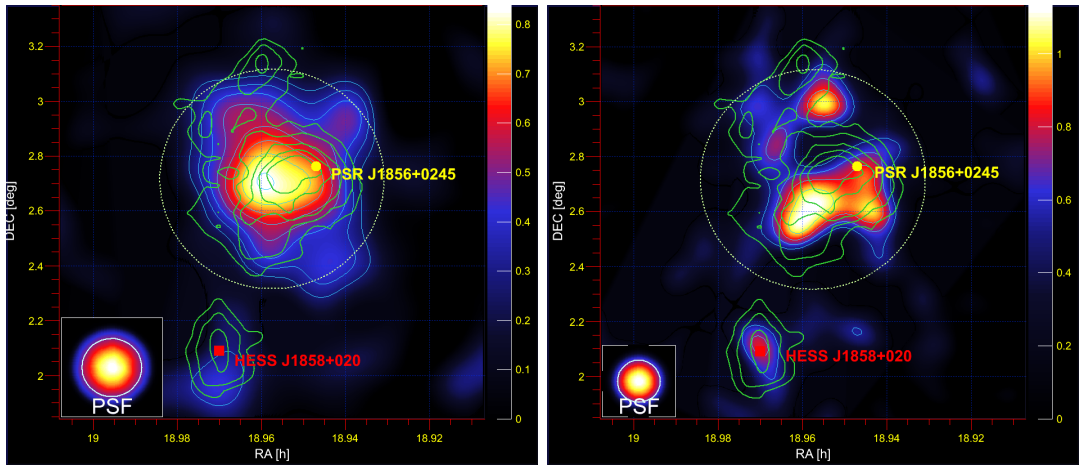

Figure 8.7: MAGIC gamma-ray flux maps in arbitrary units. Same legend as in Figure 8.4 Left hand side: 300-1000 GeV. Right hand side: >1000 GeV. The source evolves into two components at high energies.

The emission in the lower energy range is compatible with the integral skymap obtained above 150 GeV (see Fig. 8.4). At high energies the emission evolves into two components, connected by a marginally significant bridge emission. The skymap obtaine by HESS at energies $\gtrsim$1000 GeV shows a similar feature towards the north. However, the northern emission observed by MAGIC appears displaced with respect to that of HESS.

8.3.2 Projections

Similar to the approach used in the analysis of W51 (see Chapter 7) possible substructures are investigated by projecting the excess onto a line. To determine if two independent sources can be statistically established, a line is defined connecting the centroid of the HESS emission (HESS-main) and the most significant point of the northern tail (HESS-north RA= 18.960 h; DEC=3.14°) seen by HESS. A box in the excess map of MAGIC is projected onto that line (prior to the smearing of the map). The length of the line (1°) was chosen to cover the complete emission. The width was chosen to be 8 times the PSF as a compromise between coverage and contamination of the surrounding. Figure 8.8 shows the projections obtained from both skymaps.
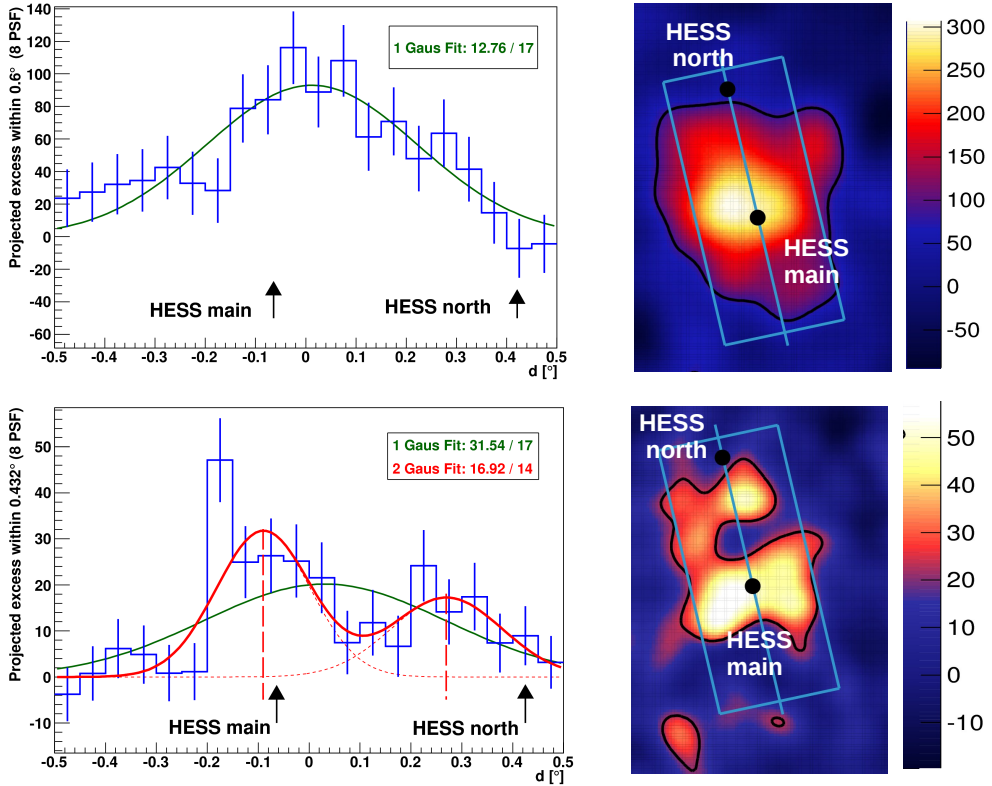
Figure 8.8: Projection of the excess inside the marked box in both differential sky maps: 300 GeV to 1000 GeV (top) and above 1000 GeV (bottom) along the line connecting HESS-north and HESS-main. The projection is done with the unsmeared distribution. The projected excess is fitted with one (green) and two (red) Gaussian curves. The positions of HESS-main and HESS-north (black arrows) and the obtained centroid of the two Gaussian scenarios (red-dotted lines) are marked. The goodness of the fit (χ^2/NDF) is displayed in addition. On the right-hand side a sketch of the skymaps in both energy ranges is shown to illustrate the projected areas. The box has a length of $1°$ and a width of 8 gaussian sigma of the instrumental PSF. The sky maps show the smeared excess (for comparison with Fig. 8.7) with the black contour marking the 3 TS contour.

In the energy range 300-1000 GeV the projected excess is well described by a single Gaussian. At higher energies a two-peak structure appears. The description of the projected excess above 1 TeV by a single Gaussian function is excluded with 98.3% probability. Instead, the obtained distribution is well described in a two Gauss scenario ((χ^2/NDF $= 16.92/14$)). Changing the width of the used box by $\pm 10\%$ does not influence the results.

8.3.3 Position and significance of individual regions

To determine the significance of the individual regions first the centroid positions are determined by means of a Gaussian fit to the skymap above 1 TeV. The region in the north is

denoted: MAGIC-north and the emission surrounding HESS J1857+026 is named MAGIC-main. The following positions are derived:

$$\text{MAGIC} - \text{main}: \quad \text{RA} = (18.959 \pm 0.001_{\text{stat.}})\,\text{h} \quad , \quad \text{DEC} = (2.62 \pm 0.02_{\text{stat.}})^{\circ}$$

$$\text{MAGIC} - \text{north}: \quad \text{RA} = (18.956 \pm 0.001_{\text{stat.}})\,\text{h} \quad , \quad \text{DEC} = (3.00 \pm 0.03_{\text{stat.}})^{\circ}$$

The systematic uncertainties of the position accuracy are estimated to be $\pm 0.05^{\circ}$ in each direction. This estimate has been derived varying the fit radius, and seed values. Note that for too large fit radii the fit gets disturbed as the emission of both regions start to contaminate one another.

Next the significance is determined for the two regions above 1 TeV. A conservative integration area of radius 0.14°, large enough to cover all emission around MAGIC-north, is chosen first. 81.3 ± 15.4 excess events are found over a background of 76.7 ± 9.0, resulting in a significance of 5.3σ. For the integration area around the position of MAGIC-main, a radius of 0.24° was used in order to maximize the coverage without overlapping with the source region of MAGIC-north. 166.6 ± 27.8 excess events are found over a background of 298.4 ± 17.6 resulting in a significance of 6σ. For comparison, the integration area with 0.4° radius (covering all emission) yields a 9σ signal of 401.8 ± 43.2 excess events above a background level of 720.2 ± 27.3 events. Thus, the discovery of two spatially distinct sources[2] at energies above 1 TeV is concluded. Figure 8.9 shows the skymap above 1 TeV together with the determined positions and the integration areas.

For MAGIC-north no significant extension is found with respect to our PSF, in agreement with the point-like appearance in the skymap. MAGIC-main shows an intrinsic extension derived from a two dimensional Gaussian fit of

$$\sigma_{Ra*} = (0.22 \pm 0.02)^{\circ},$$

$$\sigma_{Dec*} = (0.08 \pm 0.03)^{\circ},$$

$$\text{Angle}: (20 \pm 5)^{\circ} \ \text{(counterlockwise with respect to Ra)},$$

which nicely resembles the elongated shape seen in the skymap. The inferior angular resolution at lower energies and a potentially larger extension of MAGIC-main at lower energies prevents do not allow to resolve the emission down to the lowest energies. To determine the energy above which a separation is possible, skymaps of different energy thresholds are produced. At energies $\gtrsim 500$ GeV the two sources are visible as two, individually significant, distinct regions, with compatible morphological properties as obtained for energies above 1 TeV. At lower energies it can not be concluded from the sky maps, if the extended emission of MAGIC-main obscures MAGIC-north.

---

[2]Note that this does not exclude one common astrophysical origin of the emission
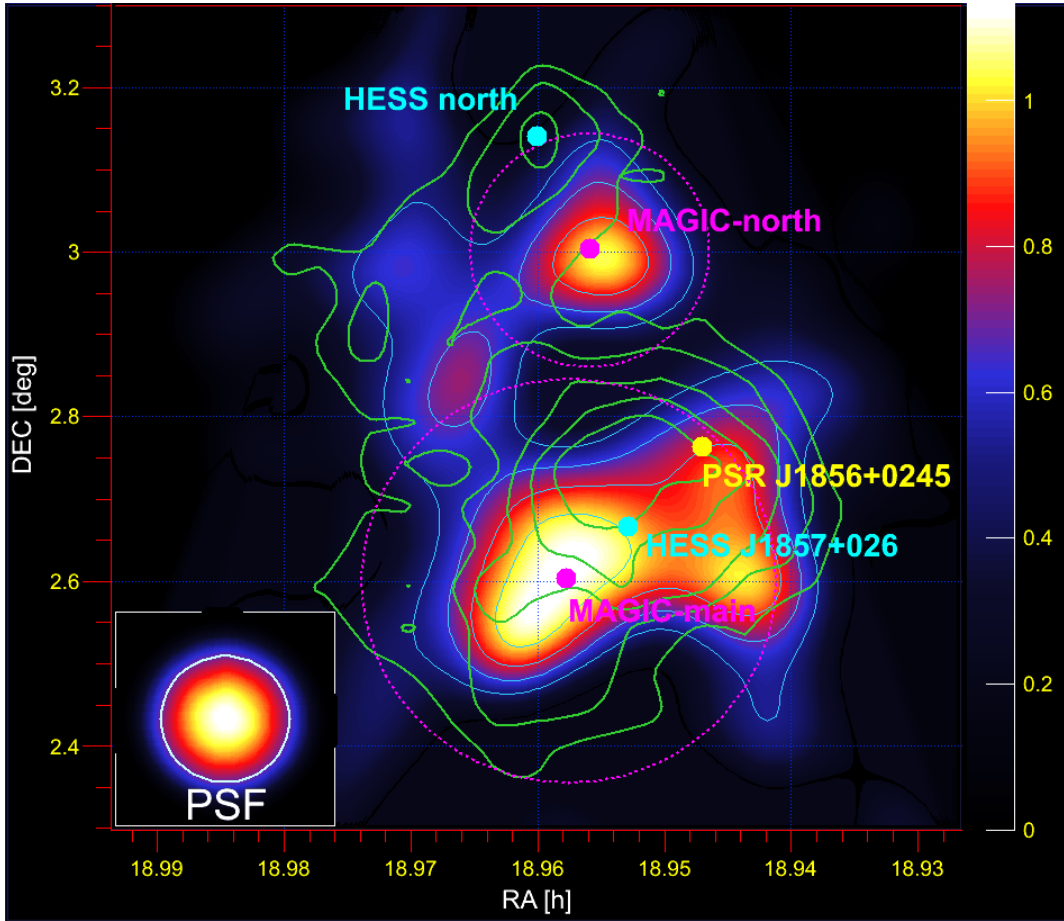
Figure 8.9: Zoom of the skymap above 1 TeV. The color scale represents the MAGIC flux in arbitrary units. Marked are the positions of HESS-north, HESS J1857+026, MAGIC-north and MAGIC main as described in the text. In addition the used integration regions for MAGIC-main and MAGIC-north are shown as the pink-dotted circles.

8.3.4 Spectra of MAGIC-main and MAGIC-north

The unresolved emission at low energies challenges the derivation of spectral properties of the two regions. In addition the elongated shape of MAGIC-main cannot be fully covered by a θ^2 cut due to the vicinity of MAGIC-north. First, the integration areas used to determine the significance above 1 TeV are used to determine the spectra within these individual regions. Both obtained spectra are well described by a power law:

Spectrum contained in $0.14°$ radius around MAGIC-north :
$\Gamma = 2.2 \pm 0.2_{\text{stat}}$
$N_0 = (7.6 \pm 1.7_{\text{stat}}) \times 10^{-13} \text{cm}^{-2}\text{s}^{-1}\text{TeV}^{-1}$
Spectrum contained in $0.24°$ radius around MAGIC-main:
$\Gamma = 2.3 \pm 0.1_{\text{stat}}$

$N_0 = (2.1 \pm 0.2_{\mathrm{stat}}) \times 10^{-12} \mathrm{cm}^{-2} \mathrm{s}^{-1} \mathrm{TeV}^{-1}$.
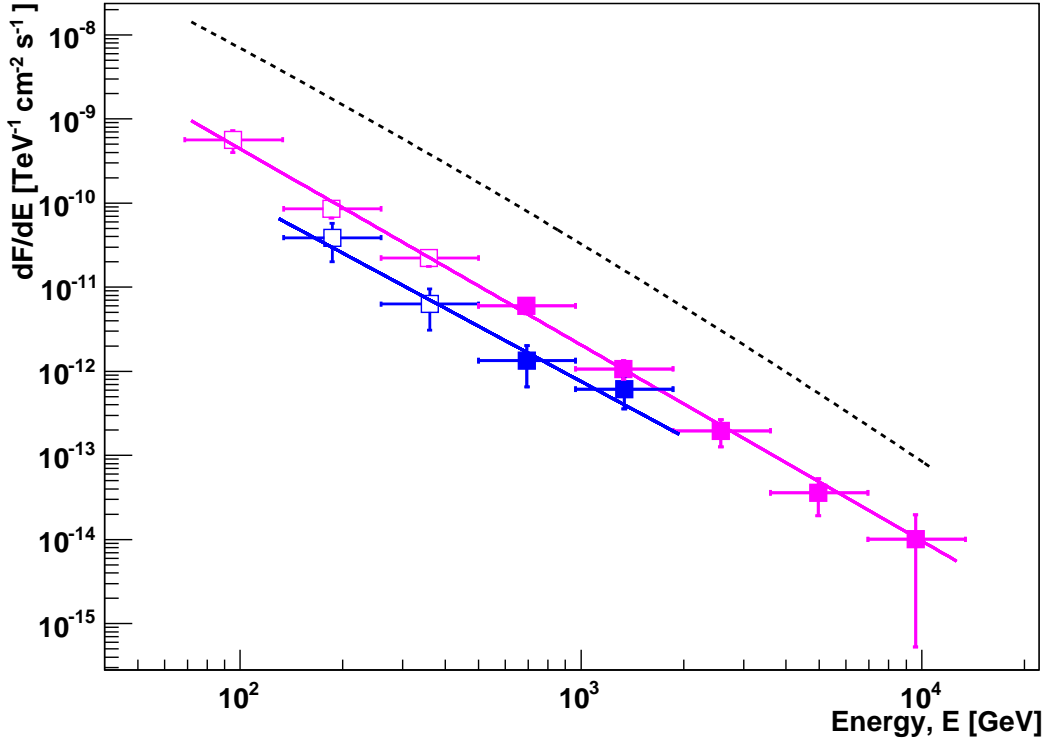

Figure 8.10: Spectra obtained for regions around MAGIC-north (blue points) and MAGIC-main (pink points). The used integration areas correspond to θ^2-cuts of $0.02^{\circ 2}$ and $0.06^{\circ 2}$ around the determined positions of MAGIC-north and MAGIC-main, respectively. To account for the fact that two distinct emission regions are only resolved at energies >500 GeV, spectral points below this energy are marked with open squares. No significant difference of the spectral behavior below and above this energy are found. The black dashed line shows the flux of the Crab Nebula for comparison (Aleksić et al. 2012).

At 1 TeV the derived spectra correspond to $\sim 5\%$ and $\sim 2\%$ of the flux of the Crab Nebula for MAGIC-main and MAGIC-north, respectively. The individual spectra are shown in figure 8.10. When deriving the spectra it was assumed that the excess found in the used integration areas can be completely attributed to MAGIC-main and MAGIC-north, respectively. Note that for energies below ~ 500 GeV this is likely not true as the emission of both regions will contaminate each other. This should be kept in mind when discussing spectral points below this energy (marked as open squares). However, no significant difference of the spectral shape below and above ~ 500 GeV is found for both spectra. The spectral slopes of both individual spectra agree within the statistical errors. The derived slopes do also agree with the spectral slope determined for the overall emission.

The region around MAGIC-north contributes approximately 13–18% to the spectrum from the overall emission. The flux contribution of MAGIC-main region is estimated as 48–53%.

Thus, the sum of both regions reproduces only $\sim 2/3$ of the spectrum derived from the overall integration area including both regions (see Fig. 8.5). While a few percent discrepancy could be explained by statistical fluctuations a *missing flux* of $\sim 30\%$ can not.

The complete coverage of the excess of MAGIC-north by the used integration area and point-like appearance of the region at high energies disfavors an explanation where the missing flux is attributed to MAGIC-north. Also the level of the missing flux is higher than the flux obtained from MAGIC-north itself. One source of uncertainty could arise from the bridge emission connecting the two regions (see Fig. 8.9). However, at least at energies > 500 GeV the bridge emission appears weaker than the emission of MAGIC-north (see also the projection in Fig. 8.8). Thus, to explain the missing flux from the bridge emission does not seem plausible. However, the integration region used to extract the spectrum of MAGIC-main does not completely cover the elliptical shape of the emission (see Fig. 8.9). This is due the selected circular integration region to avoid overlap with the source region of MAGIC-north. The combined integration areas of MAGIC-main and MAGIC-north cover only $\sim 50\%$ of the integration area used to extract the overall spectrum. Thus, the derived spectrum of MAGIC-main is most likely systematically underestimated, offering a plausible explanation of the missing flux. In this sense the derived spectrum has to be understood as the emission contained within the used integration region, yielding a minimum differential flux arising from the source MAGIC-main.

The maximum possible differential flux arising from MAGIC-main is given by the overall spectrum reduced by the contribution of MAGIC-north. The contribution of MAGIC-north is computed under the assumption that MAGIC-north is a point-like source at all energies. Two methods are used to determine the excess arising from MAGIC-north: first a constant integration region of $0.14°$ radius is used at all energies, analog to the way the spectrum was derived previously. In the second approach the integration radius grows dynamically with decreasing energy to $0.2°$ at ~ 100 GeV to account for the energy dependence of the angular resolution. However, the larger integration area at low energies is more affected by possible contamination arising from MAGIC-main. The resulting spectral energy distributions of both methods are shown in Figure 8.11

Also in the dynamic case (cyan points) a power law describes the data very well. No significant differences between the obtained power law using dynamic cuts ($\Gamma = 2.4 \pm 0.2_{\mathrm{stat}}$ and $N_0 = (7.8 \pm 1.6_{\mathrm{stat}}) \times 10^{-13}\mathrm{cm}^{-2}\mathrm{s}^{-1}\mathrm{TeV}^{-1}$) and the previously found parameters using the static cut have been found. A trend of a slightly higher flux at energies below ~ 500 GeV is found for the dynamic approach, resulting in a slightly steeper spectral slope. Based on the presented data it can not be distinguished if this is caused by a contamination from MAGIC-main or a source intrinsic behavior of MAGIC-north. Therefore, the difference has to be understood as a systematic uncertainty, caused by source confusion (*sc*) at low energies. Under the assumption of a point-like source the derived spectrum of MAGIC-north is described by a power law of the following parameters:

$$\text{MAGIC-north (assuming a point like source):}$$
$$\Gamma = 2.2 \pm 0.2_{\mathrm{stat}} \pm 0.2_{\mathrm{sc}} \pm 0.2_{\mathrm{sys}}$$
$$N_0 = (7.6 \pm 1.7_{\mathrm{stat}} \pm 0.2_{\mathrm{sc}} \pm 1.5_{\mathrm{sys}}) \times 10^{-13}\mathrm{cm}^{-2}\mathrm{s}^{-1}\mathrm{TeV}^{-1}$$

The systematic uncertainties (*sys*) arise from the analysis technique (see Section 4.4, and references therein). Clearly, these systematic errors address the absolute precision of the

measurement technique. Therefore, they will affect the individual spectra derived in this work in a highly correlated way.
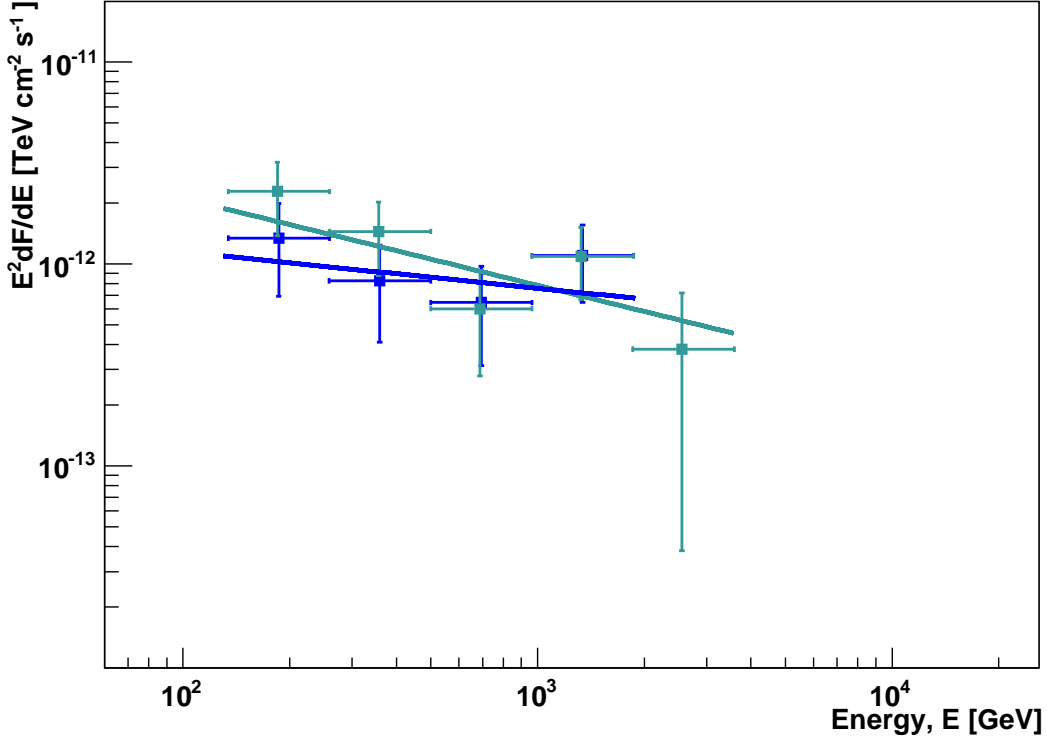

Figure 8.11: Unfolded spectral energy distribution of MAGIC-north derived with a static integration area (blue data points, same as in Fig. 8.10) and a dynamic integration area (cyan data points) to account for the energy dependence of the angular resolution. Note, that at energies below ∼ 500 GeV source confusion may affect the derived values, in particular for the dynamic approach. Lines show power law fits to the data.

To derive the spectrum of MAGIC-main the excess obtained in differential energy bins of MAGIC-north is subtracted from the differential excess obtained from the excess found within 0.4° radius around the center of observations. The resulting distribution is then unfolded. Both methods to derive the contribution of MAGIC-north are compared. The resulting unfolded spectral energy distributions of the overall emission reduced by the contribution of MAGIC-north are shown in Figure 8.12.

The parameters of the power law fits to the data agree within statistical errors. The spectral slope are $-2.36 \pm 0.09_{\text{stat}}$ and $-2.31 \pm 0.07_{\text{stat}}$ for the overall emission reduced by the statically and dynamically determined excess of MAGIC-north, respectively. Accordingly the normalization constants at $1\,\text{TeV}$ in units of $10^{-12}\text{cm}^{-2}\text{s}^{-1}\text{TeV}^{-1}$ are $N_0 = (3.9 \pm 0.4_{\text{stat}})$ and $N_0 = (3.8 \pm 0.4_{\text{stat}})$. The obtained spectral slopes agrees well with the emission obtained for the region around MAGIC-main. However, the obtained flux level is about 65% higher. The derived constraints on the spectrum of MAGIC-main are as follows:

MAGIC-main (defined as the overall flux corrected for the contribution of MAGIC-north):

$$\Gamma = 2.3 \pm 0.1_{\mathrm{stat}} \pm 0.05_{\mathrm{sc}} \pm 0.2_{\mathrm{sys}},$$

$$N_0 = (3.8 \pm 0.4_{\mathrm{stat}} - 1.6_{\mathrm{sc}} + 0.1_{\mathrm{sc}} \pm 1.5_{\mathrm{sys}}) \times 10^{-12} \mathrm{cm}^{-2}\mathrm{s}^{-1}\mathrm{TeV}^{-1},$$

$$\mathrm{where}\ N_0 \geq (2.1 \pm 0.2_{\mathrm{stat}}) \times 10^{-12} \mathrm{cm}^{-2}\mathrm{s}^{-1}\mathrm{TeV}^{-1}.$$
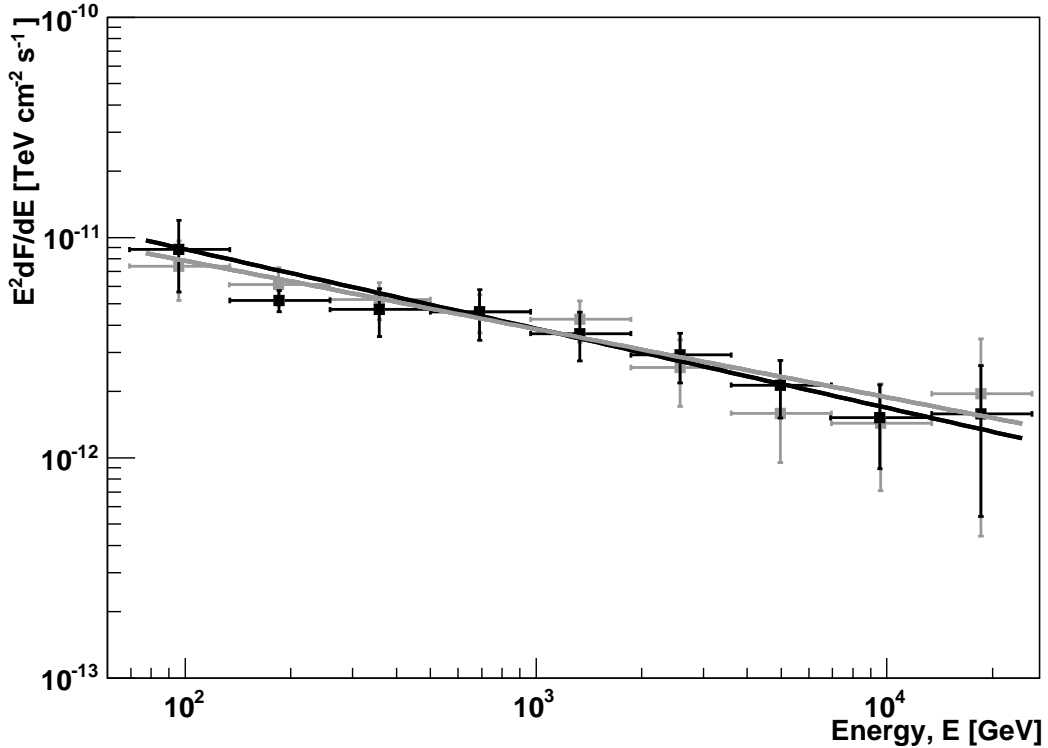

Figure 8.12: Unfolded spectral energy distribution of the overall emission reduced by the emission arising from MAGIC-north. The grey data points were obtained by subtracting the contribution of MAGIC-north derived from an energy independent (static) integration area. For the results shown in black a dynamic integration area was used to determine the contribution of MAGIC-north. The lines represent power-law fits to the data.

Here, the lower limit of the flux normalization correspond to the obtained flux contained within 0.24° around the position of MAGIC-main. MAGIC-main and MAGIC-north show no significant difference in the spectral slope and agree within statistical errors also with the slope of the overall emission. Given the large uncertainties, somewhat different slopes for the two sources can however, not be excluded.

8.3.5 J1858+020

This section briefly addresses the source HESS J1858+020. The average distance of the source to the camera center is $\sim 0.8°$ reducing the sensitivity of the observations by a factor of approximately two (Aleksić et al. 2012). No significant emission of HESS J1858+020 is

detected from our data. However in all obtained skymaps a hint of emission ($\sim$3–4 σ) spatially coincident with the source is found. At energies above 1 TeV 34.4 ± 9.5 excess events with a significance of 3.6σ are found. Taking into account that a significant TeV source has been detected by HESS (Aharonian et al. 2008a), and was later identified as a supernova remnant (Paron & Giacani 2010) one would expect that the spectrum obtained by HESS continues to lower energies. Although the source is not detected with MAGIC alone (in the sense of the fulfilling the $\geq 5\sigma$ criteria) it seems to be likely that the emission with 3.6σ is caused by the known source.

8.4 Discussion

In this section the question if the two resolved emission regions discovered in this work reveal two independent sources, or a complex morphology of one commonly-found astrophysical source is discussed. The compatible spectral shape of MAGIC-main and MAGIC-north does not allow to conclude that both emissions arise from physically different sources, nor is this scenario ruled out. The existence of a pulsar within the region of MAGIC-main suggests the presence of a pulsar wind nebula, likely associated to the emission of MAGIC-main. Furthermore, an extended emission is not unusual in the case of a PWN. Rousseau et al. (2012) discussed a PWN scenario in detail, attributing all the observed TeV-emission to a possible PWN. The here derived spectrum for MAGIC-main is only slightly lower ($\sim 12\%$) than the overall emission and still allows a smooth transition to the spatially consistent data obtained with *Fermi*/LAT. Thus taking into account the statistical and systematic uncertainties of both data, the main conclusions derived by Rousseau et al. (2012) are not expected to change significantly. Based on an upper limit of the X-ray flux they conclude that any leptonic model requires a low magnetic field ($\sim 3\mu G$) as otherwise a strong X-ray synchrotron emission would be expected. They showed that a scenario, in which the observed non-thermal emission is attributed to a PWN, is able to reproduce the observed emission. They conclude that in a leptonic dominated scenario the emission has to be dominated by relic electrons/positrons which escaped the PWN core into a weakly magnetized region at earlier epochs. The displaced centroid of MAGIC-main could be an indication that this is indeed the case. There are two possible ways to explain the elongated shape of MAGIC-main in such a scenario. One is that the relativistic particles escape in a non-uniform way, with one preferred direction towards the centroid of MAGIC-main. It is noted that this would be the same direction as towards the centroid of the HESS emission. The elongated shape of MAGIC-main could also be interpreted in the case where the pulsar itself moves along the major axis of the ellipsoid describing MAGIC-main. On his way the pulsar might leave behind a trail of high energy particles. In both explanation it is challenging to account also for the emission observed in MAGIC-north. That is, in both scenarios it is not obvious to explain why emission connecting the centroid of MAGIC-main and the pulsar is found but no emission is observed connecting MAGIC-north and the pulsar (> 1 TeV).

It might be possible to explain the source with only one emitter outside the pulsar wind scenario. IN the skymaps of both, MAGIC and HESS, indications of a potential bridge emission are observed. However, the marginally significant bridge emission could also be caused by projection effects of two source located close to another in the sky. As originally no counterpart associated to HESS J1857+026 (Aharonian et al. 2008a) was found, it appears

unlikely that a potential common source reflecting the overall structure has already been discovered in any other wavelength than VHE gamma rays.

Given the plausible identification of MAGIC-main as a PWN associated to PSR J1856+0245, and the not-trivial explanation of a spatially distinct TeV source also associated to the pulsar, it appears likely that MAGIC-north has an independent astrophysical origin. Nonetheless, no clear conclusions can be drawn from the data presented in this work.

8.4.1 Possible counterparts of MAGIC-north

An extensive search for possible counterparts of MAGIC-north at other wavelength is still ongoing. No clear association could be found to date. The ongoing search covers the following wavelengths: high energy gamma rays, X-rays, and radio. The closest high energy gamma-ray source is the unidentified source 2FGL J1857.8+0355c. Lee et al. (2012), list this source as possible pulsar, so even an extended PWN at VHE energies might exist. However, the large displacement with respect to MAGIC-north ($\sim 0.8°$) would even in such a scenario require a rather short distance to the object of about $\lesssim 0.75$kpc. If the PWN is significantly more extended than ~ 10 pc in radius a higher distance might be possible. The fact that no extension is found for MAGIC-north and neither for 2FGL J1857.8+0355c challenges this scenario.

One interesting potential counterpart is IRAS 18551+0302. This source was listed in an CS(2-1) survey of IRAS point sources that are potential ultra compact HII regions (Bronfman et al. 1996). The source has then been associated with MSX6C G036.4057+00.0230, which is an HII region in the RMS survey catalog of 6 cm continuum VLA observations towards candidate massive Young Stellar Objects (Urquhart et al. 2009). Gamma ray emission from such objects could be explained in two ways. The illumination of the dense material by the galactic (maybe locally enhanced) cosmic ray flux could produce gamma ray emission in proton-proton collisions and subsequent decay of neutral pions. A second explanation would be that highly relativistic particles, and subsequently gamma rays are produced in massive young stellar objects (e.g., Romero 2010, and references therein). However, it is not clear if any of these mechanisms can account for the observed flux. In particular, a reliable distance measurement is crucial for any further consideration. The results of the search for possible counterparts will be presented in an article in preparation along with the MAGIC results based on the here presented work.

8.5 Conclusions

MAGIC observed HESS J1857+026 during 2010 to investigate the possible PWN nature of its emission and to find out more about the northern tail of the emission seen by HESS. Moreover, the source was used to validate the performance of the MAGIC telescopes for extended sources. After collecting ~ 30h of data MAGIC detected an extended emission coincident with HESS J1857+026 showing more than 12σ significance above the energy threshold of 150 GeV.

A spectrum was derived by integrating a $0.4°$ radius around the center of observations. The derived spectral energy density spans over two orders of magnitude in energy and closes the gap between the result obtained by HESS and *Fermi*/LAT. A spectral break is observed at ~ 100 GeV constrained by the results obtained in this analysis and by the data of *Fermi*/LAT from the low energy side. The SNR HESS J1858+020 is not detected at a 5σ-level. In all

investigated energy ranges hints for emission around $\lesssim 3\sigma$ have been found plausibly caused by the known source.

This work presents the first detailed morphological study of the extended TeV emission from HESS J1857+026. Skymaps and projections are produced in two differential energy ranges. At energies > 1 TeV two spatially distinct sources can be statistically established. A description of the projected excess by a single Gaussian function at this energies is excluded with 98% probability. Integration regions defined around the derived positions for MAGIC-main and MAGIC-north reveal a statistically significant signal of more than 5σ, each. Thus, the discovery of the sources MAGIC-main and MAGIC-north is established. MAGIC-north is compatible with a point-like source. MAGIC-main shows a clearly elongated shape with the major axis inclined by $\sim 20°$ to the right ascension axis. Spectra of both regions have been measured. Even though at energies < 500 GeV source confusion starts to play an important role, spectral information for both sources could be extracted down to ~ 100 GeV. Both spectra are well described by a power law showing no significant spectral difference between MAGIC-main and MAGIC-north. MAGIC-main could be plausibly explained as the PWN of a Vela-like pulsar enclosed in the TeV emission. The challenging explanation of MAGIC-north as a distinct emission region caused by the same PWN might indicate an independent astrophysical origin.

Chapter 9

Conclusions and outlook

The main topic of this thesis was to investigate the origin of galactic cosmic rays usinig very high energy gamma ray astronomy. The observations presented in this work where carried out with the two MAGIC telescopes which allow to observe VHE gamma rays in the energy range from 50 GeV to multi TeV. Currently, the MAGIC telescopes offer the highest sensitivity for energies $\lesssim$ 200 GeV worldwide. The relatively low energy threshold allows to efficiently combine MAGIC data with those from HE instruments such as the *Fermi*/LAT because the energy ranges are overlapping. In this way it is possible to constrain the underlying particle distributions from sub GeV energies beyond TeV and thus for $\gtrsim$ 4 orders of magnitude in energy without significant gaps.

Moreover the comparable good angular resolution of MAGIC allows to resolve structures down to $\sim$ 1 pc scales at a distance of 1 kpc. Thus, MAGIC observations do not only allow to extend the spectral information to VHE energies, but also to perform morphological studies for large sources like supernova remnants and pulsar wind nebulae.

The potential of MAGIC was substantial improved during this thesis, most importantly by the development of a generalized background determination, the change of the standard observation modus from 2 to 4 wobble positions, and the adjustment of the Monte-Carlo simulations based on the analysis of cosmic muon events. As a result of these improvements, two main scientific observations were possible and the results are summarized in the following.

9.1 Ongoing hadron acceleration in the SNR W51C

The system W51 hosts two big star forming regions (W51A and W51B) as well as a SNR (W51C), which interacts with the large molecular cloud of W51B. A possible PWN associated to W51C (Koo et al. 2002) makes the situation quite complex. Extended emission was detected from the W51 region in the gamma regime by *Fermi*/LAT and HESS. Ionization by cosmic rays (CRs) towards the interaction zone between remnant and cloud was reported to be enhanced by a factor of $\sim$ 100 compared to the value in the standard interstellar medium. This has been interpreted as a high flow of freshly accelerated sub-GeV protons in that region.

During the years 2010 and 2011 more than 50 hours of MAGIC data of W51 haven been collected. An extended emission is detected with high significance (11 σ) and the spectrum measured by *Fermi*/LAT could be extended up to $\sim$5 TeV. The gamma ray spectrum can be described by a single power law with a slope of $\sim$ -2.7 from $\sim$ 10 GeV up to $\sim$ 5 TeV. The spatial origin of the emission is clearly pinpointed to the interaction zone between cloud and remnant. In addition, a feature of the emission extending towards the possible PWN was found. Even though two individual sources can not be established statistically, the contribution of the PWN (assuming a point-like source) is independent of the investigated energy

range and around 20% of the overall detected emission. The W51 region is the first case where a detailed morphological study of the observed emission was carried out using the MAGIC telescopes. The modeling of multi-wavelength data strongly suggests a hadronic origin of the emission. Moreover, the preliminary result of a differential upper limit around ~ 100 MeV presented by the *Agile*-collaboration further challenges a leptonic explanation of the gamma ray flux. The hadronic scenario implies that $\sim 16\%$ of the kinetic energy of the supernova shock wave has been transformed to CRs. The morphology of the source might indeed indicate that MAGIC observes the emission produced directly at the acceleration side of CRs. Three main scenarios are possible: if the PWN is indeed responsible for $\sim 20\%$ of the emission, then the inferred proton flux (or matter density) is overestimated by this amount. In this case the hadronic emission is closely confined to the interaction zone between remnant and molecular cloud and thus to the suspected acceleration zone. The morphology could also be explained by an asymmetric escape of CRs from the interaction zone generated by, e.g. the global magnetic field orientation. A suppressed diffusion towards/inside the molecular cloud may be explained with the high ambient density. In the last scenario a variation of the injection efficiency of along the shock surface of the supernova remnants could be able to explain the tail emission. It is interesting to note that the injection efficiency is largest for a magnetic field orientation parallel to the shock normal. Thus, the latter two scenarios could be distinguished by measuring the magnetic field orientation in the system. In all of the above addressed scenarios at least some acceleration is likely still ongoing, which is supported by the measurement of the enhanced CR ionization. Therefore, the observed gamma ray spectrum may provide direct information about the source spectrum of CRs in W51C. Among a few other sources such as W51C represents one of the most promising galactic CR accelerators.

The emission seen by MILAGRO with a median energy of 10 TeV (Abdo et al. 2009d), if proven at this flux level, would imply an additional harder component of the emission above the energy accessed in this work. A harder component at high energies can not be explained in the usual framework of DSA in SNRs and would imply an additional underlying mechanism. To understand the highest energies in the system the understanding of the putative PWN is essential. To conclude about a significant structure in the signal above 1 TeV the statistics have to be more than doubled. Additional observations could allow to verify or falsify the flux level reported by MILAGRO. It will be also of great interest to see if the emission arising from the *cloud* region extends even further in energy, or if the emission shows a cut-off. Moreover, if CRs escape the system the highest energies might reach the molecular cloud W51A and produce detectable gamma ray emission at multi TeV energies from this region. The combination of the data presented here with future observations will, however, not be straightforward as the MAGIC telescopes have undergone significant changes during the recent upgrade. An extension of the spectrum towards higher energies could also be achieved with systems like HESS or VERITAS, which offer a higher collection area at for multi-TeV energies compared to MAGIC. The planned Cherenkov Telescope array (CTA), however, will have an about one order of magnitude better sensitivity than the current generation of Cherenkov telescopes, a much higher collection area for TeV energies, and an improved angular resolution over the complete energy range. The CTA, at the latest, will be able to reveal the morphological and spectral properties of W51 at TeV energies and beyond.

The measurements of the ionization degree of specific molecules towards W51C could be extended to determine the spatial distribution of the ionization at and around the observed GeV-TeV emission. This would allow to draw conclusions about where particles have been

injected and are accelerated along the shock front. This will shed light on the question if the location of the gamma-ray emission is due to the high local gas density or also to the main region of CR acceleration. In addition, it will give a handle to estimate the surface of efficient injection of particles in the acceleration process and therefore allow to estimate the total injection rate at the present epoch. If the PWN is responsible for a part of the gamma ray emission the likely leptonic nature of PWN would imply a low CR ionization value at its position.

The high hadronic gamma ray luminosity of the supernova remnant W51C, its peculiar morphology, a potential harder gamma ray component at 10 TeV, and the evidence of ongoing proton acceleration at least up to 50 TeV render this source as a laboratory to investigate the origin of CRs also for future observations and experiments.

9.2 Resolving the unidentified gamma ray source HESS J1857+026

The second object observed in the framework of this thesis was the unidentified gamma ray source HESS J1857+026. This object is clearly extended and shows a flux of about 15% of that of the Crab Nebula above 1 TeV as measured by HESS. The reported spectrum follows a simple power law of a slope around -2.4 between $800\,\mathrm{GeV}$ and $45\,\mathrm{TeV}$. The emission located at the northern edge of the source might be an independent source, however, no clear conclusions could be drawn from the available data. An energetic pulsar coincident with the HESS position has been discovered, suggesting a PWN nature of the VHE emission.

During 2010 a total of $29\,\mathrm{h}$ of data have been collected by MAGIC resulting in a detection of the source with more than 12σ above an energy threshold of $150\,\mathrm{GeV}$. Preliminary MAGIC data together with the results obtained from *Fermi*/LAT showed that the spectral energy density undergoes a hardening for energies below $100\,\mathrm{GeV}$. This hardening happens exactly in the energy region connecting the MAGIC and *Fermi*/LAT results and is only evident by combining the data from both instruments. In this thesis the first detailed analysis of the MAGIC data including morphological studies in differential energy bins is presented. For energies above $1\,\mathrm{TeV}$ the emission evolves in two spatially distinct components named MAGIC-main and MAGIC-north. The projected excess can be well described with two Gaussians. The significance of the excess is $> 5\sigma$ for both regions individually. Position, extension, and spectra are obtained for both components. The emission of MAGIC-north shows no significant extension and appears point-like. MAGIC-main is elongated with the major axis inclined by $\sim 20°$ with respect to the right ascension axis. For energies < 500 GeV the two regions can not be resolved. At $1\,\mathrm{TeV}$ the here derived spectra correspond to ~ 5–9% and $\sim 2\%$ of the flux of the Crab Nebula for MAGIC-main and MAGIC-north, respectively. The large statistical and systematic errors do not allow to draw firm conclusion on the possibility of different spectral slopes. However, both spectra are compatible with a power law of index -2.3.

The extended nature of MAGIC-main indicates that MAGIC-main could be the pulsar wind nebula of the nearby pulsar. It is not clear if MAGIC-north has in independent astrophysical origin, but the observed morphology is hard to explain in a scenario where the emission is caused from the same PWN as MAGIC-main. An intensive search for counterparts of MAGIC-north in other wavelength is still ongoing. Possible candidates are the unidentified *Fermi* source 2FGL J1857.8+0355c and the ultra compact HII region MSX6C G036.4057+00.0230. The nature of the emission of HESS J1857+026 is still puzzling. One of the largest uncertainty

in the obtained spectra arises from source confusion at low energies. The use of an elliptical integration region for MAGIC-main would improve the situation, but not solve the problem at the lowest energies. A theoretical modeling of the spectra and its morphology could, however, allow to extrapolate the spectra to energies where the emission is not resolved. Such a modeling would obviously strongly depend on the underlying nature of both emission regions. Therefore, the highest priority for any further investigation is the identification of possible counterparts for MAGIC-north. A particularly interesting candidate is the ultra compact HII region IRAS 18551+0302, as such objects are places of ongoing massive star formation, and the jets of massive young stellar objects (MYSOs) particles could be able to accelerate particles to high enough energies. In such a scenario, MAGIC would see the cumulative emission of all MYSOs in the HII region. The amount (and population) of MYSOs in the system as well as its distance are crucial but unknown parameters for any estimation of the expected flux. Finally, the understanding of unidentified VHE gamma ray sources, such as HESS J1857+026, is crucial to understand the physics of particle accelerations and the type of sources able to produce VHE emission.

9.3 Outlook

In Summer 2012 a new camera has been installed in MAGIC I. Early results based on new data showed a compatible PSF and a higher light collection efficiency compared to the results found in this work as expected from the improved PMTs used in the new camera. Also triggered by the results of the muon analysis presented in this work a huge effort has been made in refining many parts of the simulations, which already reduced significantly the mismatch between data and MC. Tighter constraints on the gamma hadron separation cuts which would further improve the sensitivity of MAGIC may thus become possible in the near future. The effect of the asymmetric acceptance investigated in this thesis is expected to be significantly reduced to the now larger trigger region of the new MI camera. Moreover, the larger trigger area in MI is expected to improve the collection area at low energies in particular for larger distances from the source position to the camera center. Such an improvement is very interesting for the future study of extended sources, as it could increase the area in the sky with a high exposure. The analysis of individual regions in W51 and HESS J1857+026 showed impressively that MAGIC is able to resolve structures in sources. However, the complexity of such structures and source confusion in the case of neighboring sources showed clearly the limitations of the standard signal determination in VHE gamma ray astronomy: the spherical θ^2-cut. For the future a more advanced method should be developed which is able to adopt for more complex shapes of the sources. The better the shape of an integration area can be optimized to the shape of a real source, the smaller region covered with no signal which will improve the sensitivity for extended sources. However, the introduction of a not trivial source shape, introduces additional assumptions and should therefore be used with care. The continuously improving performance of the MAGIC telescopes will allow more advanced and detailed results in the near future.

The advantage of determining the spatial structures of galactic sources, is to locate the region of gamma ray production and therefore potentially the acceleration zone of CRs. In addition, the flux of escaping CRs can be obtained by resolving the gamma ray emission arising from

molecular clouds near CR sources. The current angular resolution of gamma ray instruments is not sufficient to resolve extragalactic objects, like AGNs. Thus, galactic sources allow unique insights into the physics of cosmic ray acceleration.

As of today, the gamma ray emission of most middle age remnants in the vicinity of molecular clouds is associated with a hadronically dominated gamma ray emission, while the situation for young remnants is more diverse. While there is little doubt that SNRs are indeed the sources of galactic cosmic rays, the details of cosmic ray acceleration and their release are not fully understood. With the current generation of VHE instruments the known population of gamma ray emitting SNRs is not expected to increase dramatically in the next years. Deep observations can, however, reveal the physical properties of known sources and thus allow to predict the gamma ray properties of yet undiscovered SNRs. Moreover, results from HE instruments, such as *Fermi*/LAT and *Agile*, allow to estimate the VHE flux and give therefore important indications indications for Cherenkov telescopes. Understanding the differences between the gamma ray emission of remnants like, e.g. W51C, W44, IC443 and W28, are crucial to access the dynamics of CR acceleration in middle-age SNRs. In addition, differences between young an middle-age remnants might reveal the dynamics of CR acceleration in SNRs on larger timescales.

The future of VHE astronomy will be the currently planned Cherenkov telescope array (CTA), which will consist of about 100 telescopes. About an order of magnitude higher sensitivity and significantly improved angular and energy resolution promise a new era of observations. The amount of discovered sources in VHEs is expected to increase by an order of magnitude. The large amount of SNRs expected to be discovered by the CTA will for the first time allow population studies with a sufficient amount of objects. Moreover, the high quality of the individual observations promise detailed constrains on the physical parameters in many of the sources. In addition, the higher collection area of CTA will allow to access even higher energies, which could reveal different spectral behaviors of different SNRs at yet unaccessible energies. Finally, the higher sensitivity in the complete energy band could reveal new types of sources and will substantially improve our current understanding of the extreme universe.

Nowadays only a few SNRs are known in HE and VHE energies which indicate CR acceleration. To understand the origin of cosmic rays each of this sources has to understood in detail. The continuously all sky monitoring in the GeV band (*Fermi*/LAT and *Agile*) and deep observations with Cherenkov telescopes (MAGIC, H.E.S.S., VERITAS) will reveal more sources and more precise spectral and morphological properties of possible GCR accelerators. In the future, the CTA is expected to enlarge the amount of known VHE sources by a factor of ten with substantially improved precision of each individual observation. It will allow for the first time to study the population of VHE emitting SNRs and push the accessible energy range significantly beyond that of today. With the new generation of observatories in mm/submm (e.g., ALMA) but also in the infrared (e.g., SOFIA) CR-ionization measurements can in addition to HE and VHE observations also play a major part in understanding the underlying physics of CR acceleration.

Bibliography

2012, Solar luminosity: http://nssdc.gsfc.nasa.gov/planetary/factsheet/sunfact.html

2012, *root* software: http://root.cern.ch

Abdo, A. A., Ackermann, M., Ajello, M., et al. 2010a, ApJ, 710, L92

Abdo, A. A., Ackermann, M., Ajello, M., et al. 2011a, ApJ, 734, 28

Abdo, A. A., Ackermann, M., Ajello, M., et al. 2011b, Science, 331, 739

Abdo, A. A., Ackermann, M., Ajello, M., et al. 2010b, ApJ, 718, 348

Abdo, A. A., Ackermann, M., Ajello, M., et al. 2009a, Nature, 462, 331

Abdo, A. A., Ackermann, M., Ajello, M., et al. 2009b, Phys. Rev. D, 80, 122004

Abdo, A. A., Ackermann, M., Ajello, M., et al. 2009c, ApJ, 706, L1

Abdo, A. A., Ackermann, M., Ajello, M., et al. 2010c, Science, 327, 1103

Abdo, A. A., Ackermann, M., Ajello, M., et al. 2010d, ApJ, 712, 459

Abdo, A. A., Ackermann, M., Ajello, M., et al. 2011c, ApJ, 734, 116

Abdo, A. A., Allen, B. T., Aune, T., et al. 2009d, ApJ, 700, L127

Acciari, V. A., Aliu, E., Arlen, T., et al. 2009, ApJ, 698, L133

Acciari, V. A., Aliu, E., Arlen, T., et al. 2011, ApJ, 730, L20

Acero, F., Aharonian, F., Akhperjanian, A. G., et al. 2010, A&A, 516, A62

Acero, F., Aharonian, F., Akhperjanian, A. G., et al. 2009, Science, 326, 1080

Ackermann, M., Ajello, M., Atwood, W. B., et al. 2010, Phys. Rev. D, 82, 092004

Ackermann, M., Ajello, M., Atwood, W. B., et al. 2012, ApJ, 750, 3

Actis, M., Agnetta, G., Aharonian, F., et al. 2011, Experimental Astronomy, 32, 193

Adriani, O., Barbarino, G. C., Bazilevskaya, G. A., et al. 2011, Science, 332, 69

Aharonian, F., Akhperjanian, A., Beilicke, M., et al. 2004a, ApJ, 614, 897

Aharonian, F., Akhperjanian, A. G., Barres de Almeida, U., et al. 2008a, A&A, 477, 353

Aharonian, F., Akhperjanian, A. G., Bazer-Bachi, A. R., et al. 2008b, A&A, 481, 401

Bibliography

Aharonian, F., Akhperjanian, A. G., Bazer-Bachi, A. R., et al. 2007, A&A, 464, 235

Aharonian, F., Buckley, J., Kifune, T., & Sinnis, G. 2008c, Reports on Progress in Physics, 71, 096901

Aharonian, F. A., Akhperjanian, A. G., Aye, K.-M., et al. 2004b, Nature, 432, 75

Aharonian, F. A. & Atoyan, A. M. 1996, A&A, 309, 917

Aharonian, F. A., Atoyan, A. M., & Voelk, H. J. 1995, A&A, 294, L41

Ahn, H. S., Allison, P., Bagliesi, M. G., et al. 2010, ApJ, 714, L89

Aielli, G., Camarri, P., Iuppa, R., et al. 2010, The Astronomer's Telegram, 2921, 1

Albert, J., Aliu, E., Anderhub, H., et al. 2007a, Nuclear Instruments and Methods in Physics Research A, 583, 494

Albert, J., Aliu, E., Anderhub, H., et al. 2007b, ApJ, 664, L87

Albert, J., Aliu, E., Anderhub, H., et al. 2008, Nucl.Instrum.Meth., A588, 424

Aleksić, J., Alvarez, E., Antonelli, L., et al. 2012, Astroparticle Physics, 35, 435

Aleksić, J., Alvarez, E. A., Antonelli, L. A., et al. 2012a, A&A, 539, L2

Aleksić, J., Alvarez, E. A., Antonelli, L. A., et al. 2012b, A&A, 541, A13

Aleksić, J., Alvarez, E. A., Antonelli, L. A., et al. 2011, ApJ, 742, 43

Aleksić, J., Alvarez, E. A., Antonelli, L. A., et al. 2012c, A&A, 540, A69

Aleksić, J., Antonelli, L. A., Antoranz, P., et al. 2010, ApJ, 723, L207

Alfvén, H. 1949, Physical Review, 75, 1732

Aliu, E., Anderhub, H., Antonelli, L. A., et al. 2008, Science, 322, 1221

Aliu, E., Anderhub, H., Antonelli, L. A., et al. 2009, Astroparticle Physics, 30, 293

Amano, T. & Hoshino, M. 2007, ApJ, 661, 190

Anderson, C. D. 1933, Physical Review, 43, 491

Antoni, T., Apel, W. D., Badea, A. F., et al. 2005, Astroparticle Physics, 24, 1

Araya, M. & Frutos, F. 2012, MNRAS, 425, 2810

Axford, W. I., Leer, E., & Skadron, G. 1977, in International Cosmic Ray Conference, Vol. 11, International Cosmic Ray Conference, 132–137

Bamba, A., Yamazaki, R., Yoshida, T., Terasawa, T., & Koyama, K. 2005, ApJ, 621, 793

Baring, M. G., Ellison, D. C., Reynolds, S. P., Grenier, I. A., & Goret, P. 1999, ApJ, 513, 311

Bell, A. R. 1978a, MNRAS, 182, 147

Bell, A. R. 1978b, MNRAS, 182, 443

Bell, A. R. 2004, MNRAS, 353, 550

Bell, A. R. & Lucek, S. G. 2001, MNRAS, 321, 433

Berezhko, E. G., Ksenofontov, L. T., & Völk, H. J. 2003, A&A, 412, L11

Berezhko, E. G., Ksenofontov, L. T., & Völk, H. J. 2012a, ApJ, 759, 12

Berezhko, E. G., Ksenofontov, L. T., & Völk, H. J. 2012b, ApJ, 759, 12

Beringer, J., Arguin, J.-F., Barnett, R. M., et al. 2012, Phys. Rev. D, 86, 010001

Bhandari, N. 1986, Indian Academy of Sciences Proceedings: Earth and Planetary Sciences, 95, 183

Biland, A., Garczarczyk, M., Anderhub, H., & et al. 2008, in International Cosmic Ray Conference, Vol. 3, International Cosmic Ray Conference, 1353–1356

Blandford, R. D. & Ostriker, J. P. 1978, ApJ, 221, L29

Blasi, P. & Amato, E. 2012a, Journal of Cosmology and Astroparticle Physics, 1, 10

Blasi, P. & Amato, E. 2012b, Journal of Cosmology and Astroparticle Physics, 1, 11

Blasi, P., Gabici, S., & Vannoni, G. 2005, MNRAS, 361, 907

Blumenthal, G. R. & Gould, R. J. 1970, Reviews of Modern Physics, 42, 237

Blümer, J., Engel, R., & Hörandel, J. R. 2009, Progress in Particle and Nuclear Physics, 63, 293

Briggs, M. S., Fishman, G. J., Connaughton, V., et al. 2010, Journal of Geophysical Research (Space Physics), 115, 7323

Brogan, C. L., Frail, D. A., Goss, W. M., & Troland, T. H. 2000, ApJ, 537, 875

Bronfman, L., Nyman, L.-A., & May, J. 1996, A&AS, 115, 81

Caprioli, D. 2012, Journal of Cosmology and Astroparticle Physics, 7, 38

Caprioli, D., Kang, H., Vladimirov, A. E., & Jones, T. W. 2010, MNRAS, 407, 1773

Carpenter, J. M. & Sanders, D. B. 1998, AJ, 116, 1856

Cassam-Chenaï, G., Hughes, J. P., Reynoso, E. M., Badenes, C., & Moffett, D. 2008, ApJ, 680, 1180

Ceccarelli, C., Hily-Blant, P., Montmerle, T., et al. 2011, ApJ, 740, L4+

Compton, A. H. & Getting, I. A. 1935, Phys. Rev., 47, 817

Bibliography

Copetti, M. V. F. & Schmidt, A. A. 1991, MNRAS, 250, 127

Cordes, J. M. & Lazio, T. J. W. 2002, ArXiv Astrophysics e-prints

CTA cons. 2012, http://www.cta-observatory.org/

Di Sciascio, G. & for the ARGO-YBJ Collaboration. 2012, ArXiv e-prints

Diehl, R., Halloin, H., Kretschmer, K., et al. 2006, Nature, 439, 45

Diehl, R. & Timmes, F. X. 1998, PASP, 110, 637

Domingo-Santamaria, E., Flix, J., Rico, J., Scalzotto, V., & Wittek, W. 2005, in International Cosmic Ray Conference, Vol. 5, International Cosmic Ray Conference, 363

Draine, B. T. & McKee, C. F. 1993, ARA&A, 31, 373

Drury, L. O. 1983, Reports on Progress in Physics, 46, 973

Drury, L. O., Duffy, P., Eichler, D., & Mastichiadis, A. 1999, A&A, 347, 370

Ellison, D. C., Drury, L. O., & Meyer, J.-P. 1997, ApJ, 487, 197

Ellison, D. C., Patnaude, D. J., Slane, P., & Raymond, J. 2010, ApJ, 712, 287

Erlykin, A. D. & Wolfendale, A. W. 2002, Journal of Physics G Nuclear Physics, 28, 359

Erlykin, A. D. & Wolfendale, A. W. 2012, Astroparticle Physics, 35, 449

Fang, J. & Zhang, L. 2010, MNRAS, 405, 462

Fermi, E. 1949, Physical Review, 75, 1169

Ferrari, F. & Szuszkiewicz, E. 2009, Astrobiology, 9, 413

Fiasson, A., Marandon, V., Chaves, R. C. G., & Tibolla, O. 2009, in Proceedings of the 31st ICRC, Lodz

Finke, J. D. & Dermer, C. D. 2012, ApJ, 751, 65

Finnegan, G. & for the VERITAS Collaboration. 2011, ArXiv e-prints

Fomin, V. P., Stepanian, A. A., Lamb, R. C., et al. 1994, Astroparticle Physics, 2, 137

Funk, S. 2012, ArXiv e-prints

Gabici, S. 2012, ArXiv e-prints

Gabici, S., Aharonian, F. A., & Blasi, P. 2007, Ap&SS, 309, 365

Gabici, S., Aharonian, F. A., & Casanova, S. 2009a, MNRAS, 396, 1629

Gabici, S., Aharonian, F. A., & Casanova, S. 2009b, MNRAS, 396, 1629

Gabici, S., Casanova, S., Aharonian, F. A., & Rowell, G. 2010, in SF2A-2010: Proceedings of the Annual meeting of the French Society of Astronomy and Astrophysics, ed. S. Boissier, M. Heydari-Malayeri, R. Samadi, & D. Valls-Gabaud , 313–+

Gaisser, T. K. 2007, in Energy Budget in the High Energy Universe, ed. K. Sato & J. Hisano, 45–55

Gaisser, T. K. & Stanev, T. 2012, ArXiv e-prints

Garczarczyk, M. & MAGIC Collaboration. 2011, Nuclear Instruments and Methods in Physics Research A, 639, 33

Gargaté, L. & Spitkovsky, A. 2012, ApJ, 744, 67

Giacinti, G., Kachelrieß, M., & Semikoz, D. V. 2012, Physical Review Letters, 108, 261101

Gieseler, U. D. J., Jones, T. W., & Kang, H. 2000, A&A, 364, 911

Giglietto, N., Allafort, A., Brigida, M., et al. 2012, Nuclear Instruments and Methods in Physics Research A, 692, 262

Ginzburg, V. L. 1988, Soviet Physics Uspekhi, 31, 491

Ginzburg, V. L. & Syrovatskii, S. I. 1964, The Origin of Cosmic Rays

Giordano, F., Naumann-Godo, M., Ballet, J., et al. 2012, ApJ, 744, L2

Giuliani, A., Cardillo, M., Tavani, M., et al. 2011a, ApJ, 742, L30

Giuliani, A., Cardillo, M., Tavani, M., et al. 2011b, ApJ, 742, L30

Giuliani, A., Tavani, M., Bulgarelli, A., et al. 2010, A&A, 516, L11

Goebel, Bartko, H., Carmona, E., et al. 2007, ArXiv e-prints

Gozzini, S. R. 2012, private communication

Green, A. J., Frail, D. A., Goss, W. M., & Otrupcek, R. 1997, AJ, 114, 2058

Guiliano, A., Agile collaboration, & et al. 2013, 5th International Symposium on High-Energy Gamma-Ray Astronomy (Heidelberg), slides of the presentation available for private use: http://www.mpi-hd.mpg.de/hd2012/pages/presentations.htm

Hanlon, W. 2012, Cosmic ray spectrum: www.physics.utah.edu/∼whanlon/spectrum.html

Heck, D., Knapp, J., Capdevielle, J. N., Schatz, G., & Thouw, T. 1998, CORSIKA: a Monte Carlo code to simulate extensive air showers.

Helder, E. A., Vink, J., Bykov, A. M., et al. 2012, Space Sci. Rev., 72

Hess, V. F. 1912, Physikalische Zeitschrift, 13, 10841091

H.E.S.S. coll. 2012, http://www.mpi-hd.mpg.de/hfm/HESS/pages/about/telescopes/

Bibliography

Hessels, J. W. T., Nice, D. J., Gaensler, B. M., et al. 2008, ApJ, 682, L41

Hillas, A. M. 1985, in International Cosmic Ray Conference, Vol. 3, International Cosmic Ray Conference, ed. F. C. Jones, 445–448

Hillas, A. M. 2005, Journal of Physics G Nuclear Physics, 31, 95

Hinton, J. A. & Hofmann, W. 2009, ARA&A, 47, 523

Holder, J. 2012, ArXiv e-prints

IceCube collaboration, Abbasi, R., Abdou, Y., et al. 2012, ArXiv e-prints

Čerenkov, P. A. 1937, Phys. Rev., 52, 378

Kampert, K.-H. & Watson, A. A. 2012, European Physical Journal H, 37, 359

Kang, H., Jones, T. W., & Gieseler, U. D. J. 2002, ApJ, 579, 337

Kellermann, H. 2011, Diploma Thesis, Munich University for Applied Sciences, private use at http://www.magic.mppmu.mpg.de.

Kelner, S. R., Aharonian, F. A., & Bugayov, V. V. 2006, Phys. Rev. D, 74, 034018

Klepser, S. 2011, in International Cosmic Ray Conference, Vol. 7, International Cosmic Ray Conference, 172

Koo, B.-C., Heiles, C., Stanimirović, S., & Troland, T. 2010, AJ, 140, 262

Koo, B.-C., Kim, K.-T., & Seward, F. D. 1995a, ApJ, 447, 211

Koo, B.-C., Kim, K.-T., & Seward, F. D. 1995b, ApJ, 447, 211

Koo, B.-C., Lee, J.-J., & Seward, F. D. 2002, AJ, 123, 1629

Koo, B.-C., Lee, J.-J., Seward, F. D., & Moon, D.-S. 2005, ApJ, 633, 946

Koo, B.-C. & Moon, D.-S. 1997a, ApJ, 475, 194

Koo, B.-C. & Moon, D.-S. 1997b, ApJ, 485, 263

Krause, J., Carmona, E., Reichardt, I., & for the MAGIC Collaboration. 2011, ArXiv e-prints

Krymskii, G. F. 1977, Akademiia Nauk SSSR Doklady, 234, 1306

Lagage, P. O. & Cesarsky, C. J. 1983, A&A, 125, 249

Lazarian, A., Vlahos, L., Kowal, G., et al. 2012, ArXiv e-prints

Lee, K. J., Guillemot, L., Yue, Y. L., Kramer, M., & Champion, D. J. 2012, MNRAS, 424, 2832

Letessier-Selvon, A. & Stanev, T. 2011, Reviews of Modern Physics, 83, 907

Li, T.-P. & Ma, Y.-Q. 1983, ApJ, 272, 317

Lombardi, S., Berger, K., Colin, P., et al. 2011, ArXiv e-prints

Longair, M. S. 2010, High Energy Astrophysics

Lorenz, E. & Wagner, R. 2012, European Physical Journal H, 37, 459

MAGIC coll. 2012, http://magic.mppmu.mpg.de/

Malkov, M. A. 1998, Phys. Rev. E, 58, 4911

Malkov, M. A., Diamond, P. H., & Sagdeev, R. Z. 2012a, ArXiv e-prints

Malkov, M. A., Diamond, P. H., Sagdeev, R. Z., Aharonian, F. A., & Moskalenko, I. V. 2012b, ArXiv e-prints

Malkov, M. A. & O'C Drury, L. 2001a, Reports on Progress in Physics, 64, 429

Malkov, M. A. & O'C Drury, L. 2001b, Reports on Progress in Physics, 64, 429

Malkov, M. A. & Voelk, H. J. 1995, A&A, 300, 605

Mariotti, M. 2010, The Astronomer's Telegram, 2967, 1

Marisaldi, M., Fuschino, F., Labanti, C., et al. 2011, ArXiv e-prints

Meyer, M. 2005, MAGIC-TDAS, private use at http://www.magic.mppmu.mpg.de.

Mirzoyan, R. 1997, in International Cosmic Ray Conference, Vol. 7, International Cosmic Ray Conference, 265

Mirzoyan, R., Garczarczyk, M., Hose, J., & Paneque, D. 2007, Astroparticle Physics, 27, 509

Mirzoyan, R., Sobczynska, D., Lorenz, E., & Teshima, M. 2006, Astroparticle Physics, 25, 342

Moisés, A. P., Damineli, A., Figuerêdo, E., et al. 2011, MNRAS, 411, 705

Montmerle, T. 1979, ApJ, 231, 95

Moon, D.-S. & Koo, B.-C. 1994, Journal of Korean Astronomical Society, 27, 81

Moralejo, A., Gaug, M., Carmona, E., et al. 2009, ArXiv e-prints 0907.0943

Mori, M. 2009, Astroparticle Physics, 31, 341

Morlino, G. 2011, MNRAS, 412, 2333

Morlino, G. & Caprioli, D. 2012, A&A, 538, A81

Motoki, M., Sanuki, T., Orito, S., et al. 2003, Astroparticle Physics, 19, 113

Müller, D. 2012, European Physical Journal H, 37, 413

Nava, L. & Gabici, S. 2012, ArXiv e-prints

Neronov, A. & Semikoz, D. V. 2010, ArXiv e-prints

Bibliography

Nolan, P. L., Abdo, A. A., Ackermann, M., et al. 2012, ApJS, 199, 31

O'C. Drury, L. 2012, ArXiv e-prints

Ohira, Y., Murase, K., & Yamazaki, R. 2011, MNRAS, 410, 1577

Ong, R. A. 2010, The Astronomer's Telegram, 2968, 1

Ong, R. A., Acciari, V. A., Arlen, T., et al. 2009, ArXiv e-prints

Ostriker, J. P. & McKee, C. F. 1988, Reviews of Modern Physics, 60, 1

Paneque et al., O. 2011, in Proceedings of the Fermi Symposium, Rome

Paron, S. & Giacani, E. 2010, A&A, 509, L4

Ptuskin, V. S. & Zirakashvili, V. N. 2003, A&A, 403, 1

Ptuskin, V. S. & Zirakashvili, V. N. 2005, A&A, 429, 755

Reynolds, S. P., Gaensler, B. M., & Bocchino, F. 2012, Space Sci. Rev., 166, 231

Reynolds, S. P. & Gilmore, D. M. 1986, AJ, 92, 1138

Riquelme, M. A. & Spitkovsky, A. 2011, ApJ, 733, 63

Romero, G. E. 2010, Mem. Soc. Astron. Italiana, 81, 181

Romero, G. E., Okazaki, A. T., Orellana, M., & Owocki, S. P. 2007, A&A, 474, 15

Rossi, B. & Hall, D. B. 1941, Physical Review, 59, 223

Rothenflug, R., Ballet, J., Dubner, G., et al. 2004, A&A, 425, 121

Rousseau, R., Grondin, M.-H., Van Etten, A., et al. 2012, A&A, 544, A3

Sato, M., Reid, M. J., Brunthaler, A., & Menten, K. M. 2010, ApJ, 720, 1055

Schure, K. M., Bell, A. R., O'C Drury, L., & Bykov, A. M. 2012, Space Sci. Rev., 14

Sedov, L. I. 1959, Similarity and Dimensional Methods in Mechanics (Similarity and Dimensional Methods in Mechanics, New York: Academic Press, 1959)

Seward, F. D. & Wang, Z.-R. 1988, ApJ, 332, 199

Simpson, J. A. 1983a, Annual Review of Nuclear and Particle Science, 33, 323

Simpson, J. A. 1983b, Annual Review of Nuclear and Particle Science, 33, 323

Sitarek, J. 2010, Ph.D. Thesis, University of Lodz, private use at http://www.magic.mppmu.mpg.de.

Sobczynska, D. 2007, Journal of Physics G Nuclear Physics, 34, 2279

Spiering, C. 2012, European Physical Journal H, 37, 515

Strong, A. W. & Moskalenko, I. V. 1998, ApJ, 509, 212

Strong, A. W., Moskalenko, I. V., & Ptuskin, V. S. 2007, Annual Review of Nuclear and Particle Science, 57, 285

Strzys, M. 2012, private communication

Tavani, M., Bulgarelli, A., Vittorini, V., et al. 2011, Science, 331, 736

Tavani, M., Giuliani, A., Chen, A. W., et al. 2010, ApJ, 710, L151

Tescaro, D., Aleksic, J., Barcelo, M., et al. 2009, ArXiv e-prints

Uchiyama, Y., Aharonian, F. A., Tanaka, T., Takahashi, T., & Maeda, Y. 2007, Nature, 449, 576

Uchiyama, Y., Blandford, R. D., Funk, S., Tajima, H., & Tanaka, T. 2010, ApJ, 723, L122

Uchiyama, Y. & et al. 2011, ArXiv e-prints

Uchiyama, Y., Funk, S., Katagiri, H., et al. 2012, ApJ, 749, L35

Urquhart, J. S., Hoare, M. G., Purcell, C. R., et al. 2009, A&A, 501, 539

Vacanti, G., Fleury, P., Jiang, Y., et al. 1994, Astroparticle Physics, 2, 1

van den Bergh, S. & Tammann, G. A. 1991, ARA&A, 29, 363

VERITAS coll. 2012, http://veritas.sao.arizona.edu/

VERITAS Collaboration, Acciari, V. A., Aliu, E., et al. 2009, Nature, 462, 770

VERITAS Collaboration, Aliu, E., Arlen, T., et al. 2011, Science, 334, 69

Völk, H. J., Berezhko, E. G., & Ksenofontov, L. T. 2003, A&A, 409, 563

Völk, H. J., Berezhko, E. G., & Ksenofontov, L. T. 2005, A&A, 433, 229

Wagner, R. 2006, Ph.D. Thesis, Technische Universität München, private use at http://www.magic.mppmu.mpg.de.

Wakely, S. & Horan, D. 2012, TeVCat: http://tevcat.uchicago.edu

Weekes, T. C. 2003, Very high energy gamma-ray astronomy

Weekes, T. C., Cawley, M. F., Fegan, D. J., et al. 1989, ApJ, 342, 379

White, R. L. & Long, K. S. 1991, ApJ, 373, 543

Wiedenbeck, M. E., Binns, W. R., Christian, E. R., et al. 1999, ApJ, 523, L61

Winston, R. 1970, Journal of the Optical Society of America (1917-1983), 60, 245

Wittek, W. 2002, MAGIC-TDAS, private use at http://www.magic.mppmu.mpg.de.

Bibliography

Yanasak, N. E., Wiedenbeck, M. E., Mewaldt, R. A., et al. 2001, ApJ, 563, 768

Yuan, Q., Yin, P.-F., & Bi, X.-J. 2011, Astroparticle Physics, 35, 33

Zanin, R. 2011, in International Cosmic Ray Conference, Vol. 7, International Cosmic Ray Conference, 71

Zanin, R. 2011, Ph.D. Thesis, Universitat Autonoma de Barcelona, private use at http://www.magic.mppmu.mpg.de.

Zirakashvili, V. N. & Ptuskin, V. S. 2011, ArXiv e-prints

Acknowledgements

First of all, I would like to thank Masahiro Teshima for giving me the opportunity to join the MAGIC experiment and to do my PhD thesis at the Max-Planck-Institute for physics. I want to thank Razmik Mirzoyan for his supervision and support. I am grateful to Christian Kiesling for being my *Doktorvater* at the Ludwig-Maximilian-Universität München. I enjoyed very much all the physics discussions with them and found them very constructive and motivating. Furthermore I want to express my thank for the possibility to join several summer schools and national and international conference.

Many thanks to Tobias Jogler, as my day-to-day supervisor he was always a great help. Many thanks for the supervision, the discussions, the reading of my thesis, but also for the advices concerning timelines, proposals, and so on.

Special thanks goes to my former office mate Julian Sitarek, who not only taught me many basics of gamma ray astronomy as well as technical details but also made the office of the Julians a nice working place. Also special thanks to Emiliano Carmona, for the support in technical details and software, some very good advices and good ideas. Furthermore to Pierre Collin who always had time for discussions and many fruitful suggestions.

I want to appreciate the fantastic working conditions among the people of the W51 team. It was a pleasure to work with Ignasi Reichardt, Rebecca Gozzini, and Emiliano Carmona for almost two years on this source. I will not forget the thousands(?) of emails and dozens of hours of skype discussions. Many details of the final outcome reveal the extraordinary commitment of you guys and girls! The work with the people HESS1857 was (and still is) by no means less inspiring: Many thanks to Stefan Klepser and Victor Stamatescu.

I want to say thank you to the people I shared my time with on the island La Palma. Sometimes, the weather was good, sometimes there was a fun car, sometimes there were pirates and sometimes there was Arehucas or Dorada or wonderful cookies, but also sometimes the weather was less good or the were killer waves, but it always was a great experience. Thanks to the shift crew of P87: Karsten Berger, Dorothee Hildebrand, Thomas Kraehenbuehl, Ben Huber and of P98: Koji Saito, Rubn Lpez, Daniela Dorner and Luigi Cossio and not to forget the upgrade crew: Daniel Mazin, Diego Tescaro, Gianlucca Giavitto, Alicia Lopez, Jose Luis Lemus, and Valeria Scapin.

I am very happy for the great atmosphere in the whole MAGIC collaboration. Special thanks to Marlene Doert, Malwina Ullenbeck, Marc Ribo, Pere Munar-Adrover, Paolo Da Vela, Francesco Dazzi, Iva Snidaric, Tomislav Terzic, Elina Lindfors and all of you for sharing ideas, discussions, time, and drinks.

Bibliography